


Spring 2011

Ultrafast High-Energy Electron Diffraction Study of Photoexcited Bismuth Nanoclusters by Femtosecond Laser Pulses

Ahmed R. Esmail
Old Dominion University

Follow this and additional works at: https://digitalcommons.odu.edu/ece_etds

 Part of the [Condensed Matter Physics Commons](#), and the [Optics Commons](#)

Recommended Citation

Esmail, Ahmed R.. "Ultrafast High-Energy Electron Diffraction Study of Photoexcited Bismuth Nanoclusters by Femtosecond Laser Pulses" (2011). Doctor of Philosophy (PhD), dissertation, Electrical/Computer Engineering, Old Dominion University, DOI: 10.25777/afr9-1j61
https://digitalcommons.odu.edu/ece_etds/68

This Dissertation is brought to you for free and open access by the Electrical & Computer Engineering at ODU Digital Commons. It has been accepted for inclusion in Electrical & Computer Engineering Theses & Dissertations by an authorized administrator of ODU Digital Commons. For more information, please contact digitalcommons@odu.edu.

ULTRAFAST HIGH-ENERGY ELECTRON DIFFRACTION STUDY OF
PHOTOEXCITED BISMUTH NANOCCLUSERS BY
FEMTOSECOND LASER PULSES

by

Ahmed R. Esmail
M.S. February 1997. Cairo University, Egypt
B.S. May 1990. Cairo University, Egypt

A dissertation Submitted to the Faculty of Old Dominion University
In Partial Fulfillment of the Requirements for the Degree of

DOCTOR OF PHILOSOPHY
ELECTRICAL AND COMPUTER ENGINEERING
OLD DOMINION UNIVERSITY
May 2011

Approved by:

_____ /
Hani Elsayed-Ali (Director)

_____ /
Helmut Baumgart (Member)

_____ /
Gen Yankoon (Member)

_____ /
Abdelmagued Elmustafa (Member)

ABSTRACT

ULTRAFAST HIGH-ENERGY ELECTRON DIFFRACTION STUDY OF PHOTOEXCITED BISMUTH NANOCCLUSERS BY FEMTOSECOND LASER PULSES

Ahmed R. Esmail
Old Dominion University, 2011
Director: H. Elsayed-Ali

The advancement in ultrafast electron crystallography (UEC) over the past few decades facilitated the study of structural dynamics in all phases of matter induced by femtosecond laser pulses. This technique became very powerful when the spatial resolution was combined with the temporal resolution, and succeeded in studying chemical reactions by ultrafast electron diffraction, bulk crystal phonons and melting by X-ray diffraction.

In this dissertation, I demonstrate the uniqueness of UEC and its potential in monitoring in real time the structural dynamics of bismuth (Bi) nanoclusters and islands induced by femtosecond laser pulses. Our approach to accomplish this task includes building a time-resolved high energy electron diffraction setup that is capable of delivering high energy and short electron pulses, less than 3 ps, which will facilitate the real time measurement of the Bragg diffraction ring intensity, shift in the peak position and the diffraction ring full width at half maximum (FWHM) at different delay times with respect to the femtosecond excitation. Additionally, the temperature evolution of the same parameters, intensity, position and FWHM of the diffraction peaks, was monitored by using conventional direct current heating stage.

The data collected from the static heating measurements showed that:

- The Bragg peak intensity varies exponentially with temperature and follows Debye-Waller effect up to $T = 464 \pm 6$ K.
- The melting temperature of Bi nanoclusters, $T_{m(\text{nanoclusters})} = 525 \pm 6$ K, is less than that of the bulk Bi, $T_{m(\text{bulk})} = 544$ K, as expected.
- The onset of melting was found to start at $T = 500 \pm 6$ K, which is also confirmed from the temperature-dependent FWHM, since the FWHM is related to the cluster size, we found that the cluster size starts to decrease at $T = 500 \pm 6$ K.
- The Debye temperature of the annealed nanoclusters was found to be 53 ± 6 K along the $\langle 012 \rangle$ direction and 86 ± 9 K along $\langle 110 \rangle$ direction. This confirms the anisotropic nature of Bi nanoclusters. At $T = 464 \pm 6$ K, the diffraction intensity started to deviate from Debye-Waller behavior due to increased lattice anharmonicity.

Another interesting observation was found from the dependence of the relative change in Bragg peak position, $\Delta d/d$ (lattice strain) on temperature in two different directions, $\langle 012 \rangle$ and $\langle 110 \rangle$. I noticed that the thermal expansion coefficient of the Bi (012) and (110) planes is positive up to $\sim 499 \pm 11$ K. However, the expansion coefficient of the Bi (012) planes showed a transition from a positive to a negative value that occurs over the temperature range $T_c \sim 499 \pm 11$ K to 511 ± 8 K. For the Bi (110) planes, the thermal expansion coefficient is positive up to their melting point, which is 525 ± 6 K. This behavior can be explained in terms of vibrational (phonon excitation) and/or non-vibrational (lattice potential deformation) effects on the lattice near melting.

- The study of the FWHM of the diffraction rings as a function of temperature confirmed the formation of a liquid shell of Bi at the onset of solid-liquid transformation. This shell includes Bi atoms in the liquid phase, detached atoms with high vibrational amplitude and vacancies.

Another task was accomplished in which I utilized the pump-probe ultrafast electron diffraction setup that I built and tested with picoseconds laser pulses in PERI lab - Old Dominion University, transferred later to the Applied Research Center where a femtosecond laser system was used to characterize the transient effects induced in Bi nanoclusters due to femtosecond laser excitation. The sample under consideration is excited by a femtosecond laser pulses with moderate fluence just to induce an observable change in the diffraction pattern and far from sample damage. The femtosecond laser pulses induce changes in the charge carrier distribution function of Bi nanoclusters, which leads to a disturbance in the lattice potential and drives the solid-liquid phase transformation. The melting is detected as decrease in the integrated intensity of the Bragg peaks with time delay.

Another interesting behavior is observed in these experiments in which a lattice contraction following femtosecond laser excitation and proceeding over a time period of ~ 6 ps precedes the lattice expansion in Bi (012) planes. Again, the electronic excitation, here, plays an important role in inducing a sudden change in the interatomic forces which leads to A_{1g} phonon excitation. Due to the limited resolution of our system (2-3 ps) we were not able to detect the A_{1g} oscillation frequency/wavelength, but its effects which appear as lattice contraction upon its decay can be seen from the temporal evolution of the Bragg peak position over the time period, $0 < t < 6$ ps.

The incident laser fluence was not high enough to induce full melting, but was enough to induce partial lattice melting. This was observed as a gradual increase in the FWHM of the Bragg peaks as a function of delay time, i.e., formation of thin liquid layer which increases in size with time when the lattice temperature increases through electron-phonon and/or phonon-phonon relaxation.

Also, the time evolution of the relative Bragg peak intensity, $\Delta d/d$ and FWHM were monitored for Bi islands. Bi islands were prepared by annealing the as-deposited Bi thin film (5 nm, average coverage) solely by either raising its temperature slowly up to ~ 525 K or with ultrafast laser pulses of fluence $0.8 \text{ mJ/cm}^2 - 2.4 \text{ mJ/cm}^2$.

In summary,

- The lattice thermalization time of Bi islands in $\langle 012 \rangle$ direction is higher than that along $\langle 110 \rangle$ direction.
- I did not detect a change in $\Delta d/d$ with time, which is not expected and need further study of different factors that may affect this behavior. These factors are, but not limited to, thermal history, annealing temperature, laser fluence, substrate cluster size distribution, and morphology of the sample surface.
- The time evolution of the percentage change in molten layer thickness measured from the change in FWHM showed that the sample is partially melted, and the thickness of the molten layer is a function of the incident fluence.
- An interesting behavior was also detected, which is the transient times for Bi nanoclusters as measured from the time evolution of relative change in the diffraction intensity for Bi nanoclusters is higher than that measured from Bi islands. This will be explained in terms of the effect of the cluster size on the

electronic energy band structure of Bi, which leads to the creation of energy sub-bands as well as increase in the energy gap between the conduction and the valence band as the dimensions of the Bi sample decreases.

Dedicated to my wife, Hwaida
with love.



ACKNOWLEDGMENTS

I would like to express my deep thanks and appreciation to Dr. H. Elsayed-Ali for giving me the opportunity to do my Ph.D. thesis research in his lab at the Applied Research Center at Old Dominion University and for his support and guidance during my work there. Thanks to the committee members, Dr. Helmut Baumgart, Dr. Gon Namkoong, and Dr. Abdelmageed Elmustafa who gave their valuable time to evaluate and help me to revise my dissertation and for their valuable input.

Also, I would like to specially thank the people I worked with during my stay in the lab, M. Abdel-Fattah and I. El-Kholy. Without their advice, discussion and support, this work would not see the light of day.

A special thanks to my daughter Rana who helped me in editing and reviewing different parts of my dissertation.

Last, but not the least, thank you to my wife, without whom my whole life and my stay here to finish my Ph.D. could not be possible. I'm totally indebted to her and if there is a person who deserves to be awarded the Ph.D. degree, it is she.

To her I dedicate this Ph.D. and my life.

TABLE OF CONTENTS

LIST OF TABLES		xvi
LIST OF FIGURES		xvii
Chapter		
1. CRYSTAL STRUCTURE OF BISMUTH AND REVIEW OF PREVIOUS WORK		
1.1	Bismuth, Why?	1
1.2	Bulk Bi Crystal Structure	1
1.2.1	Rhombohedral structure	3
1.2.2	Hexagonal structure	5
1.2.3	Pseudocubic Structure	5
1.3	Electronic Band Structure of Bi	5
1.4	Size-Dependent Melting Point Depression	8
1.5	Surface Melting and Superheating	9
1.6	Previous Work in Time-Resolved Electron Diffraction Studies on Bi	11
1.7	Dissertation Motivation and Organization.....	15
1.8	References of Chapter 1.....	19
2. THEORY OF ELECTRON DIFFRACTION		
2.1	Introduction:	29
2.2	Theory of Electron Diffraction.....	30
2.2.1	De Broglie Waves	30
2.2.2	Laws of Diffraction, the Contribution of Laue, Bragg and Ewald	32
2.2.2.1	Bragg's law of diffraction.....	32
2.2.2.2	Laue diffraction condition.....	35
2.2.2.3	Ewald sphere (reflecting sphere).....	38
2.3	Intensity of the Diffracted Beam	39
2.3.1	The atomic scattering factor.....	40
2.3.2	The geometrical structure scattering factor	41
2.4	Debye-Waller Effect	42
2.5	Transient Structure Dynamics	44
2.6	References of Chapter 2	46
3. EXPERIMENTAL SETUP		
3.1	Introduction	47
3.2	Photoactivated Electron Gun, Construction and Operation.....	48
3.3	Vacuum System	51
3.4	Sample Heating and Manipulation	52
3.5	Laser System	53
3.5.1	Ti:sapphire oscillator (seed laser)	53

3.5.2	Laser amplifier, (stretcher - regenerative amplifier - compressor)	56
3.6	Electron Diffraction Pattern Acquisition and Data Analysis ...	58
3.7	Expected Improvement.....	58
3.8	Reference of Chapter 3.....	60
4. THIN FILM PHOTOEXCITATION BY FEMTOSECOND LASER PULSES.....		
4.1	Introduction	61
4.2	Bi on the Reduced Dimension, (Thin Films, Nanowires, and Nanoclusters)	63
4.3	Ultrafast Laser Excitation and Dynamics in Bi Nanoclusters ...	66
4.3.1	Electron and lattice dynamics induced by ultrafast laser pulses.....	67
4.3.2	The one and the two temperature model.....	71
4.3.3	Mechanism of coherent phonon excitation	73
4.4	References of Chapter 4.....	76
5. OBSERVATION OF LATTICE CONTRACTION WITH HEATING OF BISMUTH NANOCLUSTERS NEAR ITS MELTING POINT.....		
5.1	Introduction.....	80
5.2	Melting, is it Abrupt or Continuous?.....	80
5.3	Experiment	83
5.4	Results and Discussion.....	84
5.4.1	Morphology and diffraction pattern indexing of the grown bismuth nanoclusters.....	84
5.4.2	Debye-Waller factor.....	90
5.4.3	Bragg peak position.....	93
5.4.4	Full width at half maximum.....	95
5.5	Discussion.....	96
5.6	Conclusions.....	98
5.7	References of Chapter 5	100
6. RESULTS, DATA ANALYSIS AND DISCUSSION OF TIME-RESOLVED DATA COLLECTED FROM Bi NANOCLUSTERS.....		
6.1	Introduction.....	106
6.2	Laser Fluence Dependent Electron Diffraction.....	108
6.3	Time-Resolved Electron Diffraction Data Analysis.....	115
6.4	References of Chapter 6.....	130
7. TIME-RESOLVED COMPARATIVE STUDY, BI ISLANDS VS BI NANOCLUSTERS		
7.1	Introduction.....	132
7.2	Experiment.....	133
7.3	Results.....	135
7.4	Discussion.....	148

7.5	Conclusions.....	152
7.6	References of Chapter 7.....	153
8.	SUMMARY AND CONCLUSIONS.....	155
8.1	References of Chapter 8.....	161
APPENDICES		
A.	Characterization of the Electron Pulse.....	162
B.	Evaporator and Procedures to Make Samples	167
C.	Vacuum System Pump Down and Bringing Back to Atmosphere Procedure.....	170
D.	Femtosecond Laser System Operation.....	174
E.	Pump-Probe Setup	178
F.	Procedures Used to Acquire Data (E-Beam Alignment With Laser, Laser Alignment on Target, and Condition of Working Photocathode).....	180
G.	Operation of the Camera, Image Acquisition and Delay Stage Software.	182
H.	How Bragg Peak Intensity, Position and FWHM Were Measured?.....	185
I.	Data on Continuous Heating	198
J.	Time-resolved Data Summary Collected from Bi Nanoclusters	214
K.	Time-Resolved Data Summary Collected From Bi Islands	233
L.	Data Collected to Study Superheating of Bismuth Islands	244
M.	List of Vendors and Different Components Used in Film Preparation and Time-Resolved Electron Diffraction Setup	253
VITA	255

LIST OF TABLES

Table		Page
1.1	Summary of the bulk melting points and degree of superheating of various elements and compounds. These values were adopted from Ref. [29], chapter I and references therein unless otherwise noted.....	10
6.1	Summary of the radial average parameters used in Fig. 6.1.(d).....	111
6.2	Summary of the fitting parameters and functions of the data presented in Fig. 6.2.(a) - (c).....	112
6.3	Summary of calculated molten layer thickness at different laser fluence calculated from the data presented in Fig. 6.2.(c).....	115
7.1	Summary of temperature rise calculation from Eq. 5.4 per incident laser fluence.....	137
7.2	Summary of the fitting parameters used in equation 7.1. The error in fluence measurements was found not to exceed 5% of the measured value.	138

LIST OF FIGURES

Figure	Page	
1.1	Crystal structure of bulk Bi. Rhombohedral unit cell is represented by the solid and short dashed lines incorporated in the hexagonal unit cell represented by long dashed lines. The white and black solid spheres represent the two atoms in the rhombohedral unit cell. The short dashed and solid black lines represent the vectors spanning the rhombohedral and hexagonal lattice, respectively. The Cartesian coordinate systems used here are: bisectrix (C_1, y), binary (C_2, x) and trigonal (C_3, z).	3
1.2	Bulk structure of Bi(111). (a) Top view and (b) Side view of the first four layers. Solid lines represent the covalent bonds between the atoms. Reproduced from Ref. [17]. The angle between any two basis vectors is $\alpha_r = 57^\circ 14'$. Therefore the crystal structure of Bi is completely identified by a_{rh} , α_r and the position of the two basis atoms.	4
1.3	First Brillouin zone of bulk Bi and some important symmetry points, L and T are electron and holes pockets, respectively, in the Fermi surface (shaded area)..	7
1.4	Electron energy in linear atomic chain where atoms are not equally spaced. Reproduced from Ref. [27].	7
2.1	Davisson and Germer experiment. The electron beam intensity is Maximum at an angle 50° with respect to the incident beam. Reproduced from Ref. [2].	32
2.2	(a) Bragg's law where $AB = BC = d_{hkl}$ and the path difference $(AB+BC) = 2d_{hkl} \sin\theta$. (b) Bragg's law for a general case in which $AB \neq BC$, again $(AB+BC) = 2d_{hkl} \sin\theta$	33
2.3	The CsCl structure viewed along (100) plane. The scattered waves are in phase if they are scattered off the atoms of the same type. Destructive interference results form a phase difference of $2\pi\Delta/\lambda$ between the scattered waves from successive planes. Reproduced from Ref. [2].....	35
2.4	Scattering of incident waves from two atoms located at two lattice sites O and P, with graphical details of phase difference calculation of the scattered waves. Reproduced from Ref. [2].....	36

2.5	The change in momentum vector $\Delta \bar{k}$ in terms of the diffraction Bragg angle θ . Reproduced from Ref. [2].	38
2.6	Graphical and vector representation of Bragg's law. Reproduced from Ref. [2].	40
2.7	Ewald Sphere (reflection sphere), the reciprocal sphere is not shown. Reproduced from Ref. [2].	40
2.8	The position of the j th atom relative to the origin is specified by the vector \vec{r}_j . Reproduced from Ref. [2].	43
2.9	Different mechanisms of lattice response to ultrashort laser pulses (a, c, e and g), and their effect on the detected diffraction pattern (b, d, e, and f). In the upper side of the graph, the blue circles represent the unperturbed lattice, and the red circles represent the perturbed lattice. a) Thermal effects induce lattice disorder, which in turn is translated as reduced intensity in the diffraction peak (b) due to Debye-Waller effect. (c) Homogeneous lattice disorder can lead to lattice expansion or contraction, red peak or green peak in (d), respectively. (e) Creation of satellite peaks in (f) due to the generation of longitudinal acoustic phonons. (g) Excitation of homogeneous optical phonons can reduce the detected diffraction peak intensity (h) but do not affect the peak position.	44
3.1	(a) Schematic diagram of the lab-made photoactivated electron gun as well as the set of air-cooled electromagnets used to focus and direct the electron beam towards the sample. The photocathode can be operated at -40 kV, but for experimental and system stability purposes we chose to operate it at -35 kV. (b) Corresponding picture of the electron gun assembly.	49
3.2	Layout of the time-resolved electron diffraction setup. A 120fs pulse is generated from Ti:sapphire chirped pulse amplifier. The system is running at 1 kHz. In this setup, the laser pulse is divided into two parts; one is frequency tripled and used to generate photoelectron from photoactivated electron gun (probe beam), and the other part is used to excite the sample (pump beam). The synchronization between the two pulses is granted since they are generated from a single beam.....	51
3.3	Block diagram for femtosecond laser, SDG II stands for synchronization and delay generator. Reproduced from Spitfire Spectra Physics manual.	54
3.4	Schematic of a multi-mode laser output, showing the fluctuations of its output. Reproduced from Ref. [6].	55

3.5	Modelocked laser output, (a) spectrum, (b) laser output in time domain. Reproduced from Ref. [6].	55
3.6	Schematic diagram showing the active and the passive modelocking [7]. (a) Active modelocking; in this technique, modulation of the radiation in the laser cavity is done by a signal derived from an external clock source, to the modulator, and matched to the cavity roundtrip time. (b) Passive modelocking, in which the laser radiation itself generates a modulation through the action of non linear device in the laser cavity [7], and it is thus synchronized to the cavity round trip frequency. Reproduced from Ref. [7].	57
3.7	Schematic diagram of CPA technique.....	57
3.8	Grating-pair arrangement for seed pulse stretching resulting in a longer laser pulse that is seeded to the regenerative amplifier.....	58
4.1	Band structure of bulk Bi, (green lines, Ref. [6], red lines, Ref. [7]). Reprinted from Ref. [1]	62
4.2	Semimetal-semiconductor phase transition in Bi at different temperatures and thicknesses. At constant temperature, Bi can be semimetal (phase III) or semiconductor (phase I) or undergoes SM-SC transition as the temperature is reduced from 300 to 0 K. Reproduced from Ref. [13].	64
4.3	Schematic diagram showing the electronic band structure of bulk Bi (dashed lines) compared to that of the nanowires/nanoclusters (solid lines). Δ_c is the conduction-valence band overlap. Reproduced from Ref. [13].	65
4.4	Time scale of different processes induced in the lattice as a result of ultrashort laser pulse excitation. The dark bars show an approximate time scale of occurrence of these processes. Reproduced from Ref. [17].	68
4.5	Schematic of the different electron and lattice processes induced by ultrashort laser pulses: (a) single and multiphoton absorption, (b) Carrier absorption, (c) Ionization, (d) Carrier distribution before scattering, (e) Carrier - carrier scattering, (f) Carrier - phonon scattering, (g) Radiative recombination, (h) Auger recombination, (i) Diffusion of excited carriers, (j) Thermal diffusion, (k) Ablation (l) Resolidification or condensation. Reproduced from Ref. [17]......	70
4.6	Bi lattice structure showing the optical phonons with symmetry A_{1g} and E_g . Reproduced from Ref. [34].	74

5.1	Temperature dependence of Gibbs free energy of a simple substance near its melting point. Reprinted from Ref. [12].	81
5.2	High resolution transmission electron microscopy (HRTEM) images and the corresponding diffraction pattern of (a) as-deposited Bi 5 nm film, (b) after thermal annealing up to 525 K, (c) after annealing with femtosecond laser pulses at a fluence of $\sim 0.8 \text{ mJ/cm}^2$ with 1 kHz repetition rate, and (d) thermally annealed at 450 K while simultaneously exposing to the laser pulses.	86
5.3	The length distribution of the major axis and the minor axis of the nanoclusters shown in Fig. 5.2.(d).	87
5.4	(a) Diffraction pattern of as-deposited Bi and annealed sample and (b) the corresponding radial average as a function of momentum transfer $S = 2\pi/d$	88
5.5	High resolution transmission electron microscopy HRTEM images of (a) as-deposited and (b) annealed samples. The as-deposited samples show flat islands, while those annealed thermally and simultaneously with the laser show nanoclusters.	89
5.6	Temperature dependence of the natural log of intensity at temperature T normalized to that at temperature = 323 K (I_T/I_0) of the (012) and (110) Bragg peaks of Bi nanoclusters is shown in Fig. 5.2.(d). The inset shows the diffraction pattern at different temperatures.	92
5.7	Temperature-dependent strain of the Bi (012) and Bi (110) planes.....	94
5.8	Temperature dependence of the percentage change in the molten layer thickness, calculated from diffraction ring FWHM at temperature T normalized to that at temperature $T = 323 \text{ K}$	96
6.1	(a) Radial average of the diffraction pattern at $t = 26.6 \text{ ps}$ when the pump laser is OFF compared to that when the pump laser is ON with fluence = 3.7 mJ/cm^2	108
	(b) Isolated peaks of the diffraction pattern at $t = 26.6 \text{ ps}$ when the pump laser is ON, with fluence = 3.7 mJ/cm^2	109
	(c) Isolated peaks of the diffraction pattern at $t = 26.6 \text{ ps}$ when the pump laser is OFF.....	110
	(d) Radial average of the same diffraction pattern analyzed with different parameters of the radial average ring to show the sensitivity of the data analysis to any misfit between the ring and the pattern.....	110
6.2	(a) Normalized Bragg peak intensity as a function of the incident laser fluence.	113

	(b) Normalized Bragg peak position change as a function of the incident laser fluence.	114
	(c) Normalized Bragg peak FWHM as a function of the incident laser fluence calculated from the (012) Bragg peak.	114
6.3	Snapshots of the diffraction pattern of Bi at different delay times.....	118
6.4	Radial average of the diffraction pattern shown in Fig. 6.3 after background removal, (a) full range of diffraction ring pattern and (b) the first three diffraction rings.	119
6.5	(a) Time evolution of the strain detected along (012) and the corresponding normalized change in intensity due to femtosecond laser excitation pulses of fluence 2.9 mJ/cm^2	120
	(b) Percentage change FWHM as a function of delay time at 2.0 mJ/cm^2 and 2.9 mJ/cm^2 calculated from (012) Bragg peak.....	121
6.6	Time evolution of the strain detected along (110) and the corresponding normalized change in intensity due to femtosecond laser excitation pulses of fluence 2.9 mJ/cm^2	123
6.7	Normalized Bragg peak center position of (012) Bragg peak as a function of delay time at two different fluences.....	124
6.8	Different planes in hexagonal unit cell of Bi.....	126
6.9	Change in Debye-Waller factor with different interplanar spacing. The error bars were calculated by software in the form of the deviation of the actual data points from the linear fitting function.....	128
7.1	HRTEM images and diffraction pattern of (a) laser annealed Bi samples, S1 and (b) laser annealed sample simultaneously with continuous heating up to 470 K, S2.....	134
7.2	Time dependent normalized intensity of Bragg peak (012) of photoexcited Bi islands by laser fluence $1.9 \pm 5\% \text{ mJ/cm}^2$ and $2.4 \pm 5\% \text{ mJ/cm}^2$	139
7.3	Time dependent normalized intensity of Bragg peak (110) of photoexcited Bi islands by laser fluence of $1.9 \pm 5\% \text{ mJ/cm}^2$ and $2.4 \pm 5\% \text{ mJ/cm}^2$	140
7.4	Time dependent normalized intensity of Bragg peak (012) of photoexcited Bi nanoclusters by laser fluence of 1.9 mJ/cm^2 and 2.4 mJ/cm^2	141

7.5	Time dependent normalized intensity of Bragg peak (110) of photoexcited Bi nanoclusters by laser fluence of $1.9 \pm 5\%$ mJ/cm ² and $2.4 \pm 5\%$ mJ/cm ²	142
7.6	Time evolution of Bragg peak intensity for (a) (012) planes, (b) (110) planes at two different fluences.	143
7.7	Relative change in Bragg peak position ($\Delta d/d$) as a function of delay time for Bragg peak (012) of photoexcited Bi nanoclusters by laser fluence of $1.9 \pm 5\%$ mJ/cm ² and $2.4 \pm 5\%$ mJ/cm ²	144
7.8	Relative change in Bragg peak position ($\Delta d/d$) as a function of delay time for Bragg peak (110) of photoexcited Bi nanoclusters by laser fluence of $1.9 \pm 5\%$ mJ/cm ² and $2.4 \pm 5\%$ mJ/cm ²	145
7.9	Relative change in Bragg peak FWHM as a function of delay time of photoexcited Bi nanoclusters by laser fluence of 1.9 mJ/cm ² and 2.4 mJ/cm ² for (012) Bragg peak.	146
7.10	Percentage change in Bragg peak FWHM as a function of delay time of photoexcited Bi islands by laser fluence of 1.9 mJ/cm ² and 2.4 mJ/cm ² for (012) Bragg peak.	147
7.11	Sample graph that shows the poor fitting of the exponential and Sigmoidal functions which therefore cannot be used to calculate the lattice thermalization time. A proper model is needed to fit properly such behavior.	148
7.12	Schematic diagram showing the electronic band structure of bulk Bi (dashed lines) compared to that of the nanowires/nanoclusters (solid lines). Reproduced from Ref. [9]. Δ_0 is the conduction-valence band overlap.	150
A.1	Schematic of the photoactivated electron gun (PAEG) components.....	164
A.2	Effect of the drift region length on the electron pulse broadening for two cases in which number of electrons/pulse = 1000 electrons and 5000 electrons, reprinted from Ref. [1].	164
A.3	FWHM of the probe pulse versus propagation time in the drift region for Gaussian and “top hat” beams, reprinted from Ref. [2].....	165
B.1	Evaporator system components.....	169
C.1	TR vacuum chamber.	172

C.2	Pumping station consists of a turbo molecular pump and a mechanical pump.	173
D.1	Femtosecond laser system.	175
D.2	Main controller for the Darwin laser (pumping laser).....	176
D.3	Control unit for the oscillator (seed laser).....	177
D.4	SDG for seed laser and external trigger unit of pumping laser.....	177
E.1	Layout of the time-resolved electron diffraction setup. A 120fs pulse is generated from Ti:sapphire chirped-pulse amplifier. The system is running at 1 kHz. In this setup, the laser pulse is divided into two parts; one is frequency tripled and used to generate photo-electron from the photoactivated electron gun (probe beam), and the other part is used to excite the sample (pump beam). The synchronization between the two pulses is granted since they are generated from a single beam.	178
E.2	Actual pump-probe setup with pump and probe beam paths.....	179
G.1	Winview software main panel for image acquisition.....	183
G.2	Delay stage software starting window.....	184
G.3	Delay stage software main control window.....	184
I.1	(a) Diffraction pattern of Bi nanoclusters at different temperatures and (b) The corresponding radial profile.....	198, 199
J.1.1	Time evolution of Bragg peak intensity for (a) (012) planes, (b) (110) planes at different laser fluences.....	214
J.1.2	Time evolution of relative change in Bragg peak ring size at different laser fluences for (a) (012) planes and (b) (110) planes.....	216
J.1.3	Time evolution of Bragg peak average FWHM at different fluences....	218
J.2.1	Time evolution of Bragg peak intensity and relative change in ring radius ($\Delta d/d$) for (a) (012) planes, (b) (110) planes at $2.4 \pm 5\%$ mJ/cm ² laser fluence.	219
J.3.1	Time evolution of Bragg peak intensity and relative change in ring radius ($\Delta d/d$) for (a) (012) planes, (b) (110) planes at $2.1 \pm 5\%$ mJ/cm ² laser fluence.	222

J.3.2	Time evolution of Bragg peak FWHM at $2.1 \pm 5\%$ mJ/cm ² laser fluence.	224
J.4.1	Time evolution of relative change in Bragg peak intensity at different fluences for (a) (012) planes and (b) (110) planes.....	225
J.4.2	Time evolution of relative change in Bragg peak ring radius at different fluences for (a) (012) planes and (b) (110) planes.....	227
J.4.3	Time evolution of relative change in Bragg peak FWHM at different fluences.	229
J.5	Fluence dependence of the Bragg (a) peak intensity, (b) $\Delta d/d$, and (c) normalized FWHM.	230
K.1.1	Time evolution of Bragg peak intensity for (a) (012) planes, (b) (110) planes.	233
K.1.2	Time evolution of Bragg peak FWHM.....	235
K.2.1	Time evolution of Bragg peak intensity for (a) (012) planes, (b) (110) planes at two different fluences.	236
K.2.2	Time evolution of relative change in Bragg peak FWHM at different fluences.	238
K.3.1	Time evolution of Bragg peak intensity for (a) (012) planes and (b) (110) planes at two different fluences.....	239
K.3.2	Time evolution of Bragg peak FWHM at different fluences.....	241
K.4	Fluence dependence of the Bragg (a) peak intensity, (b) $\Delta d/d$, and (c) normalized FWHM.	242

CHAPTER 1*

CRYSTAL STRUCTURE OF BISMUTH AND REVIEW OF PREVIOUS WORK

1.1. Bismuth, Why?

Due to its unusual properties and the polymorphic nature of the crystal structure, bismuth (Bi) has been a subject of extensive studies especially in reduced size scale form. Over decades, Bi thin films, nanoclusters and nanowires were shown to have some properties that are different from those of the bulk and made them technologically important. For example, superconductivity was observed in Bi thin films [1] and in particles with reduced dimensions [2], while others have reported that a Bi thin film possesses nonlinear properties [3] and shows quantum size effects [4]. Although bulk Bi was classified as a semimetallic material due to the small overlap between the conduction and valence bands, a transition to a semiconductor with indirect band gap was observed at a critical thickness [5-10]. This makes Bi a useful material in developing optical and electro-optical applications. In addition, Bi has enhanced thermoelectric efficiency [11] and large magnetoresistance [12]. Extensive work has been done to study the dependence of the film structure on the thickness [6, 13-15], as well as the dependence of electrical transport properties on the structure [16].

1.2. Bulk Bi Crystal Structure

Bi is a member of group V semimetals, such as arsenic (As) and antimony (Sb), with α -arsenic or A7 structure [17-19]. The semimetallic nature is attributed to the high anisotropic and complex nature of the Fermi surface of the rhombohedral structure of Bi

* The reference model of this work follows the SPIE format.

[11]. The rhombohedral unit cell of Bi, space group $R\bar{3}m$, has two atoms per unit cell with cell parameters, $a_r = 4.7459 \text{ \AA}$, $\alpha_r = 57^\circ 14'$ [21]. The two atoms are occupying the positions $(0, 0, 0)$ and $(2u, 2u, 2u)$ where $u = 0.237$ [21].

The rhombohedral structure of Bi may be visualized as a distorted simple-cubic structure which may be obtained by, 1) straining the unit cell along the body diagonal and reducing the rhombohedral angle from 60° to α_r , and 2) displacing the atom at the center toward its neighboring atom along the body diagonal till the position $2u$ is reached.

This distortion results in atoms with the following arrangement:

- Each atom has three equidistant nearest neighbor atoms (forming pyramidal intra-layer covalent bond) and another three equidistant atoms that are farther away which lie in the adjacent layer (forming inter-layer bonds of metallic or weak intermolecular attractive forces of Van der Waals nature) [22-24].
- This atomic arrangement (bilayer array) allows the bonding within each layer to be much stronger than the inter bilayer bonding, which in turn makes the Bi crystals easily cleaved along (111) plane, Fig. 1.1.

In general, the bulk structure of Bi, and consequently the surfaces, can be described in three different ways: by using the rhombohedral notation, hexagonal notation, or pseudocubic notation. The relation between rhombohedral and hexagonal unit cells is shown in Fig. 1.1. This is in addition to cubic structure notation, which can be used to describe the bulk structure of Bi. However, we will consider the rhombohedral and hexagonal description and the reader can refer to Ref. [18] for more details about the pseudocubic indexing. Figure 1.2 shows the top and the side views of the atomic arrangement of the bulk Bi along $\langle 111 \rangle$ direction.

1.2.1. Rhombohedral structure

Rhombohedral lattice with two atoms per unit cell is adopted to describe the Bi structure. The basis vectors of the unit cell are \vec{a}_1 , \vec{a}_2 , and \vec{a}_3 , and represented by short dashed lines in Fig. 1.1, where, $|\vec{a}_1| = |\vec{a}_2| = |\vec{a}_3| = a_{rh} = 4.7459 \text{ \AA}$.

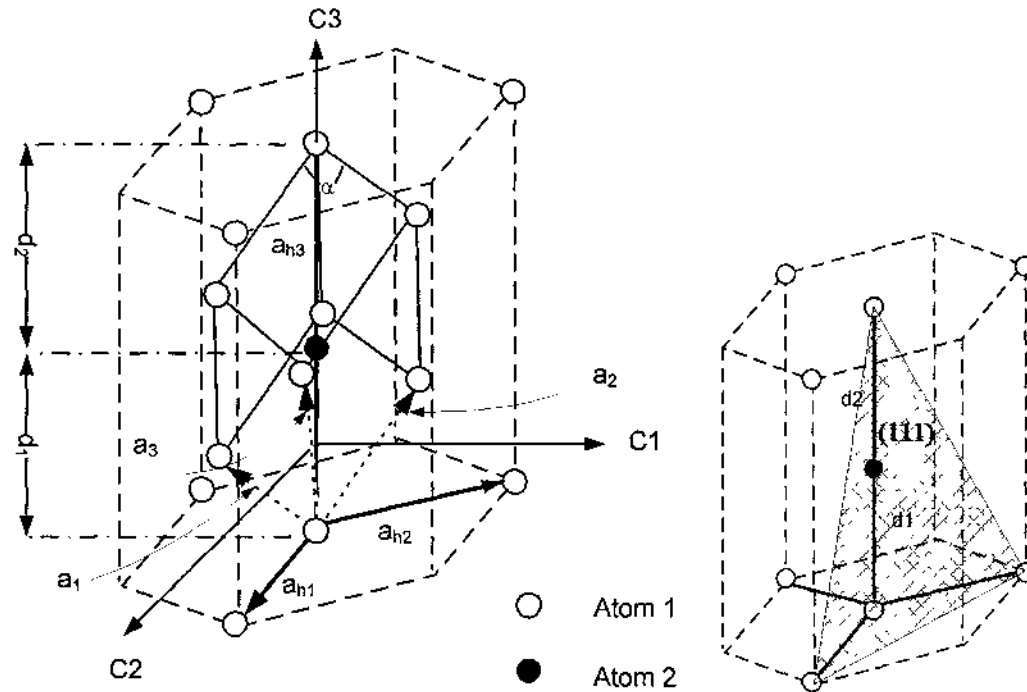
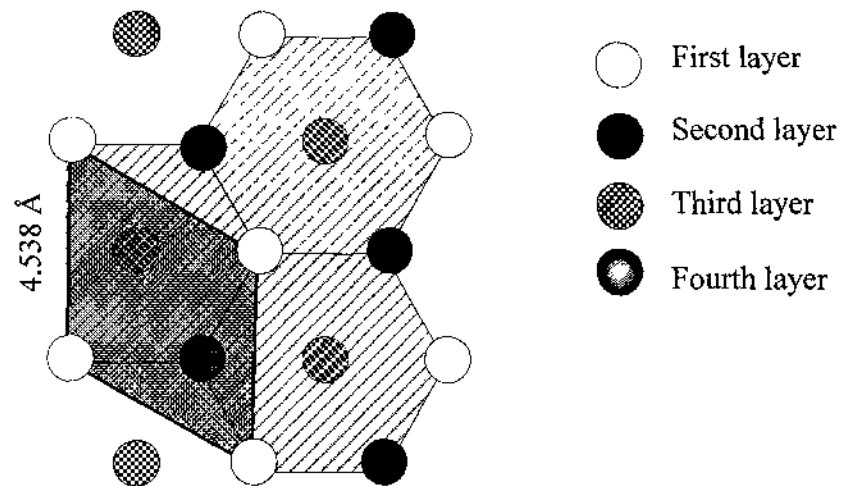


Fig. 1.1. Crystal structure of bulk Bi. Rhombohedral unit cell is represented by the solid and short dashed lines incorporated in the hexagonal unit cell represented by long dashed lines. The white and black solid spheres represent the two atoms in the rhombohedral unit cell. The short dashed and solid black lines represent the vectors spanning the rhombohedral and hexagonal lattice, respectively. The Cartesian coordinate systems used here are: bisectrix (C_1, y), binary (C_2, x) and trigonal (C_3, z).

To relate the rhombohedral unit cell to the hexagonal one, the unit vectors \vec{a}_1 , \vec{a}_2 and \vec{a}_3 , which are represented by short dashed lines in Fig. 1.1, are expressed in terms of the hexagonal lattice parameters, $a = 4.5332 \text{ \AA}$, and $c = 11.7967 \text{ \AA}$ as follows, [25]

$$\left. \begin{aligned} \bar{a}_1 &= \left(-\frac{1}{2}a, -\frac{\sqrt{3}}{6}a, \frac{1}{3}c\right) \\ \bar{a}_2 &= \left(\frac{1}{2}a, -\frac{\sqrt{3}}{6}a, \frac{1}{3}c\right) \\ \bar{a}_3 &= \left(0, -\frac{\sqrt{3}}{3}a, \frac{1}{3}c\right) \end{aligned} \right\}$$

(a) Top View



(b) Side View

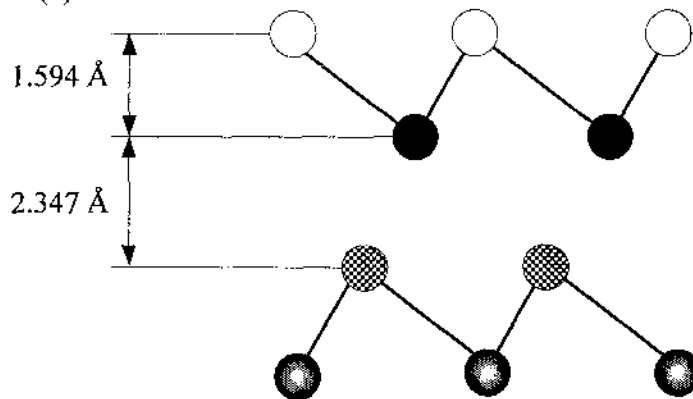


Fig. 1.2. Bulk structure of Bi (111). (a) Top view and (b) Side view of the first four layers. Solid lines represent the covalent bonds between the atoms. Reproduced from Ref. [17]. The angle between any two basis vectors is $\alpha_r = 57^\circ 14'$. Therefore the crystal structure of Bi is completely identified by a_{rh} , α_r and the position of the two basis atoms.

1.2.2. Hexagonal structure

The hexagonal unit vectors are expressed in terms of the rhombohedral ones as follows, [25]

$$\left. \begin{aligned} \vec{a}_{h1} &= \vec{a}_1 - \vec{a}_3 \\ \vec{a}_{h2} &= \vec{a}_2 - \vec{a}_1 \\ \vec{a}_{h3} &= \vec{a}_1 + \vec{a}_2 + \vec{a}_3 \end{aligned} \right\}$$

and can be written in terms of the rhombohedral unit cell as,

$$\left. \begin{aligned} \vec{a}_{h1} &= \left(-\frac{1}{2}a, -\frac{\sqrt{3}}{6}a, 0\right) \\ \vec{a}_{h2} &= (a, 0, 0) \\ \vec{a}_{h3} &= (0, 0, c) \end{aligned} \right\}$$

In hexagonal notation, four indices are used $(hkil)$ compared to three, (hkl) , in rhombohedral structure, where $i = -(h+k)$.

1.2.3. Pseudocubic structure

One should be careful when using the pseudocubic notation because it may look like the rhombohedral notation, but it represents a different surface. For example, the (100) and (110) surfaces have different geometries and different electronic structures in rhombohedral, but in pseudocubic notation both surfaces are represented by the (111) surface. Therefore, to eliminate any confusion, we will not be using any pseudocubic notation through the rest of this dissertation. But readers who are seeking further and detailed discussion about the pseudocubic structure indexing should refer to Ref. [18,26].

1.3. Electronic Band Structure of Bi

It was mentioned earlier that the Bi crystal structure is a distorted simple cubic cell, but a quick question might pop up; what force law can hold the atoms in the unit cell

and make that structure in a stable configuration? A satisfactory answer to this paradox was introduced by H. Jones and revisited by Peirles and was later termed “Peirles-Jones mechanism” [27].

What Jones suggested is that Bi lattice has the symmetry of a face-centered cubic (fcc) lattice with two atoms per unit cell. Therefore, the first Brillouin zone (BZ) of Bi is that of fcc, Fig. 1.3. But the lattice potential is modified because one of the atoms is displaced with respect to the other, and this potential modification produces discontinuities in the surfaces of the second zone which lie inside the Bi unit cell, Fig. 1.4.

Therefore, the new zone will have a certain number of orbital states that are equivalent to half the number of the atoms per unit cell. Then, Jones’ argument was that the new discontinuous surface is very close to the surface with constant energy of the undistorted lattice, i.e., in the case of Bi with atomic number of 83, the Fermi surface is very close to coincide with the new boundary and the electrons in the valence band will spill over to the next higher band to fill it, leaving few holes behind. If the Fermi surface is to coincide with the zone boundary, Bi would be an insulator, because the lower bands will be completely filled, and the next will be empty, but this is not the case with Bi. Based on the previous discussion, in the case of Bi, the density of charge carrier responsible for the conduction is direction dependent and limited to the energy pockets (L and T), Fig. 1.3, where the energy bands become separated leading to the creation of sub-bands (energy quantization of charge carriers) as the sample dimensions are reduced (similar to the quantum particle problem in a potential well). Another factor, the lattice stress, can modify the shape of the Brillouin zone and consequently the energy pockets of

charge carriers occupying them. More details of the electronic band structure of Bi and corresponding graphical representation can be found in Ref. [28,29].

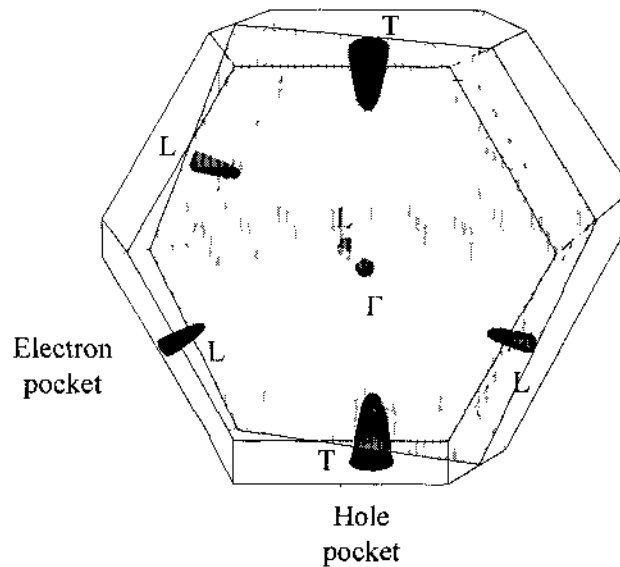


Fig. 1.3. First Brillouin zone of bulk Bi and some important symmetry points; L and T are electron and holes pockets, respectively, in the Fermi surface (shaded area).

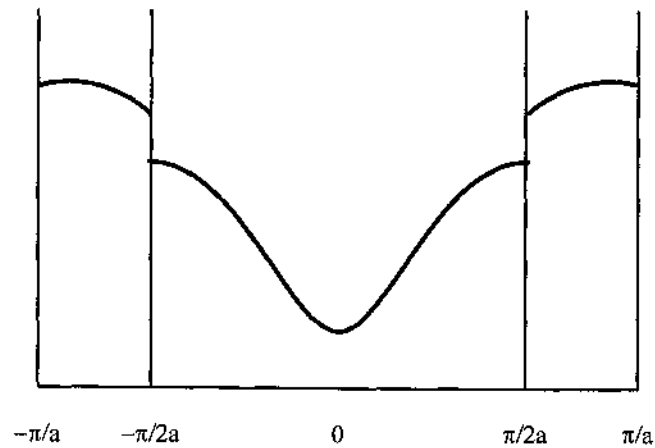


Fig. 1.4. Electron energy in a linear atomic chain where atoms are not equally spaced. Reproduced from Ref. [27].

1.4. Size-Dependent Melting Point Depression

Melting point depression was first introduced theoretically by Pawlaw [30] in 1909 and confirmed experimentally in Bi by many groups [31-35]. Classical thermodynamics and modern simulation methods are used widely to investigate the melting point depression in small particles [36,37]. Accordingly, [38-42] [3,5,10-12,26] the melting of small particles was understood in terms of the reduction in the total energy of the solid (*s*), liquid (*l*), and vapor (*v*) interfaces ($\Delta\gamma$), where, $\Delta\gamma = \gamma_{lv} + \gamma_{sl} - \gamma_{sv} < 0$, and γ is the interfacial energy per unit area.

In general, the depression observed in the melting point is related to the particle size through the following formula [43,44]:

$$\Delta T = T_m^{bulk} - T_m(r) \approx \frac{2T_m^{bulk}}{H_m^{bulk}} \times \frac{\alpha}{r} \quad 1.1$$

where T_m^{bulk} and H_m^{bulk} are the bulk melting temperature and bulk latent heat of fusion respectively. r is the radius of the spherical particle and α is the interfacial tension between the solid phase and its environment. Eq. 1.1 was predicted based on three different models used to describe the melting of small particles. These models are [43]:

(1) Homogeneous melting and growth model (HMG) [31,45]. This model assumes a state of equilibrium between the entire solid and the entire liquid state and α is given by,

$$\alpha_{HGM} = \gamma_{sv} - \gamma_{lv} \left(\frac{\rho_s}{\rho_l} \right)^{2/3} \quad 1.2$$

where, ρ_s and ρ_l are the densities of the solid and the liquid states, respectively.

(2) The liquid shell model (LSM) [31,46], assumes the formation of thin layer of the molten particles of thickness r_o , at the solid surface. Accordingly,

$$\alpha_{HGM} = \frac{\gamma_{sl}}{1 - \frac{r_0}{r}} + \gamma_{lv} \left(1 - \frac{\rho_s}{\rho_l}\right) \quad 1.3$$

(3) The liquid nucleation and growth model (LNG) [47-50] considers that the melting begins by the formation of a liquid layer at the surface and grows very slowly at the expense of the solid material.

$$\alpha_{sl} < \alpha_{LNG} < \frac{3}{2} (\gamma_{sv} - \gamma_{lv} \frac{\rho_s}{\rho_l}) \quad 1.4$$

Although applying these models is beyond our interest in this work, it is worth mentioning the different proposed models that have been used for decades to shed some light on the melting mechanism of nanostructures.

1.5. Surface Melting and Superheating

Despite being a simple phase transition in which a transformation from solid to a liquid state occurs at a specific temperature, T_m (melting temperature), and a phenomenon that has been studied for decades, melting is still considered a mysterious phenomenon in nature. Melting was classified as either homogeneous or heterogeneous in nature depending on the locus of the melting nucleation site. Melting is classified as homogeneous if it starts at crystal defects (vacancies, interstitial, dislocation or impurities), while heterogeneous melting nucleates at grain boundaries, interfaces and free surfaces.

For perfect crystalline material, surface melting is the most preferred mechanism. This is due to the fact that the solid-vapor interfacial energy is much higher than that of both the solid-liquid and liquid-vapor [51,52]. This may result in the formation of a molten thin layer on the surface below the melting temperature T_m , the thickness of which increases as the temperature moves toward T_m . In some cases, the quasi-liquid layer does

not propagate through the material and may result in either incomplete melting or crystal superheating [53,54]. Superheated solid materials do not lose their long range order at temperatures above their melting point T_m . There are many factors that may affect the superheating of the solid before its complete melting; these factors include, but are not limited to, free surfaces, defects, and heating rates (Q).

Superheating is rarely observed in low heating rates experiments ($Q \sim 1$ K/s) due to heterogeneous nucleation. On the other hand, high heating rates may result in an appreciable degree of superheating. Such high rates of heating are easily achieved by using the proper heating source. Heating rates as high as 10^{14} K/s and more are easily achieved by very short laser pulses (picosecond and femtosecond). Such laser sources made it possible and opened unprecedented opportunities to investigate the kinetic limits

Table 1.1: Summary of the bulk melting points and degree of superheating of various elements and compounds. These values were adopted from Ref. [32] and references therein unless otherwise noted.

Material	T_m (K)	degree of superheating (K)	Ref.
SiO ₂ (quartz)	1700	300	
P ₂ O ₅	836	50	
<i>p</i> -toluidine	318	0.6	
As ₂ O ₃	551	60	
H ₂ O	273	0.28	
Bi	544	>5	(55)
Bi (0001)	544	90	(56)
Ga	303	0.2	
Ge	1210	134	(57)
In (111)	430	73	(58)
Pb (111)	601	120 [†]	(54)
		2	(59)
		3	(60)
Sn	544	2	

[†] at $\sim 10^{11}$ K/s

of superheating. Superheating was studied and seen in some materials; some of them are listed in Table 1.1.

Bi is one of those elements that can preserve its solid integrity, and superheat at temperatures above T_m^{Bulk} . According to Ref. [32,45], Bi was superheated 7 degrees above its bulk melting temperature T_m^{Bulk} . A study on nano-sized clusters of Bi, In, Pb and As by Allen et al. [31] confirmed the superheating by 8 degrees in Bi but not in the other elements.

Also, bulk crystalline Bi showed superheating of 90 K through a time-resolved reflection of high energy electron diffraction study by E. Murphy et al. [56]. Murphy et al. used an ultrafast laser to heat the crystalline Bi and probed the changes in the diffraction pattern of Bi induced by such very high heating rates, 10^{11} K/s by using high energy electrons diffracted off the Bi surface. A 120 K superheating was observed in Pb (111) in another study [61] using the same technique, while Pb (001) surface did not show any superheating [62].

1.6. Previous Work in Time-Resolved Electron Diffraction Studies on Bi

X-ray and electron diffraction have been widely used for decades to study the crystal structure of solid materials. In general, both techniques are complementing each other, but in some cases electrons have an advantage over X-ray in diffraction experiments. The advantage of electron diffraction over X-ray arises from, first, the extremely short wavelength (λ) of the electron beam with respect to that of the X-ray beam of the same energy. Therefore, according to Bragg's law ($2d \sin\theta = n\lambda$), this leads to a smaller Bragg angles for electrons than for X-rays. Second, the ease of focusing electrons into a very narrow, high intensity beam, allow measurements of a very small

sample volumes, i.e. high spatial resolutions. Third, electrons interact with and are diffracted by the electrostatic potential of both orbital electrons and atomic nuclei, while X-rays interact with and are diffracted by orbital electrons. This means that electron scattering cross section is higher than that for X-ray by about six orders of magnitude [63], and enables researchers to study the structures of gases, surfaces, and thin crystallites (nanometers size scale), which is beyond the capabilities of X-ray crystallography. Fourth, the damage effects due to electron-matter interaction are much less than that of X-rays at the same wavelength.

Incorporating electron diffraction in time resolved experiments did not start until the mid 80's, when Williamson et al. [64] used a picosecond electron diffraction to monitor in real time the melting of Al thin film induced by picosecond laser pulses. This technique was later improved by M. Aeschlimann et al. [65]. Due to the poor time resolution of the earlier experiments, it was difficult to monitor the fast lattice dynamics that occur in the sub-picosecond time scale. By introducing the femtosecond lasers in the 1980's, the resolution of the time resolved electron diffraction experiments are consequently improved and reached a sub picosecond (ps) time resolution by the improvements introduced by Cao et al. [66].

The time-resolved pump probe technique was utilized over decades, and much research work has been done on Bi. It is beyond of our capabilities to address every single work, but some of them will be mentioned here, and I can categorize the experimental work into three main categories: (1) pump-probe optical studies [67-72], (2) pump-probe X-ray studies [73,74], and (3) electron diffraction studies [56, 75-78]. This is in addition to the theoretical investigation of the electronic structure of Bi and the size

effect on the band structure made by Shick et al. [79] and the references therein. In all of these studies, the main objective is to study the impact of ultrashort excitation pulses on the physical properties as a function of time. In the optical pump-probe technique, the change in reflectivity and/or transmission with time following laser excitation is monitored. Although vast information could be extracted from an optical pump-probe in regard to carrier density change due to laser excitation and its subsequent relaxation that results in the excitation of coherent optical phonons in Bi, it is indirectly related to the changes in the atomic structure [81]. Generation of coherent vibrational optical phonons of symmetry A_{1g} was monitored in Bi and its frequency was found to be a function of the pumping laser fluence [81-84].

Hase et al. [82] attributed the frequency chirp to the anharmonicity in the lattice potential which lead to the amplitude-frequency dependence. Fahy and Reis [85] explained that frequency change in terms of the softened electronic potential and the behavior of the photoexcited carrier during excitation and relaxation processes. A later study confirmed this mechanism, and the anharmonic effects were negligible [83]. Due to the insensitivity of the optical pump probe setup to monitor the atomic positions, the amplitude of the atomic displacement resulting from phonon excitation could not be measured.

On the other hand, pump-probe X-ray diffraction can give a clear picture of the time evolution of structure dynamics induced by ultrashort laser pulses.

An X-ray was used in a pump probe setup [73] to map the change in interatomic potential due to the change in carrier density photoexcited by ultrashort laser pulses. According to this study, they were able to characterize quantitatively the interatomic potential energy

surface at high excitation fluence by monitoring in real time the change in atomic displacement. Accordingly, a potential energy shift and softening was detected with the increased carrier density as a result of valence electrons excitation to the conduction band.

The work done so far, to the best of our knowledge, on Bi using time-resolved electron diffraction is not extensive and summarized in the following paragraphs. One of the earliest studies was done by E. Murphy et al. [56]; they aimed at studying the Bi (0001) superheating using high energy electron diffraction in the reflection mode. They were able to detect 90 K superheating using a pump-probe setup with 200 ps time resolution. Recently, Krenzer et al. [75] studied the energy dissipation in an epitaxially grown Bi on Si (001) due to femtosecond laser excitation and were able to determine the thermal boundary conductance from the transient thermal response of the Bi film by means of ultrafast electron diffraction in the reflection mode. The same group studied the dynamics of surface temperature of Bi thin film grown on Si (001) induced by fs laser pulses [76]. Rajkovic [78] studied a highly oriented free standing Bi thin film (20 nm), and all his observations and conclusions were based on two exponential fit functions of the normalized diffraction peak intensity. The first decay time is short, sub-picosecond, was attributed to the nonthermal effects while the second is few picoseconds, and was explained in terms of carrier relaxation through Auger mechanism. Although he was able to pump the Bi film with 1.5 mJ/cm^2 laser pulses, for some reason, no change in diffraction peak FWHM or position was detected. Recently, G. Sciaini et al. [77] studied the melting mechanism in 30 nm thick free standing Bi induced by femtosecond laser pulses. According to this study, the melting mechanism of Bi at high pumping fluences (7

mJ/cm² and 23 mJ/cm²) was attributed to a nonthermal effects which induces modification in the potential energy surface as a result of excitation of fully symmetric normal mode of vibration of A_{1g} symmetry.

1.7. Dissertation Motivation and Organization

The unusual physical properties of small Bi structures, which sometimes are different from those of the bulk, have motivated us to study the photoexcitation of Bi nanoclusters by ultrashort laser pulses. To accomplish this goal, I have built a time-resolved high energy electron diffraction setup of resolution better than 3 ps. Additionally, to the best of our knowledge, so far no time-resolved work has been done on Bi nanoclusters (5 nm). Also, a direct current heating stage was used to study the melting of the grown Bi nanoclusters.

The first goal of our experiment is to study the melting of Bi nanoclusters by using the direct current heating stage. To do so, the intensity, diffraction ring position and FWHM were measured at different temperatures. We found that the Debye temperature of the annealed nanoclusters was 53 ± 6 K along the $\langle 012 \rangle$ direction and 86 ± 9 K along $\langle 110 \rangle$ direction. At $T = 464 \pm 6$ K, the diffraction intensity started to deviate from Debye-Waller behavior due to increased lattice anharmonicity. The onset of the melting of the Bi nanoclusters was $T \sim 500 \pm 6$ K, as measured by the reduction of the nanocluster size through the formation of a liquid shell detected by the width of the diffraction rings. The thermal expansion of the Bi (012) planes showed that the transition from a positive to a negative value is not abrupt but occurs over the temperature range $T_c \sim 499 \pm 11$ to 511 ± 8 K, while for Bi (110) planes, the thermal expansion coefficient is positive up to their melting point, which is $\sim 525 \pm 6$ K.

Second, a time-resolved experiment is conducted to study the photoexcitation of Bi nanoclusters and the structure response to moderate laser fluences $\sim 1.9 \pm 5\% \text{ mJ/cm}^2$ - $2.9 \pm 5\% \text{ mJ/cm}^2$. We found that the thermalization time has changed significantly for Bi islands when compared to Bi nanoclusters. Additionally, the thermalization time is direction dependent; for example, the thermalization time measured along $\langle 012 \rangle$ direction was found to be longer than that measured along the $\langle 110 \rangle$ direction. This was explained in terms of the sensitivity of the electronic band structure along the $\langle 012 \rangle$ direction compared to that along the $\langle 110 \rangle$ direction.

Bi islands were obtained by annealing the grown film solely either by the heating stage or by femtosecond laser pulses of energy density within the range of $0.9 \pm 5\% \text{ mJ/cm}^2$ - $2.4 \pm 5\% \text{ mJ/cm}^2$. While Bi nanoclusters were obtained by raising the temperature of the grown sample up to $\sim 450 \text{ K}$ while exposing it to laser pulses of fluence $0.9 \pm 5\% \text{ mJ/cm}^2$ - $2.4 \pm 5\% \text{ mJ/cm}^2$.

The dramatic change in the thermalization time was explained in terms of the modification in the electronic band structure of Bi as a result of cluster size change. Additionally, the diffraction peak position was monitored at different delay times and it was found that, for (012) planes, just after $t = 0 \text{ ps}$, a contraction of the lattice in that direction is detected over 6 ps, followed by expansion over a long time period ($\sim 20 \text{ ps}$). At the same time, no abnormal change in the (110) diffraction peak was detected other than expansion at $t > 0$. Although this behavior is prominent and repeatedly observed in Bi nanoclusters, the Bragg peak ring size for Bi islands did not show any change in the measured $\Delta d/d$ and needs careful and further study of the effect of different factors that may contribute to such behavior. These factors are, but are not limited to, annealing

temperature, laser fluence, cluster size distribution and growth direction. We have used the FWHM of the Bragg peaks to calculate the percentage change in molten layer thickness, which showed an increase with delay time in both samples, indicating the partial melting of the Bi sample due to thermal effects.

This dissertation is organized as follows:

Chapter 1 (this chapter) deals with crystal structure, physical properties, electronic properties and an overview of superheating of Bi as well as some literature review of previous work done on Bi thin film.

Chapter 2 covers the basics of electron diffraction theory and how the electron diffraction is used to extract useful information about the lattice structure modification induced by ultrashort laser pulses.

Chapter 3 explains in detail the experimental setup, which includes the operation of the femtosecond laser system, lab-made photoactivated electron gun (PAEG), vacuum system, data acquisition and data analysis.

Chapter 4 covers the general mechanism of ultrashort photoexcitation of thin solid film.

Chapter 5 covers sample preparation and studies the melting of Bi nanoclusters. The melting temperature of Bi nanoclusters was found to be less than that of the bulk as expected. Additionally, the lattice thermal expansion coefficient was calculated at two different directions and we found that, the Bi lattice is suffering from an expansion in one direction $\langle 110 \rangle$ till near the melting point, while along $\langle 012 \rangle$ direction, the lattice starts to expand followed by contraction at certain temperature.

In chapter 6, the time-resolved data is presented for Bi nanoclusters, in which a detailed study of the time evolution of Bragg peak relative intensity, strain ($\Delta d/d$) and percentage change in molten layer thickness as measured from the FWHM.

In chapter 7, a time-resolved comparative study is made between the Bi islands and Bi nanoclusters.

In chapter 8, conclusions and a summary of the work presented here are given, along with suggested future work.

1.8. References of Chapter 1

- [1] Y. Liu, K. A. Mcgreer, B. Nease, D. B. Haviland, G. Martinez, J. W. Halley, and A. M. Goldman, "Scaling of the insulator-to-superconductor transition in ultrathin amorphous Bi films," *Phys. Rev. Lett.* 67, 2068-2071 (1991).
- [2] Z. Zhang, X. Sun, M. Dresselhaus, J. Ying, and J. Heremans, "Electronic transport properties of single-crystal bismuth nanowire arrays," *Phys. Rev. B* 61, 4850-4861 (2000).
- [3] E. R. Youngdale, J. R. Meyer, C. A. Hoffman, F.J. Bartoli, D.L. Partin, C. M. Trush, and J. P. Heremans, "Nonlinear optical properties of molecular beam epitaxy grown $\text{Bi}_{1-x}\text{Sb}_x$," *Appl. Phys. Lett.* 57, 336-338 (1990).
- [4] N. Garcia, Y. K. Kao, and M. Strongin, "Galvanomagnetic studies of bismuth films in the quantum-size-effect region," *Phys. Rev. B* 5, 2029-2039 (1988).
- [5] C. A. Hoffmann, J. R. Meyer, F. Bartoli, A. Di Venere, X.J. Yi, C.L. Hou, H. C. Wang, J. B. Ketterson, and G. K. Wong, "Semimetal-to-semiconductor transition in bismuth thin films," *Phys. Rev. B* 48, 11431-11434 (1993).
- [6] Y. Oshima, K. Takayanagi, and H. Hirayama, "Structural anomaly of fine bismuth particles observed by ultra-high vacuum TEM," *Z. Phys. D* 40, 534-538 (1997).
- [7] J. L. Costa-Kramer, N. Garcia and H. Olin, "Conductance quantization in bismuth nanowires at 4 K," *Phys. Rev. Lett.* 78, 4990-4993 (1997).
- [8] K. Liu, C. L. Chien, P. C. Searson and Y. Z. Kui, "Structural and magneto-transport properties of electrodeposited bismuth Nanowires," *Appl. Phys. Lett.* 73, 1436-1438 (1998).

- [9] M. R. Black, M. Y. Lin, S. B. Cronin, O. Rabin and M. S. Dresselhaus, "Electronic properties of bismuth nanowires," *Phys. Rev. B* 65 195417(1-9) (2002).
- [10] M. R. Black, P. L. Hagelstein, S. B. Cronin, Y. M. Lin, and M. S. Dresselhaus, "Optical absorption from an indirect transition in bismuth nanowires," *Phys. Rev. B* 68, 235417(1-10) (2003).
- [11] L. Hicks, T. Harman and M. Dresselhaus, "Use of quantum-well superlattices to obtain a high figure of merit from nonconventional thermoelectric materials," *Appl. Phys. Lett.* 63, 3230-3232 (1993).
- [12] S. Cho, Y. Kim, A. Freeman, G. Wong, J. Ketterson, L. Olafsen, I. Vurgaftman, J. Meyer and C. Hoffman, "Large magnetoresistance in postannealed Bi thin films," *Appl. Phys. Lett.* 79, 3651-3654 (2001).
- [13] S. Nahm, L. Salamanca-Riba, D.L. Partin, and J. Heremans, "Transmission electron microscopy studies of bismuth films," *J. Mater. Res.* 5, 784-788 (1990).
- [14] A. A. Ramadan, A. M. El-Shabiny, and N. Z. El-Sayed, "Size-dependent structural characteristics of thin bismuth films," *Thin Solid Films* 209, 32-37 (1992).
- [15] Y. Oshima, H. Hirayama, and K. Takayanagi, "Structural transition of bismuth nano-particle observed by ultrahigh-vacuum TEM," *Electron microscopy and analysis 1997 : proceedings of the Institute of Physics Electron Microscopy and Analysis Group conference, Cavendish Laboratory, University of Cambridge, 2-5 September* 233-236 (1997).
- [16] A. Kumar and O. P. Katyal, "Electrical resistivity of thin bismuth films," *J. Mater. Sci.* 1, 51-56 (1990).

- [17] H. Mönig, J. Sun, Yu. M. Koroteev, J. Wells, G. Bihlmayer, E. V. Chulkov, K. Pohl and Ph. Hofmann, "The structure of the (111) surface of bismuth," *Phys. Rev. B* 72, 085410(1-7) (2005).
- [18] F. Jona, "Low-energy electron diffraction study of surfaces of antimony and bismuth," *Surf. Sci.* 8, 57-76 (1967).
- [19] R. J. Needs, R. M. Martin, and O. H. Nielsen, "Total-energy calculation of the structural properties of the group-V element arsenic," *Phys. Rev. B* 33, 3778-3784 (1986).
- [20] W. Klement Jr., A. Jayaraman, and G. C. Kennedy, "Phase diagrams of arsenic, antimony and bismuth at pressures up to 70 kbars," *Phys. Rev.* 131, 632-637 (1963).
- [21] R. W. G. Wyckoff, *Crystal Structures*, Vol. 1 (Interscience, New York, 1960).
- [22] H. Hume-Rothery, *Atomic Theory for Students of Metallurgy* (London, 1962).
- [23] C. C. Barrett, *Structure of Metals*, (McGraw-Hill, New York, 1952).
- [24] C. A. Coulson, *Valence*, (Clarendon Press, Oxford, 1956).
- [25] P. Hofmann, "The surfaces of bismuth: Structural and electronic properties," *Prog. in Surf. Sci.* 81, 191-245 (2006).
- [26] M. H. Cohen, "Energy bands in the bismuth structure. I: A nonellipsoidal model for electrons in Bi," *Phys. Rev.* 121, 387-395 (1961).
- [27] R. E. Peierls, "More Surprises in Theoretical Physics," Princeton University Press, 24-26, (1991).
- [28] Y. Liu and R. E. Allen, "Electronic structure of the semimetals Bi and Sb," *Phys. Rev. B* 52, 1566-1577(1995).
- [29] V. S. Edel'man, "Electrons in bismuth," *Advances in Physics* 25, 555-613 (1976).

- [30] P. Pawlow, "About the dependence of the melting point of the surface energy of a solid body (Supplementary)," *Z. Phys. Chem.* 65, 545-548 (1909).
- [31] G. L. Allen, R. A. Bayless, W. W. Gile, and W. A. Gesser, "Small particle melting of pure metals," *Thin Solid Films* 144, 297-308 (1986).
- [32] S. J. Peppiatt, "The melting of small particles. II. Bi," *Proc. R. Soc. Lond. A.* 345, 401-412 (1975).
- [33] M. K. Zayed and H. E. Elsayed-Ali, "Condensation on (002) graphite of liquid bismuth far below its bulk melting point," *Phys. Rev. B* 72, 205426(1-9) (2005).
- [34] M. K. Zayed and H. E. Elsayed-Ali, "Melting and solidification study of as-deposited and recrystallized Bi thin films," *J. Appl. Phys.* 99, 123516(1-11) (2006).
- [35] E. A. Olson, M. Yu. Efremov, M. Zhang, Z. Zhang, and L. H. Allen, "Size dependent melting of Bi nanoparticles," *J. Appl. Phys.* 97, 034304(1-9) (2005).
- [36] G. Bertsch, "Melting in clusters," *Science* 277, 1619 (1997).
- [37] H.-P. Cheng and R. S. Berry, "Surface melting of clusters and implications for bulk matter," *Phys. Rev. A* 45, 7969-7980 (1992).
- [38] J. G. Dash, "Surface melting," *Contemp. Phys.* 30, 89-100 (1989).
- [39] J. W. M. Frenken and J. F. van der Veen, "Observation of surface melting," *Phys. Rev. Lett.* 54, 134-137 (1985).
- [40] B. Pluis, A. W. D. van der Gon, J. W. M. Frenken, and J. F. van der Veen, "Crystal-face dependence of surface melting," *Phys. Rev. Lett.* 59, 2678-2681 (1987).
- [41] B. Pluis, A. W. D. van der Gon, J. F. van der Veen, and A. J. Riemersma, "Surface-induced melting and freezing I. Medium-energy ion scattering investigation of the melting of Pb{hkl} crystal faces," *Surf. Sci.* 239, 265-281 (1990).

- [42] J. C. Heyraud, J. J. Métois, and J. M. Bermond, "Surface melting and equilibrium shape; the case of Pb on graphite," *J. Cryst. Growth* 98, 355-362 (1989).
- [43] K. F. Peters, J. B. Cohen and Ch. Yip-Wah, "Melting of Pb nanocrystals," *Phys. Rev. B* 57, 13430-13438 (1998).
- [44] R. Defay and I. Prigogine, *Surface tension and adsorption*, Wiley, New York, 1951-English translation, (1966).
- [45] P. A. Buffat and J. P. Borel, "Size effect on the melting temperature of gold particles," *Phys. Rev. A* 13, 2287-2298 (1976).
- [46] H. Reiss and I. B. Wilson, "The effect of surface on melting point," *J. Colloid Sci.* 3, 551-561(1948).
- [47] H. Reiss, P. Mirabel, and R. L. Whetten, "Capillarity theory for the "coexistence" of liquid and solid clusters," *J. Phys. Chem.* 92, 7241-7246 (1988).
- [48] P. R. Couchman and W. A. Jesser, "Thermodynamic theory of size dependence of melting temperature in metals," *Nature* 269, 481-483 (1977).
- [49] V. P. Skripov, V. P. Koverda, and V. N. Skokov, "Size effect on melting of small particles," *Phys. Status Solidi A* 66, 109-118 (1981).
- [50] R. R. Vanfleet and J. M. Mochel, "Thermodynamics of melting and freezing in small particles," *Surf. Sci.* 341, 40-50 (1995).
- [51] Z. H. Jin, P. Gumbsch, K. Lu, and E. Ma, "Melting mechanisms at the limit of superheating," *Phys. Rev. Lett.* 87, 055703(1-4) (2001).
- [52] J. F. van der Veen, "Melting and freezing at surfaces," *Surf. Sci.* 433-435, 1-11 (1999).

- [53] P. Carnevali, F. Ercolessi, and E. Tosatti, "Melting and nonmelting of the Au(111) surfaces," *Phys. Rev. B* 36, 6701-6704 (2000).
- [54] J. W. Herman and H. Elsayed-Ali, "Time resolved structural studies of the low index faces of lead," *Phys. Rev. B* 49, 4886-4897 (1994).
- [55] M. Blackman, S. I. Peppiatt, and J. R. Samples, "Superheating of bismuth," *Nat. Phys. Sci.* 239, 61-62 (1972).
- [56] E. A. Murphy, H. E. Elsayed-Ali, and J. W. Herman, "Superheating of Bi(0001)," *Phys. Rev. B* 48, 4921-4924 (1993).
- [57] X. Zeng and H. E. Elsayed-Ali, "Time-resolved structural study of low-index surfaces of germanium near its bulk melting temperature," *Phys. Rev. B* 64, 085410(1-11) (2001).
- [58] B. Lin and H. E. Elsayed-Ali, "Temperature dependent reflection electron diffraction study of In(111) and observation of laser-induced transient surface superheating," *Surf. Sci.* 498, 275-284 (2002).
- [59] G. D. T. Spiller, "Time-dependent melting and superheating of lead crystallites," *Philos. Mag. A* 46, 535-549 (1982).
- [60] J. J. Métois and J. C. Heyraud, "The overheating of lead crystals," *J. Phys. France* 50, 3175-3179 (1989).
- [61] J. W. Herman and H. E. Elsayed-Ali, "Superheating of Pb(111)," *Phys. Rev. Lett.* 69, 1228-1231 (1992).
- [62] J. W. Herman and H. E. Elsayed-Ali, "Time-resolved study of surface disordering of Pb(110)," *Phys. Rev. Lett.* 68, 2952-2955 (1992).

- [63] A. Zewail, "Diffraction, crystallography and microscopy beyond three dimensions: Structural dynamics in space and time," *Phil. Trans. R. Soc. A.* 363, 315-329 (2005).
- [64] S. Williamson, G. Mourou, and J. C. M. Li, "Time resolved laser-induced phase transformation in Aluminum," *Phys. Rev. Lett.* 52, 2364-2367 (1984).
- [65] M. Aeschlimann, E. Hull, J. Cao, C. A. Schmuttenmaer, L. G. Jahn, Y. Gao, H. E. Elsayed-Ali, D. A. Mantell, and M. R. Scheinfein, "A picosecond electron gun for surface analysis," *Rev. Sci. Instrum.* 66, 1000-1009 (1995).
- [66] J. Cao, Z. Hao, H. Park, C. Tao, D. Kau, and L. Blaszczyk, "Femtosecond electron diffraction for direct measurement of ultrafast atomic motions," *Appl. Phys. Lett.* 83, 1044-1046 (2003).
- [67] H. J. Zeiger, J. Vidal, T. K. Cheng, E. P. Ippen, G. Dresselhaus, and M. S. Dresselhaus, "Theory for displacive excitation of coherent phonons," *Phys. Rev. B* 45, 768-778 (1992).
- [68] M. Hase, K. Mizoguchi, H. Harima, S. Nakashima, M. Tani, K. Sakai, and M. Hangyo, "Optical control of coherent optical phonons in bismuth," *App. Phys. Lett.* 69, 2474-2476 (1996).
- [69] M. Hase, M. Kitajima, S. Nakashima, and K. Mizoguchi, "Dynamics of coherent anharmonic phonons in bismuth using high density photoexcitation," *Phys. Rev. Lett.* 88, 067401(1-4) (2002).
- [70] R. Merlin, "Generating coherent THz phonons with light pulses," *Solid State Communications* 102, 207-220 (1997).

- [71] E. D. Murray, D. M. Fritz, J. K. Wahlstrand, S. Fahy, and D. A. Reis, "Effect of lattice anharmonicity on high-amplitude phonon dynamics in photoexcited bismuth. *Phys. Rev. B* 72, 060301(1-4) (2005).
- [72] D. Boschetto, E. G. Gamaly, A. V. Rode, B. Luther-Davies, D. Glijer, T. Garl, O. Albert, A. Rousse, and J. Etchepare, "Small atomic displacements recorded in bismuth by the optical reflectivity of femtosecond laser-pulse excitations," *Phys. Rev. Lett.* 100, 027404(1-4) (2008).
- [73] D. M. Fritz, D. M. Fritz, D. A. Reis, B. Adams, R. A. Akre, J. Arthur, C. Blome, P. H. Bucksbaum, A. L. Cavalieri, S. Engemann, S. Fahy, R. W. Falcone, P. H. Fuoss, K. J. Gaffney, M. J. George, J. Hajdu, M. P. Hertlein, P. B. Hillyard, M. Horn-von Hoegen, M. Kammler, J. Kaspar, R. Kienberger, P. Krejcik, S. H. Lee, A. M. Lindenberg, B. McFarland, D. Meyer, T. Montagne, É. D. Murray, A. J. Nelson, M. Nicoul, R. Pahl, J. Rudati, H. Schlarb, D. P. Siddons, K. Sokolowski-Tinten, Th. Tschentscher, D. von der Linde and J. B. Hastings, "Ultrafast bond softening in bismuth: Mapping a solid's interatomic potential with x-rays," *Science* 315, 633-636, (2007).
- [74] K. Sokolowski-Tinten, C. Blome, J. Blums, A. Cavalleri, C. Dietrich, A. Tarasevitch, I. Uschmann, E. Förster, M. Kammler, M. Horn-von-Hoegen and D. von der Linde, "Femtosecond x-ray measurement of coherent lattice vibrations near the Lindemann stability limit," *Nature* 422, 287-289 (2003).
- [75] B. Krenzer, A. Janzen, P. Zhou, D. von der Linde and M. Horn-von Hoegen, "Thermal boundary conductance in heterostructures studied by ultrafast electron diffraction," *New Journal of Physics* 8, 190(1-8) (2006).

- [76] A. Janzen, B. Krenzer, P. Zhou, D. von der Linde, and M. Horn-von Hoegen, "Ultrafast electron diffraction at surfaces after laser excitation," *Surf. Sci.* 600, 4094-4098 (2006).
- [77] G. Sciaini, M. Harb, S. Kruglik, T. Payer, C. Hebeisen, F. Heringdorf, M. Yamaguchi, M. Hoegen, R. Ernstorfer and R. J. Dwayne Miller, "Electronic acceleration of atomic motions and disordering in bismuth," *Nature* 458, 56-60 (2009).
- [78] I. Rajkovic, "Ultrafast electron diffraction studies of optically excited thin bismuth films," Ph.D. Dissertation, Dept. of Physics, University of Duisburg, Essen - Germany (2008).
- [79] A. B. Shick, J. B. Ketterson, D. L. Novikov, A. J. Freeman, "Electronic structure, phase stability, and semimetal-semiconductor transitions in Bi," *Phys. Rev. B* 60, 15484-15487 (1999).
- [80] Yu-M. Sheu, "Ultrafast dynamics of photoexcited bismuth films," Ph.D. Dissertation, Dept. of Physics, University of Michigan (2010).
- [81] M. F. DeCamp, D. A. Reis, P. H. Bucksbaum, and R. Merlin, "Dynamics and coherent control of high-amplitude optical phonons in bismuth," *Phys. Rev. B* 64, 092301(1-3) (2001).
- [82] M. Hase, M. Kitajima, S. Nakashima, and K. Mizoguchi, "Dynamics of coherent anharmonic phonons in bismuth using high density photoexcitation," *Phys. Rev. Lett.* 88, 67401(1-4) (2002).
- [83] E. D. Murray, D. M. Fritz, J. K. Wahlstrand, S. Fahy, and D. A. Reis, "Effect of lattice anharmonicity on high-amplitude phonon dynamics in photoexcited bismuth," *Phys. Rev. B* 72, 060301(1-4) (2005).

- [84] S. Hunsche, K. Wienecke, T. Dekorsy, and H. Kurz, "Impulsive softening of coherent phonons in Tellurium," *Phys. Rev. Lett.* 75, 1815-1818 (1995).
- [85] S. Fahy and D. A. Reis, "Coherent phonons: Electronic softening or anharmonicity?," *Phys. Rev. Lett.* 93, 109701(1 page) (2004).

CHAPTER 2

THEORY OF ELECTRON DIFFRACTION

2.1. Introduction

Diffraction pattern analysis plays a very important role in a wide range of applications, especially in solving molecular structures, identifying compounds, and the fabrication of materials. Diffraction patterns from crystalline compounds can provide a lot of information about the atomic structure of the compound. However, many compounds can only be prepared in a powder form. Although a powder diffraction pattern yields less information than that generated by a single crystal, it is unique to each substance and is very useful for identification purposes.

The diffraction pattern is a 2-D picture obtained by allowing a short-wavelength radiation to fall onto a material. If the incident radiation is scattered coherently (Thomson scattering) by the atoms making up the material, the resultant scattered radiation produces an interference pattern that is dependent upon the relative positions of those atoms.

White X-ray radiation (deceleration radiation) was the first radiation used in crystal diffraction, after early theories of crystal structure were proposed in which crystals were postulated to be composed of regular sub-units. These theories led von Laue, in 1912, to suggest that a crystal could act as the "grating" needed for the X-ray experiment. Soon, the first X-ray diffraction patterns were produced [1,2]. Later, the same theories were used to determine crystal structure with electron diffraction (Thomson and Reid on 1927) [1,2]. Therefore, electron diffraction (ED) and X-ray

diffraction have been used for decades and are known as powerful tools for characterizing the structure of materials, including perfect crystals and defect structures.

Although the diffraction principles are the same, there are major differences resulting from the nature of each radiation. The advantages of ED over X-ray arise from the extremely short wavelength (λ) of the electron with respect to that of the X-ray. As an example, 200 keV electrons have $\lambda = 2.5 \times 10^{-3}$ nm while Cu ($K\alpha$) radiation has $\lambda = 2.5 \times 10^{-1}$ nm, which is approximately two orders of magnitude less than that of electrons. Therefore, according to Bragg's law ($2d \sin\theta = n\lambda$), this leads to smaller Bragg angles for electrons than for X-rays. As will be shown later, the difference in scattering angles has a major effect on the ways diffraction data are collected. Also, the ease of focusing electrons into a very narrow, high intensity beam, allows measurements of very small sample volumes, i.e. high spatial resolutions. That is why atom cluster can be detected.

Another major difference is that, electrons interact with and are diffracted by the electrostatic potential of both orbital electrons and atomic nuclei, while X-rays interact with and are diffracted by orbital electrons. This means that electron scattering is much more efficient than for X-rays by a factor of 10^2 - 10^3 . Therefore the electron diffraction patterns are obtained in less time, and facilitate the study of interior structure of the matter down to cubic nanometers in size, which is beyond the capability of X-ray crystallography.

2.2. Theory of Electron Diffraction

2.2.1. De Broglie waves

The wave-particle duality is a concept that was introduced by De Broglie in 1924 in which all particles have wave-like properties [1]. The wave-like nature of the

particles is proven through the phenomenon of diffraction. De Broglie predicted that the wave-like behavior of material particles, such as electrons, can be treated as quanta of electron waves. According to his postulate, an electron with momentum $p = mv$, is associated with a wavelength λ and both are related to each other through the following simple relation, $\lambda = h/p$, where m is the electron mass the v is its speed.

This implies that,

$$\lambda = \frac{h}{\sqrt{2m_0E}} \quad \text{for non relativistic case (E} \ll E_0\text{),} \quad 2.1$$

$$\lambda = \frac{h}{\sqrt{2m_0E(1 + E/2E_0)}} \quad \text{for relativistic case (E} \gg E_0\text{),} \quad 2.2$$

$E = eV$, (electron kinetic energy), $E_0 = m_0c^2$ (rest energy), e is the electronic charge, V is the accelerating voltage, m_0 is the rest mass of the electron, and c is the speed of light in vacuum.

Substituting numeric values for the constants in Eq. (2.2)

$$\lambda = \frac{12.26}{\sqrt{V(1 + 0.9788 \times 10^{-6}V)}} \text{ \AA} \quad 2.3$$

where V is measured in volts.

De Broglie's hypothesis was verified accidentally by Davisson and Germer in 1927 when they were measuring the intensity of an electron beam reflected from the surface of nickel [2]. They noticed that the reflected beam intensity was maximum in a certain direction in space with respect to the incident beam, Fig. 2.1. The diffraction of electrons by a crystal is very similar to diffraction of X-rays of the same wavelength.

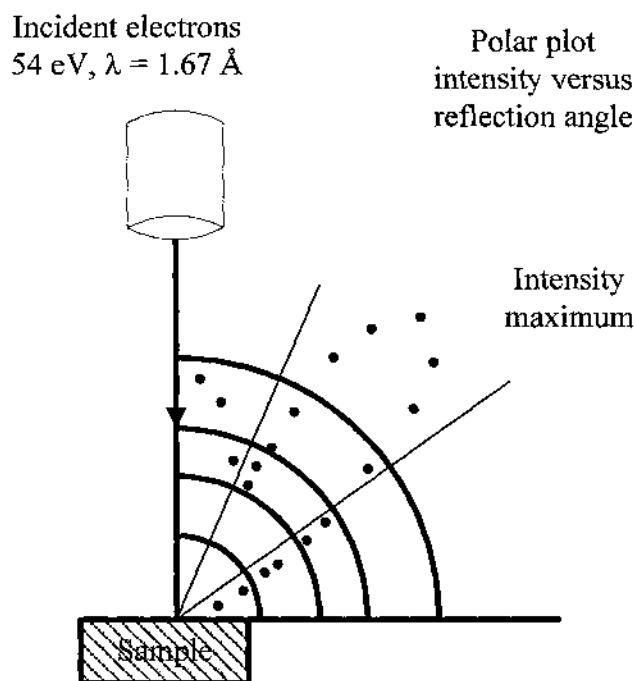


Fig. 2.1. Davisson and Germer experiment. The electron beam intensity is maximum at an angle 50° with respect to the incident beam. Reproduced from Ref. [2].

2.2.2. Laws of diffraction, the contribution of Laue, Bragg and Ewald

The contribution of Laue, Friedrich and Knipping in the discovery of the X-ray diffraction in crystal is very well known as is the subsequent development by Bragg. Ewald introduced the concept of reflecting sphere (Ewald sphere) which provided an obvious way of interpreting the geometry of the diffraction patterns [2]. Later, after the wave nature of electrons was proposed by de Broglie and the experimental validation by Davisson and Germer, the same laws that have been used for X-ray diffraction are also valid for electron diffraction.

2.2.2.1. Bragg's law of diffraction

The lattice points, or the atoms, in the crystal are arranged in sets or families of parallel planes. These planes were suggested by Bragg and called Bragg

planes [2]. Fig. 2.2 shows a set of such planes of Miller indices (hkl) where d_{hkl} is the perpendicular distance between these planes.

If an electron beam of wavelength λ is incident on these planes with an angle θ , Fig. 2.2, the path difference of the reflected rays from adjacent planes will be;

$$(AB+BC) = d_{hkl} \sin\theta$$

These rays reinforce each other and interfere constructively when the path difference is an integral multiple, n , of wavelengths, λ . Therefore,

$$2 d_{hkl} \sin\theta = n \lambda \quad 2.4$$

Where n is the order of reflection and Eq. 2.4 is known as Bragg's law of diffraction and it holds true either if $AB = BC$, Fig. 2.2.(a) or $AB \neq BC$, Fig. 2.2.(b).

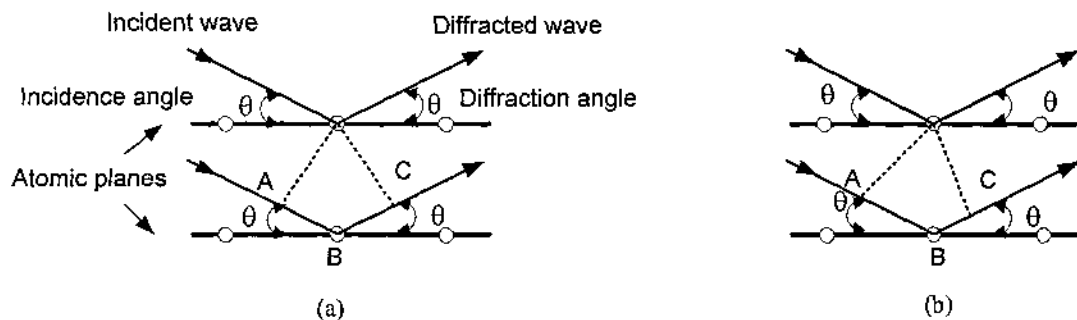


Fig. 2.2.(a) Bragg's law where $AB = BC = d_{hkl}$ and the path difference $(AB+BC) = 2d_{hkl} \sin\theta$. (b) Bragg's law for a general case in which $AB \neq BC$, again $(AB+BC) = 2d_{hkl} \sin\theta$.

Although the derivation of Bragg's law might be very simple, the problems involved in the electron diffraction are not. In fact, the relative intensities of the diffracted beams at different angles depend on [2]:

- (1) The electron distribution of the atoms in the unit cell, and
- (2) The number and the relative position of these atoms in the unit cell

The first one is related to the atomic scattering factor (form factor), and it is due to the fact that rays are mainly out of phase when they are scattered by different electrons in the atom. Therefore, these secondary scattered rays will, partially, destructively interfere with each other, and the amplitude of the scattered radiation by an atom containing Z electrons is less than that scattered by Z coincident electrons.

The second factor mentioned above is related to the geometrical structure factor, i.e., the dependence of the relative intensity on the arrangement of the atoms in the unit cell [2]. To clarify the effect of this factor on the scattered intensity, we may consider Fig. 2.3. It represents the CsCl unit cell projected on the (001) plane. The Cl atoms (big grey circles) are located at the corners of the unit cell and define the sides of the unit cell. The Cs atoms (small white circles) define another set of planes located halfway between the first set of planes. Therefore for a diffraction angle θ , the Cl atoms scatter the incident rays in phase with each other and similarly do the Cs atoms. But the path difference, Δ , between the scattered rays is less than one wavelength λ . Therefore, the atomic array do not scatter in phase with each other and this leads to partial destructive interference, which results in a reduction in the amplitude of the diffracted waves, i.e. less than that for in phase scattering by all atoms. If $\Delta = \lambda/2$, we will have a complete destructive interference, because the scattered waves are out of phase. Therefore, the intensity of the diffracted rays is determined by the actual atomic array or the crystal structure of the solid [2].

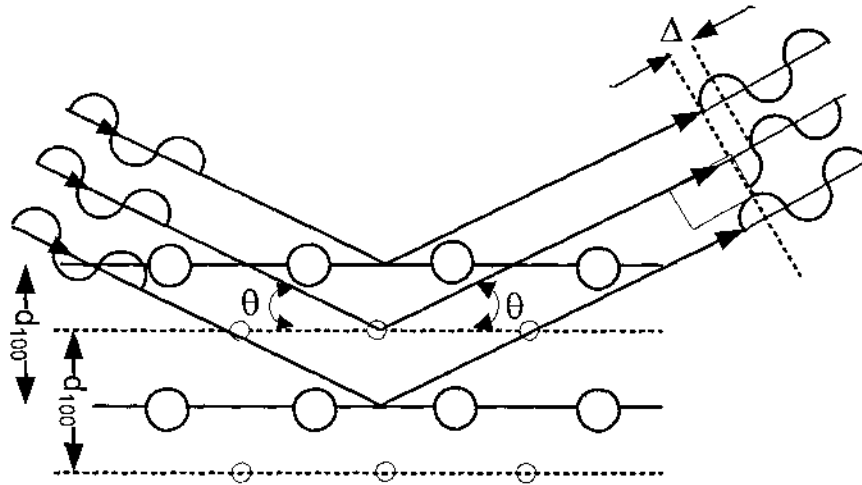


Fig. 2.3. The CsCl structure viewed along (100) plane. The scattered waves are in phase if they are scattered off the atoms of the same type. Destructive interference results from a phase difference of $2\pi\Delta/\lambda$ between the scattered waves from successive planes. Reproduced from Ref. [2].

2.2.2.2. Laue diffraction condition.

The Laue diffraction condition utilizes the concept of reciprocal lattice and relates it to the diffraction of the incident rays. For the derivation of Laue condition, Fig. 2.4 is adopted, in which an electron beam of wave vector \vec{k} and wavelength λ is allowed to fall on a crystal and scattered by two atoms located at the lattice points O and P separated by a lattice vector $\vec{\rho} = \vec{a} + \vec{b} + \vec{c}$, where \vec{a} , \vec{b} and \vec{c} are the crystal lattice vectors. If \vec{s} and \vec{s}' are unit vectors perpendicular to the incident and scattered wave-fronts respectively, then we can write;

$$\vec{k} = \frac{2\pi}{\lambda} \vec{s}$$

$$\vec{k}' = \frac{2\pi}{\lambda} \vec{s}'$$

Also, the path difference and the phase difference between scattered waves from these points are given respectively by;

$$\text{path difference} = \overline{OO_1} - \overline{PP_1} = \vec{\rho} \cdot \vec{s}' - \vec{\rho} \cdot \vec{s} = \vec{\rho} \cdot (\vec{s}' - \vec{s}) \quad 2.5$$

$$\text{phase difference} = \phi = \left(\frac{2\pi}{\lambda}\right) \vec{\rho} \cdot (\vec{s}' - \vec{s}) \quad 2.6$$

$$\text{where, } \Delta\vec{k} = (\vec{k}' - \vec{k})$$

Since the waves are scattered elastically, therefore,

$$|\vec{k}| = |\vec{k}'| = k = \frac{2\pi}{\lambda} \quad 2.7$$

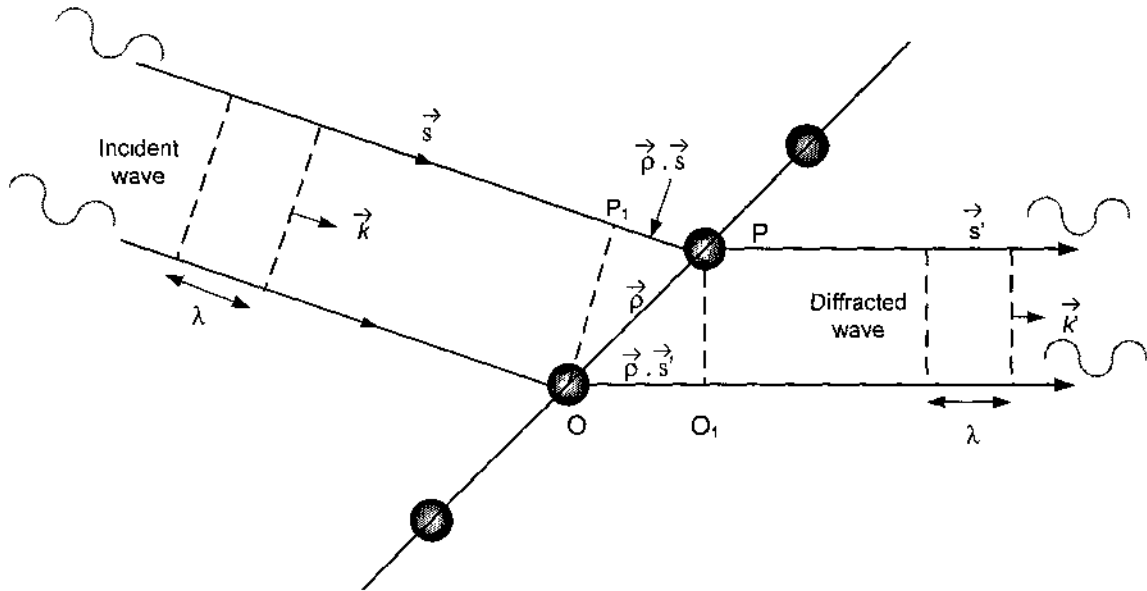


Fig. 2.4. Scattering of incident waves from two atoms located at two lattice sites O and P, with graphical details of phase difference calculation of the scattered waves. Reproduced from Ref. [2].

For the intensity of the diffracted waves to be maximum, constructive interference, the phase difference between the amplitude of the scattered radiation should be integral multiple of 2π , i.e.,

$$\phi = \vec{\rho} \cdot \Delta\vec{k} = 2\pi \times \text{integer} \quad 2.8$$

If $\vec{\Delta k} = \Delta k_x \vec{e}_x + \Delta k_y \vec{e}_y + \Delta k_z \vec{e}_z$ and recalling that $\vec{\rho} = \vec{a} + \vec{b} + \vec{c}$, then Eq. 2.8 can be written in a component form as follows,

$$\begin{aligned}\phi_a &= \vec{a} \cdot \vec{\Delta k}_x = 2\pi q \\ \phi_b &= \vec{b} \cdot \vec{\Delta k}_y = 2\pi r \\ \phi_c &= \vec{c} \cdot \vec{\Delta k}_z = 2\pi s\end{aligned}\tag{2.9}$$

where q , r , and s are integers. That set of equations, Eqs. 2.9 are called the *three Laue equations*.

These equations can be related to the reciprocal lattice by making use of the expression of the reciprocal lattice vector, ($\vec{d}_{hkl}^* = h\vec{a}^* + k\vec{b}^* + l\vec{c}^*$), as well as the following relations:

$$\vec{a} \cdot \vec{d}_{hkl}^* = 2\pi h$$

$$\vec{b} \cdot \vec{d}_{hkl}^* = 2\pi k$$

$$\vec{c} \cdot \vec{d}_{hkl}^* = 2\pi l$$

By adding these equations,

$$\vec{a} \cdot \vec{d}_{hkl}^* + \vec{b} \cdot \vec{d}_{hkl}^* + \vec{c} \cdot \vec{d}_{hkl}^* = (\vec{a} + \vec{b} + \vec{c}) \cdot \vec{d}_{hkl}^* = 2\pi (h + k + l), \text{ i.e.,}$$

$$\vec{\rho} \cdot \vec{d}_{hkl}^* = 2\pi \times \text{integer}\tag{2.10}$$

Comparing Eq. 2.13 to Eq. 2.11, we can write,

$$\vec{\Delta k} = \vec{d}_{hkl}^*\tag{2.11}$$

Eq. 2.11 is called the *Laue diffraction condition*. The Laue diffraction condition can lead to Bragg's law of diffraction by considering Fig. 2.5 [1-3]. The vector $\vec{\Delta k}$ in the reciprocal lattice is simply the vector normal to the reflection plane. If 2θ is the angle between \vec{k} and \vec{k}' , therefore, θ is the angle of incidence and from Eq. 2.7 we get,

$$|\vec{k}| = 2k \sin \theta = (4\pi / \lambda) \sin \theta \quad 2.12$$

$$|\vec{d}_{hkl}^*| = 2\pi / d_{hkl} \quad 2.13$$

Therefore,

$$2d_{hkl} \sin \theta_{hkl} = n \lambda \quad 2.14$$

For $n = 1$, first order diffraction condition, and in its general form,

$$2d_{hkl} \sin \theta_{hkl} = n\lambda$$

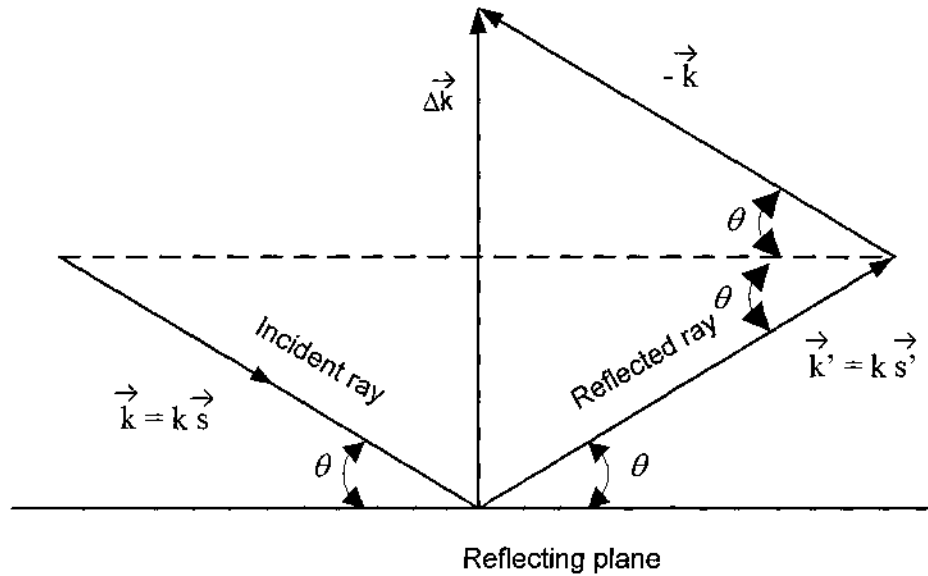


Fig. 2.5. The change in momentum vector, $\Delta \vec{k}$ in terms of the diffraction Bragg angle θ . Reproduced from Ref. [2].

2.2.2.3. Ewald sphere (reflecting sphere)

According to Bragg's law of diffraction where $n = 1$

$$\sin \theta = \frac{1/d_{hkl}}{2/\lambda} = \frac{2\pi/d_{hkl}}{4\pi/\lambda} = \frac{|\vec{d}_{hkl}^*|}{4\pi/\lambda} \quad 2.15$$

In Fig. 2.6, the triangle COP is the graphical representation of Bragg's law. Also, note that the incident beam is along the diameter of the circle in Fig. 2.6. Since the circle

has a radius of $(2\pi/\lambda)$, then CO and CP represent the incident and the diffracted wave-vectors, \vec{k} and \vec{k}' , respectively, and 2θ is the angle between them. Also point C is the center of the circle and represents the location of the (hkl) plane in the crystal [2]. That plane makes an angle θ with \vec{k} and \vec{k}' . Since $\overline{OP} = \overline{CP} - \overline{CO} = \vec{k}' - \vec{k} = \Delta\vec{k} = \vec{d}_{hkl}^*$, and point "O" represents the origin of the reciprocal lattice of the crystal and the diffraction occurs only if the reciprocal lattice point lies on that circle.

For a polycrystalline sample, the reciprocal lattice is the superposition of the reciprocal lattices of the individual crystallites making it. To clarify this point, consider one reciprocal lattice vector \vec{d}_{hkl}^* . If the number of crystallites in the powder is large and randomly oriented, then the reciprocal lattice vector will point in all possible directions and the corresponding reciprocal lattice points lie on the surface of a sphere of radius $|\vec{d}_{hkl}^*|$.

It is obvious that there exists a separate sphere for each value of \vec{d}_{hkl}^* so that the reciprocal lattice is a set of concentric spheres. Since the origin of the reciprocal lattice of each crystallite is located at O, each reciprocal lattice sphere cuts the sphere of reflection (*Ewald sphere*) provided that $|\vec{d}_{hkl}^*| < 2\pi/\lambda$, Fig. 2.7.

2.3. Intensity of the Diffracted Beam

According to section 3.2.1, the intensity of the diffracted beam depends on the atomic scattering factor and the structure factor. The first describes the results of interference effects within the scattering atoms, which is due to the finite size effects of the atom with respect to the wavelength. The latter arises from the interference effects of the radiation scattered from the atoms located at different locations in the unit cell.

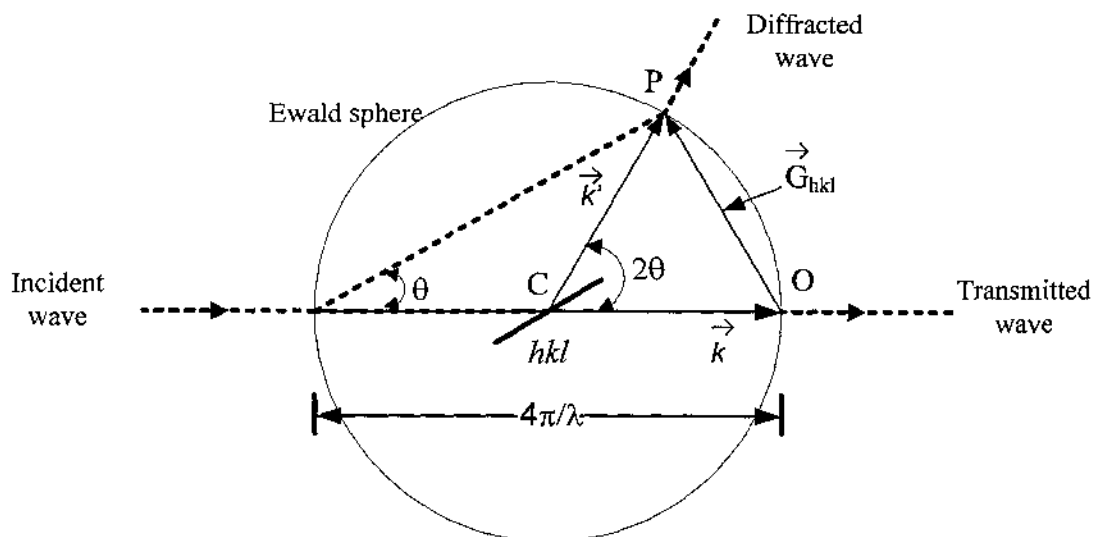


Fig. 2.6. Graphical and vector representation of Bragg's law. Reproduced from Ref. [2].

2.3.1. The atomic scattering factor

The electron atomic scattering factor, $f_e(\theta)$, is obtained after solving the time independent Schrödinger equation, [4]

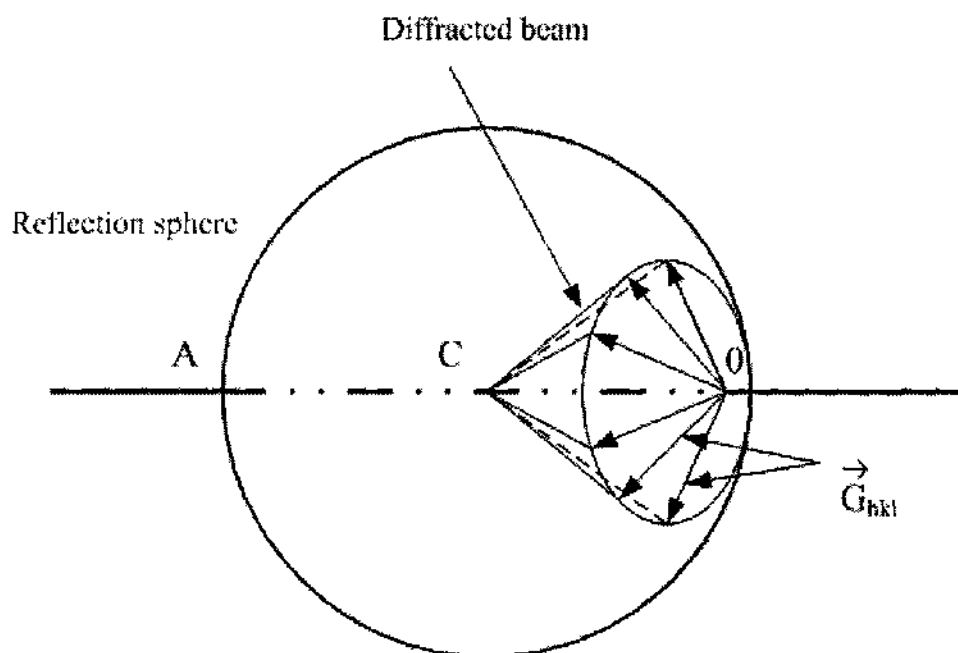


Fig. 2.7. Ewald Sphere (reflection sphere). The reciprocal sphere is not shown. Reproduced from Ref. [2].

$$H\Psi_{k,\alpha} = E\Psi_{k,\alpha} \quad 2.16$$

Where H is the total Hamiltonian of the incident electron-lattice system,

$$H = -\left(\frac{\hbar^2}{2m}\right)\nabla^2 + U + H_o \quad 2.17$$

U is the interaction potential between the incident electrons and the lattice and H_o is the Hamiltonian of the lattice.

If $\Psi_{k,\alpha}$, is the wave function of the interacting electron-lattice system, then

$$\left[-\left(\frac{\hbar^2}{2m}\right)\nabla^2 + U + H_o\right]\Psi_{k,\alpha} = E\Psi_{k,\alpha} \quad 2.18$$

where $E = E_k + E_\alpha$ is the total energy of the system (incident electron and the lattice) [4].

Solving Schrödinger's Eq. gives, [4]

$$f_e(\theta) = \frac{m_o \times e^2}{2\hbar^2} \left(\frac{\lambda}{\sin\theta}\right)^2 (Z - Z_o) \quad 2.19$$

where, Z is the atomic number and Z_o represents the electrons coupled to the atom. For neutral atoms, $Z = Z_o$.

Note that for relativistic effects, i.e. high energy electrons, $f(\theta)$ must be corrected by replacing m_o in Eq. 2.19 by $m_o/(1 - v^2/c^2)^{1/2}$.

2.3.2. The geometrical structure scattering factor

If the incident waves are reflected off a set of planes (hkl) , the structure factor amplitude $|F(hkl)|$ corresponding to (hkl) is the reflection amplitude E_{hkl} divided by the amplitude of the scattered wave by a single electron, i.e., [4]

$$|F(hkl)| = E_{hkl} / E_e$$

$$F(khl) = \sum_j f_j \cdot e^{-i\varphi_j} = \sum_j f_j \cdot e^{-i\vec{r}_j \cdot \Delta\vec{k}} \quad 2.20$$

Where, f_j is the scattering factor from j th atom, φ_j is the phase difference between the j th atom with respect to that at the origin, \vec{r}_j is the position vector of the j th atom, Fig. 2.8.

It follows from Eq. 2.20 that the intensity of the diffracted electron from (hkl) plane is given by:

$$I_{hkl} \propto F(hkl)^2 \quad 2.21$$

But this equation is valid only if the atoms are fixed at specific positions in the lattice which is not the case in real world.

Debye and Waller [5] found that due to the continuous thermal vibrations of the atoms, the intensity of the diffracted beam decreases with temperature and follows what is later called “Debye-Waller factor”.

2.4. Debye-Waller Factor

The effect of temperature on the diffracted beam intensity was quantified according to Debye-Waller effect as follows:

$$I(T) = I_0 e^{-2M} \quad 2.22$$

Where, $I(T)$ is the intensity at T , I_0 is the intensity at reference temperature T_0 , and M is given by, $2M = G^2 \langle \Delta u^2 \rangle$,

where, $\langle \Delta u^2 \rangle$ is the mean square atomic displacement, and G is the change in the electron wave vector as a result of scattering.

$$\langle \Delta u^2 \rangle = \frac{3\hbar^2}{mk_B} \left(\frac{T}{\Theta_D^2} \right) \quad 2.23$$

where, Θ_D is Debye temperature, m is the atomic mass, k_B is Boltzmann's constant, \hbar is

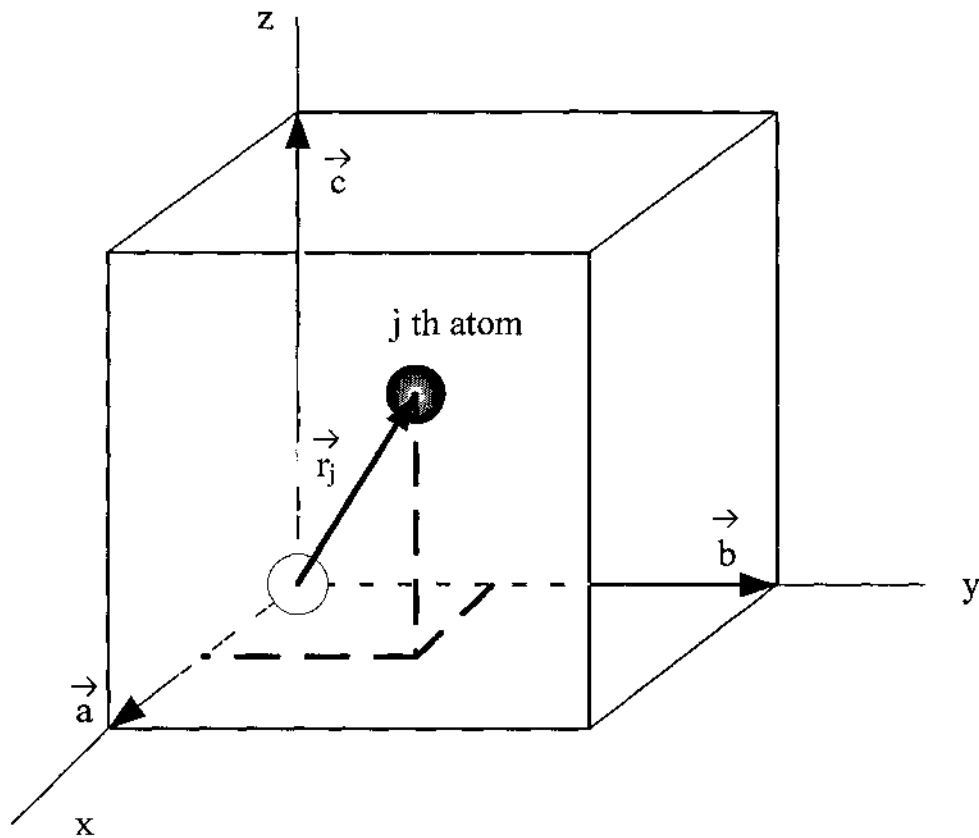


Fig. 2.8. The position of the j th atom relative to the origin is specified by the vector \vec{r}_j . Reproduced from Ref. [2].

Planck's constant divided by 2π . Therefore, from Eq. 2.22 we can see that the effect of temperature is to increase the mean square atomic displacement, which in turn decreases Debye-Waller factor (e^{-2M}) and leads to a decrease in the diffracted beam intensity. According to Eq. 2.22, the Debye-Waller effect, i.e. more intensity drop, is more pronounced for small θ_D and large momentum transfer G .

A direct application of the Debye-Waller factor is to estimate the transient surface temperature of a thin film as a result of laser irradiation, which is a process that occurs over a few picoseconds and cannot be monitored by regular means. This is done by a

proper calibration process. The calibration is done by following the temperature dependence of the diffraction pattern with a conventional heating stage, from which the surface temperature can be estimated as a result of laser heating.

2.5. Transient Structure Dynamics

In general, photoexcitation of the crystal lattice is reflected on the position and shape of the Bragg peaks. Depending on the laser pulse fluence, a lattice disorder or a structural phase transition can be detected. A universal behavior was observed as a result of this kind of interaction, which includes the displacement of the Bragg peak position, intensity decrease and modification of the full width at half maximum of the diffraction ring. Fig. 2.9 summarizes schematically the expected photo-induced changes in the lattice [6,7]. Lattice disorder accompanying the solid-liquid phase transition is a well-known behavior of the photoexcited crystal, which in turn loses its long range order and leads to

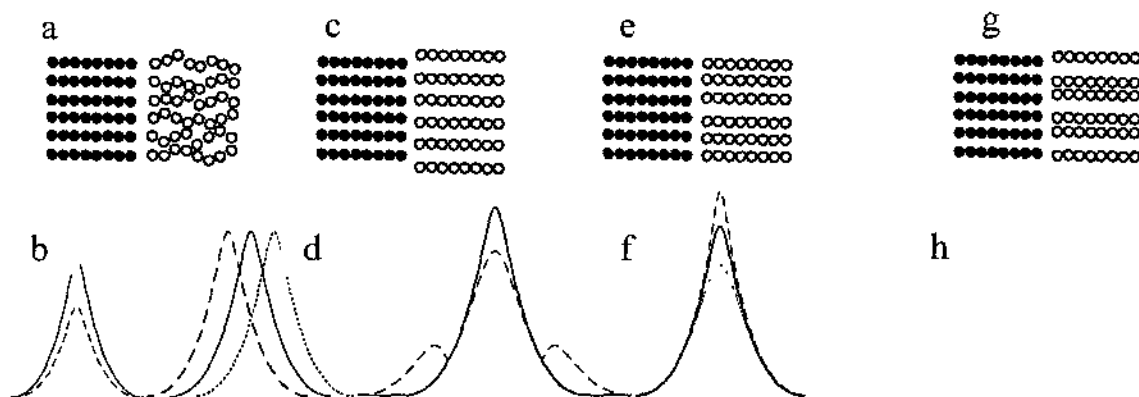


Fig. 2.9. Different mechanisms of lattice response to ultrashort laser pulses (a, c, e and g), and their effect on the detected diffraction pattern (b, d, f, and h). In the upper side of the graph, the blue circles represent the unperturbed lattice, and the red circles represent the perturbed lattice. (a) Thermal effects induce lattice disorder, which in turn is translated as reduced intensity in the diffraction peak (b) due to Debye-Waller effect. (c) Homogeneous lattice disorder can lead to lattice expansion or contraction, red peak or green peak in (d), respectively. (e) Creation of satellite peaks in (f) due to the generation of longitudinal acoustic phonons. (g) Excitation of homogeneous optical phonons can reduce the detected diffraction peak intensity (h) but do not affect the peak position.

dimming or disappearance of the Bragg peak depending on the liquid/solid ratio that's formed due to photoexcited lattice, Fig. 2.9.(a), (e).

If the laser-lattice interaction resulted in homogeneous acoustic lattice deformation, therefore, a lattice contraction/expansion is observed and will be detected as a shift in the Bragg peak position. Inhomogeneous excitation of the lattice occurs whenever the crystal has excited parts adjacent to nonexcited parts, which may lead to the formation of side bands and consequently results in Bragg peak broadening. Crystal size reduction as a result of thin film of liquid formation can lead also to Bragg peak broadening. Both effects are summarized in the following equation:

$$\beta \times \cos \theta = C \times \lambda / D + \eta \times \sin \theta, \quad 2.24$$

where, β is FWHM of the Bragg peak, θ is the diffraction angle, C is constant = 1 for most solids, λ is the electron wavelength, D is the cluster size, and η is the strain. Instrumental effect and defects may also contribute to the Bragg peak broadening.

2.6. References of Chapter 2

- [1] M. De Graef, "Introduction to conventional transmission electron microscopy," Cambridge University Press (2003).
- [2] H. A. Ghalib, A. F. Hassan, and M. M. Al-Fallah "An introduction to the powder method of X-ray diffraction," University of Kuwait (1973).
- [3] C. Hammond "The basics of crystallography and diffraction," 2nd Ed. International Union of Crystallography, Oxford Science publications (2004).
- [4] L. - M. Peng, "Electron atomic scattering factors, Debye-Waller factors and the optical potential for high-energy electron diffraction," J. Elect. Micro. 54, 199-207 (2005)
- [5] A. Matsumuro, M. Kobayashi, T. Kikegawa, and M. Senoo, "X-ray determination of the Debye temperature at high pressure using high-energy synchrotron radiation," J. Appl. Phys. 68, 2719-2722 (1990).
- [6] M. Bargheer, N. Zhavoronkov, M. Woerner, and T. Elsaesser, "Recent progress in ultrafast X-ray diffraction," Chem. Phys. Chem. 7, 783-792 (2006).
- [7] A. Rouse, C. Rischel, and J. Gauthier, "Colloquium: Femtosecond X-ray crystallography," Rev. Mod. Phys. 73, 17-31 (2001).

CHAPTER 3

EXPERIMENTAL SETUP

3.1. Introduction

Time resolved electron diffraction experimental setup is basically used to monitor structure dynamics induced by ultrashort laser pulses. The time factor is introduced in that technique by using a simple delay unit. The purpose of this unit is to change the distance traveled by the probe/pump pulse to reach the sample with respect to that of the pump/probe pulse. This spatial variation results in a time delay between the pump and the probe pulses and enables us to probe in real time the transient dynamics that may occur in solids in a very short time scale as a result of the pump pulse.

In the following, we will describe a pump-probe time-resolved high energy electron diffraction experimental setup, in the transmission mode that is used to monitor thin film structural phase changes in the picoseconds time scale. This experiment, transmission high energy electron diffraction (THEED), is performed in a system that uses a 120 fs laser pulses from Ti:sapphire laser system. The laser beam is split into two parts, one of which is used to pump the sample while the other part is frequency tripled to generate photo-electrons and used as a probe. A variable delay is introduced between the two beams. The integrity of the delay stage is crucial for obtaining accurate scans. The pump beam hits the sample where the high energy electron probe beam should cross. The sample is placed on an X-Y-Z-rotational stage in a high vacuum chamber. The probe electron beam is focused and steered by a set of electromagnets, located outside the vacuum chamber, to the samples, generates a diffraction pattern which is viewed on a

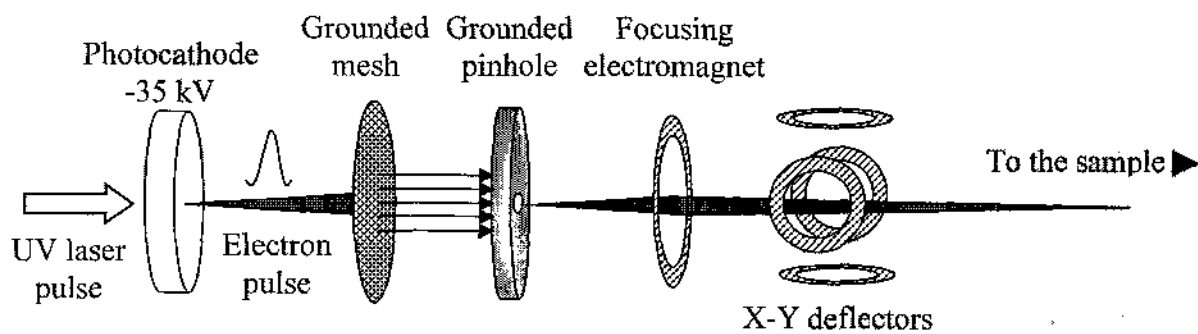
microchannel plate (MCP) detector and captured by an electrically cooled CCD camera. It is imperative to have a dependable evaporation system to prepare a variety of samples of different materials, single crystals or polycrystalline, single material or a complex structure of multilayers. Film diagnostic tools are helpful as well like an optical microscope, a transmission electron microscope (TEM), and atomic force microscopy (AFM).

3.2. Photoactivated Electron Gun, Construction and Operation

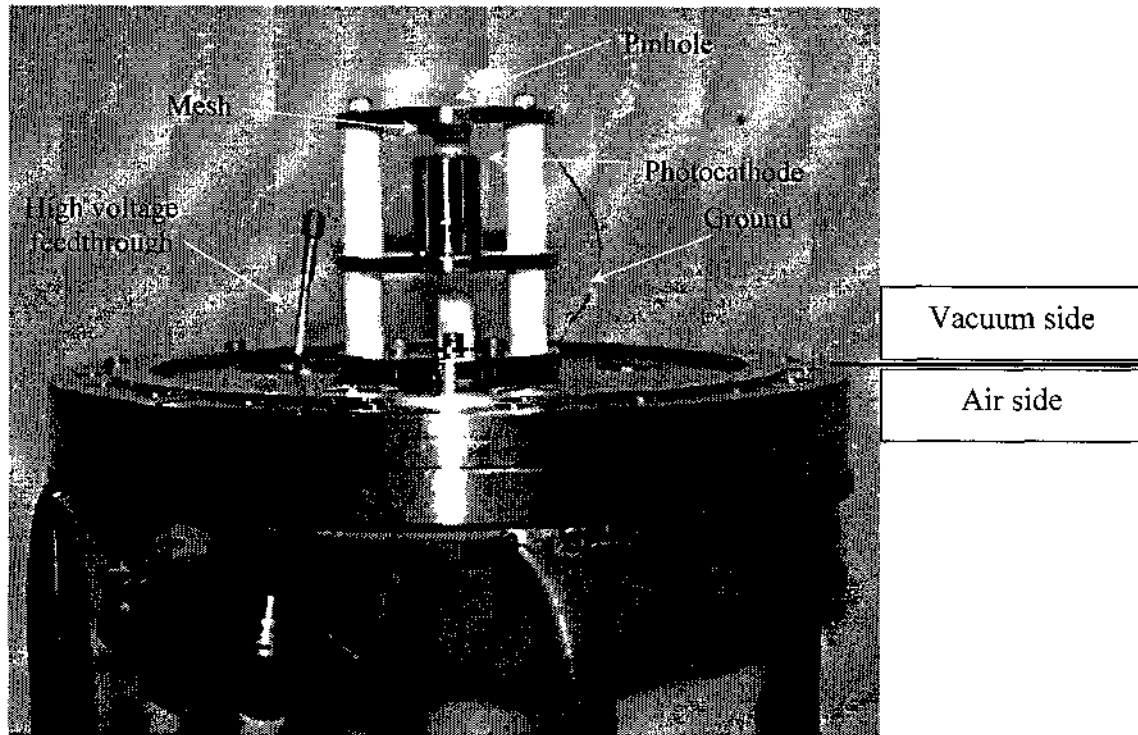
The photoactivated electron gun (PAEG) is the most important component of the system under consideration. In order to study the ultrafast processes of interest, we need the fastest possible probe that can be correlated to the pump beam. An electron pulse that is generated by a portion of the laser beam sounds like a good candidate for obvious reasons. On the one hand it can be focused into a very small spot, a few hundred micrometers, its intensity can be controlled, the trajectory of the beam can be manipulated, it is easily detected and imaged, its interaction with the sample is mainly with the lattice, and above all it is rather easily generated. On the other hand, space-charge effect can effectively broaden the electron pulse and may ruin in some cases the resolution of the system. For these reasons, the distance between the cathode and the anode is supposed to be as minimum as possible, and the distance between the electron gun and the sample should be as small as well.

The detailed layout of the electron gun and the corresponding picture is shown in Fig. 3.1. (a) and (b) respectively.

The photoactivated electron gun is a lab-made unit. The photocathode is $\sim 250 \text{ \AA}$ thick film made out of silver which is thermally evaporated on a sapphire window, using



(a)



(b)

Fig. 3.1 (a) Schematic diagram of the lab-made photo-activated electron gun as well as the set of air-cooled electromagnets used to focus and direct the electron beam towards the sample. The photocathode can be operated at -40 kV, but for experimental and system stability purposes we chose to operate it at -35 kV. (b) Corresponding picture of the electron gun assembly.

tungsten filament and high quality grade silver wire, in a separate vacuum chamber and transferred immediately in the ultrahigh vacuum chamber for testing and operation. This window was placed in a photocathode support electrode groove of thickness that is exactly equal to that of sapphire window [1]. Electric contact to the silver film was made by silver paint. In general, metals are used to fabricate the laser driven photocathodes because of the ease of preparation, high damage threshold, and large free-electron density [2]. The main drawbacks of metals are low quantum efficiencies and high work function (4-5 eV), which require UV photons for linear (one photon) photo-emission [2]. A grounded mesh located 3.8 mm away from the photocathode serves as extraction mesh followed by a grounded 150 μm pinhole for electron beam collimation and reshaping.

The operation of a PAEG is based on the photo-electric effect. The laser beam is split into two parts, one of which is frequency-multiplied and aimed at the main component of the PAEG, the photocathode. The photocathode is biased at -35 keV, which will energize the photogenerated electrons; the electron beam then passes through the grounded extraction mesh followed by the grounded pin-hole (anode assembly), which is ideally imaged on the detector. An external set of electromagnets is air cooled and employed for focusing and steering the beam towards the sample. The schematic details of the e-gun design are shown in Fig. 3.1.

Another important factor that helped in improving the electron gun performance and operation and led to eliminating arcing and electric discharge, is reducing the surface roughness of the stainless steel components used. This is done by polishing the components with diamond compound of different grades, $\frac{1}{4}$ μm - 6 μm , into a mirror finish shape.

The PAEG is mounted on an 8" port of the vacuum chamber opposite to the screen assembly. The screen assembly consists of a double Chevron-type microchannel plate (MCP) followed by a phosphorous screen. A CCD thermoelectrically cooled camera is used to record electron diffraction pattern.

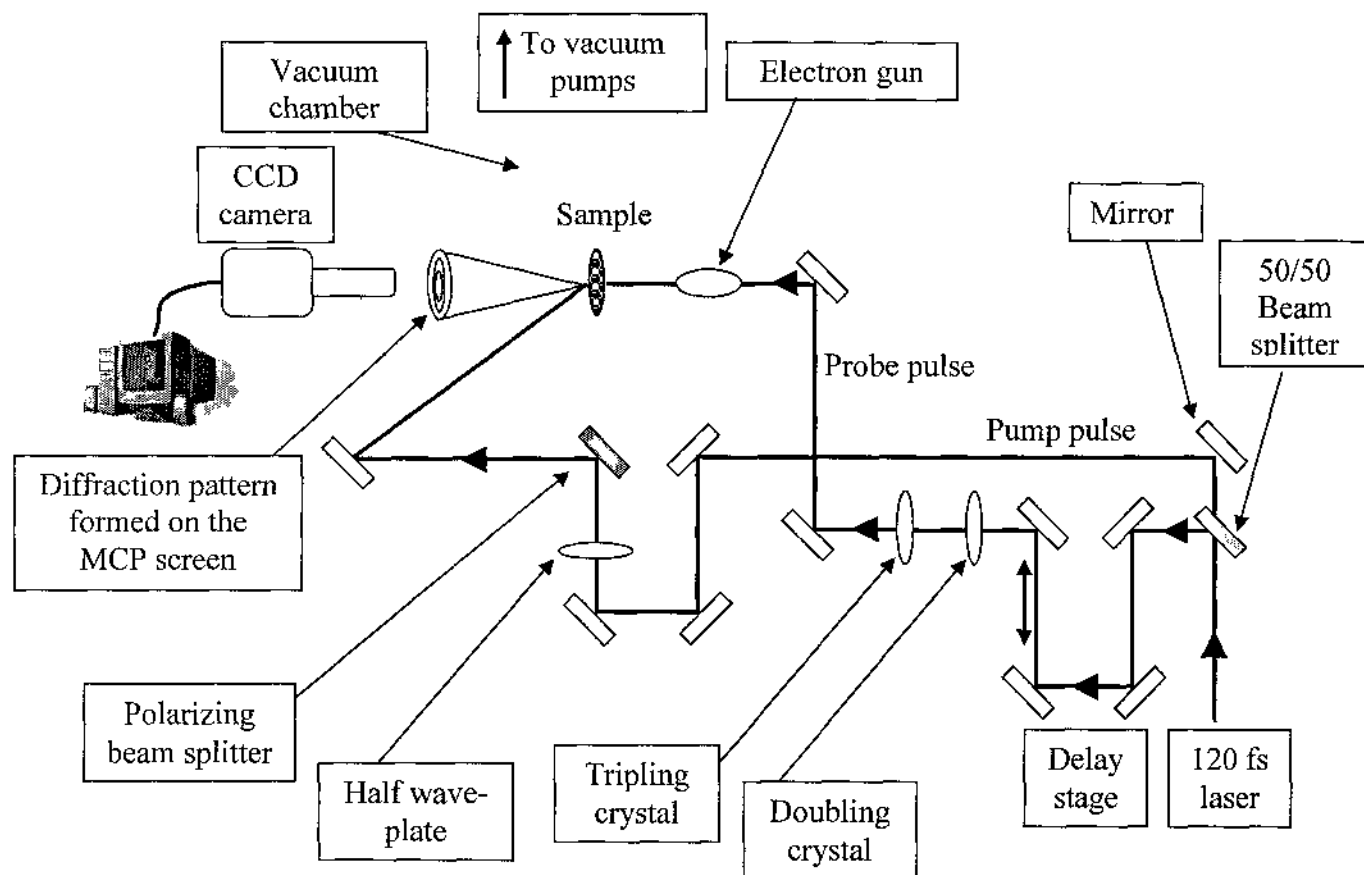


Fig. 3.2. Layout of the time-resolved electron diffraction setup. A 120 fs pulse is generated from Ti:Sapphire chirped pulse amplifier. The system is running at 1 kHz. In this setup, the laser pulse is divided into two parts; one is frequency tripled and used to generate photo-electron from photo-activated electron gun (probe beam), and the other part is used to excite the sample (pump beam). The synchronization between the two beams is granted since they are generated from a single beam.

3.3. Vacuum System

The ultrahigh vacuum chamber is custom made to fulfill our needs and made out of 304 stainless steel and shown in Fig. 3.2 and pictured in appendix C. To achieve the

ultrahigh vacuum needed to maintain the stable operation of the electron gun and other parts inside the chamber, two independent pumping stations are used. The first one is a 300 ℓ /s turbomolecular pump supported by a roughing mechanical pump. This pumping station is able to pump down the system to high 10^{-8} Torr range. This vacuum improves after bake-out. A manual high vacuum valve is used to isolate the turbo pumping station from the chamber. The second pumping station is 270 ℓ /s ion pump, which is connected directly to the vacuum chamber and can pump down the chamber to the 10^{-9} Torr range and goes further to 10^{-10} range after baking the system. The two pumping stations do not operate simultaneously; the turbo station is turned on just after loading the new sample for faster pumping, then the ion pump is turned on after turning off the turbo station.

3.4. Sample Heating and Manipulation

The samples were properly mounted on a lab-made heating stage. The heating stage is properly fitted in the system and allows the operation of the system in the transmission mode. Additionally, the heating wires were carefully embedded and installed inside a thin and highly conductive metal sheet to allow a uniform heating of the samples under study. The heating stage is held on an X-Y-Z rotational stage manipulator. For temperature measurements we have used a K-type thermocouple that is imbedded inside the heater and as close as possible to the samples, 2 mm, for accurate temperature measurements. The thermocouple went through different calibration procedures to insure the accurate measurement of the sample temperature. As a result, the temperature measurement was accurate enough within an error of ± 1 °C.

3.5. Laser System

To resolve in real time the picosecond strain pulses generated as a result of laser-sample interaction, very short optical pulses are required. A good candidate for this purpose is the Ti:sapphire amplifier system, which is based on the chirped-pulse amplification technique [3,4]. Such systems are capable of producing optical pulses of width in the range of few tens of femtoseconds. However, for generation of reasonable and detectable strain that produces detectable deformation, a few mJ.cm^{-2} optical pulses are needed. These specifications are now available in commercial laser systems with reliable stability [5].

The laser system used in our experiment is described in the following section and the block diagram is shown in Fig. 3.3.

In general, it consists of the following parts:

- Femtosecond oscillator (seed laser)
- Stretcher
- Regenerative amplifier
- Pump laser
- Compressor

3.5.1. Ti:sapphire oscillator (seed laser)

Ti:sapphire lasers are good candidates whenever ultrashort optical pulses are needed. Ti:sapphire in these lasers is adopted over any other material because (a) it has a broad absorption band in the blue and green region, which facilitates the use of frequency doubled Nd:YLF laser system as a pumping source; and (b) it has tunable, near infrared broad emission band centered around 800 nm line. Additionally, this system has an

output of a few to tens of femtosecond laser pulses in the 800 nm wavelength range after being modelocked. Modelocking is a technique used to have laser modes in the cavity with fixed phase relationship.

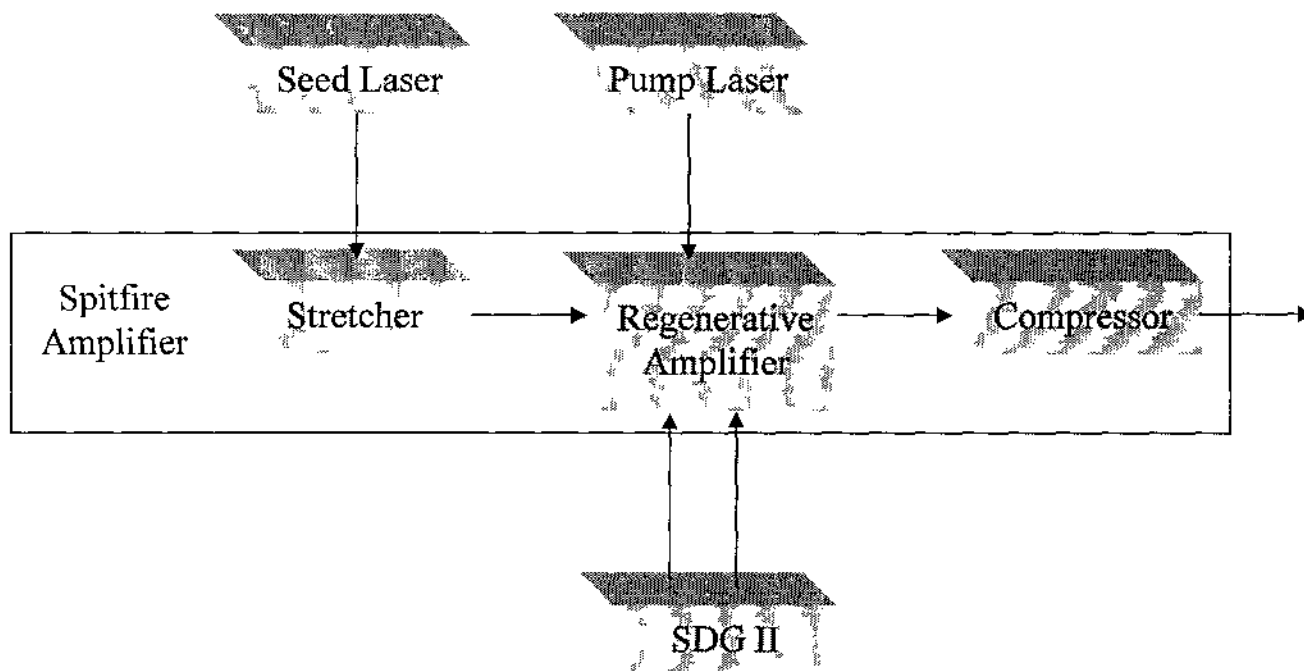


Fig. 3.3. Block diagram for femtosecond laser; SDG II stands for synchronization and delay generator. Reproduced from spitfire manual.

In the absence of modelocking, the light will travel back and forth between the two end mirrors and interfere constructively with itself, forming a standing wave in the laser cavity. The modes within each standing wave have no fixed phase relationship and consequently will oscillate independently. Consequently, the output from a multimode continuous wave laser is fluctuating due to the interference between the modes as shown in Fig. 3.4 and will be noise as with no fixed phase relation. Modelocking technique will manipulate the phases of these modes to get a useful output, Fig. 3.5.

The purpose of mode-locking is to create a phase relationship between the modes, resulting in completely constructive interference between all the modes at one point and destructive interference everywhere else. Therefore a light pulse will travel back and forth between the end-mirrors, giving a pulse output each time it is incident upon the semi-transparent output mirror. Techniques of mode-locking lasers fall into two broad categories: active mode-locking and passive modelocking [7], and are shown schematically in Fig. 3.6. The details of these techniques are beyond our interest, but can be found in more details in Ref. [7].

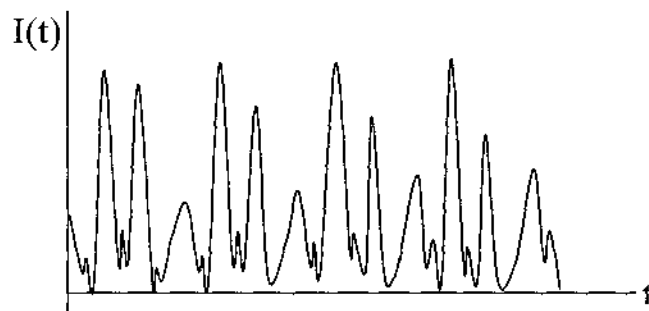


Fig. 3.4. Schematic of a multi-mode laser output, showing the fluctuations of its output. Reproduced from Ref. [6].

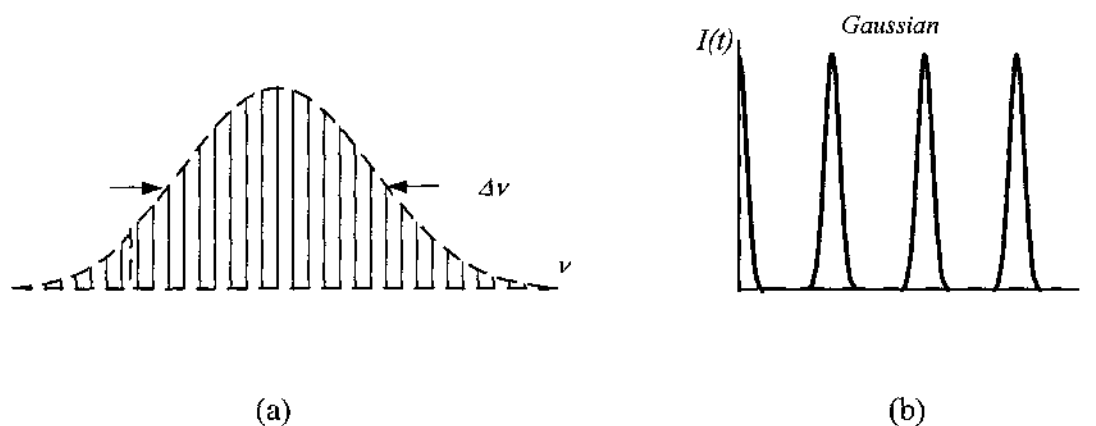


Fig. 3.5. Modelocked laser output, (a) spectrum, (b) laser output in time domain. Reproduced from Ref. [6].

3.5.2. Laser amplifier, (stretcher - regenerative amplifier - compressor)

The output from the previously mentioned self modelocked oscillator can be as low as 65 fs laser pulses with 790 nm wavelength with high repetition rate and energy ~ 1 nJ/pulse. Although Ti:sapphire crystal in the regenerative amplifier has a high damage threshold, it cannot directly amplify the femtosecond pulses from the oscillator, as this will damage the optical components in the amplifier as well as the crystal itself. To overcome this limitation and avoid the nonlinear effects that may be induced in the crystal, Chirped Pulse Amplification (CPA) [8,9] was adopted. CPA is a three step process shown schematically in Fig. 3.7. First, the ultrashort seed pulse from the oscillator is stretched. This stretching results in a reduction in the pulse peak power, which in turn reduces the probability of damaging the Ti:sapphire crystal. A stretcher is basically composed of a pair of gratings aligned such that the seed pulse components with longer wavelength will arrive earlier than shorter wavelength components; this results in a stretched pulse (pulse duration increased) traveling towards the amplifier, Fig. 3.8.

The second step in CPA is an amplification process to stretch the pulse, the scenario of which is as follows. The output from pump laser, Fig. 3.3, is used to excite the Ti:sapphire crystal, creating population inversion just before the arrival of the stretched seed pulse. The seed pulse induces stimulated emission in the crystal and thus amplifies the pulse at the same wavelength and direction.

The final step in the CPA, is to undo the process initiated by the stretcher, i.e., to arrange a special pair of grating such that the longer wavelength components of the amplified pulse travel longer distance through it than the shorter wavelength ones. The

output pulses are ~ 120 fs in width, and 800 nm wavelength and average energy 1.4 mJ/pulse. The pulse repetition rate is tunable from 1 Hz to 1000 Hz.

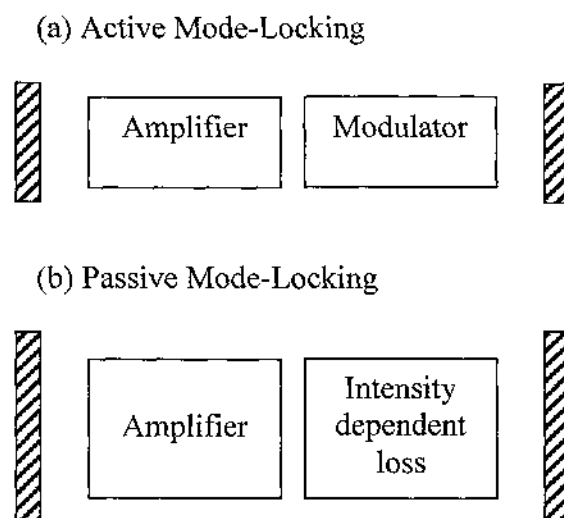


Fig. 3.6. Schematic diagram showing the active and the passive modelocking [7]. (a) Active modelocking: in this technique, modulation of the radiation in the laser cavity is done by a signal derived from an external clock source, to the modulator, and matched to the cavity roundtrip time. (b) Passive modelocking, in which the laser radiation itself generates a modulation through the action of non linear device in the laser cavity, and it is thus synchronized to the cavity round trip frequency. Reproduced from Ref. [7].

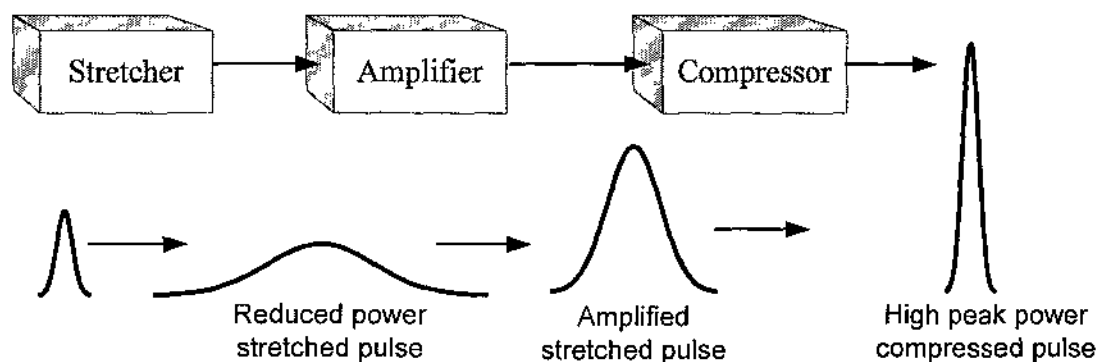


Fig. 3.7. Schematic diagram of CPA technique.

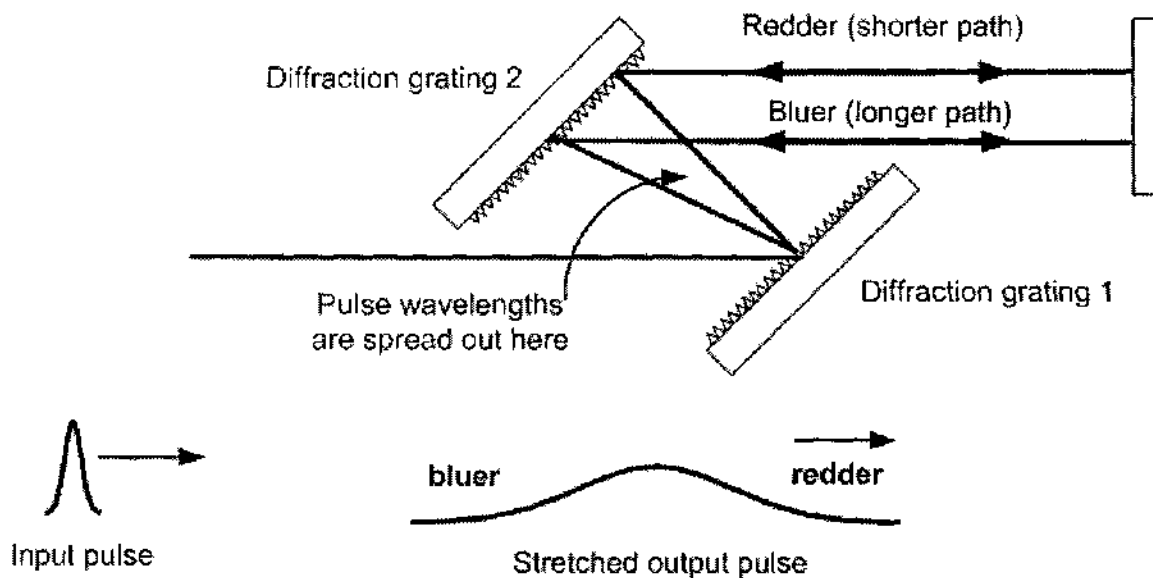


Fig. 3.8. Grating-pair arrangement for seed pulse stretching resulting in a longer laser pulse that is seeded to the regenerative amplifier.

3.6. Electron Diffraction Pattern Acquisition and Data Analysis

The electron diffraction pattern of the sample under study is formed on an MCP-phosphorus screen assembly. The pattern is captured by a computer controlled CCD camera and stored in a proper format for data analysis.

A series of softwares were used, one after another, to radially average and analyze each diffraction pattern to extract the intensity, the position and full width at half maximum of each Bragg diffraction ring at different delay time, appendix H.

3.7. Expected Improvement

For time resolved electron diffraction experiments, the most important issues are related to the resolution of probe and the synchronization between the pump and the probe pulses. To improve the resolution of the electron probe pulses, I suggest the following for the built system:

- 1- Minimizing the distance between the anode and the cathode, acceleration region.

- 2- Minimizing the distance traveled by the electron bunches from the anode to the sample, drift region.
- 3- Transferring the electromagnets set inside the vacuum chamber between the electron gun and the samples.

3.8. Reference of Chapter 3

- [1] H. E. Elsayed-Ali and J. W. Herman, "Ultrahigh vacuum picosecond laser-driven electron diffraction system," *Rev. Sci. Instrum.* 61, 1636-1647 (1990).
- [2] M. Aeschlimann, E. Hull, J. Cao, C. A. Schmuttenmaer, L. G. Jahn, Y. Gao, H. E. Elsayed-Ali, D. A. Mantell, and M. R. Scheinfein, "A picosecond electron gun for surface analysis," *Rev. Sci. Instrum.* 66, 1000-1010 (1995).
- [3] D. Strickland and G. Mourou, "Compression of amplified chirped optical pulses," *Optics Communications* 55, 447-449 (1985).
- [4] M. Pessot, P. Maine, and G. Mourou, "1000 times expansion/compression of optical pulses for chirped pulse amplification," *Optics Commun.* 62, 419-421 (1987).
- [5] S. H. Lee, "Time-resolved X-ray measurements of energy relaxation in ultrafast laser excited semiconductors," Ph.D. dissertation, University of Michigan (2006).
- [6] <http://www.df.unipi.it/~fisapp/Gruppi/Metrologia/spiegazioni/boris.pdf>, last visited, 10/07/2008.
- [7] P. M. French, "The generation of ultrashort laser pulses," *Rep. Prog. Phys.* 58, 169-267, (1995).
- [8] X. Liu, D. Du, and G. Mourou, "Laser ablation and micromachining with ultrashort laser pulses," *IEEE J. Quant. Elect.* 33, 1706-1716 (1997).
- [9] O. E. Martínez, "Design of high-power ultrashort pulse amplifiers by expansion and recompression," *IEEE J. Quant. Elect.*, QE-23, 1385-1387 (1987).

CHAPTER 4

THIN FILM PHOTOEXCITATION BY FEMTOSECOND LASER PULSES

4.1. Introduction

An atomic number of 83 of Bi has classified it to belong to group V elements in the periodic table with electronic configuration $[Xe]4f^{14}5d^{10}6s^26p^3$. The two s states and the three p states are filled with the ten valence electrons in the Bi unit cell, (two atoms per unit cell, with 5 electrons per atom in the valence shell). But the band structure of Bi is not that simple, since the p bands penetrate the Fermi level and create hole pockets and electron pockets at T point and L point, respectively, Fig. 4.1 [1,4]. That penetration is not that deep, 27.3 eV for electrons and 10.8 eV for holes, and results in charge carriers densities of $3 \times 10^{17} \text{ cm}^{-3}$, which are quite small with a small electron effective mass along $\langle 111 \rangle$ direction ($m^* = 0.003 m_0$) [1,3].

Although Bi was classified as a semimetal (poor metal) with very low thermal conductivity, it has the highest Hall coefficient [2]. Lovett [5] mentioned that Bi may behave as a semiconductor or close to narrow band gap semiconductor due to the band gap that covers most of the Brillouin zone.

It is instructive to compare the Bi rhombohedral electronic structure to that of the simple cubic Bi. This is because the two atoms per rhombohedral unit cell will be reduced to one in the simple cubic unit cell, and consequently, the even number of valence electrons becomes an odd number. This predicts the cubic unit cell of Bi to have metallic character, where the rhombohedral unit cell could be seen as an insulator, but the small overlap between the energy bands leads to the semimetallic behavior of Bi.

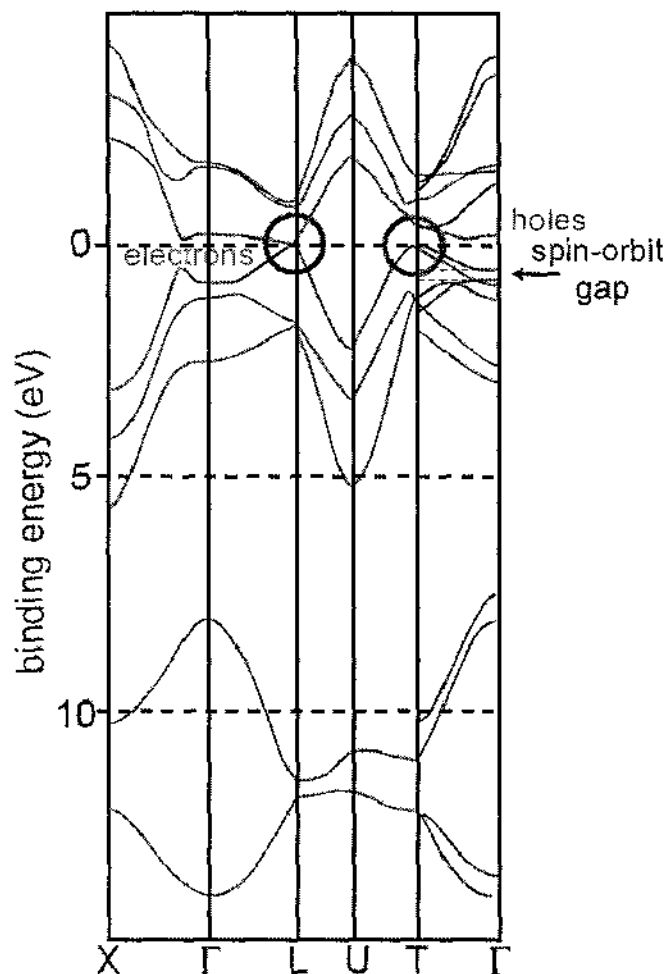


Fig. 4.1: Band structure of bulk Bi, (green lines, Ref. [6], red lines, Ref. [7]). Reprinted from Ref. [1].

Therefore, our previous discussion aimed at a very important point, which is, structural changes at the surfaces will have a great impact on the electronic structure [1]. Shick et al. [8] showed that the semimetal to semiconductor transition is possible in Bi and can be controlled by a minor change in the structure. A factor that may affect the crystal structure is the surface reconstruction. Since the atoms are covalently bonded in Bi, the surface atoms may not reconstruct and thus affect the surface electronic structure and enhance the semiconducting nature of the surface atoms, which are located on top of a semimetallic core atoms [4].

4.2. Bi on the Reduced Dimension, (thin films, nanowires, and nanoclusters)

The properties of the small structures like thin films, nanowires and nanoclusters can be very different from those of the bulk. For example, Bi nanowires were shown to have enhanced thermoelectric properties compared to that of the bulk [9]. The figure of merit (ZT), Eq. 4.1, that defines the thermoelectric nature of 7 nm Bi nanowires, oriented along $\langle 111 \rangle$ direction, was found to be ~ 2 at room temperature which makes it an efficient thermoelectric cooler.

$$ZT = \frac{S^2 \sigma}{K_e + K_L} T \quad 4.1$$

Where, $S = \frac{\Delta V}{\Delta T}$ is Seebeck coefficient and is defined as the change in the induced thermoelectric voltage (ΔV) due to a temperature change ΔT , σ is the electrical conductivity, T is the temperature, K_e and K_L are the electronic and phonon thermal conductivity.

The semimetallic nature of bulk Bi, arising from the C-V band overlap, makes it a poor thermoelectric material, and the contribution from the electron and holes to the Seebeck effect cancel out each other. However, the contribution from the holes can be diminished by increasing the band gap between the conduction and valence bands. This can be accomplished by combining Bi with antimony (Sb) to make Bi-Sb alloy and applying a strong magnetic field (1.7 T) to the Bi-Sb alloy [10]. But this field is high, which is not suitable for commercial use. The band gap can also be reduced, or completely removed, by reducing the size of the bulk material to the nanoscale. Confinement effects in Bi nanoclusters, nanowires and thin films can shift the lowest

energy states of the electrons above the highest energy states of the holes and force the semimetal-semiconductor (SM-SC) transition [11,12].

The SM-SC transition was predicted [13] at 77 K in 49 nm thick Bi wires grown along $\langle 012 \rangle$ and at room temperature for 16 nm thick wires, Fig.4.2. The reduced dimensionality creates energy sub-bands with separation “ Δ' ”, Fig. 4.3, while Δ_0 is the conduction-valence band overlap, that's inversely proportional to the cluster diameter square “ D^2 ” and the electronic effective mass “ m^* ” according to; [14]

$$\Delta' = \frac{\pi^2 \hbar^2}{m^* D^2} \quad 4.2$$

where \hbar is Planck's constant divided by 2π .

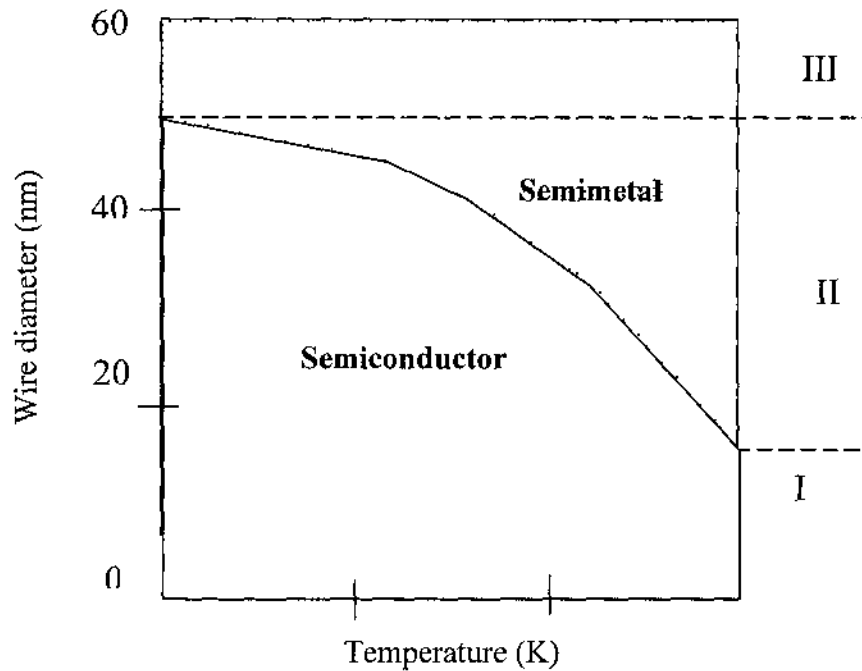


Fig. 4.2. Semimetal-semiconductor phase transition in Bi at different temperature and thicknesses. At constant temperature, Bi can be semimetal (phase III) or semiconductor (phase I) or undergoes SM-SC transition as the temperature is reduced from 300 to 0 K. Reproduced from Ref. [13].

Therefore the electron effective mass as well as the cluster size have a direct impact on the C-V band separation. As the cluster size goes beyond a critical value, a gap is formed between the conduction and the valence bands, and the overlap no longer exists, forcing the SM-SC transition, which enhances the thermoelectric properties of Bi nanowires.

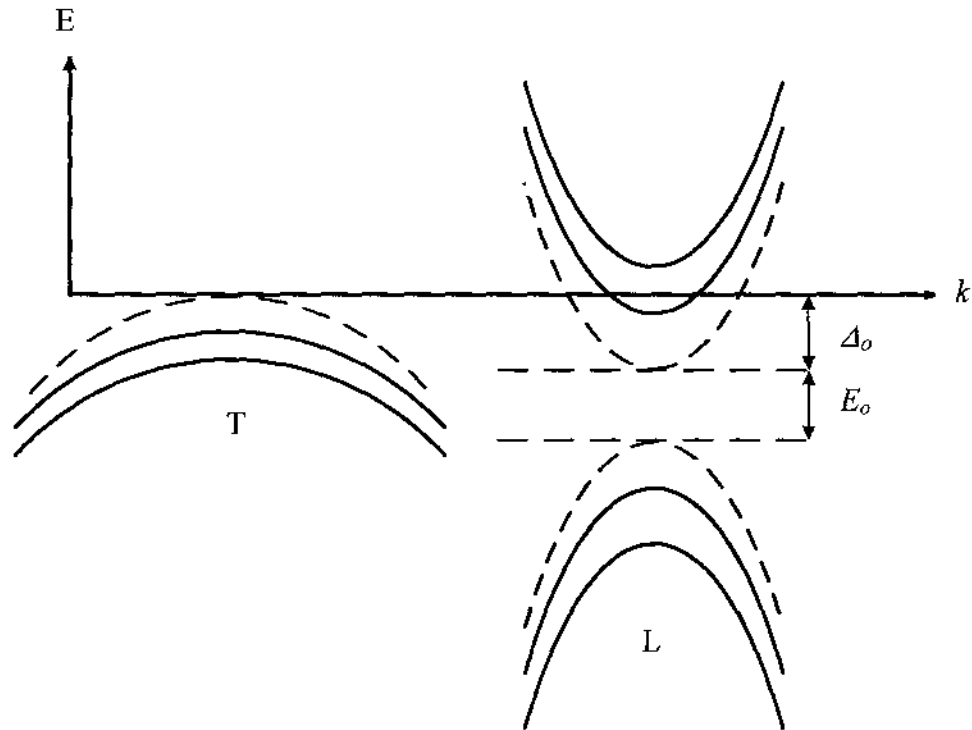


Fig. 4.3. Schematic diagram showing the electronic band structure of bulk Bi (dashed lines) compared to that of the nanowires/nanoclusters (solid lines). Δ_o is the conduction-valence band overlap. Reproduced from Ref. [13].

Quantum size effect is another consequence of the reduced dimensionality of Bi. Quantum size effect is dictated by quantum mechanics for particles with very small dimensions D compared to de Broglie wavelength λ_B of the electrons that are trapped and reflected off the particle's boundary. This phenomenon was described by the quantum box model, which was introduced by Efros and Efros [15]. They described the motion of

the electrons to be restricted in all directions by impenetrable walls. This model also describes the dependence of the energy gap (E_g) on the particle size (D), $E_g \propto \frac{1}{D^2}$.

Another consequence of the quantum size effect is that the particles have atomic like energy levels, not continuous energy bands like bulk material. This leads to discrete absorption/emission spectra in contrast to the continuous spectrum of the bulk.

The early work of Ogrin et al. [16] on Bi thin film grown in $\langle 111 \rangle$ direction, was the spark that has started the fire of the field of research of quantum size effects in thin films. They were able to detect the oscillations in the transport properties induced by the quantum size effect as a function of the Bi film thickness.

In summary, reducing the dimensions of the Bi clusters will change the electronic structure due to the quantum size effects. Additionally, the surfaces of the small structures can possess different electronic properties from the bulk, which makes them technologically important [1].

4.3. Ultrafast Laser Excitation and Dynamics in Bi Nanoclusters

In general, light pulses with sufficient energy can excite electrons to higher energy states which relax to their original state through different processes. Upon electron excitation, holes are created in the original energy band. The photoexcitation of electrons can be classified as a direct or indirect process.

The direct excitation process is not accompanied by a change in the wave vector, while the indirect process is accompanied by a wave vector change due to emission or absorption of phonons where the conservation of total system momentum still holds. This electronic excitation is followed by a de-excitation process through which the electrons may go through different scattering processes, electron-electron and electron phonon

scattering processes, before they recombine with the holes in the valence band. The scattering processes are either elastic, where the total energy and the momentum of the system are conserved or non elastic, which is accompanied by creation or annihilation of phonons to maintain the conservation of the total energy of the system. In some cases, the response of photoexcited lattice is complex, and in the next section, I will go over some basic and common lattice dynamics as a result of ultrashort laser excitation.

4.3.1. Electron and lattice dynamics induced by ultrafast laser pulses

As mentioned earlier, following the photoexcitation with ultrashort pulses, the lattice may go through different relaxations processes prior to equilibration. The different pathways that can be identified during carrier excitation and relaxation are; (i) carrier excitation, (ii) thermalization, (iii) carrier removal and (iv) thermal and structural effects. Fig. 4.4 summarizes the different time scales characterizing these processes, while Fig. 4.5 shows these processes in action [17,18]. It is worth noting that these processes are not happening one after the other, but rather overlap in time. As an example, thermalization of charge carriers occurs during carrier-lattice thermalization. Additionally, non-thermal effects can lead to metastable structures over a very short period of time while the lattice temperature is still almost constant.

(i) Carrier excitation

The probability of carrier excitation by single photon absorption is high as long as the incident photon energy is higher than the bandgap of the absorbing medium. For indirect bandgap SC, excitation by single photon absorption is possible, but this process necessitates the presence of a phonon for momentum conservation. On the other hand, multiphoton absorption on the right side of Fig. 4.5.(a) is possible in direct band gap SC

if the incident photon energy is less than the band gap. In metals, free carrier excitation increases their energy but not their energy density, Fig. 4.5.(b). The only way to increase that number is through impact ionization, Fig. 4.5.(c).

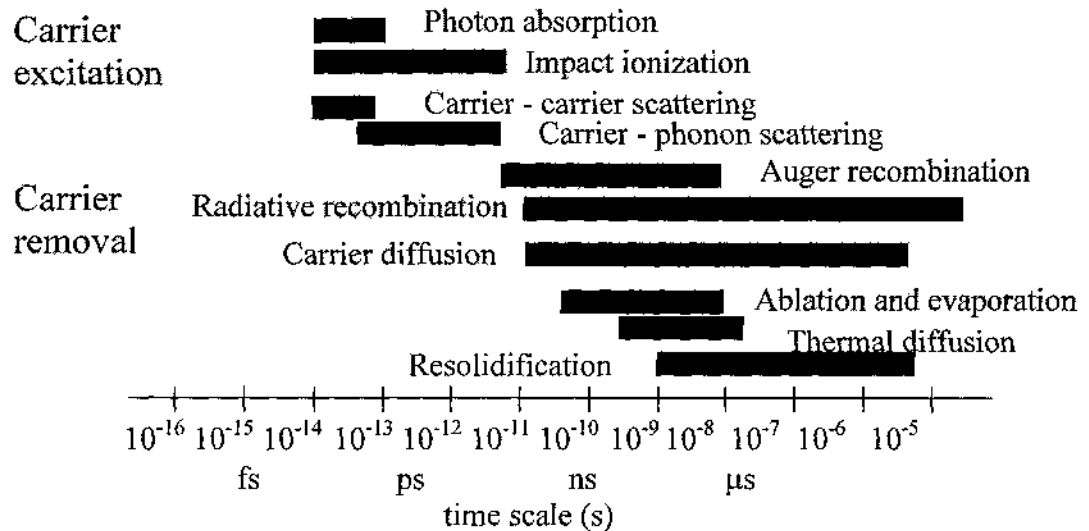


Fig. 4.4. Time scale of different processes induced in the lattice as a result of ultrashort laser pulse excitation. The dark bars show an approximate time scale of occurrence of these processes. Reproduced from Ref. [17].

(ii) Thermalization

Two regimes are considered following charge carrier excitation, namely, carrier-carrier and carrier-phonon scattering, through which thermalization of excited carrier occurs. In the carrier-carrier scattering process, two carriers are involved, Fig. 4.5.(d), and the total energy of the excited carriers are conserved as well as their number. In the carrier-phonon scattering process, the total energy and momentum of the system is not conserved and therefore a phonon is created or annihilated to account for the energy lost during this process. This is illustrated in Fig. 4.5.(e) if it is an intraband scattering and in Fig. 4.5.(f) for interband scattering.

Again, during the carrier-phonon scattering process, the total number of carriers is conserved, but their energies decrease as a result of phonon creation, which in turn gives off its energy to the lattice. Carrier relaxation usually occurs over a few hundred femtoseconds, while several picoseconds are needed for carriers and lattice to be in thermal equilibrium, and the material is in a thermal state characterized by temperature T . This temperature rise causes the lattice to expand, which in turn generates acoustic coherent phonons propagating into the bulk [19] and stresses the lattice.

(iii) Carrier removal

Many processes are considered and contribute to the removal of excited charge carriers that are not yet in thermal equilibrium with the lattice, and consequently its density reduction in the excitation region. These processes are, but are not limited to, electron-hole recombination and/or diffusion into deeper region in the sample and leaving the area of excitation. Electron - hole recombination may be radiative or non radiative in nature. In radiative processes, opposite to excitation, a photon is emitted that carries the excess carrier energy, Fig. 4.5.(g). While in nonradiative recombination process, which includes Auger recombination, an electron recombines with a hole and the excess energy will be carried out by another electron and excited to a higher energy level, Fig. 4.5.(h). Excited carriers can be removed from the excitation region by diffusion into the sample, Fig. 4.5.(i).

(iv) Thermal and structural effects

Thermal and structural effects come into the picture when the charge carrier and the lattice are in thermal equilibrium and the final lattice temperature is determined by the initial energy deposited by the ultrashort laser pulses into the sample. Melting or

vaporization can occur if the lattice temperature exceeds the lattice melting or boiling temperature, respectively. In some cases, the material preserves its solid integrity at temperatures above its melting point, and in this case the lattice is said to be superheated

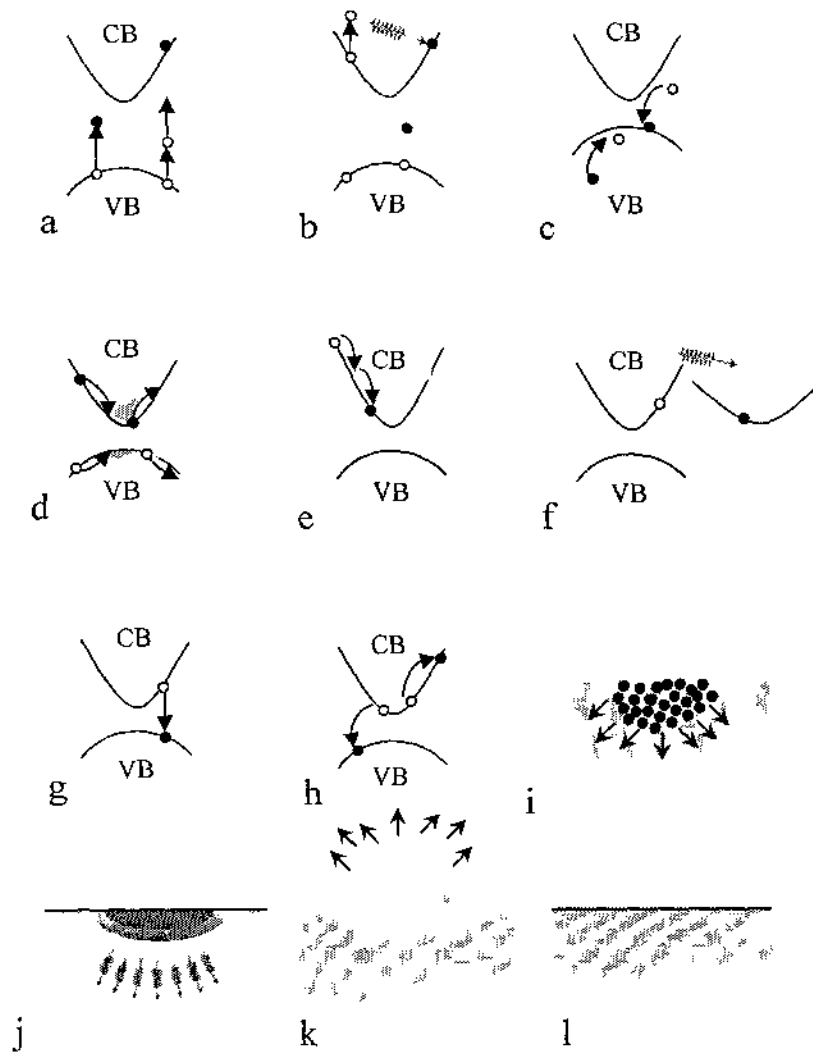


Fig. 4.5. Schematic of the different electron and lattice processes induced by ultrashort laser pulses: a) single and multiphoton absorption, b) Carrier absorption, c) Ionization, d) Carrier distribution before scattering, e) Carrier-carrier scattering, f) Carrier-phonon scattering, g) Radiative recombination, h) Auger recombination, i) Diffusion of excited carriers, j) Thermal diffusion, k) Ablation l) Resolidification or condensation. Reproduced from Ref. [17].

until liquid and gas sites start to nucleate at the surface, Fig. 4.5.(j). Ablation is a consequence of partial removal of lattice ions, atoms, and clusters at high excitation fluence, Fig. 4.5.(k). If the photoexcitation of the material did not induce any phase transition, the final temperature of the material recovers to a value determined by the surroundings over a microsecond time scale. At low excitation fluence, the sample can recover (resolidifies), Fig 4.5.(l), after melting when its temperature becomes less than the melting point. In some cases, the sample does not maintain its original structure after being photoexcited by ultrashort laser pulses [20, 21].

Although the processes included in ultrafast photoexcited material are complex and each process can stand as a different topic of study, the energy exchange process between excited carrier and the lattice can be simplified and described in terms of either the one or the two temperature model based on the laser pulse duration relative to the lattice equilibration time [22, 23].

4.3.2. The one and the two temperature model

Upon photoexcitation with ultrashort laser pulses, the first thing to respond are the electrons, due to their low specific heat capacity compared to that of the lattice. Carrier-carrier scattering relaxes the excited carriers, and their temperature can be characterized by T_e and follow Fermi-Dirac distribution. This process occurs over tenths of picoseconds, while the lattice is still at its original temperature T_l following Bose-Einstein distribution. This process summarizes what is known as the two temperature model (TTM), and usually considered especially when the excitation source is very short pulses with duration t_{exc} less than the carrier-lattice thermalization time t_{lat} .

In this case, the system is characterized by a set of coupled equations in terms of T_e and T_l [22].

$$C_e(T_e) \frac{\partial T_e}{\partial t} = K_e \frac{\partial^2 T_e}{\partial z^2} - g(T_e - T_l) + S(z, t) \quad 4.3$$

$$C_l \frac{\partial T_l}{\partial t} = g(T_e - T_l) \quad 4.4$$

Where the subscripts e and l stand for electrons and lattice, respectively. C is the heat capacity, K_e is the thermal conductivity of electrons, $S(x, t)$ is the laser source term given by Eq. 4.6 and g is the electron-phonon coupling factor estimated by, [23]

$$g = \frac{\pi^2 m_e n_e C_s^2}{6\tau_{e-p}} \quad 4.5$$

where m_e is the electron mass, n_e is the electron density, τ_{e-p} is the electron-phonon collision time and c_s is the speed of sound in bulk material calculated by, [24]

$$c_s = \sqrt{\frac{B}{\rho_m}}$$

where B is the bulk modulus and ρ_m is the density.

Assuming the absorption coefficient to be constant and using the definition of optical penetration depth $\delta = 1/\alpha$, the laser source term $S(z, t)$ in units of W/cm^3 is given by; [22]

$$S(z, t) = \frac{0.94J}{t_p \delta} (1 - R(t)) \exp\left(-2.77 \left(\frac{t}{t_p}\right)^2 - \frac{z}{\delta}\right) \quad 4.6$$

where J is the laser fluence in J/cm^2 ; t_p is the pulse duration; R is the reflectivity, and α is the absorption coefficient.

Note that heating the sample with ultrafast laser pulses raises the electron temperature up to few thousand Kelvin; therefore, C_e cannot be treated as constant

because it is temperature dependent. Additionally, the carrier diffusion is usually ignored if the sample dimensions are comparable or less than the optical penetration depth of the excitation source.

On the other hand, if the laser pulses are long compared to the equilibrium time, then the excited carriers will relax over a very short period of time comparable to that of the excitation pulse duration. In this case, the temperature of the carriers is given by; [23]

$$C_l \frac{\partial T}{\partial t} = K_l \frac{\partial^2 T}{\partial z^2} + S(z, t) \quad 4.7$$

Eq. 4.7 is the known heat diffusion equation with the heat source term S to supply energy to the system over the pulse duration.

4.3.3. Mechanism of coherent phonon excitation

Although the methodology used to excite coherent lattice vibrations is the same, the generation mechanism of these vibrations is different in different materials, superconductors [24,25], semiconductor [26-28] and semimetals [29]. For example, in semimetals a large modulation in the reflectivity was attributed to the modification in the electronic band structure resulting from the displacive excitation of coherent phonon mechanism (DECP) [30,31].

The sample response to the femtosecond laser pulses is a collective contribution from the change in excited carrier density, change in carrier temperature, and change in coherent phonon amplitude [30]. The contribution from the later term can be recognized and separated from the other contributions because of its oscillatory nature that is superimposed on an exponentially decaying term, (the reader can refer to page 50 Ref. [30] for more details about the graphical representation of this effect). This term arises from the DECP and the following evolution of the lattice.

The DECP mechanism was adopted over any other mechanism, such as impulsive stimulated Raman scattering (ISRS), because in the first, the coherent phonons are excited after absorbing a significant amount of energy from the exciting source frequency, while in the latter, no absorption is required because the excitation source has energy less than the bandgap of the medium [32]. Additionally, the coherent phonon amplitude $Q(t)$ of displacive nature has $\cos(\omega_0 t)$ dependence while in ISRS it has $\sin(\omega_0 t)$ dependence, where ω_0 is the frequency of the excited optical phonons with symmetry A_g [30].

Bi has three active normal modes of vibrations, $(3N-M)$, where $N = 2$ is the number of atoms/unit cell and $M = 3$ is the number of acoustic modes). One of these modes has A_{1g} symmetry (totally symmetric breathing mode) and the other two have E_g symmetry (doubly degenerate), Fig. 4.6. All of these modes (A_{1g} and E_g) are Raman active with amplitude ratio 4:1 [30].

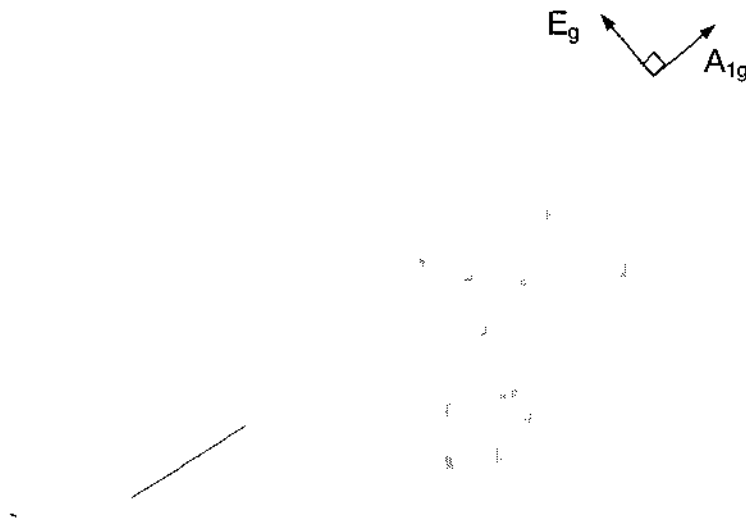


Fig. 4.6. Bi lattice structure showing the optical phonons vibrational direction with symmetry A_{1g} and E_g . Reproduced from Ref. [34].

Therefore, in DECP theory, the photoexcited lattice with ultrashort laser pulses increases the density of excited carriers in the conduction band through the interband

transition, and/or raises the electron gas temperature through photon absorption. The impact of these effects is to displace the equilibrium atomic positions due to the change in the atomic bond strength, which eventually launches large amplitude coherent phonons of symmetry A_{1g} of displacive origin [27,31]. Consequently, the frequency of these phonons is now less than that before the excitations due to the softening of the bond strength. 10 ps later, these phonons restore its original frequency [33].

In summary, excitation and de-excitation processes occur over a very short periods of time, picoseconds and sub picoseconds, and to monitor the dynamics of excited states as a function of time we need a proper setup with temporal resolution similar or better than the time scale of these processes. That's why pump-probe setup based on ultrashort laser pulses is now used extensively to monitor these dynamics.

4.4. References of Chapter 4

- [1] Ph. Hofmann, "The surfaces of bismuth: Structural and electronic properties," *Prog. Surf. Sci.* 81, 191-245 (2006).
- [2] Y.- N. Sheu, "Ultrafast dynamics of photoexcited bismuth films," Ph.D. thesis, The University of Michigan (2010).
- [3] S. Golin "Band structure of bismuth: Pseudopotential approach," *Phys. Rev.* 166, 643-651 (1968).
- [4] C. S. Søndergaard "An investigation of surface electronic structure and electron-phonon interaction by photoemission spectroscopy," Ph.D. thesis, Institute for Storage Ring Facilities - University of Aarhus, Denmark (2001).
- [5] D. R. Lovett "Semimetals and narrow-bandgap semiconductors," Pion Limited, London, (1977).
- [6] Y. Liu and A. Roland, "Electronic Structure of the semimetals Bi and Sb," *Phys. Rev. B* 52, 1566-1577 (1995).
- [7] X. Gonze, J.-P. Michenaud, and J.-P. Vigneron, "First-principles study of As, Sb, and Bi electronic properties," *Phys. Rev. B* 41, 11827-11836 (1990).
- [8] A. B. Shick, J. B. Ketterson, D. L. Novikov, and A. J. Freeman, "Electronic structure, phase stability, and semimetal-semiconductor transitions in Bi," *Phys. Rev. B* 60, 15484-15487 (1999).
- [9] G. Dresselhaus, M. S. Dresselhaus, Z. Zhang, and X. Sun, in *International Conference on Thermoelectrics, Nagoya, Japan, IEEE, Piscataway, NJ*, p. 43 (1988).
- [10] J. F. van der Veen, B. Pluis and A. W. D. van der Gon, "In chemistry and physics of solid surfaces VII," *Springer-Verlag*, 455-490 (1988).

- [11] V. N. Lutskii. Features of optical absorption of metallic films in region where metal turns into a dielectric. *Sov. Phys. JETP Lett.* 2, 245-248 (1965).
- [12] V. B. Sandomírskii “Quantum size effect in a semimetal film,” *Sov. Phys. JETP* 25, 101-106 (1967).
- [13] M. R. Black, “The optical properties of bismuth nanowires,” Ph.D. thesis, Department of Electrical Engineering and Computer Science, Massachusetts Institute of Technology, P. 39 (2003).
- [14] S. B. Cronin, Yu-Ming Lin, O. Rabin, M. R. Black, G. Dresselhaus and M. S. Dresselhaus, “Thermoelectric transport properties of individual bismuth nanowires,” In *Thermoelectric Materials 2001 - Research and Applications: MRS Symposium Proceedings*, edited by G. S. Nolas, D. C. Johnson, and D. G. Mandus, Materials Research Society Press, Boston, MA, December 2001.
- [15] Al. L. Efros, and A. L. Efros “Pioneering effort I,” *Sov. Phys. Semicond.* 16, 772-775 (1982).
- [16] Y. F. Ogrin, V. N. Lutskii, and M. I. Elinson “Observation of quantum size effects in thin bismuth films,” *JETP Letters*, 3, 71-73 (1966).
- [17] S. K. Sundaram, E. Mazur, “Inducing and probing non-thermal transitions in semiconductors using femtosecond laser pulses,” *Nat. Mater.* 1, 217-223 (2002).
- [18] J. P. Callan, “In ultrafast dynamics and phase changes in solids excited by femtosecond laser pulses,” Ph. D. Thesis, Harvard Univ., Cambridge, 59-104 (2000).
- [19] C. Thomsen, H. T. Grahn, H. J. Maris, and J. Tauc “Surface generation and detection of phonons by picosecond light pulses,” *Phys. Rev. B* 34, 4129-4138, (1986).

- [20] E. N. Glezer, Y. Siegel, L. Huang, and E. Mazur, "The behavior of χ^2 during laser induced phase transitions in GaAs," *Phys. Rev. B.* 51, 9589-9596 (1995).
- [21] J. Solis, C. N. Afonso, J. F. Trull, and M. C. Morilla, "Fast crystallizing GeSb alloys for optical data storage," *J. Appl. Phys.* 75, 7788-7794 (1994).
- [22] S. I. Anisimov, B. L. Kapeliovich, and T. L. Perelman, "Electron emission from metal surfaces exposed to ultrashort laser pulses," *Soviet Physics - JETP* 39, 375-377 (1974).
- [23] J. G. Fujimoto, J. M. Liu, E. P. Ippen, and N. Bloembergen, "Femtosecond laser interaction with metallic tungsten and nonequilibrium electron and lattice temperatures," *Phys. Rev. Lett.* 53, 1837-1840 (1984).
- [24] J. M. Chwalek, C. Uher, J. F. Whitaker, G. A. Mourou, J. Agostinelli and M. Lelental, "Femtosecond optical absorption studies of nonequilibrium electronic processes in high T_c superconductors" *App. Phys. Lett.* 57, 1696-1698 (1990).
- [25] W. Kutt, W. Albrecht and H. Kurz, "Generation of coherent phonons in condensed media" *IEEE J. Quant. Electron.* 28, 2434-2444 (1992).
- [26] G. C. Cho, W. Kutt, and H. Kurz, "Subpicosecond time-resolved coherent-phonon oscillations in GaAs," *Phys. Rev. Lett.* 65, 764-766 (1990).
- [27] T. K. Cheng, J. Vidal, H. J. Zeiger, E. P. Ippen, G. Dresselhaus and M. S. Dresselhaus, "Mechanism for displacive excitation of coherent phonons in Sb, Bi, Te, and Ti_2O_3 ," *Appl. Phys. Lett.* 59, 1923-1925 (1991).
- [28] R. Scholtz, T. Pfeifer and H. Kurtz, "Density-matrix theory of coherent phonon oscillations in germanium," *Phys. Rev. B.* 47, 16229-16236 (1993).

- [29] T. K. Cheng, S. D. Brorson, A. S. Kazeroonian, J. S. Moodera, G. Dresselhaus, M. S. Dresselhaus, and E. P. Ippen “Impulsive excitation of coherent phonons observed in reflection in bismuth and antimony,” *Appl. Phys. Lett.* 57, 1004-1006 (1990).
- [30] T. K. Cheng “The excitation and dynamics of coherent lattice vibrations in semimetals and narrow-gap semiconductors,” Ph.D. Dissertation, Dept. of Electrical and Computer Engineering, Massachusetts Institute of Technology, 44-77 (1994).
- [31] H. J. Zeiger, J. Vidal, T. K. Cheng, E. P. Ippen, G. Dresselhaus and M. S. Dresselhaus, “Theory for displacive excitation of coherent phonon,” *Phys. Rev. B.* 45, 768-778 (1992).
- [32] R. Merlin, “Generating coherent THz phonons with light pulses,” *Solid State Comm.* 102, 207-220 (1997).
- [33] M. Hase, M. Kitajima, S. Nakashima, and K. Mizoguchi, “Dynamics of coherent anharmonic phonons in bismuth using high density photoexcitation,” *Phys. Rev. Lett.* 88, 067401(1-4) (2002).
- [34] T. Dumitrică, “Bismuth under intense laser pulses: A Fano-like interference description,” *J. Phys.: Condens. Matter* 19, 181003(1-2) (2007).

CHAPTER 5

OBSERVATION OF LATTICE CONTRACTION WITH HEATING OF BISMUTH NANOCCLUSERS NEAR ITS MELTING POINT

5.1. Introduction

Melting and solidification are amongst the most dramatic phase change exhibited by a condensed matter. Although these phenomena are common processes that everyone may encounter on a daily basis, sometimes it is difficult to answer a very simple question regarding such phase transitions, such as *how does a condensed matter turn into liquid or solid?*

The answer to this question stimulated, for decades, many scientific groups who became involved theoretically and experimentally [1-11] and put forward their utmost efforts to answer this question in order to clarify the pathways of the melting and solidification processes. In this chapter we review and summarize, to our best, some of these efforts as well as general information on the melting of solids under various conditions.

5.2. Melting, Is It Abrupt or Continuous?

Melting of a solid matter usually occurs when it is heated to a specific temperature, T_m . Although melting of a certain substance will occur at a specific temperature, T_m , other substances may retain their solid phase integrity at temperatures higher than T_m (superheating).

To answer the question, *how does a solid melt?*, different points were considered. The first one dealt with melting from a very simple point of view. It was mentioned that solid-liquid phase transition is first order in nature, a discontinuous phase transformation.

Accordingly, there is no intermediate state involved and hence it is impossible to extract any detailed information on the progress of a melting transition. Another point of view dealt with melting as a continuous or nearly continuous phase transition.

The most recent studies adopted the continuous melting point of view and it is believed that it is a characteristic of bulk materials and affected by the material boundaries. Classical thermodynamics has helped in understanding the process of melting by relating the Gibbs free energy of the solid (G_s) to that of the liquid (G_l). Therefore, the melting temperature, T_m , can be regarded as the temperature at which the solid and the melt are in thermodynamic equilibrium while keeping the pressure constant. In this case, the Gibbs free energies are equal, i.e. $G_s(P,T) = G_l(P,T)$, Fig. 5.1. Although Gibbs free energy is continuous during the melting process, the entropy, internal energy, volume, and heat capacity are discontinuous.

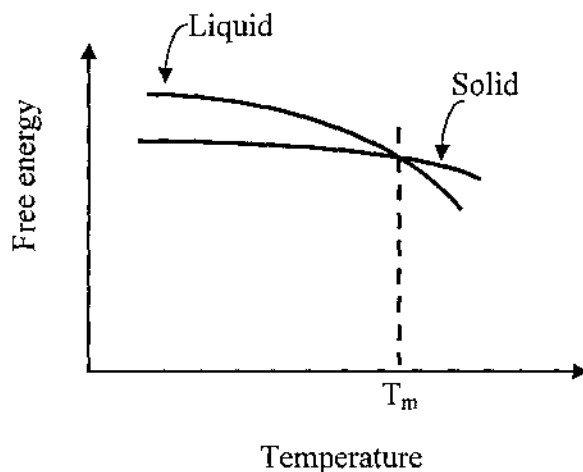


Fig. 5.1. Temperature dependence of Gibbs free energy of a simple substance near its melting point. Reproduced from Ref. [12].

The contribution of thermodynamics to the understanding of melting is undeniable, but the melting process cannot be completely visualized without considering the size of the

sample under consideration. This is due to the direct impact of the cluster size on the melting point, as mentioned in chapter 1 of this dissertation. In general it was found that the melting point is inversely proportional to the cluster size [13-17]. This behavior was confirmed experimentally in many elements, including gold [18,19], lead [20], and bismuth [21-25].

The elastic properties of nanoclusters also show dependence on the cluster size. The magnitude of the thermal expansion coefficient was found to have inverse relation with the cluster size for some elements, e.g., copper [26] and selenium [27], and remains constant for some other elements, e.g., palladium [27]. Another study showed that palladium nanoclusters have the same behavior as copper and selenium nanoclusters [28]. Other factors that affect the physical properties of the nanoclusters are their morphology and history of heat treatment [27,29].

In this chapter, I studied the effect of reduced dimensionality on the physical properties (melting temperature and elastic properties) of Bi nanoclusters. A transmission high-energy electron diffraction (THEED) was used to study the thermal expansion of annealed Bi nanoclusters from room temperature up to $\sim 525 \pm 6$ K. This was accomplished by monitoring the diffraction pattern of thermally evaporated Bi nanoclusters as a function of temperature after annealing the grown samples by femtosecond laser pulses at different temperatures.

The temperature-dependent Bragg peak intensity, ring position, as well as the diffraction full width at half-maximum (FWHM) were monitored for (012) and (110) Bragg peaks. High resolution TEM was also used to characterize the as-evaporated and the annealed Bi nanoclusters.

Details of the experimental setup and data analysis are described in chapter 3 and appendices C - H.

5.3. Experiment

Bi noncontinuous film of average thickness 5 nm was grown by thermal evaporation on TEM grids coated with < 10 nm thick carbon layer. Bi chunks (99.999% pure) were loaded into a tungsten boat. The base pressure of the evaporation chamber was in the low 10^{-6} Torr range. The evaporation rate was controlled by varying the current through that boat. A quartz crystal thickness monitor was used to measure the deposition rate and thickness. Evaporation was done at room temperature at a rate of $\sim 0.5 \text{ \AA s}^{-1}$.

A transmission electron diffraction system built in our lab was used to study the melting of the Bi nanoclusters in the temperature range $300 \pm 6\text{K} - 525 \pm 6 \text{ K}$. The THEED system is operated in an ultrahigh vacuum chamber (low 10^{-9} Torr). The 35-keV photoactivated electron gun, used in electron diffraction, is capable of generating a well-collimated electron beam with beam diameter $745 \pm 54 \text{ }\mu\text{m}$, measured at the sample location. A microchannel plate (MCP) followed by a phosphorous screen is used for diffraction pattern detection, and a computer-controlled, charge-coupled device camera is used to capture the diffraction pattern for analysis. The electron beam was steered towards the sample by a set of electromagnets located outside the UHV chamber. Laser pulses from a 120-femtosecond Ti:sapphire laser operated at a wavelength of 800 nm, and a frequency of 1 kHz was used for nanocluster annealing.

The samples were mounted on a lab-made heating stage designed to operate in the transmission diffraction system. For temperature measurements, we used a K-type

thermocouple that was mounted inside the heater, about 1 - 2 mm away from the sample. The thermocouple was put through a calibration procedure to accurately measure the sample temperature. This was done by measuring the boiling point and the freezing point of distilled water and the melting point of a small Bi chunk. The temperature measurement accuracy is within ± 1 K.

The as-deposited Bi sample was heated from room temperature up to 450 K slowly, ~ 3 K/min, while exposing the sample to femtosecond laser pulses with a fluence of ~ 0.8 mJ/cm². At 450 K the sample was further heated by the laser pulses for about 20 s with the laser operating at 1 kHz. This resulted in the melting of the as-deposited Bi non-continuous film and its quenching to form Bi nanoclusters.

5.4. Results and Discussion

5.4.1. Morphology and diffraction pattern indexing of the grown bismuth nanoclusters

The fabricated Bi nanoclusters were studied by THEED and high-resolution TEM. Figure 5.2 shows the diffraction pattern and the TEM images of the as-deposited Bi 5 nm film (a), after thermal annealing up to 525 K (b), after annealing with femtosecond laser pulses at a fluence of $\sim 0.8 \pm 5\%$ mJ/cm² with 1 kHz repetition rate (c), and thermally annealed at 450 K while simultaneously exposing to the laser pulses (d). The stability of the system, which is determined mainly by the laser output power, was checked from time to time during collecting the data and in general was found to be $\sim 2\%$ but never exceeded 5%. The diffraction patterns were taken at room temperature. Neither laser annealing nor thermal annealing alone changed the morphology of the two-dimensional islands into nanoclusters. But simultaneous thermal annealing of the grown

Bi, while exposing it to femtosecond laser pulses, resulted in nanocluster formation due to melting and subsequent quenching of the melt. Figure 5.3 shows the length distribution of the major axis and the minor axis of the nanoclusters shown in Fig. 5.2.(d). The height analysis of the as-deposited and the annealed samples surface could not be checked due to the limited resolution of the atomic force microscopy system.

For the as-deposited sample, the Bragg peak (110) is much more intense than the other observed peaks, which reflects a preferred growth orientation. Upon tilting the sample a few degrees off the normal incidence of the electron beam with respect to the sample surface, an arc-like diffraction pattern is detected, which indicates the fiber texture of the as-evaporated Bi film. With annealing, there is no observed new Bragg peaks in the diffraction patterns, shown in Figure 5.2.(b) - (d). However, the intensity of the Bragg peaks changed. This indicates that annealing did not change the structure of the grown sample, but caused reorientation. The Bragg diffraction rings were identified, as shown in Fig. 5.4, and they all belong to the hexagonal Bi structure that precludes the presence of oxide. Figure 5.4.(b) shows the intensity of the diffraction rings as a function of the momentum transfer $S = 2\pi/d$ (\AA^{-1}) obtained after radial averaging of the intensity in Fig. 5.4.(a). Comparison of the diffraction intensity before and after annealing confirms crystal reorientation with annealing.

An aluminum thin film was used for calibration of the diffraction camera length and identification of the Bragg diffraction peaks. The simple hexagonal structure with lattice parameters $|a| = |b| = 4.54 \text{ \AA}$ and $|c| = 11.80 \text{ \AA}$ was used to identify the ring pattern of the samples.

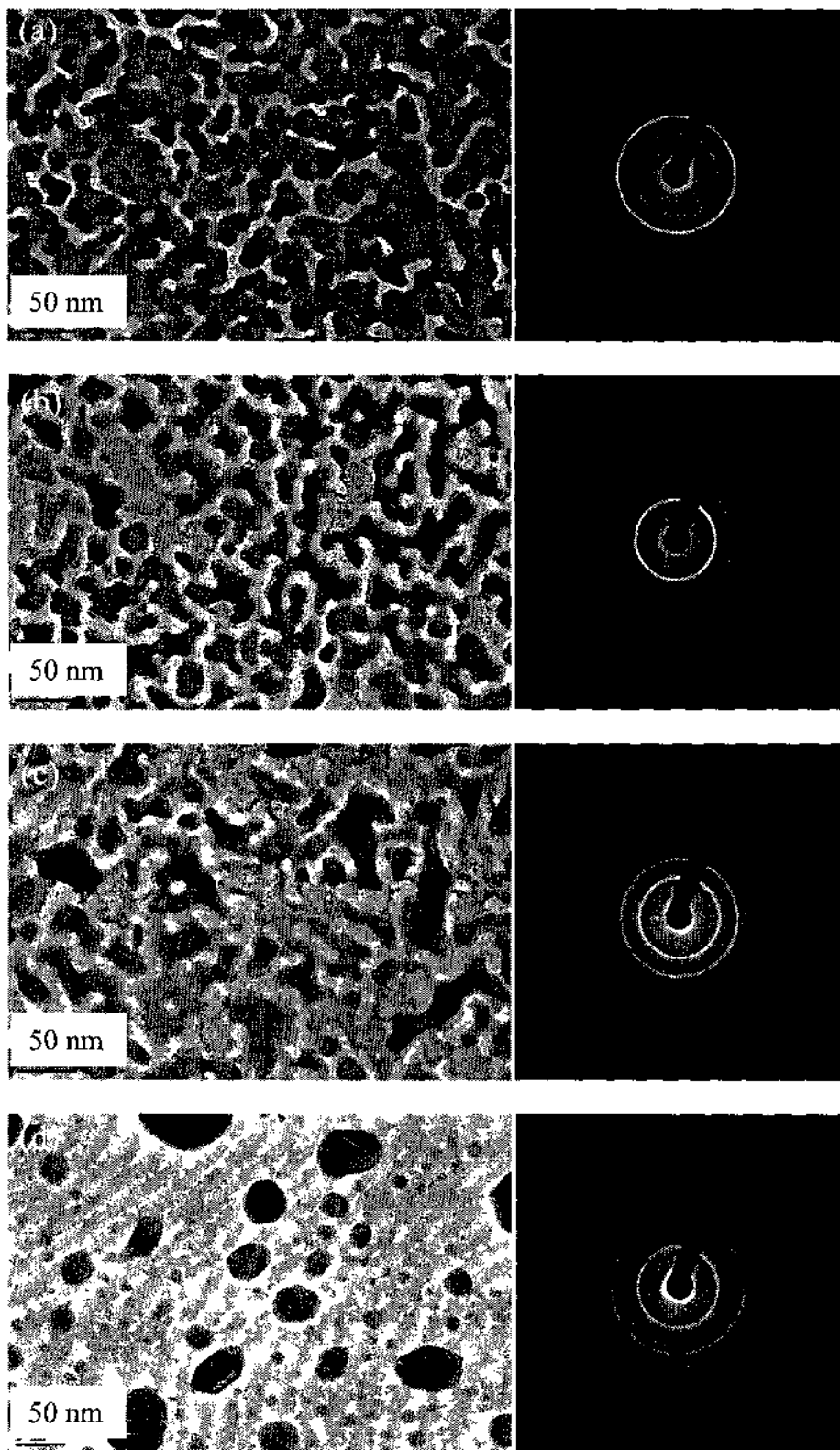


Fig. 5.2. HRTEM images and the corresponding diffraction pattern of (a) as-deposited Bi 5 nm film, (b) after thermal annealing up to 525 K, (c) after annealing with femtosecond laser pulses at a fluence of $\sim 0.8 \text{ mJ/cm}^2$ with 1 kHz repetition rate, and (d) thermally annealed at 450 K while simultaneously exposing to the laser pulses.

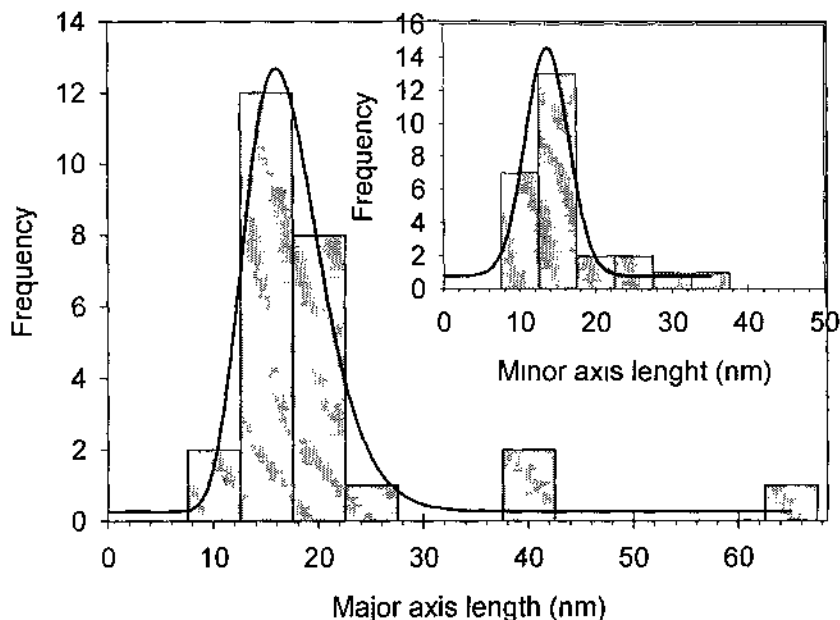


Fig. 5.3. The length distribution of the major axis and the minor axis of the nanoclusters shown in Fig. 5.2.(d).

High-resolution transmission electron microscopy images of as-deposited and annealed samples are shown in Fig. 5.5.(a) and 5.5.(b). The as-deposited samples show flat islands, while those annealed thermally and simultaneously with the laser show nanoclusters. We will refer to these samples as nanoclusters. Multi-grains are observed in some of these nanoclusters, as shown in the high-resolution TEM images in Fig. 5.5.(b). The Bi lattice parameters a and c and the unit cell volume V were calculated from Eqs. 5.1 - 5.3. The values obtained are $a = 4.6 \pm 0.1 \text{ \AA}$, $c = 11.6 \pm 0.1 \text{ \AA}$ and $V = 210.7 \pm 11.2 \text{ \AA}^3$, in agreement with the parameters reported elsewhere [30]. The calculated value of the lattice constant c is less than the reported value for bulk Bi, which can be attributed to the stress imposed on the crystal lattice by the surface tension of the surface atoms in the nanoclusters.

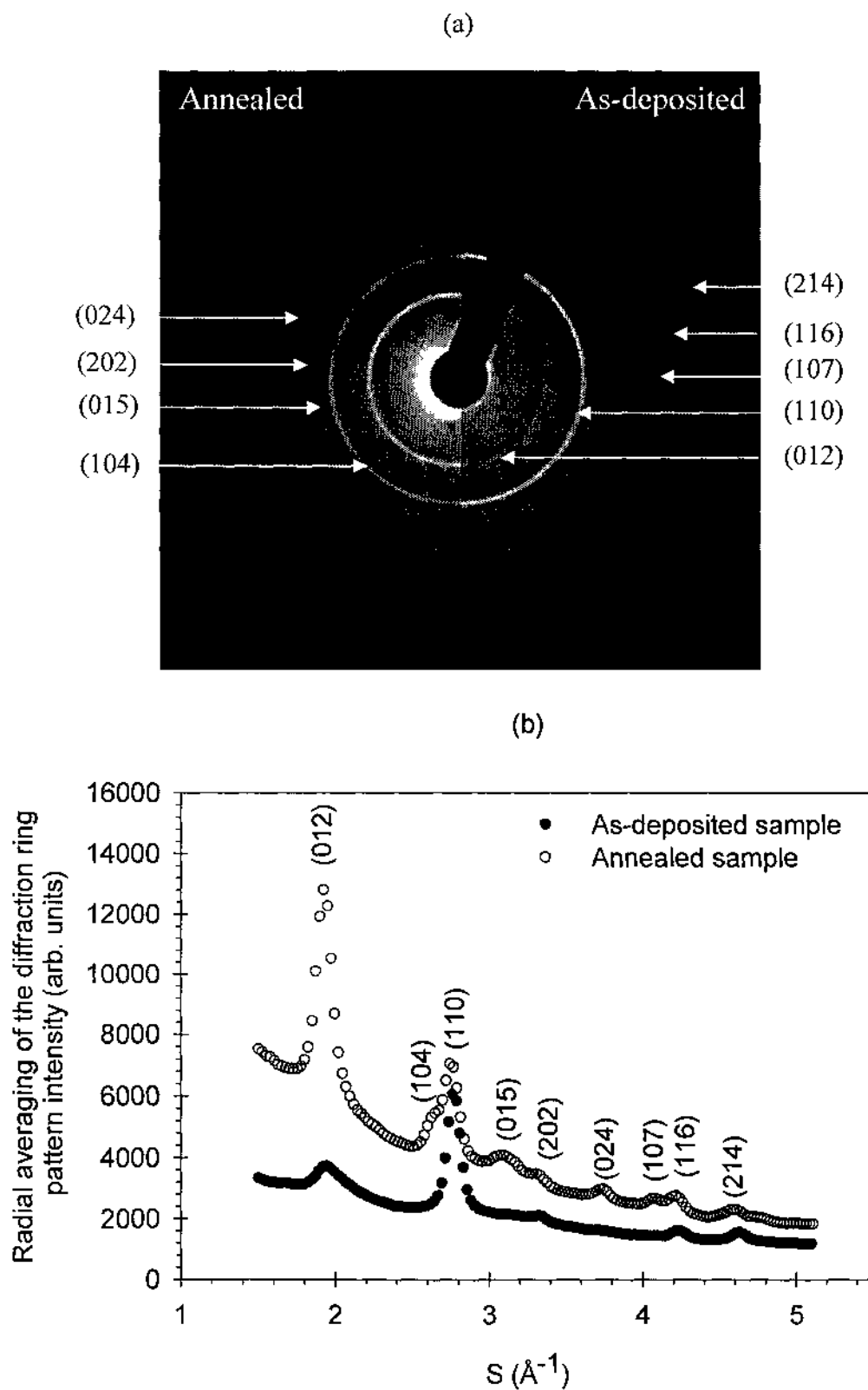


Fig. 5.4. (a) Diffraction pattern of as-deposited Bi and annealed sample and (b) the corresponding radial average as a function of momentum transfer $S = 2\pi/d$.

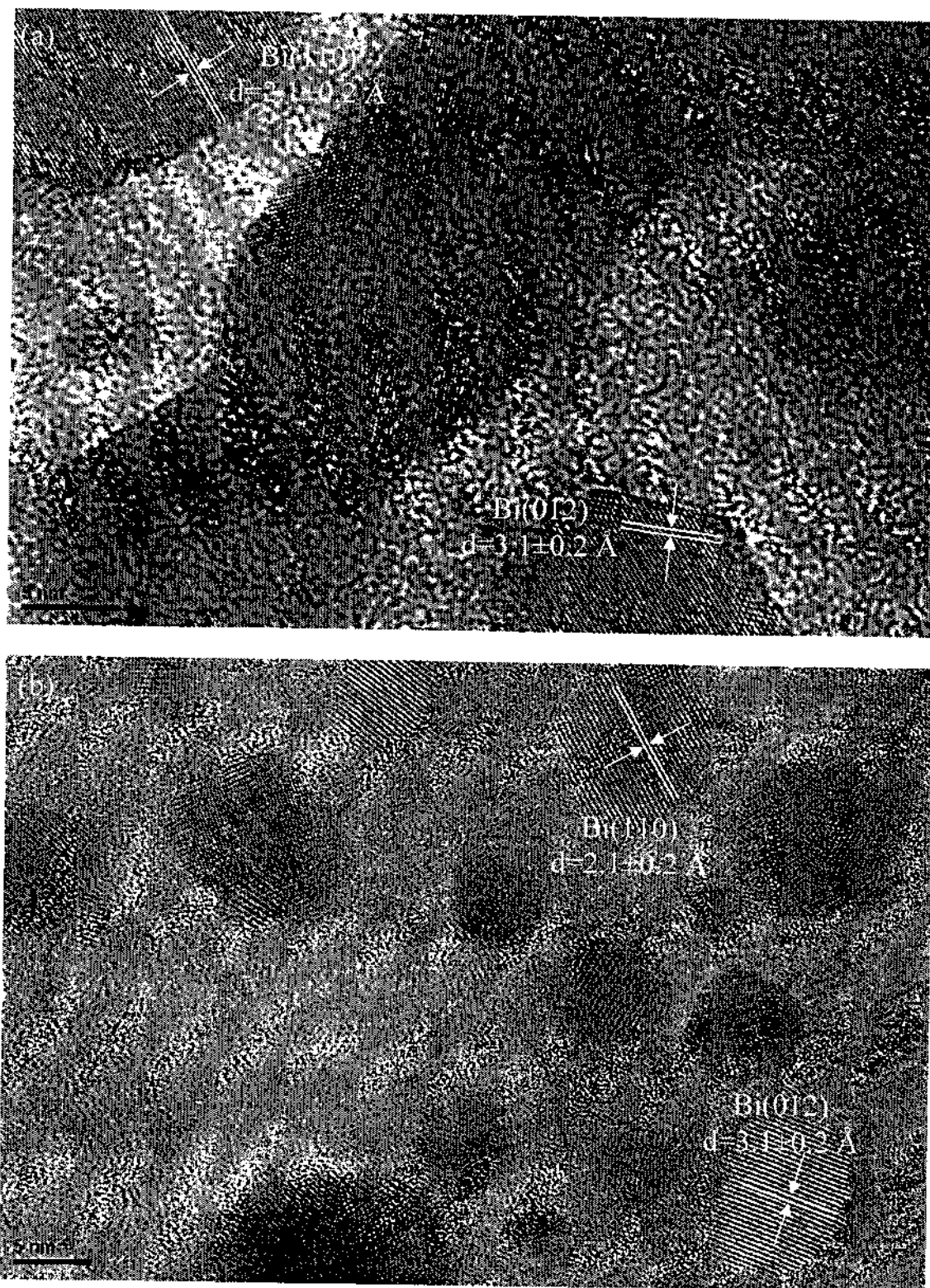


Fig. 5.5. HRTEM images of (a) as-deposited and (b) annealed samples. The as-deposited samples show flat islands, while those annealed thermally and simultaneously with the laser show nanoclusters.

$$a = 2d_1 \times d_2 \sqrt{\frac{l_1^2 \times (h_2^2 + h_2 \times k_2 + k_2^2) - l_2^2 \times (h_1^2 + h_1 \times k_1 + k_1^2)}{3 \times (d_1^2 \times l_1^2 - d_2^2 \times l_2^2)}} \quad 5.1$$

$$c = d_1 \times d_2 \sqrt{\frac{l_1^2 \times (h_2^2 + h_2 \times k_2 + k_2^2) - l_2^2 \times (h_1^2 + h_1 \times k_1 + k_1^2)}{d_2^2 \times (h_2^2 + h_2 \times k_2 + k_2^2) - d_1^2 \times (h_1^2 + h_1 \times k_1 + k_1^2)}} \quad 5.2$$

$$V = a^2 \times c \times \sin \gamma, \gamma = 120^\circ \quad 5.3$$

where, d_1 and d_2 are the interplanar spacing and (h_1, k_1, l_1) and (h_2, k_2, l_2) are Miller indices [31].

The total energy E deposited into the sample and Bi parameters are used to estimate the sample temperature rise ΔT solely due to femtosecond laser pulses with the help of equation 5.4. This results in $\Delta T \sim 93.4 \pm 9.3$ K, where m is the sample mass, and $C_p = 122 \text{ J.kg}^{-1}.\text{K}^{-1}$ is the specific heat capacity of the bulk Bi at constant pressure.

$$\Delta T = \frac{E}{m \times C_p} \quad 5.4$$

5.4.2. Debye-Waller factor

The root mean square displacement of the atoms in nanoclusters is directly related to the intensity of the Bragg peak through the Debye-Waller factor:

$$I(G, T) = I_o(G, T) \times \exp(-2 \times M_G) \quad 5.5$$

where $G = \hbar(k_f - k_i)$ is the momentum transfer vector of the scattered electrons,[32] and the exponential term is the Debye-Waller factor, where

$$2M_G = \langle u_G^2 \rangle \times \frac{16 \times \pi^2 \times \sin^2 \theta}{\lambda^2} \quad 5.6$$

λ is the electron wavelength, θ is the scattering angle, $I_o(G, T)$ is the scattered intensity of a rigid lattice, and $\langle u_G^2 \rangle$ is the *rms* vibrational amplitude in the direction of the scattering

vector G . The *rms* vibrational amplitude can be calculated using the harmonic oscillator model in the high-temperature limit, [33,34]

$$\langle u_G^2 \rangle = \left(\frac{3 \times N \times \hbar^2}{M \times k_B} \right) \left[\frac{T}{\Theta_D^2} \right] \quad 5.7$$

where Θ_D is the Debye temperature, M is the atomic weight of the sample, T is temperature, N is Avogadro's number, k_B is Boltzmann's constant, and \hbar is Planck's constant divided by 2π . Therefore, from the diffraction intensity dependence on the temperature, we can estimate Θ_D of Bi nanoclusters shown in Fig. 5.2.(d).

Figure 5.6 shows the Bragg peak intensity at temperature T normalized to that at $T = 323$ K. To estimate the error in intensity measurement, we measured the intensity of the diffraction ring pattern at room temperature for over ~ 60 minutes. We found that the intensity fluctuation did not exceed 5%. Results also showed that the recrystallized Bi nanoclusters were not affected by successive heating and cooling cycles and the diffraction peak intensity of recrystallized clusters decays with temperature according to the Debye-Waller factor up to $T = 464 \pm 6$ K, as shown in Fig. 5.6. The temperature-dependent natural log of the normalized Bragg peak intensity up to $T = 464$ K was used to calculate Debye temperature of the Bi nanoclusters and found to be $\Theta_D = 53 \pm 6$ K. This value is consistent with the reported Debye temperature of Bi thin film, $\Theta_D = 42.0 \pm 9$ K, [35] and 47 ± 5 K, [36] which is less than that for the bulk $\Theta_{D,B} = 120$ K. Since the atoms in reduced dimensionality have a smaller coordination number of surface atoms and, consequently, have thermal vibrational amplitudes greater than that of the bulk, it is expected that $\Theta_{D(\text{nanoclusters})} < \Theta_{D,B}$. The Debye temperature was also calculated using the (110) diffraction order and was found to be $= 86 \pm 9$ K. The direction-dependent Debye

temperature reflects the anisotropic nature of Bi. The reduced Debye temperature calculated from the (012) diffraction order compared to that from the (110) is indicative of the weaker atomic bonding in the $\langle 012 \rangle$ direction.

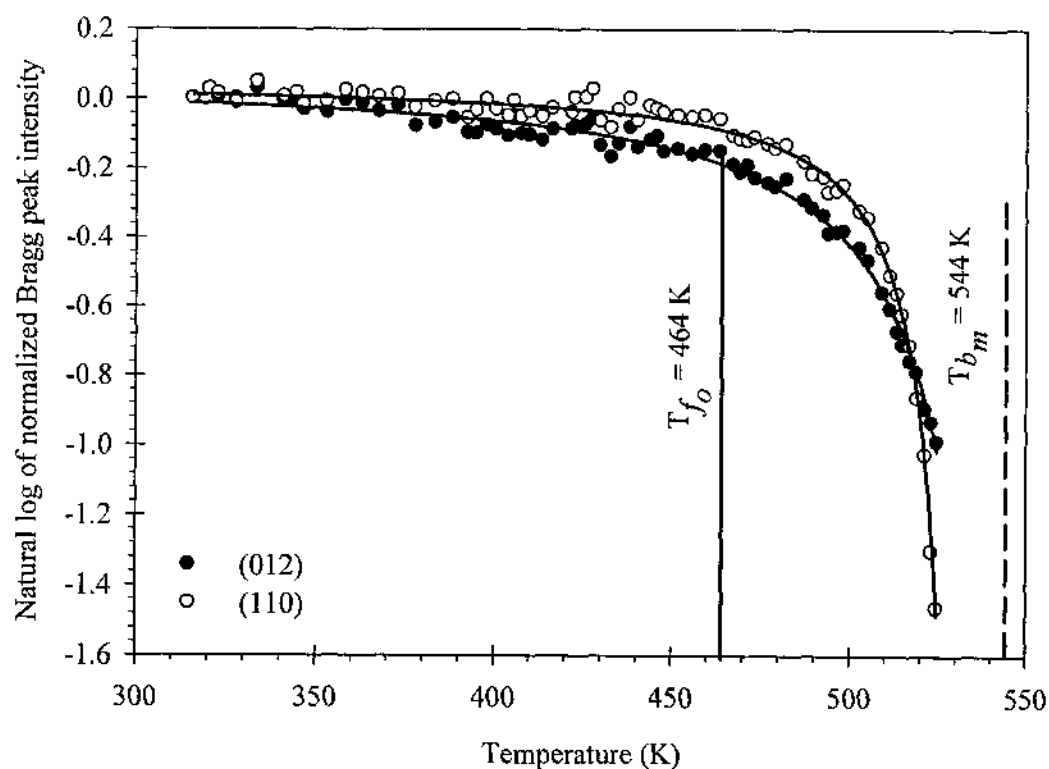
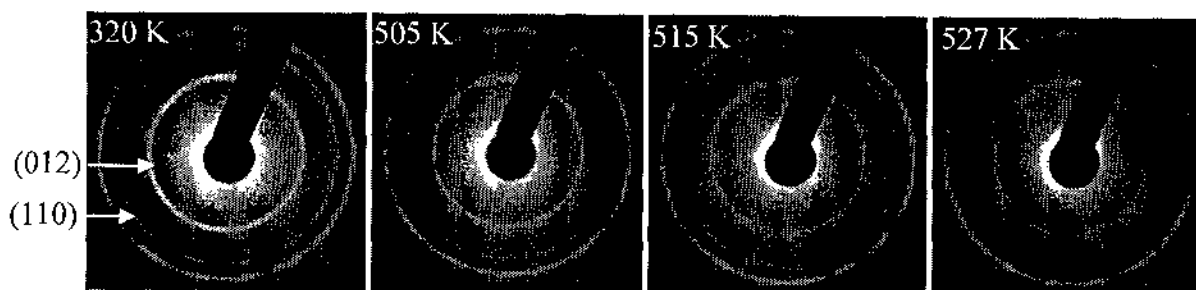


Fig. 5.6. Temperature dependence of the natural log of intensity at temperature T normalized to that at temperature = 323 K, (I_T/I_o) , of the (012) and (110) Bragg peaks of Bi nanoclusters is shown in Fig. 5.2.(d). The inset shows the diffraction pattern at different temperatures.

5.4.3. Bragg peak position

The Bragg peak position r is related to the interplanar spacing d for the set of planes producing the Bragg peak. Therefore, the relative change of the Bragg peak position ($\Delta r/r$) measured in the diffraction pattern equals the relative change of lattice plane spacing ($\Delta d/d$) according to Bragg's Law.

The temperature dependence of ($\Delta d/d$) for Bi (012) and (110) planes is shown in Fig. 5.7. The data presented in Fig. 5.7 show a crossover in lattice spacing of Bi (012) planes over the temperature range $T \sim 499 - 511$ K. At $T \sim 499$ K, the thermal expansion coefficient α in the $\langle 012 \rangle$ direction changes from $+14.4 \pm 2.9 \times 10^{-6} \text{ K}^{-1}$ to $-0.8 \pm 0.3 \times 10^{-3} \text{ K}^{-1}$, showing lattice contraction rather than expansion near melting. On the other hand, the Bi (110) planes did not show any abnormal behavior up to 525 ± 6 K with thermal expansion coefficient of $13.7 \pm 2.5 \times 10^{-6} \text{ K}^{-1}$.

Although the data presented in Figs. 5.6 - 5.8 are for one scan, all different physical parameters mentioned here were the result of the average of six different scans. The error in each calculated value is the standard deviation calculated from those scans.

The thermal expansion coefficient of nanocrystals is known to depend on their size and is larger with the reduction of size [37]. Moreover, experimental and theoretical studies showed that the lattice expansion is induced by the excess volume at grain boundaries due to relatively disordered atomic arrangements [38]. The nanoclusters studied here have a size distribution as shown in Fig. 5.3. Also, some nanoclusters have multigrains. The measured change in the lattice thermal expansion coefficient is that of the distribution of the nanoclusters since diffraction experiments cannot distinguish between the different compositions of the nanocluster distribution.

Many factors may compete and result in such an anomaly observed in the Bi $\langle 012 \rangle$ direction. Some of these factors are surface stress, surface phonons, defects, as well as finite size modification of the lattice potential [39,40]. Also, structural phase transitions can lead to similar behavior, but it was excluded in our case, since the lattice preserves its structure and no extra diffraction rings were observed up to the complete melting of the nanoclusters [39,40]. The negative expansion coefficient, as observed in Fig. 5.7, was previously explained in terms of the effect of electronic excitation on the equilibrium lattice spacing [39,40].

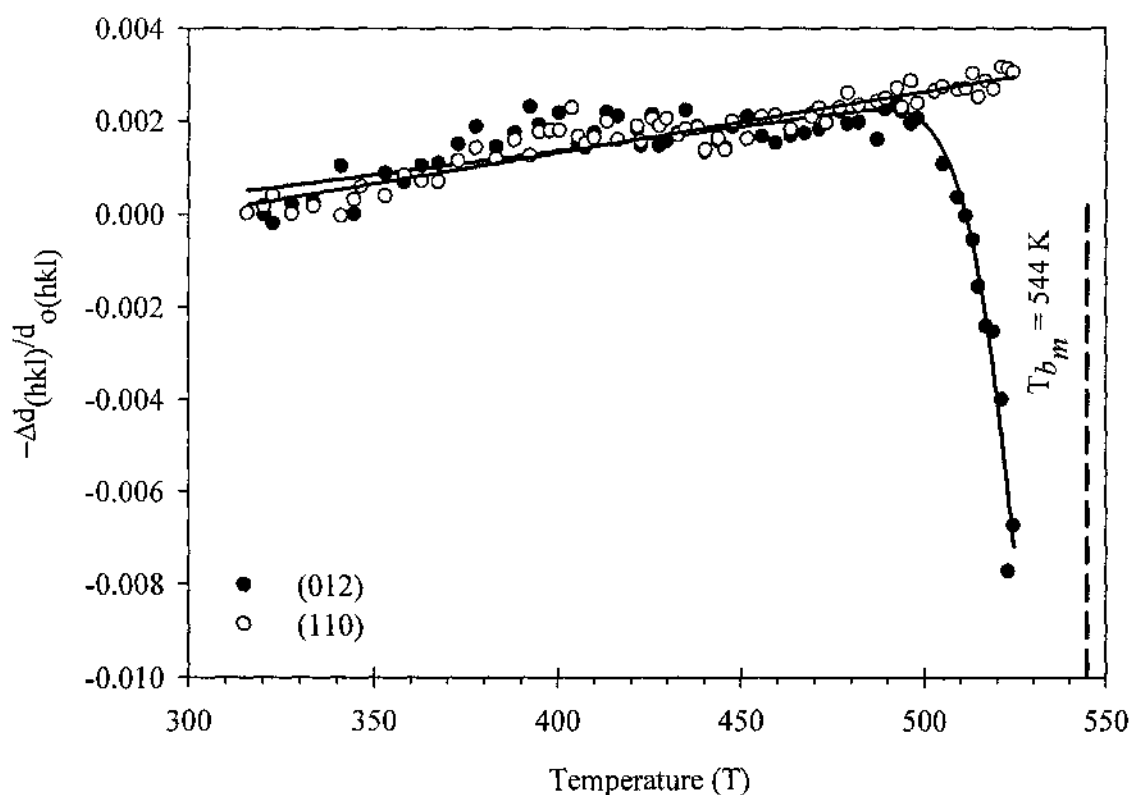


Fig. 5.7. Temperature-dependent strain of the Bi (012) and Bi (110) planes.

5.4.4. Full width at half maximum

The average full width at half maximum (FWHM) of the diffraction ring pattern of polycrystalline material is related to the crystallite size in a direction parallel to the sample surface, D , through the Debye-Scherrer formula [41].

$$D = \frac{0.9\lambda}{B \cos\theta} \quad 5.8$$

where λ is the electron wavelength, B is the FWHM expressed in radians, and θ is Bragg angle. At room temperature, an average crystallite size of 101 ± 10 Å was calculated from Eq. 5.8 and averaged over six different runs from the FWHM of (012) Bragg peak. Although the calculated value of D was done from (012) peak, in general it is considered, here as an average value, since the FWHM extracted from the fitting parameter gave an average value for FWHM and was best fit with (012) peak as well as most of the observed peaks. The details of the procedures followed to extract the intensity, ring radius and FWHM from the diffraction pattern are given in appendix H.

Figure 5.8 shows the temperature dependence of the percentage change in the molten layer thickness, calculated from the change in the diffraction ring FWHM at temperature T normalized to that at $T = 323$ K, $\Delta B/B_o$, for (012) and (110) Bragg peaks, where $B(T)$ is the FWHM at temperature T , B_o is the FWHM at 323 K, and $B = B(T) - B_o$. For temperatures up to ~ 500 K, there is no significant change in the FWHM with temperature for the (110) order; however, some changes in the (012) order appear at a lower temperature and are more significant than in the $\langle 110 \rangle$ direction. For $T > 500$ K, a significant crystallite size reduction is detected due to the formation of a thin layer of liquid Bi around the solid Bi nanocluster, which grows in size as the temperature increases until the nanocluster is fully transformed into the liquid phase [42,43]. There is

an observed anisotropy in the molten layer thickness with that observed in the $\langle 012 \rangle$ direction more than in the $\langle 110 \rangle$ direction. This result is consistent with the reduced Debye temperature in the $\langle 012 \rangle$ direction. A lower Debye temperature is generally associated with reduced melting point.

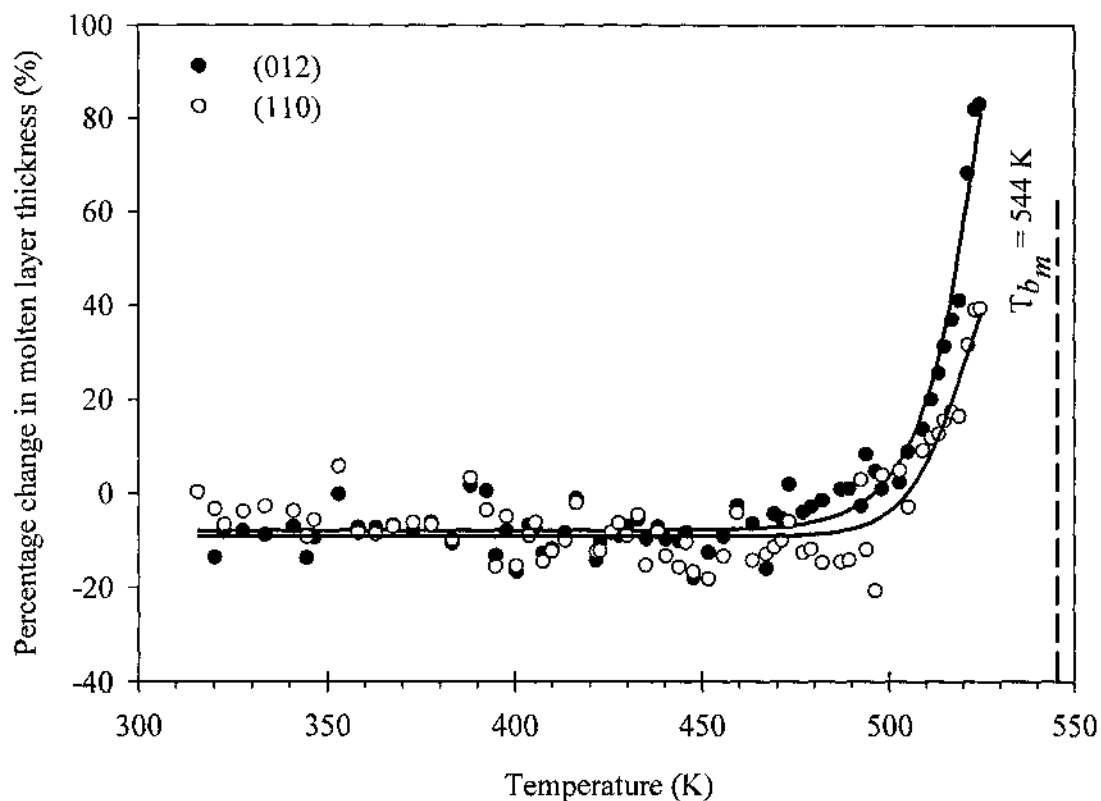


Fig. 5.8. Temperature dependence of the percentage change in the molten layer thickness, calculated from diffraction ring FWHM at temperature T normalized to that at temperature $T = 323 \text{ K}$.

5.5. Discussion

Crystal melting starts at the surface and depends on the crystal facet [44]. The high-density, close-packed surfaces are less energetically favored to be wetted by the melt, while the low-density packed ones can be wetted [44]. As the crystal temperature

approaches the melting point, a quasi-liquid layer forms on the less-packed surfaces and, with increasing temperature, melts the whole nanocluster. The quasi-liquid layer is a layer of disordered atoms which has stronger bonding than those in the melt. Such melting mechanism necessitates the presence of repulsive forces between the liquid-vapor and liquid-solid interfaces over some distance [44].

Thermal expansion upon heating occurs in most solid substances, whether they are elements or compounds. This phenomenon is generally due to a force that initiates the thermal expansion and is described by the Gruneisen parameter and the elastic reaction of the solid to this force [44,45]. This force is usually a thermal pressure induced by the strain produced in the lattice as a result of the increased lattice mean vibrational amplitude as the temperature increases.

However, some materials contract upon heating [39,40,46]. Two main contributions are considered when studying lattice contraction upon heating, namely, the vibrational and non-vibrational contribution to contraction [47]. For a crystal with anisotropic lattice parameter, contraction along one crystal direction could be accompanied with expansion along another direction [48,49]. This is due to the impact of the potential energy curve on the crystal direction. Along the direction of high compressibility in the lattice, normal modes of vibrations with high frequencies are excited at a certain temperature at the expense of those with low frequencies [47]. Therefore, along that direction, a lattice expansion is higher than that along the perpendicular direction. In this case, contraction in one direction is accompanied by an expansion in the perpendicular direction.

The data in Fig. 5.7 show that a transition from a positive thermal expansion to a

negative one for the Bi (012) planes starts at $T \sim 499 \pm 11$ K, with no structural phase transition observed. This anomaly was previously explained in terms of the effect of electronic excitation on the lattice interplaner spacing [39,40]. In Bi nanoclusters, the energy levels are few meV apart and, consequently, the potential of the electrons occupying the valence band becomes high enough to affect the lattice atomic positions. Therefore, raising the lattice temperature increases the energy level separation. This leads to a reduction in the number of excited electrons and increases the thermal energy of the already-excited electrons occupying the conduction band. These factors cause the lattice to contract, rather than expand, upon raising its temperature. This also may suggest the previous observation of semimetal-semiconductor transition in Bi nanoclusters at a critical thickness of 13 nm, [50-53] where the molten layer increases with temperature at the expense of the solid Bi.

5.6. Conclusions

Transmission electron diffraction was used to study the structural properties of bismuth nanoclusters from room temperature up to 525 ± 6 K. From the temperature-dependent diffraction intensity measurement, the Debye temperature of the annealed nanoclusters was found to be 53 ± 6 K along $\langle 012 \rangle$ direction and 86 ± 9 K along $\langle 110 \rangle$ direction. At $T = 464 \pm 6$ K, the diffraction intensity starts to deviate from the exponential Debye-Waller behavior, which indicates the increased lattice anharmonicity with temperature. In addition to the positive thermal expansion before melting, a lattice contraction starts at $\sim 499 \pm 11$ K, which can result from the disturbance in the potential of the electrons occupying the valence band that affects the lattice atomic positions. The onset of melting of the Bi nanoclusters, $T \sim 500 \pm 6$ K, was estimated from the

temperature-dependent diffraction width. The size of the nanoclusters was observed to be reduced with heating. This observation is interpreted to be due to the formation of a thin liquid shell around the nanoclusters.

5.7. References of Chapter 5

- [1] M. Born, "Thermodynamics of crystals and melting," *J. Chem. Phys.* 7, 591-603 (1939).
- [2] L. L. Boyer, "Theory of melting based on lattice instability," *Phase Trans.* 5, 1-47 (1985).
- [3] R. W. Cahn, "Melting from within," *Nature* 413, 582-583 (2001).
- [4] J. G. Dash, "History of the search for continuous melting," *Rev. of Mod. Phys.* 71, 1737-1743 (1999).
- [5] J.J. Gilvarry, "The Lindemann and Grüneisen laws," *Phys. Rev.* 102, 308-316 (1956a)
- [6] J. J. Gilvarry, "Grüneisen's law and the fusion curve at high pressures," *Phys. Rev.* 102, 317-325 (1956b).
- [7] J. J. Gilvarry, "Equation of the fusion curve," *Phys. Rev.* 102, 325-331 (1956c).
- [8] D. Kuhlmann-Wilsdorf, "Theory of melting," *Phys. Rev.* 140, 1599-1610 (1965).
- [9] M. Ross, "Generalized Lindemann melting law," *Phys. Rev.* 184, 233-242 (1969).
- [10] J.E. Lennard-Jones and A. F. Devonshire, "Critical and cooperative phenomena III: A theory of melting and the structure of liquids," *Proc. Roy. Soc. London A*169, 317-338 (1939a).
- [11] J. E. Lennard-Jones and A. F. Devonshire "Critical and cooperative phenomena IV: A theory of disorder in solids and liquids and the process of melting," *Proc. Roy. Soc. London A*170, 464-484 (1939b).
- [12] <http://phycomp.technion.ac.il/~phsorkin/thesis/node3.html>, last visited (7/20/08).

- [13] E. R. Youngdale, J.R. Meyer, C.A. Hoffman, F.J. Bartoli, D.L. Partin, C.M. Trush, and J.P. Heremans, "Nonlinear optical properties of molecular beam epitaxy grown $\text{Bi}_{1-x}\text{Sb}_x$," *Appl. Phys. Lett.* 57, 336-338 (1990).
- [14] C.A. Hoffmann, J.R. Meyer, F. Bartoli, A. Di Venere, X.J. Yi, C.L. Hou, H.C. Wang, J.B. Ketterson, and G.K. Wong, "Semimetal-to-semiconductor transition in bismuth thin films," *Phys. Rev. B* 48, 11431-11434 (1993).
- [15] L. Hicks, T. Harman and M. Dresselhaus, "Use of quantum-well superlattices to obtain a high figure of merit from nonconventional thermoelectric materials," *Appl. Phys. Lett.* 63, 3230-3232 (1993).
- [16] S. Cho, Y. Kim, A. Freeman, G. Wong, J. Ketterson, L. Olafsen, I. Vurgaftman, J. Meyer and C. Hoffman, "Large magnetoresistance in postannealed Bi thin films," *Appl. Phys. Lett.* 79, 3651-3654(2001).
- [17] M. H. Cohen, "Energy bands in the bismuth structure. I: A nonellipsoidal model for electrons in Bi," *Phys. Rev.* 121, 387-395 (1961).
- [18] T. Castro and R. Reifengerger, "Size-dependant melting temperature of individual nanometer-sized metallic clusters," *Phys. Rev. B* 42, 8548-8556 (1990).
- [19] Y. G. Chushak, and L. S. Bartell, "Melting and Freezing of Gold Nanoclusters," *J. Phys. Chem. B*, 105, 11605-11614 (2001).
- [20] K. F. Peters, J. B. Cohen, and Y. Chung, "Melting of Pb nanocrystals," *Phys. Rev. B* 57, 13430-13438 (1998).
- [21] E. A. Olson, M. Yu. Efremov, M. Zhang, Z. Zhang, and L. H. Allen, "Size-dependent melting of Bi nanoparticles," *J. Appl. Phys.* 97, 034304(1-9) (2005).

- [22] M. K. Zayed and H. E. Elsayed-Ali, "Melting and solidification study of as-deposited and recrystallized Bi thin films," *J. Appl. Phys.* 99, 123516(1-11) (2006).
- [23] M. K. Zayed and H. E. Elsayed-Ali, "Condensation on (002) graphite of liquid bismuth far below its bulk melting point," *Phys. Rev. B* 72, 205426 (1-9) (2005).
- [24] G. L. Allen, R. A. Bayless, W. W. Gile, and W. A. Jesser, "Small particle melting of pure metals," *Thin Solid Films* 144, 297-308 (1986).
- [25] S. J. Peppiatt, The melting of small particles. II. Bi, *Proc. R. Soc. Lond. A.* 345, 401-412 (1975).
- [26] L. H. Qian, S. C. Wang, Y. H. Zhao, and K. Lu, "Microstrain effect on thermal properties of nanocrystalline Cu," *Acta Mater.* 50, 3425-3434 (2002).
- [27] H. Zhang and B. Mitchell, "Thermal expansion behavior and microstructure in bulk nanocrystalline selenium by thermomechanical analysis," *Mater. Sci. Eng. A* 270, 237-243 (1999).
- [28] J.A. Eastman, M.R. Fitzsimmons, and L.J. Thompson, "The thermal properties of nanocrystalline Pd from 16 to 300 K," *Philos. Mag. B* 66, 667-696 (1992).
- [29] H. Gleiter, "Nanostructured materials: State of the art and perspectives," *Nanostruct. Mater.* 6, 3-14 (1995).
- [30] X. F. Yu, X. Liu, K. Zhang, and Z. Q. Hu, "The lattice contraction of nanometre-sized Sn and Bi particles produced by an electrohydrodynamic technique," *J. Phys.: Condens. Matter* 11, 937-944 (1999).
- [31] B. D. Cullity, *Elements of X-ray Diffraction*, 2nd ed. USA: Addison-Wesley, Reading, MA (1978).

- [32] D. A. Arms, R. S. Shah, and R. O. Simmons, "X-ray Debye-Waller factor measurements of solid ^3He and ^4He ," *Phys. Rev. B* 67, 094303(1-11) (2003).
- [33] R. M. Goodman, H. H. Farrell, and G. A. Somorjai, "Mean displacement of surface atoms in palladium and lead single crystals," *J. Chem. Phys.* 48, 1046-1051 (1968).
- [34] J. M. Morabito, Jr., R. F. Steiger, and G. A. Somorjai, "Studies of the mean displacement of surface atoms in the (100) and (110) faces of silver single crystals at low temperatures," *Phys. Rev.* 179, 638-644 (1969).
- [35] E. A. Murphy, H. E. Elsayed-Ali, and J. W. Herman, "Superheating of Bi(0001)," *Phys. Rev. B* 48, 4921-4924 (1993).
- [36] A. Janzen, B. Krenzer, P. Zhou, D. von der Linde and M. Horn-von Hoegen, "Ultrafast electron diffraction at surfaces after laser excitation," *Surf. Sci.* 600, 4094-4098 (2006).
- [37] R. Banerjee, E. A. Sperling, G. B. Thompson, H. L. Fraser, S. Bose, and P. Ayyub, "Lattice expansion in nanocrystalline niobium thin films," *Appl. Phys. Lett.* 82, 4250-4252 (2003).
- [38] Y. F. Zhu, W. T. Zheng, and Q. Jiang, "Modeling lattice expansion and cohesive energy of nanostructured materials," *Appl. Phys. Lett.* 95, 083110 (1-3) (2009).
- [39] L. Li, Y. Zhang, Y. W. Yang, X. H. Huang, G. H. Li, and L. D. Zhang, "Diameter-dependent thermal expansion properties of Bi nanowire arrays," *App. Phys. Lett.* 87, 031912 (1-3) (2005).
- [40] W.-H. Li, S. Y. Wu, C. C. Yang, S. K. Lai, K. C. Lee, H. L. Huang and H. D. Yang, "Thermal contraction of Au nanoparticles," *Phys. Rev. Lett.* 89, 135504(1-4) (2002).

- [41] B. D. Cullity, *Elements of X-ray Diffraction*, 2nd ed. USA: Addison-Wesley, Reading, MA (1978).
- [42] M. K. Zayed and H. E. Elsayed-Ali, "Melting and solidification study of as-deposited and recrystallized Bi thin films," *J. Appl. Phys.* 99, 123516(1-11) (2006).
- [43] H.-P. Cheng and R. S. Berry, "Surface melting of clusters and implications for bulk matter," *Phys. Rev. A* 45, 7969-7980 (1992).
- [44] J. W. M. Frenken and H. M. van Pinxteren, "Surface melting: dry, slippery, and faceted surfaces," *Surf. Sci.* 307-309, 728-734 (1993).
- [45] N. W. Ashcroft and N. D. Mermin, *Solid State Physics*, Chap. 25. Saunders College Publishing, Philadelphia, (1976).
- [46] X. F. Yu, X. Liu, K. Zhang, and Z. Q. Hu, "The lattice contraction of nanometre-sized Sn and Bi particles produced by an electrohydrodynamic technique," *J. Phys.: Condens. Matter* 11, 937-944 (1999).
- [47] G. D. Barrera, J. A. O. Bruno, T. H. K. Barron and N. L. Allan, "Negative thermal expansion," *J. Phys.: Condens. Matter* 17, R217-R252 (2005).
- [48] A. C. Bailey and B. Yates, "Anisotropic thermal expansion of pyrolytic graphite at low temperatures," *J. Appl. Phys.* 41, 5088-5095 (1970).
- [49] B. G. Childs, "The thermal expansion of anisotropic metals," *Rev. Mod. Phys.* 25, 665-670 (1953).
- [50] M. R. Black, P. L. Hagelstein, S. B. Cronin, Y. M. Lin, and M. S. Dresselhaus, "Optical absorption from an indirect transition in bismuth nanowires," *Phys. Rev. B* 68, 235417(1-10) (2003).

- [51] Y. Oshima, K. Takayanagi and H. Hirayama, "Structural anomaly of fine bismuth particles observed by ultrahigh-vacuum TEM," *Z. Phys. D: At. Mol. Clusters* 40, 534-538 (1997).
- [52] J. Heremans, C. M. Thrush, Z. Zhang, X. Sun, M. S. Dresselhaus, J. Y. Ying, and D. T. Morelli, "Magnetoresistance of bismuth nanowire arrays: A possible transition from one-dimensional to three-dimensional localization," *Phys. Rev. B* 58, R10091-R10095 (1998).
- [53] Z. Zhang, X. Sun, M. S. Dresselhaus, J. Y. Ying, and J. P. Heremans, "Magnetotransport investigations of ultrafine single-crystalline bismuth nanowire arrays," *Appl. Phys. Lett.* 73, 1589-1591 (1998).

CHAPTER 6

RESULTS, DATA ANALYSIS AND DISCUSSION OF TIME-RESOLVED DATA COLLECTED FROM BISMUTH NANOCCLUSERS

6.1. Introduction

The data were collected by analyzing the electron diffraction pattern from annealed Bi sample at different delay times. A 5 nm Bi that is thermally evaporated on TEM carbon coated grid and transferred to the time-resolved system for further processing. The sample was subjected to about 1.5 mJ/cm^2 femtosecond laser pulses while raising its temperature to $470 \pm 6 \text{ K}$ slowly, $\sim 3 \text{ K/min}$. At 470 K the sample was further heated by the laser pulses for about 20 s with the laser operating at 1 kHz. In the next chapter, there will a time-resolved comparative study between photoexcited Bi islands versus Bi nanoclusters. Although the data presented here is from one run with Bi nanoclusters, but several data were collected and presented in appendix J and appendix K for Bi nanoclusters and Bi islands, respectively. All the data presented here and in the appendices show the same general behavior as will be explained in details later but there might be a slight difference in the extracted numbers from the collected data. This could be attributed to experimental errors, which include system stability when it runs over a long period of time (some data were collected by running the system continuously over two days with no break). Another factor is the cluster size effect, which proved to affect significantly the equilibration time as will be explained in chapter 7.

For each sample, a femtosecond laser (pump), with wavelength of 800 nm and pulse width, $\tau_p = 120 \text{ fs}$, was used as an excitation source for time-resolved measurements. The FWHM of the pump laser spot size at the sample was measured and

found to be 1.9 ± 0.14 mm while the electron probe beam was measured at the sample and was found to have FWHM of 745 ± 54 μm . The total incident laser fluence was calculated after correcting for the angle of incidence $\sim 45^\circ$, absorption, and reflection from the glass window of the vacuum chamber, which was found to be $\sim 10\%$. The Bragg peak diffraction intensity, relative change in peak position ($\Delta d/d$) and FWHM were measured after radially averaging and background removal from each diffraction pattern.

Background removal is very important because it is due to the inelastically scattered electrons, multiple scattered electrons and reflection of the pump beam off the sample surface. To do so, the IMAGEJ (Ver. 4.2) software was used to convert the raw image into two dimensional plot by radially averaging the diffraction pattern, with the X-axis representing the position of the peaks (in pixels) and the Y-axis representing the peak intensity in arbitrary units. The data points of that plot were exported to an Excel sheet to remove the data which corresponds to the central undiffracted beam.

Then PEAKFIT (Ver. 4.12) was used to redraw the selected data imported from the Excel sheet, to remove the background and to fit the data with the proper prebuilt function to find the ring diffraction intensity, position and FWHM. The processed Bragg peaks, when the pump laser “ON” compared to those when the pump laser “OFF”, are shown in Fig. 6.1.(a) - (c). The details of image analysis are explained in Appendix H.

I noticed that the choice of the parameters of the ring over which the radial average is performed is very crucial, as can be seen from Fig. 6.1.(d). In Fig. 6.1.(d), the radial average of the same diffraction pattern was analyzed with different parameters of the radial average ring, which is summarized in Table 6.1. It is clear that the wrong

choice of the radial average parameters and lead to unrealistic behavior in the data analysis. For this reason the data presented in Fig. 6.2.(a)-(c) were analyzed with different parameters, and the one which gave the least error in the measured parameter (such as lattice expansion), compared to the time-resolved data, was included. A detailed comparison is included in Appendix H.

In this chapter, I will present the detailed data analysis performed on Bi nanoclusters and in the next chapter, I will do a time-resolved comparative study between Bi islands and Bi nanoclusters.

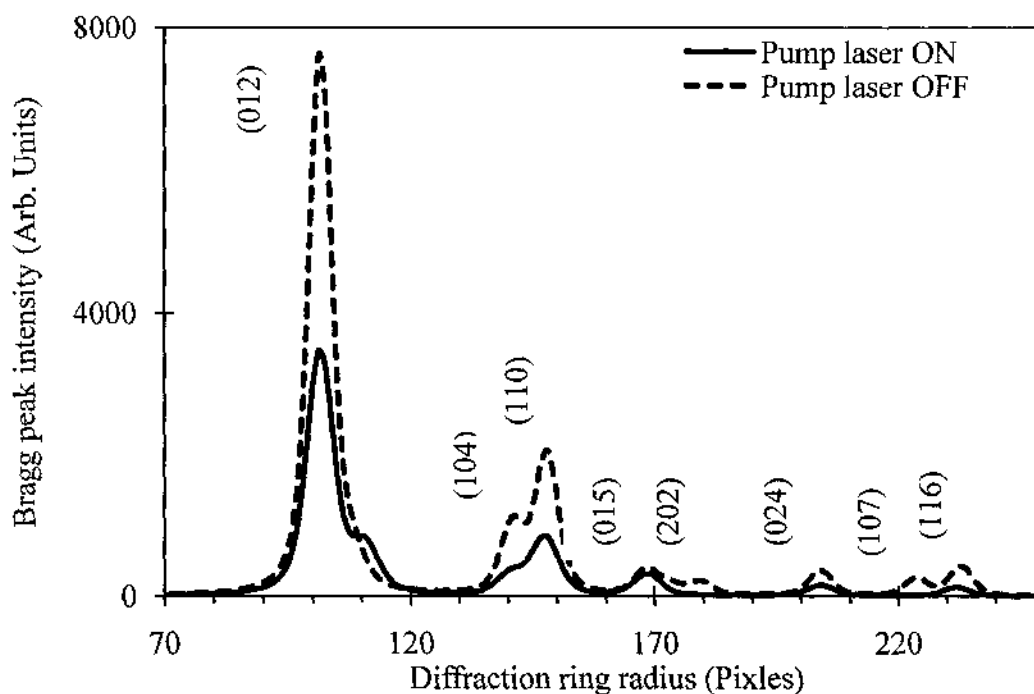


Fig. 6.1.(a) Radial average of the diffraction pattern at $t = 26.6$ ps when the pump laser is OFF compared to that when the pump laser is ON with fluence = 3.7 mJ/cm^2 .

6.2. Laser Fluence Dependent Electron Diffraction

After careful adjustment of the temporal and spatial overlap between the pump and the probe beams (appendix F), the dependence of the (012) and (110) natural log of Bragg peaks intensity, $\Delta d/d$ and normalized FWHM on the incident laser fluence were

studied and shown in Fig. 6.2.(a), (b) and (c) respectively; when the electron probe beam was delayed 27 ± 1 ps with respect to the pump beam, this delay time was calculated after careful measurement of the travel distance of both the pump and the probe d' and convert this distance into time t where $t = c \times d'$ and c is the speed of light in vacuum.

As can be seen from this study, the intensity of the diffraction pattern decreases with increasing laser fluence due to thermal effects and increase in lattice disorder. The Bragg peak relative position ($\Delta d/d$) dependence on laser fluence shows that the same behavior that was observed in statically heated samples, i.e., lattice contracts in $\langle 012 \rangle$ direction at a critical fluence and continues to expand in $\langle 110 \rangle$ direction.

There are many factors may contribute to the FWHM of the Bragg peak, as discussed in section 2.5. Inhomogeneous excitation of the lattice occurs whenever the crystal has excited parts adjacent to nonexcited parts, which may lead to the formation of side-bands and consequently results in Bragg peak broadening, Fig. 6.1.(a).

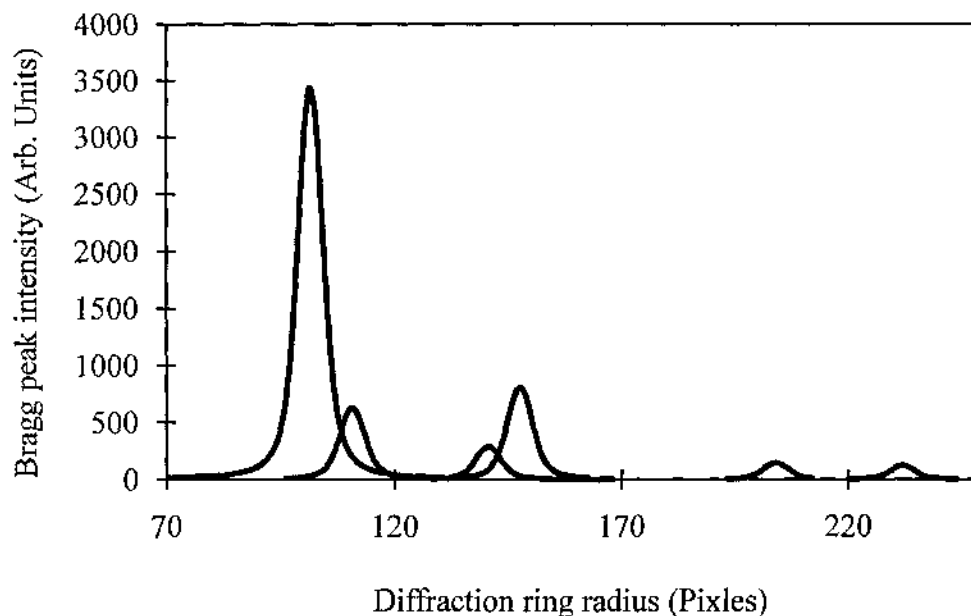


Fig. 6.1.(b) Isolated peaks of the diffraction pattern at $t = 26.6$ ps when the pump laser is ON, with fluence = 3.7 mJ/cm^2 .

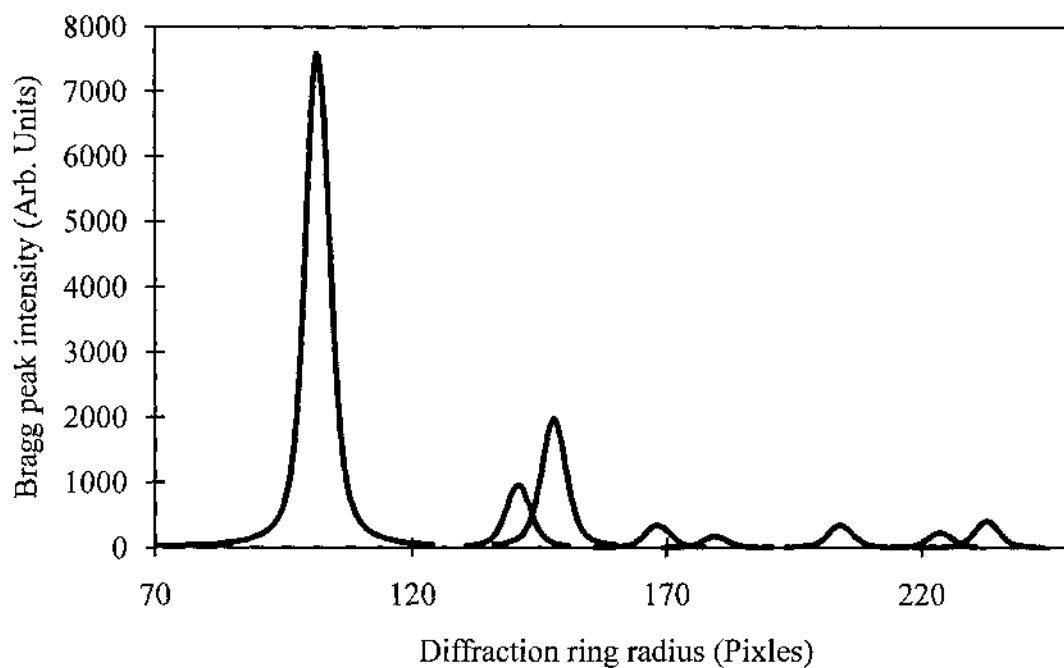


Fig. 6.1.(c) Isolated peaks of the diffraction pattern at $t = 26.6$ ps when the pump laser is OFF.

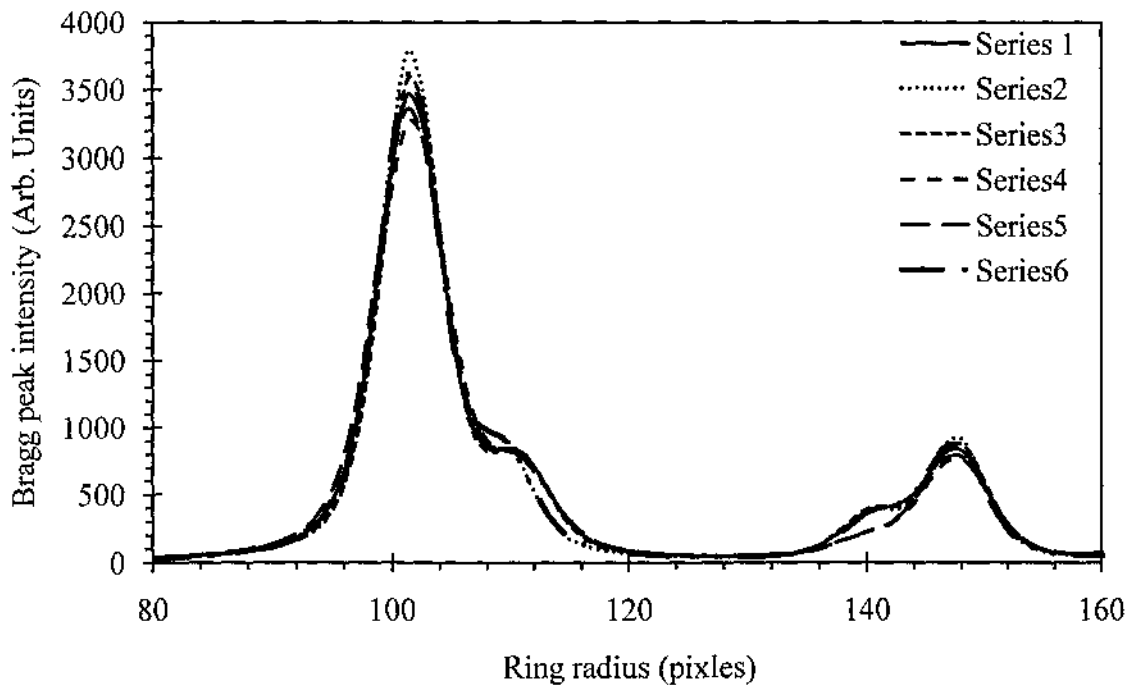


Fig. 6.1.(d) Radial average of the same diffraction pattern analyzed with different parameters of the radial average ring to show the sensitivity of the data analysis to any misfit between the ring and the pattern.

Table 6.1 Summary of the radial average parameters used in Fig. 6.1(d)

	X-position (pixels)	Y-position (pixels)	Circle diameter (pixels)
Series 1	509	499	300
Series 2	509	498	300
Series 3	510	498	300
Series 4	510	499	300
Series 5	508	499	300
Series 6	508	498	300

Crystal size reduction as a result of the formation of a thin film of liquid layer, which grows at the expense of the solid Bi as the fluence increases can also lead to Bragg peak broadening, and an increase in FWHM. Since these factors cannot be isolated from the measured FWHM and cannot be studied separately, I used the normalized FWHM, which represent the collective behavior of the lattice. Fig 6.2.(c) is the behavior of the normalized FWHM of the (012) peak with fluence, since the software used for isolating and fitting the peaks extracted from the diffraction pattern, fits best for (012) peak, I could not isolate the momentum transfer vector “ k ” effects on the FWHM.

The fitting for the (110) peak in Fig. 6.2.(b) is forced to a linear fitting because the behavior of that peak is expected to be linear from the data presented in chapter V. The fitting functions and the corresponding parameters for the other data in Fig. 6.2.(a)-(c) are summarized in Table 6.2.

Additionally, the error bars were not introduced here due to the fact that the physical properties of the grown samples is highly affected by thermal history of the sample as discussed in chapter I, but the behavior of these properties is the same, i.e., during all runs, $\Delta d/d$ continues to decrease with the fluence for the (110) peak while it starts to contract at higher critical fluence for the (012) peak, Fig. 6.2.(b).

Table 6.2 Summary of the fitting parameters and functions of the data presented in Fig. 6. 2.(a) - (c)

Bragg peak	Figure	Fitting function	Fitting parameters			
			y_0	y_1	y_2	y_3
(012)	VI. 2 (a)	$f(x) = y_0 + \frac{y_1}{1 + \exp(\frac{-(x - y_2)}{y_3})}$	-1.0638	1.0740	3.1808	-0.4946
(110)			-1.4065	1.4103	3.2557	-0.7317
(012)	VI. 2 (b)	$f(x) = y_0 + y_1 \cdot x + y_2 \cdot x^2 + y_3 \cdot x^3$	0.0001	-0.0016	5.7E-5	8.4E-5
(110)		$f(x) = y_0 + y_1 \cdot x$	0.0001	-0.001	-	-
(012)	VI. 2 (c)	$f(x) = y_0 + y_1 \cdot \exp(y_2 \cdot x)$	0.9887	0.0012	1.4318	-

I also noticed that the behavior of the normalized Bragg peak intensity for (012) and (110) peaks are in general follows Debye-Waller effect and the Debye-Waller factor calculated from (012) is always less than that calculated from (110) as mentioned in chapter V, but sometimes the slope differs from run to run (also seen in the data presented in appendix I for the static heating data). This can be explained in terms of the effect of the thermal history of the sample as well as successive heating, either by direct heating stage or femtosecond laser pulses, and quenching may change the cluster size which has a direct impact on the electronic band structure of the sample as mentioned in chapter 4 and in turn affects the calculated physical parameters of the sample. Additionally, the formation of side-bands with fluence, which becomes well pronounced at high laser fluence, near the (012) peak may affect the phonon frequency and excite low frequency phonons, which consequently affects the Debye temperature as well as the unusual behavior of thermal expansion coefficient measured along (012) direction and responsible for the slow intensity drop of (012) compared to that (110), reversed behavior to that observed in Ch.5. This behavior is pronounced, especially, when the sample

dimensions have reduced significantly and reach the nanoscale [1]. At reduced dimensions, low frequency phonons might be excited at temperatures close to the Debye temperature of the nanoclusters and affect the elastic properties of Bi nanoclusters [2], the energy of these phonons could be a function of cluster size [1]. Therefore, as the dimensions of the nanoclusters get smaller, these phonons will be excited at a lower temperature, and contribute to the side-bands detected near (012) planes. An extensive study is needed to monitor the effect of cluster size on the excitation of these phonons and consequently on the different lattice thermal properties.

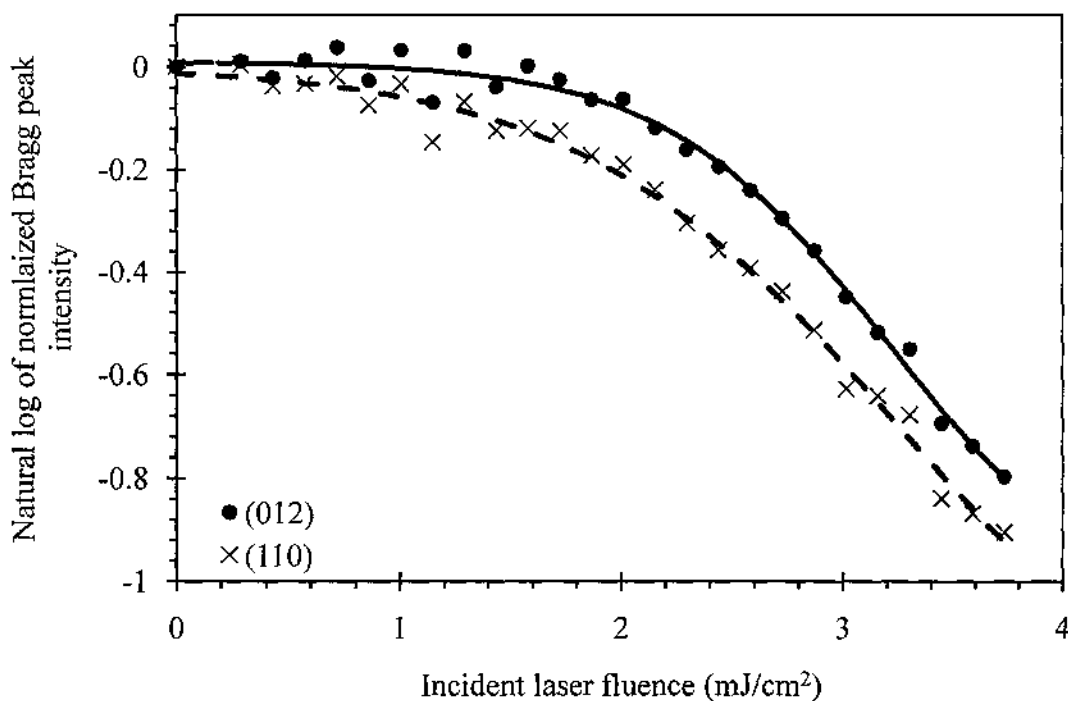


Fig. 6.2.(a) Normalized Bragg peak intensity as a function of the incident laser fluence.

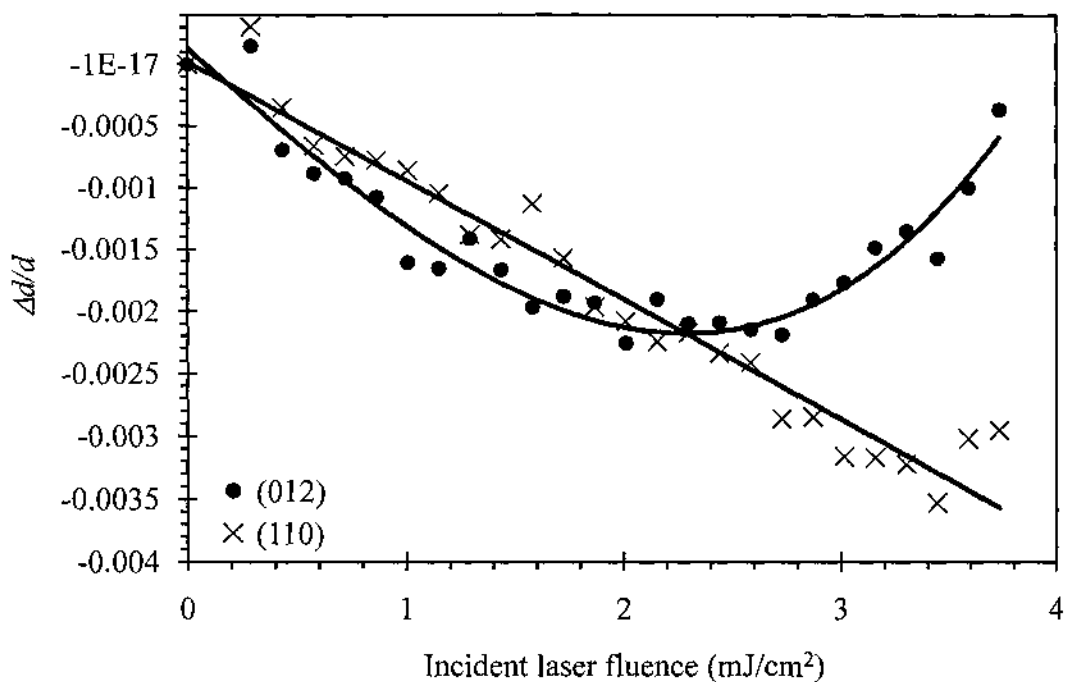


Fig. 6.2.(b) Normalized Bragg peak position change as a function of the incident laser fluence.

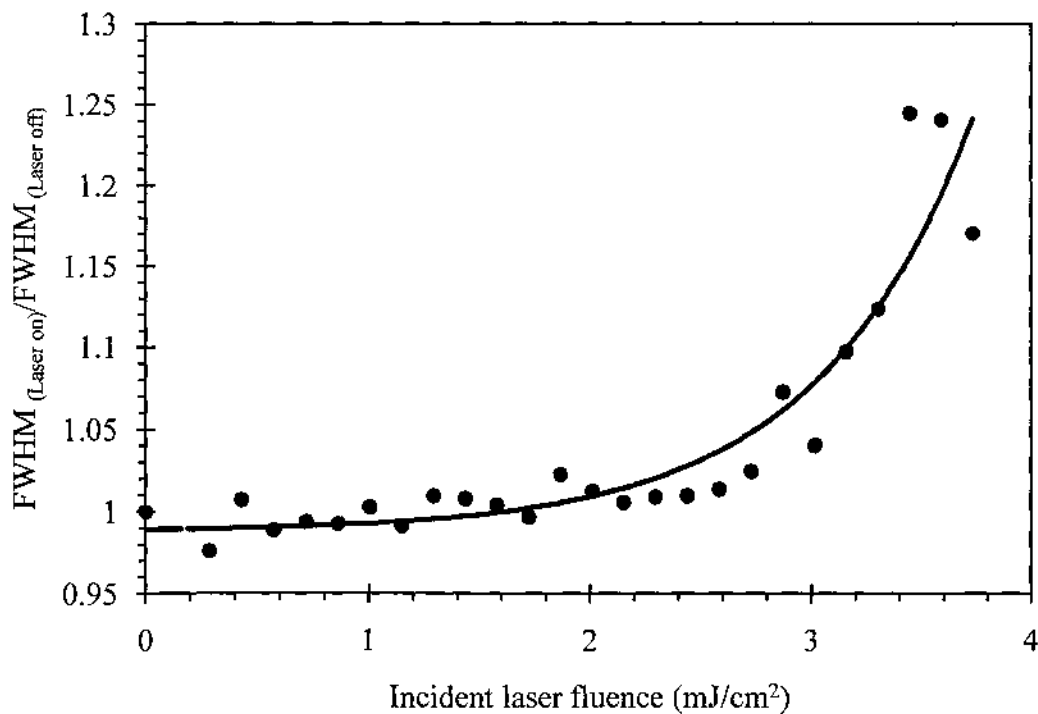


Fig. 6.2.(c) Percentage change in FWHM as a function of the incident laser fluence calculated from (012) Bragg peak.

If we were to ignore the effect of side-bands and assumed the Bragg peak broadening to be due to the formation of molten layer surrounding the Bi nanoclusters, therefore, from Eq. 5.8 and Fig. 6.2.(c) the molten layer thickness is calculated at different fluences and summarized in Table 6.3.

Table 6.3 Summary of calculated molten layer thickness at different laser fluence calculated from the data presented in Fig. 6.2.(c).

Fluence (mJ/cm ²)	Molten layer thickness (Å)
2.0	6.3
2.6	12.1
3.0	15.7
3.6	32.3

6.3. Time-Resolved Electron Diffraction Data Analysis

The data presented in the previous section guided us in determining the proper excitation fluence of Bi nanoclusters, which does not induce damage or full melting to the sample. Two sets of time-resolved data were collected at two different fluencies, 2.0 mJ/cm² and 2.9 mJ/cm². The first fluence is at the onset of partial melting, while the other fluence is high enough to induce partial melting of the sample, Table 6.3. Both fluencies were below the damage and full melting of the sample. Also, I would like to stress and clarify, for the reader, that the fitting used in the time-dependent lattice strain ($\Delta d/d$) is just to guide the eye of the reader to the general behavior of the lattice strain with time due to femtosecond laser excitation. This leads to a very important conclusion about the oscillatory behavior of $\Delta d/d$ at $t < 0$ and/or $t > 25$ ps is not real and due to the uncertainty in the measured data, which may arise from the fluctuations in the femtosecond laser, system stability or any extraneous behavior due to the long time operation of the electron gun. Additionally, the lattice thermalization time cannot be estimated from $\Delta d/d$ or

normalized change FWHM versus time due to the limited capabilities of the software used here.

The data presented in this section were collected after precise space overlap between the pump beam (laser excitation pulses) and the probe beam (short electron pulses). The temporal overlap as well as the zero delay time between the pump and probe pulses was determined in situ by iteration method. In this method, we moved the delay stage back and forth over 5 mm distance, in steps of 0.15 mm (equivalent to 1 ps delay time), and observed the change in the diffraction pattern of Bi with and without pump laser pulses till we reached a point on the stage, beyond which there is no difference between the images taken with and without laser excitation, which corresponds to $\Delta t = 0$, for more details, please refer to appendix K. We controlled the delay time, Δt , between the pump and the probe pulses to monitor in real time the structure evolution prior or after the pump pulse excitation. Fig. 6.3 shows the diffraction pattern of Bi at different delay times, and the radial averaging of the pattern at different delay times, after background removal, is shown in Fig. 6.4. I followed the procedures described in details in appendix H for data analysis and background removal. In Fig. 6.5.(a), we monitored the intensity and $\Delta d/d$ of the (012) Bragg peak as a function of delay time. We also monitored the normalized FWHM, Fig. 6.5.(b), of the same peak. Although the FWHM of the ring pattern can be related to the thickness of the liquid shell that may form around the solid sample, excitation of longitudinal acoustic phonons and or strain effects can also affect the measured FWHM as discussed earlier [3, 4].

Then, we followed the same procedures for the (110) Bragg diffraction ring in Fig. 6.6. The data shown in Fig. 6.5.(a) and 6.6 are for pump laser fluence of ~ 2.9

mJ/cm². I used the intensity drop at the asymptote from Fig. 6.5.(a) and Fig. 6.6 to estimate the final lattice temperature. By comparing these values to the static heating data presented in Fig. 5.6, a final average lattice temperature of 511 ± 6 K, can be estimated, which is above the onset of melting temperature presented in the static heating data in chapter V and can be seen from the detected diffraction pattern at that fluence; see, for example, the pattern at 83 ps in Fig. 6.3. This fluence is not high enough to induce a full sample melting, but can induce partial melting as can be seen from Table 6.3.

Since the position, θ , of the Bragg peak is related to the lattice spacing, d , therefore any deviation, $\Delta\theta$, in the angular position of the center of the Bragg ring is a fingerprint of the lattice contraction or expansion, Δd . The relative change in Bragg peak position is obtained from the Bragg's law which gives, $(\Delta d / d) = -(\Delta\theta / \tan\theta)$ [5].

From the results shown in Fig. 6.7 at laser fluence of 2.9 mJ/cm², it is clear that the lattice contracts ($\sim 0.05\%$) immediately after the photoexcitation of Bi nanoclusters at $t = 0$ (*first contraction region*, $0 < t < 6$ ps), which is fluence dependent. Following this contraction, the lattice expands to $\sim 0.22\%$ which is also fluence dependent. When the lattice reaches its maximum expansion, it contracts again, (*second contraction region*, $t > 25$ ps), to a certain position determined by the total energy absorbed by the lattice and consequently on the final lattice temperature.

The time dependent change in interplanar spacing, presented in Fig. 6.5.(a) and Fig. 6.6 along $\langle 012 \rangle$ and $\langle 110 \rangle$ directions, can be used to calculate the thermal expansion coefficient along these directions. From the definition of the linear thermal expansion coefficient, $(\Delta d / d) = \alpha \times \Delta T$, and from Fig. 6.5.(a) at the asymptote, $\Delta d / d \sim -0.002$, $\Delta T = 211$ K, therefore $\alpha_{(012)} = 9.5 \times 10^{-6} \text{ K}^{-1}$, and from Fig. 6.6 $\Delta d / d \sim -0.0022$ and

$\alpha_{(110)}=10.4\times 10^{-6} \text{ K}^{-1}$. These values are in fair agreement with the values calculated in chapter V with an estimated error of 34% and 24 % respectively. This percentage error was calculated from Eq. 6.1,

$$\% \text{ error} = \left| \frac{\alpha_{cw} - \alpha_{TR}}{\alpha_{cw}} \right| \times 100 \quad 6.1$$

where $\alpha_{cw} = 14.4\times 10^{-6} \text{ K}^{-1}$ and $13.7\times 10^{-6} \text{ K}^{-1}$ for (012) and (110) planes respectively, calculated from chapter V, and α_{TR} is the value calculated from the time resolved data as mentioned above.

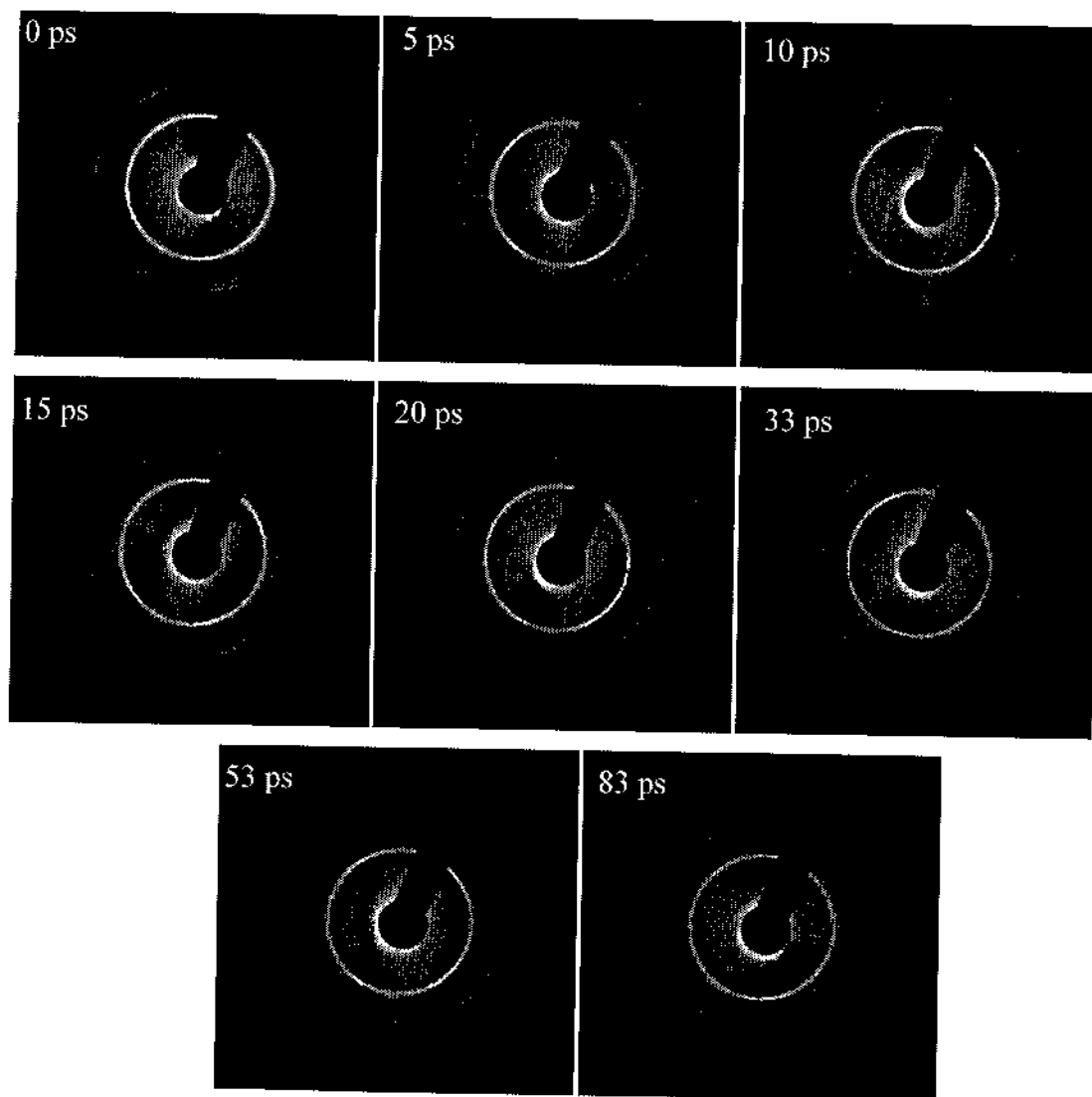


Fig. 6.3. Snapshots of the diffraction pattern of Bi at different delay times.

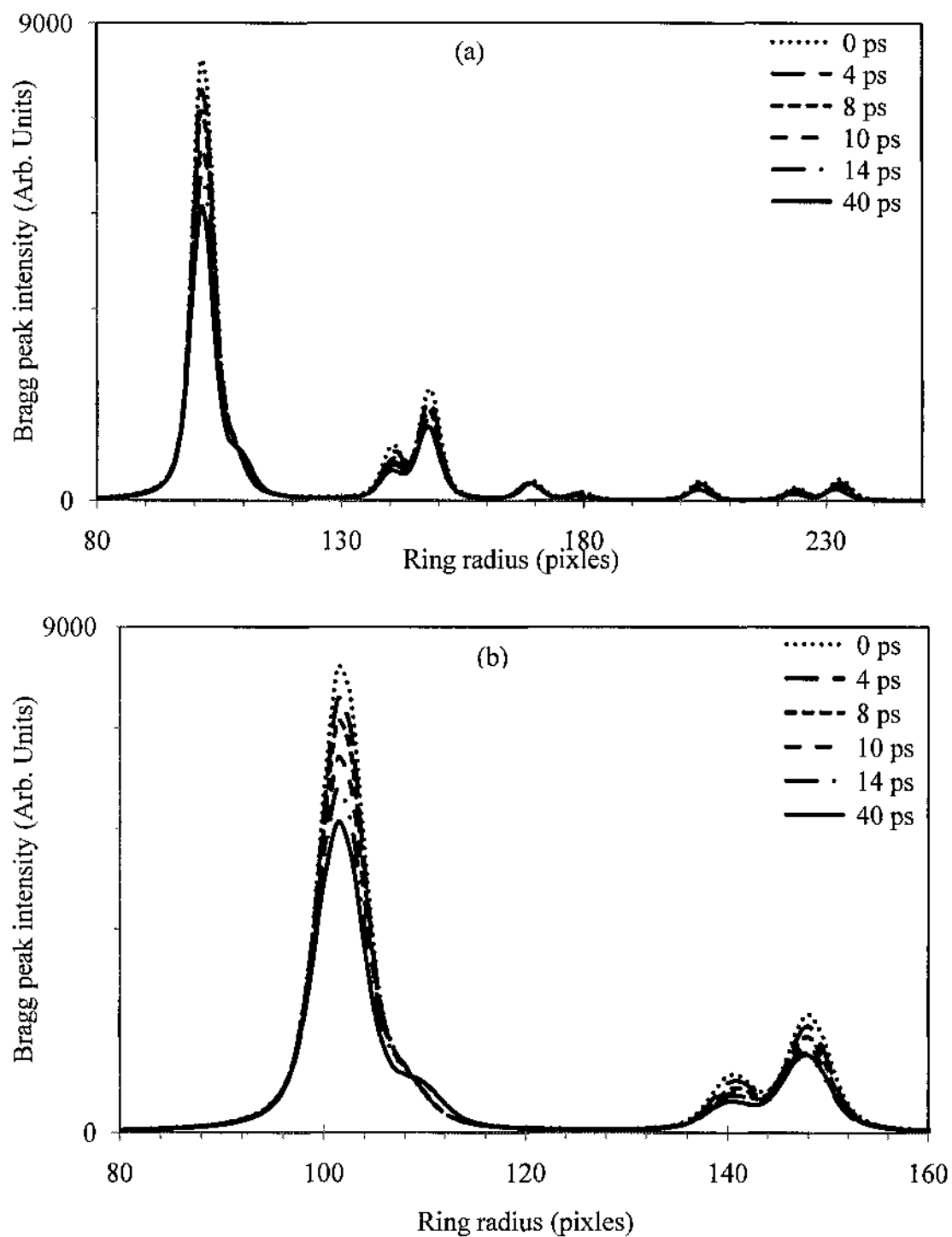


Fig. 6.4. Radial average of the diffraction pattern shown in Fig. 6.3 after background removal, (a) full range of diffraction ring pattern and (b) the first three diffraction rings.

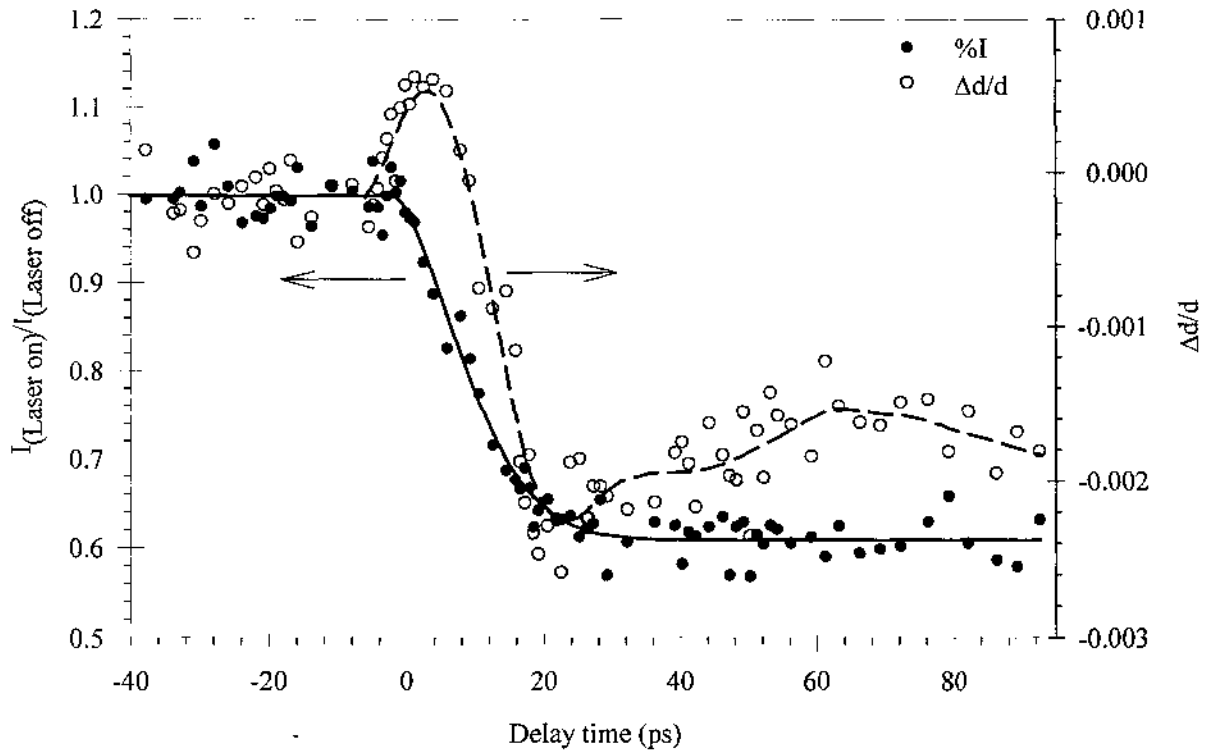


Fig. 6.5.(a) Time evolution of the strain detected along (012) and the corresponding normalized change in intensity due to femtosecond laser excitation pulses of fluence 2.9 mJ/cm^2 .

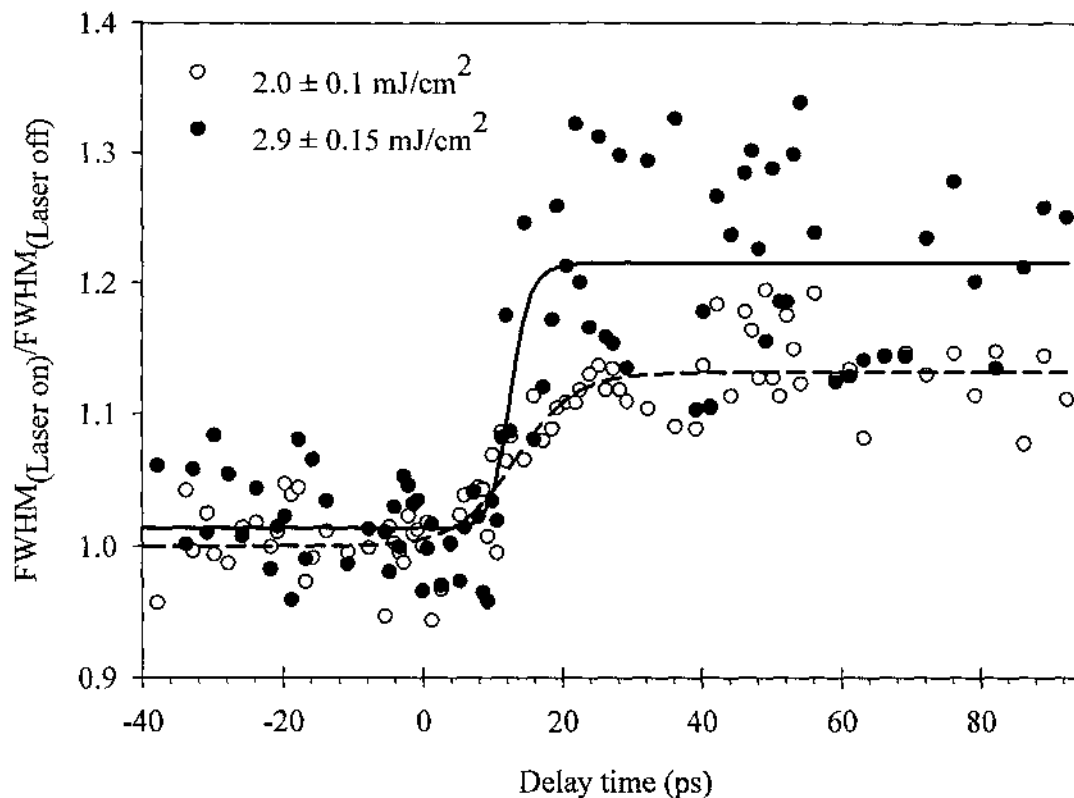


Fig. 6.5.(b) Percentage change FWHM as a function of delay time at 2.0 mJ/cm^2 and 2.9 mJ/cm^2 calculated from (012) Bragg peak.

I noticed that the first contraction that occurred over 6 ps after $\tau = 0$, over this period of time, the lattice is not yet in thermal equilibrium and its temperature cannot be defined. Therefore we suggest the nonthermal regime for initial lattice excitation [6]. This can be explained as follows: the initial lattice contraction is due to the deformation imposed by femtosecond laser pulses on the lattice potential along the c -axis of the crystal lattice. This deformation is a consequence of the decrease in the carrier density in the valence band upon excitation to the conduction band. According to Murray et al.[7], a decrease of 1% of the carriers in the valence band causes a relative change in the atomic

displacement of 10 pm, which shifts the potential energy surface minima, and in turn reduces the Peierls barrier.

The fraction of excited carriers Δn is affected by the absorbed laser fluence ΔF , which results in a lattice temperature rise ΔT , $\Delta n = 3.3 \times 10^{-5} \Delta T$ [8]. As mentioned earlier, $\Delta T = 211$ K, therefore, the fraction of excited carrier density = 0.7%. Since 1% carrier excitation causes 10 pm a relative change in atomic displacement [7], the fluence that I have used can make 7 pm change in atomic position, which is still high enough to modify the electronic structure and the energy gap which may affect the equilibration time.

Therefore, we expect that the electronic disturbance in Bi by ultrashort laser pulses changes the equilibrium atomic positions within the unit cell by displacive excitation of coherent phonons (DECP) of symmetry A_{1g} . A_{1g} (breathing mode) is one of the normal modes of vibrations of Bi that does not change the symmetry of the lattice [9, 10]. Then the excited lattice will be brought to a quasiequilibrium state over a very short period of time compared to that needed to thermalize the lattice.

Therefore, we conclude from the previous discussion that the initial contraction observed in lattice spacing along (012) is not due to the thermal effect of ultrashort laser pulses, but rather due to the carrier density disturbance within the conduction and the valence bands that excite the A_{1g} mode, which gives rise to a restoring force that drives the coherent atomic motion and leads to lattice contraction.

Following the initial contraction, lattice expansion is observed over a longer time scale, ~ 20 ps, through carrier density reduction and subsequent thermalization processes, electron-phonon and phonon-phonon interaction. Many processes are considered and contribute to charge carrier removal and consequently its density reduction. These

processes are, but are not limited to, electron-hole recombination. The diffusion is ignored in our study since the sample thickness is less than or comparable to the laser pulse penetration depth in Bi.

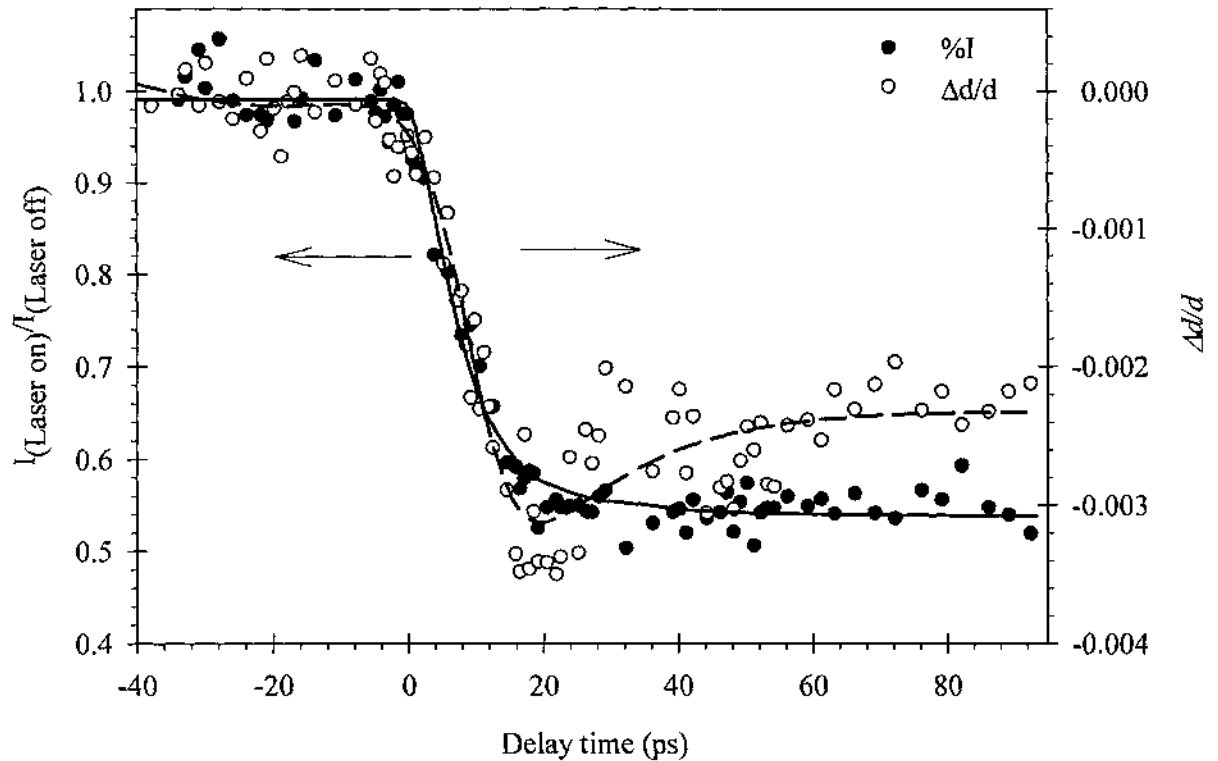


Fig. 6.6. Time evolution of the strain detected along (110) and the corresponding normalized change in intensity due to femtosecond laser excitation pulses of fluence 2.9 mJ/cm^2 .

Electron-hole recombination may be radiative or non-radiative in nature. In radiative processes, opposite to excitation, a photon is emitted that carries the excess carrier energy. While in non-radiative recombination process, which includes Auger recombination, an electron recombines with a hole and the excess energy will be carried out by another electron and excited to a higher energy level [6].

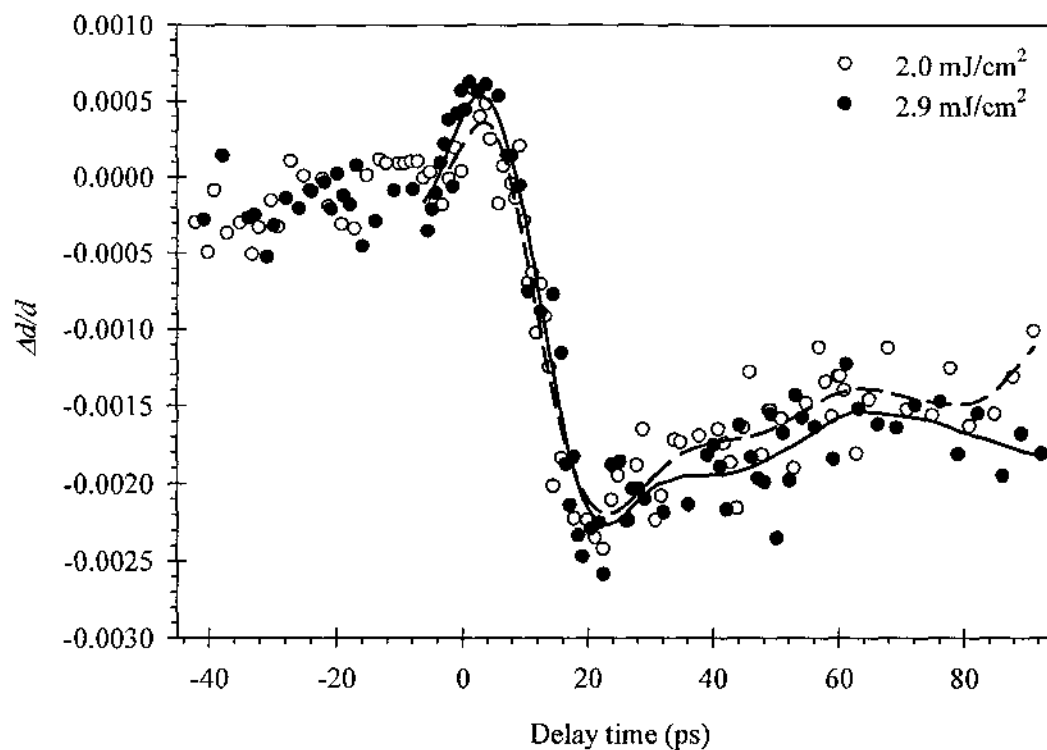


Fig. 6.7. Normalized Bragg peak center position of (012) Bragg peak as a function of delay time at two different fluences.

Thermal and structural effects come into the picture when the charge carrier and the lattice are in thermal equilibrium and the final lattice temperature is determined by the initial energy deposited by the ultrashort laser pulses into the sample. Melting or vaporization can occur if the lattice temperature exceeds the lattice melting or boiling temperature, respectively. In some cases, the material preserved its solid integrity at temperatures above its melting point, and in this case the lattice is said to be superheated. If the photoexcitation of the material did not induce any phase transition, the final temperature of the material recovers to a value determined by the surroundings over a microsecond time scale.

According to Fig. 6.5.(a), along the (012) direction, the lattice expands but after a time delay of 6 ps. Over this period of time, the electron - phonon coupling defines the lattice effective temperature increase which results in lattice disorder and reflected on the intensity drop. After $t > 6$ ps, the lattice expands to a maximum value of 0.22 % of its original value over 20 ps, followed by another contraction to a final value of ~ 0.2 % over a longer period of time. This final contraction is related to the more stable state of the lattice and it corresponds to the restoring force between the atoms which comes into effect after the lattice reaches its maximum expansion.

It is worth noting that for (110) direction, Fig. 6.6, no contraction is observed in lattice spacing, only expansion and this can be explained in terms of the sensitivity of different Bragg peaks to the excited A_{1g} optical phonons. Since all Bragg peaks, defined by Miller indices' (hkl), with $l = 0$ are insensitive to A_{1g} mode [11], therefore its effect on those Bragg peaks could not be detected, Fig. 6.6.

The temporal behavior of the diffraction ring intensity presented in Fig. 6.5.(a) and Fig. 6.6 was found to have a best fit to a single exponential decay function given by:

$$\frac{I(t)}{I_0} = \begin{cases} \sim 1 & t \leq 0 \\ A + B \times e^{-\Delta t/\tau} & t > 0 \end{cases} \quad 6.2$$

where $I(t)$ is the Bragg peak intensity at delay time t , I_0 is its intensity at $t < 0$, $A = 0.6$ and $B = 0.4$ are the fitting parameters, while τ is the decay time = 9.2 ps. The decay time can be used to interpret the different relaxation processes following femtosecond photoexcitation that may include but not limited to Auger recombination (non-radiative), radiative recombination and surface and defect recombination [6].

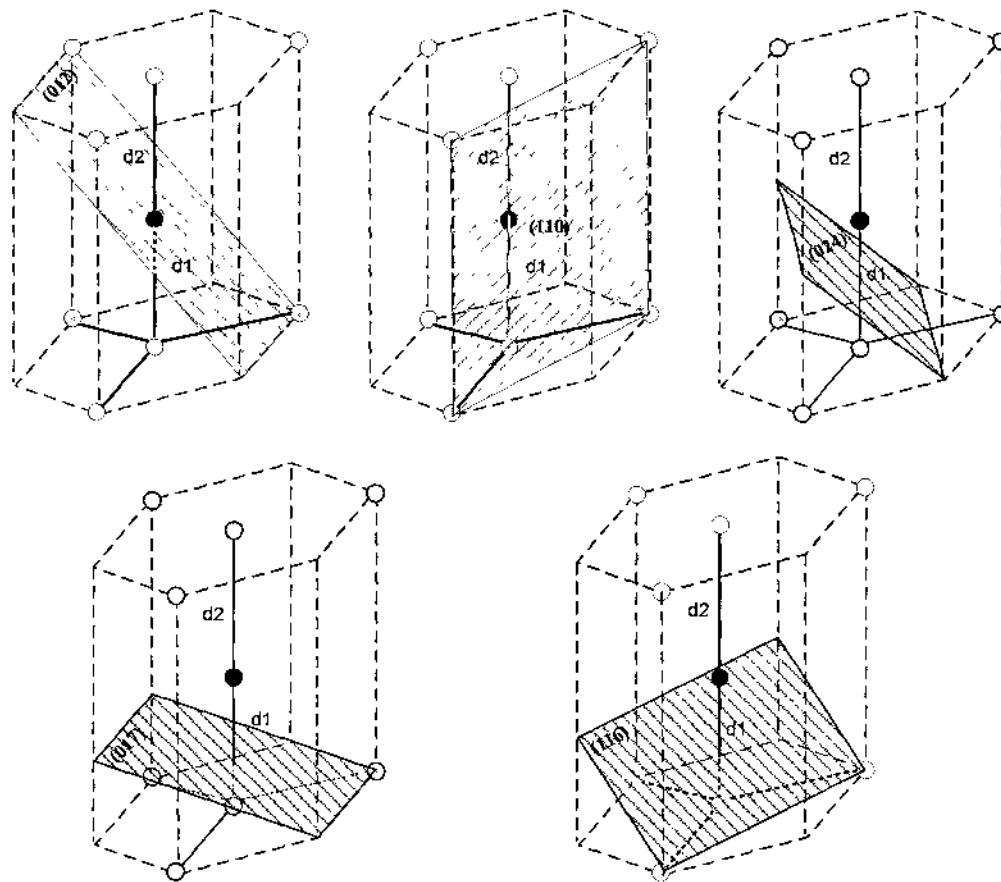


Fig. 6.8. Different planes in hexagonal unit cell of Bi.

6.4. Temperature Rise per Incident Laser Fluence

The final lattice temperature can be calculated from Debye-Waller Eq. 2.22 as follows,

$$-\ln\left(\frac{I}{I_0}\right) = C' \times \left(\frac{1}{d_{hkl}}\right)^2 \quad 6.3$$

Where I/I_0 is taken from the asymptotic behavior of the time-dependent normalized Bragg peak intensity at fluence 2.0 mJ/cm^2 .

Therefore, a plot of $-\ln\left(\frac{I}{I_o}\right)$ versus $\left(\frac{1}{d_{hkl}}\right)^2$, will produce a straight line of slope

C' , which is material dependent and related to the material parameters through the Debye-Waller Eq. as follows,

$$C' = \frac{3 \times h^2}{m \times k_B} \times \left(\frac{1}{\theta_D^2}\right) \times \Delta T = 5.6 \times 10^{-2} \times \Delta T \quad 6.4$$

where $\theta_D = 86 \pm 9$ K is the calculated Debye temperature from chapter V, and is considered here to be the average Debye temperature of the planes considered in Fig. 6.9.

Therefore, from Eq. 6.4 and Fig. 6.9, the average increase in lattice temperature (ΔT) as a result of 2.0 mJ/cm² femtosecond laser excitation is 186 K. Therefore the final sample temperature is 486 K. The temperature rise at the same excitation fluence can also be calculated from Eq. 5.4, which was found to be 211 K. Comparing these previously mentioned values of temperature rise calculated from Fig. 6.9 and Eq. 5.4, a percentage error of 12% was estimated after using Eq. 6.5.

$$\% \text{ error} = \left| \frac{T_1 - T_2}{T_1} \right| \times 100 \quad 6.5$$

where $T_1 = 211$ K and $T_2 = 186$ K.

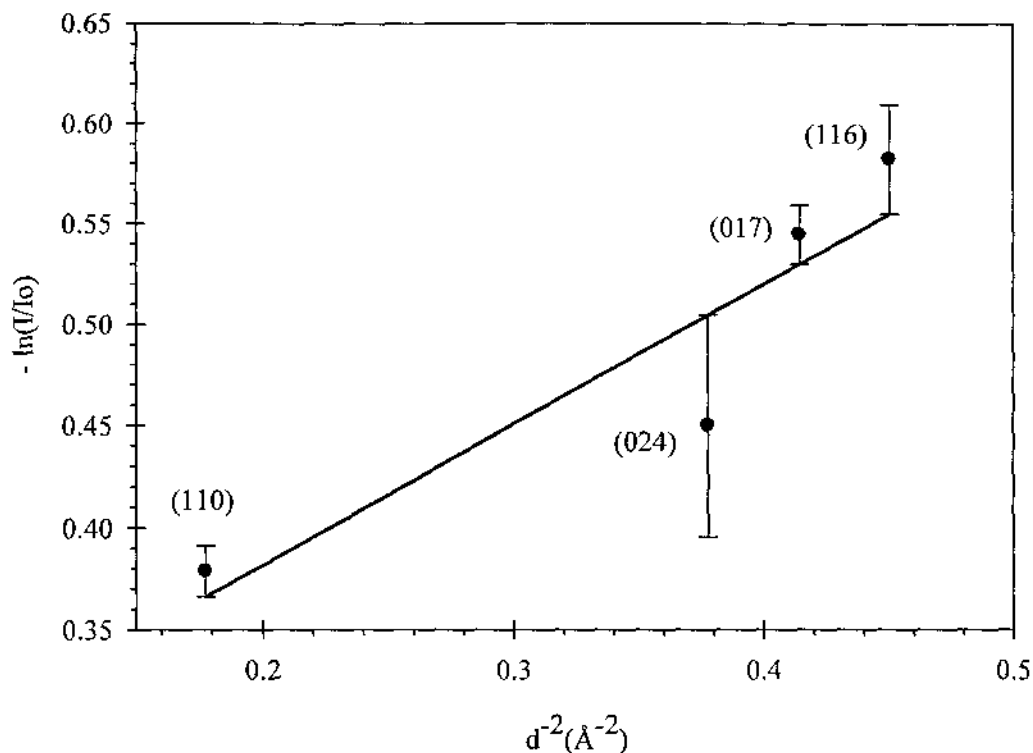


Fig. 6.9. Change in Debye-Waller factor with different interplanar spacing. The error bars were calculated by software in the form of the deviation of the actual data points from the linear fitting function.

In summary, the data presented here can give an insight view of photoexcitation of Bi nanoclusters with ultrashort laser pulses, which induces nonthermal and thermal effects. Upon photoexcitation, a significant amount of charge carriers are promoted from the valence to the conduction band. The increased carrier density in the conduction band changes the lattice configuration by excitation of optical phonons of symmetry A_{1g} which has a displacive nature. In other words, the redistribution of the charge carriers in the valence band changes the interatomic potential energy surface and give rise to the restoring force which induces the coherent atomic motion which causes the lattice to contract, (nonthermal effects). The excited phonons relax through phonon-phonon

interaction and/or Auger recombination, which results in a lattice temperature increase that leads to lattice expansion after 6 ps (thermal effects).

The data presented here opens the door for considering the thermal history and annealing effects on the physical properties of Bi. For example, I'm suggesting high resolution TEM scans after each single annealing process. This may have side-effects of successive exposure to air especially at nanostructures scale sample, as this may lead to the formation of oxide layer on the sample surface, which in turn imposes another factor that may affect the physical properties of the sample.

Additionally, the theoretical model for the data presented here is also suggested, from which the thermalization time of the lattice strain and FWHM can be extracted.

6.4. References of Chapter VI

- [1] Y. Zhu, X. Dou, X. Huang, L. Li, and G. Li, "Thermal properties of bi nanowire arrays with different orientations and diameters," *J. Phys. Chem. B* 110, 26189-26193 (2006).
- [2] J. N. Hancock, C. Turpen, Z. Schlesinger, G. R. Kowach, and A. P. Ramirez, "Unusual low-energy phonon dynamics in the negative thermal expansion compound ZrW_2O_8 ," *Phys. Rev. Lett.* 93, 225501(1-4) (2004)
- [3] M. Bargheer, N. Zhavoronkov, M. Woerner, and T. Elsaesser, "Recent progress in ultrafast X-ray diffraction," *Chem. Phys. Chem.* 7, 783-792 (2006).
- [4] A. Rousse, C. Rischel, and J. Gauthier, "Colloquium: Femtosecond X-ray crystallography," *Rev. Mod. Phys.* 73, 17-31 (2001).
- [5] P. Chen, I. V. Tomov, and P. M. Rentzepis, "Lattice dynamics of laser-heated GaAs crystals by means of time-resolved x-ray diffraction," *J. Phys. Chem. A* 103, 2359-2363 (1999).
- [6] S. K. Sundaram and E. Mazur, "Inducing and probing non-thermal transitions in semiconductors using femtosecond laser pulses," *Nat. Mater.* 1, 217-223 (2002).
- [7] E. D. Murray, D. M. Fritz, J. K. Wahlstrand, S. Fahy, and D. A. Reis, "Effect of lattice anharmonicity on high-amplitude phonon dynamics in photoexcited bismuth," *Phys. Rev. B* 72, 060301(1-4) (2005).
- [8] G. Sciaini, M. Harb, S. Kruglik, T Payer, C. Hebeisen, F. Heringdorf, M. Yamaguchi, M. Hoegen, R. Ernstorfer and R. J. Dwayne Miller, "Electronic acceleration of atomic motions and disordering in bismuth," *Nature* 458, 56-60 (2009).

- [9] H. J. Zeiger, J. Vidal, T. K. Cheng, E. P. Ippen, G. Dresselhaus, and M. S. Dresselhaus
“Theory for displacive excitation of coherent phonons,” *Phys. Rev. B* 45, 768-778
(1992).
- [10] T. K. Cheng, J. Vidal, H. J. Zeiger, G. Dresselhaus, M. S. Dresselhaus, and E. P.
Ippen, “Mechanism for displacive excitation of coherent phonons in Sb, Bi, Te, and
 Ti_2O_3 ,” *Appl. Phys. Lett.* 59, 1923-1925 (1991).
- [11] I. Rajkovic, “Ultrafast electron diffraction studies of optically excited thin bismuth
films,” Ph.D. Theses, Dept. of Physics, University of Duisburg, Essen - Germany (2008).

CHAPTER 7

TIME-RESOLVED COMPARATIVE STUDY, BISMUTH ISLANDS VERSUS BISMUTH NANOCCLUSERS

7.1. Introduction

Bismuth (Bi) thin films, nanoclusters and nanorods have a hexagonal crystal structure similar to that of the bulk with two atoms per unit cell. The Bi unit cell is a distorted cubic structure and the angle between the axis $\neq 90$. This configuration is not stabilized by a simple two or three body force law, but by Peierls–Jones mechanism [1] as described in chapter 1.

On the other hand, the reduced dimensionality has a direct impact on the electronic structure and properties [2]. Shick et al. showed how the atomic displacement as well as an increase in the shear angle can induce a change in the Bi electronic structure and lead to a metal-semimetal transition and semimetal-semiconductor transition, respectively [3]. This was attributed to the effect of an internal displacement change, $\delta = (0.25 - u)$, where $u = 0.234$, on the total energy of Bi, which has a double-well nature [3]. The double-well height can be reduced by reducing δ , and it can reach to a point that it becomes flat at some critical distance. Therefore, the electronic band structure is very sensitive to the change in the internal displacement δ , as well as the trifocal angle α . Shick et al. summarized the effect of these factors on the possible metal/semimetal/semiconductor transition, as follows, (a) $\delta = 0$ and $\alpha = 60^\circ$, this gives rise to the simple cubic structure nature of Bi at high pressure and enhances the metallic nature of Bi. (b) $\delta = 0.016$ and $\alpha = 60^\circ$, this configuration results from the displacement of one of the atoms along the (111) body diagonal and introduces a narrow band gap

along the T (single hole pocket) and L points (conductive electron pockets) in the Brillouin zone, which results in the semiconducting properties of Bi. (c) $\delta = 0.016$ and $\alpha = 57^\circ.19'$ (trigonal structure of bulk Bi), this shear drives the semiconductor-semimetal transition of bulk Bi, *the reader can refer to Fig. 4 in Ref. [3] for Bi electronic band structure.*

Therefore, the semimetallic reconstructed Bi surface can turn into a metal or semiconductor, which is very interesting in studying the two dimensional metals [2]. Additionally, some Bi surfaces, like the (110), were reported to have better metallic properties than other surfaces due to the nature of the structure along the $\langle 110 \rangle$ direction [4] which according to Ref. 2 “supports the dangling bond states on every other surface atom.”

Therefore, the possibility of a semimetal to become a semiconductor or a metal is strongly dependent on the relative displacement of the atoms in a unit cell [2]. I report here a study of the effect of reduced dimensionality of Bi nanoclusters and islands on the equilibration time of (012) and (110) surfaces upon photoexcitation by femtosecond laser pulses using transmission high-energy electron diffraction (THEED) technique.

7.2. Experiment

I followed here the same procedures that were followed in chapter VI to collect and analyze the time-resolved data and described in details in the appendices. Here, we are dealing with two samples, S1 and S2. S1 was annealed at room temperature by femtosecond laser pulses of fluence $2.4 \pm 0.12 \text{ mJ/cm}^2$, while S2 was heated from room temperature up to 470 K while being exposed to the same laser fluence, where the error in measuring the fluence was found to be, at most, 0.12 mJ/cm^2 .

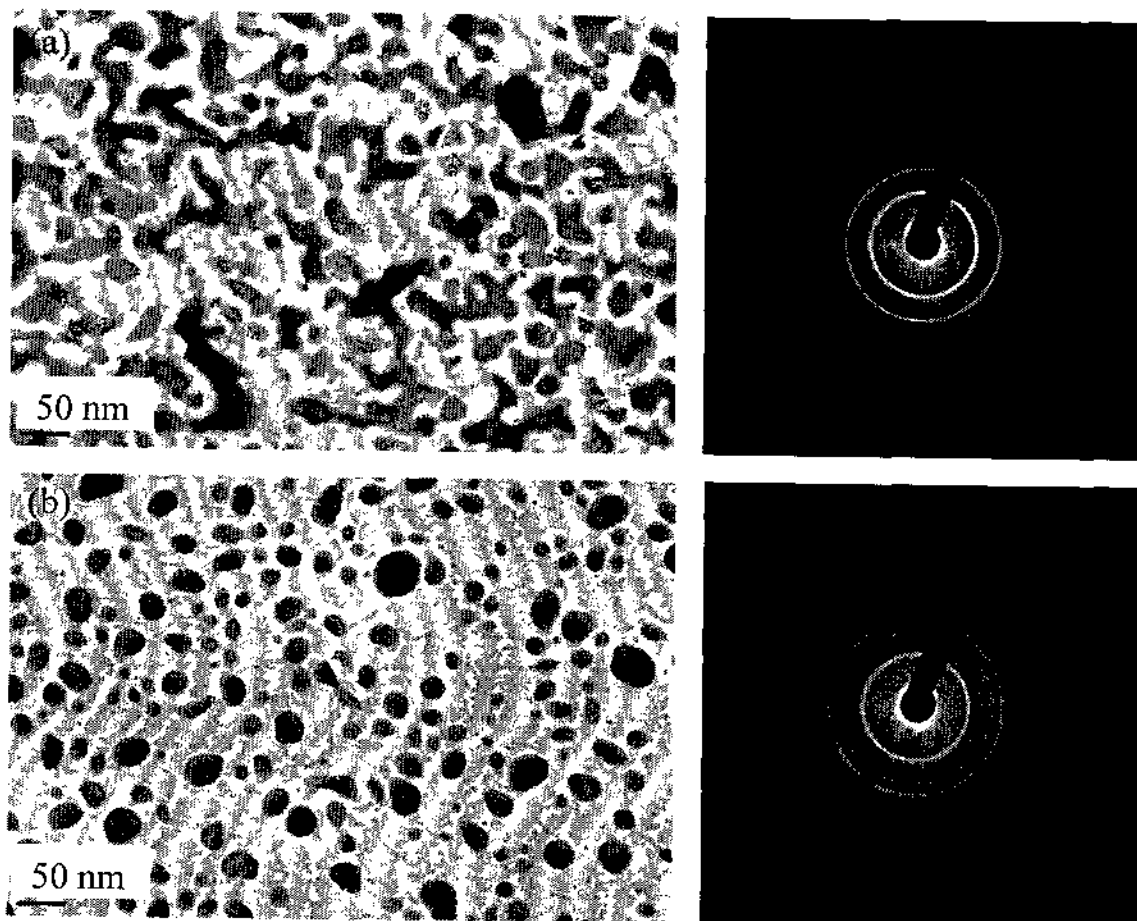


Fig. 7.1. HRTEM images and diffraction pattern of (a) laser annealed Bi samples, S1 and (b) laser annealed sample simultaneously with continuous heating up to 470 K, S2.

The TEM images for both samples were compared and we found that, the surface of S1 did not show any change in cluster shape and/or size, but rather increase the voids in the thin film due to agglomeration and coalescence of different clusters as a result of higher cohesive forces between Bi clusters than adhesion force between Bi and the substrate. Both samples have almost the same diffraction pattern except for the intensities of some rings [5] which indicated no structural phase transition occurred during annealing, Fig. 7.1.

7.3. Results

Bi islands and nanoclusters were excited with 1.9 mJ/cm² and 2.4 mJ/cm² pump pulses at room temperature. The results presented in Fig.7.2 and Fig.7.3 are collected from Bi islands and correspond to (012) and (110) planes respectively and Fig. 7.4 and Fig. 7.5 shows the data collected from Bi nanoclusters for the same planes. We fitted the data presented in Fig. 7.2 - 5 to a single exponential decay function,

$$\frac{I(t)}{I_0} = \begin{cases} \sim 1 & t \leq 0 \\ A + B \times e^{-\Delta t/\tau} & t > 0 \end{cases} \quad 7.1$$

where, A and B are the fitting parameters and τ is the decay time.

The different values for A , B and τ for $S1$ and $S2$ are summarized in Table 7.1. The value of $I(t)/I_0 = 1.00 \pm 0.02$ at $t < 0$ is calculated after taking the average of the different values from Figs. 7.2-5. The error analysis in τ written in Table 7.1 is the standard deviation calculated from the different decay times mentioned in this chapter as well as the values in Appendices J and K.

In general, I noticed the following,

(a) The thermalization time of Bi along $\langle 012 \rangle$ direction is higher than that along $\langle 110 \rangle$ direction.

(b) The thermalization time along $\langle 110 \rangle$ direction for $S1$ is less than that observed in $S2$.

(c) The fluence has no significant effect, as can be seen from data summary presented in Table 7.1, on the thermalization time of both samples as long as the excitation level is below the threshold that can cause an appreciable melting of Bi or damage to the sample [16].

(d) At a high level of excitation, Fig. 7.6 (a) - (b), the transient time has reduced significantly which is the same behavior that was seen recently by Sciani et al. [16]. Due to the limited resolution of our system, we could not measure sub-picosecond transient time as they did, but the same mechanism can still hold here where the non-thermal effect plays a significant role in the lattice disorder, as will be explained in section 7.4.

(e) Additionally, the temperature rise of the lattice was calculated from Eq. 5.4 for Bi nanoclusters and islands and the results are summarized in Table 7.1. From Table 7.1 it is clear that the temperature rise in Bi islands is higher than that for Bi nanoclusters at the same excitation level due to the higher coverage of Bi islands to the substrate when compared to that of nanoclusters, which means a higher amount of the incident fluence is absorbed in the islands (8%) than that absorbed in the nanoclusters (7%). Although there is no data collected for Bi nanoclusters at 1.5 mJ/cm^2 , the temperature rise was included in Table 7.1 just for the sake of comparison to the temperature rise of Bi islands. Additionally it is worth noting that, at 2.4 mJ/cm^2 , the temperature rise for nanoclusters is 257 K, i.e. lattice temperature = 557 K, which is higher than the melting temperature of Bi nanoclusters measured from cw data presented in chapter 5. This suggests a superheating of Bi nanoclusters of about 32 K. The preliminary observation of Bi nanocluster superheating observed here requires an extensive study at different laser excitation while the sample is held at some base temperature to be confirmed. The same argument holds for Bi islands which show a higher degree of superheating than that observed for nanoclusters at the same fluence, Table 7.1.

Table 7.1 Summary of temperature rise calculation from Eq. 5.4 per incident laser fluence.

Incident laser fluence (mJ/cm ²)	Temperature rise, ΔT (K)	
	Nanoclusters	Islands
1.5	153	174
1.9	201	228
2.4	257	295

(f) Also, I want to stress again that the fitting of the time-resolved data collected for the strain and FWHM did not fit properly to an exponential function similar to that used for the normalized peak intensity, but it is a moving average fitting just to guide the eye of the reader and to show the general behavior of the different peaks with the laser fluence. Additionally, the error bars were not introduced here due to the fact that, the physical properties of the grown samples is highly affected by thermal history of the sample as discussed in chapter I and V, but the behavior of these properties is the same, i.e., during all runs, $\Delta d/d$ for Bi nanoclusters, starts to contract over a time period t , 6 ± 1 ps $> t > 0 \pm 1$ ps; afterwards, it expands over ~ 20 ps followed by another contraction which is related to the more stable state of the lattice, and it corresponds to the restoring force between the atoms that comes into effect after the lattice reaches its maximum expansion. Therefore, I am confident in saying that the oscillatory behavior of $\Delta d/d$ at $t < 0$ and/or $t > 25$ ps is not an intrinsic behavior of the lattice and may result from the uncertainty in the measured data, which may arise from the fluctuations in the femtosecond laser, system stability or any extraneous behavior of the long time operation of the electron gun.

(g) From the previous discussion, I concluded that the Sigmaplot software cannot be used to estimate the thermalization time of the lattice from the time resolved data of

the lattice strain and normalized FWHM due to the limited number of the built-in functions that can be used to fit such irregular behavior in the lattice strain. Forcing the fitting to the exponential or Sigmoidal functions lead to unrealistic behavior and therefore we could not extract any useful information about the decay constant of the lattice; see for example Fig. 7.11.

Table 7.2 Summary of the fitting parameters used in equation 7.1. The error in fluence measurements was found not to exceed 5% of the measured value.

		<i>A</i>	<i>B</i>	$\tau(\text{ps})$
<i>S1 (012)</i>	1.5 mJ/cm ²	0.736	0.26	11.2± 2.2
	1.9 mJ/cm ²	0.74	0.29	7.1 ± 2.2
	2.4 mJ/cm ²	0.66	0.35	6.3 ± 2.2
	3.3 mJ/cm ²	0.447	0.533	4.1± 2.2
<i>S1 (110)</i>	1.5 mJ/cm ²	0.737	0.266	4.3± 0.7
	1.9 mJ/cm ²	0.78	0.23	2.9 ± 0.7
	2.4 mJ/cm ²	0.71	0.31	2.9 ± 0.7
	3.3 mJ/cm ²	0.414	0.568	3.1± 0.7
<i>S2 (012)</i>	1.9 mJ/cm ²	0.82	0.18	11.8 ± 1.1
	2.4 mJ/cm ²	0.73	0.27	9.7 ± 1.1
<i>S2 (110)</i>	1.9 mJ/cm ²	0.79	0.19	6.5 ± 1.0
	2.4 mJ/cm ²	0.71	0.27	7.7 ± 1.0

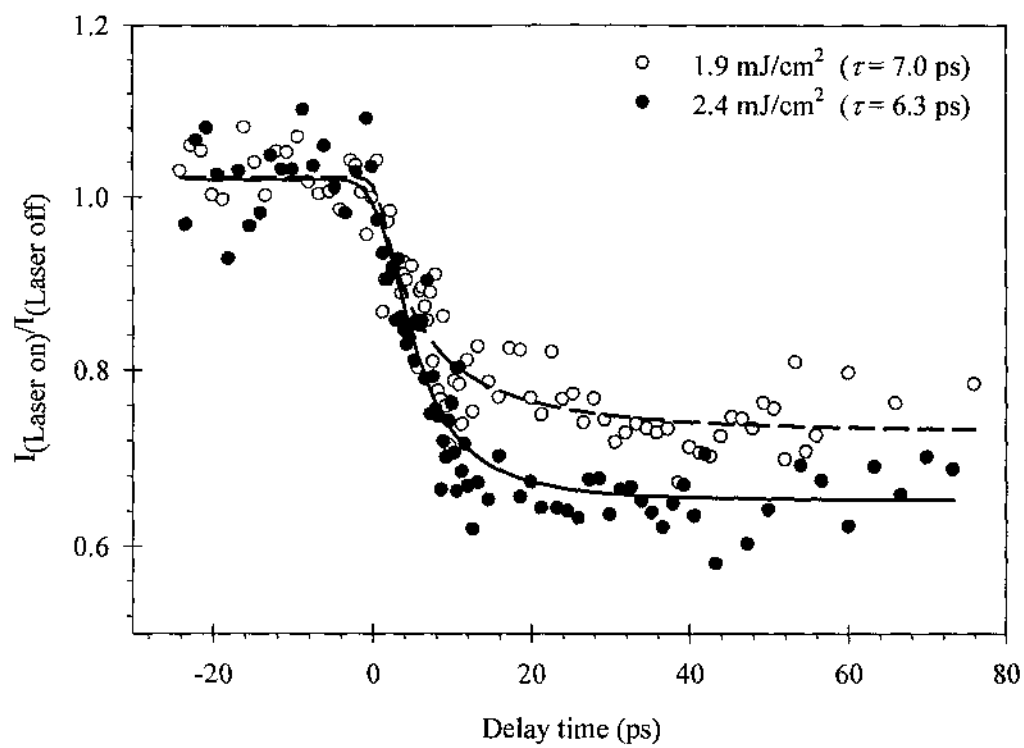


Fig. 7.2. Time dependent normalized intensity of Bragg peak (012) of photoexcited Bi islands by laser fluence 1.9 mJ/cm^2 and 2.4 mJ/cm^2 .

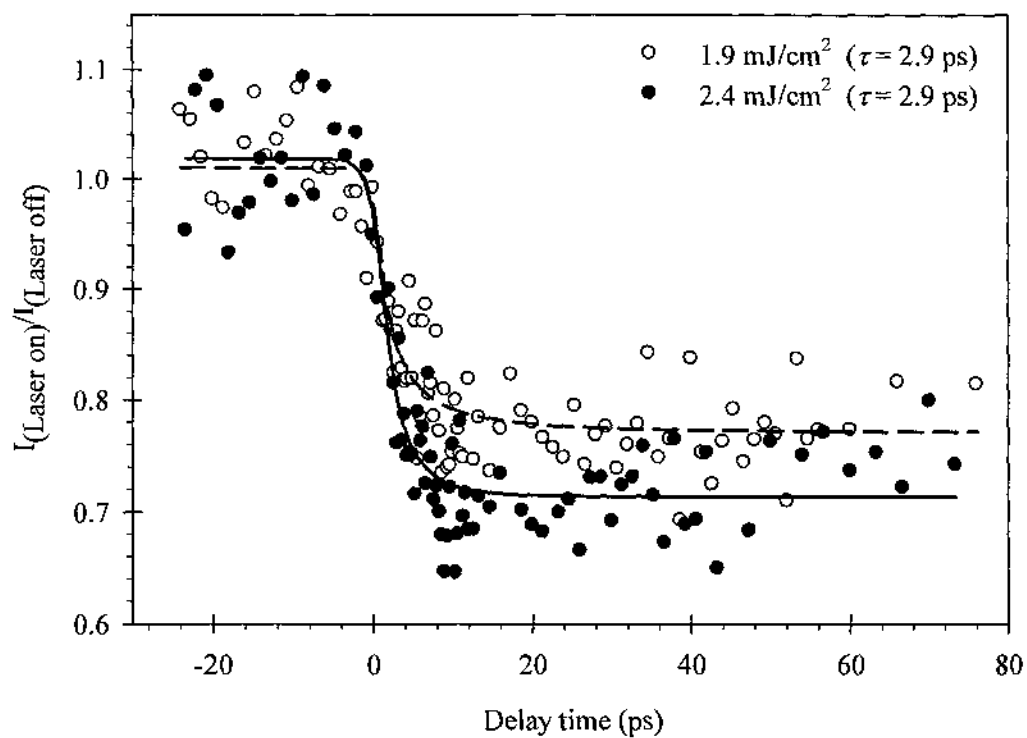


Fig. 7.3. Time dependent normalized intensity of Bragg peak (110) of photoexcited Bi islands by laser fluence of 1.9 mJ/cm² and 2.4 mJ/cm².

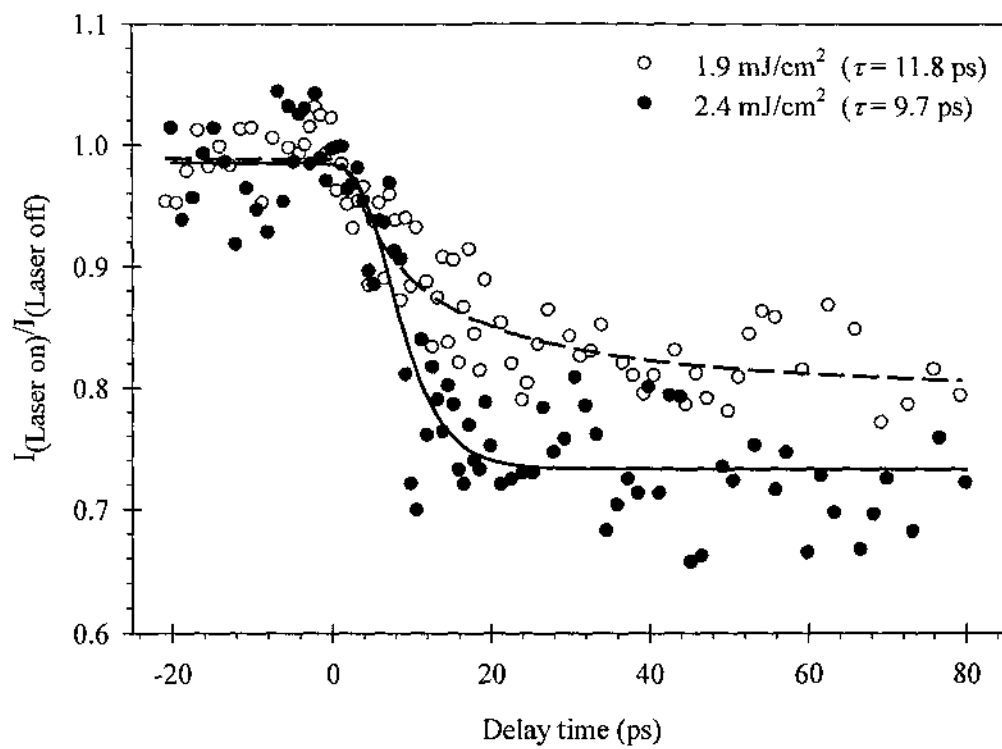


Fig. 7.4. Time dependent normalized intensity of Bragg peak (012) of photoexcited Bi nanoclusters by laser fluence of 1.9 mJ/cm^2 and 2.4 mJ/cm^2 .

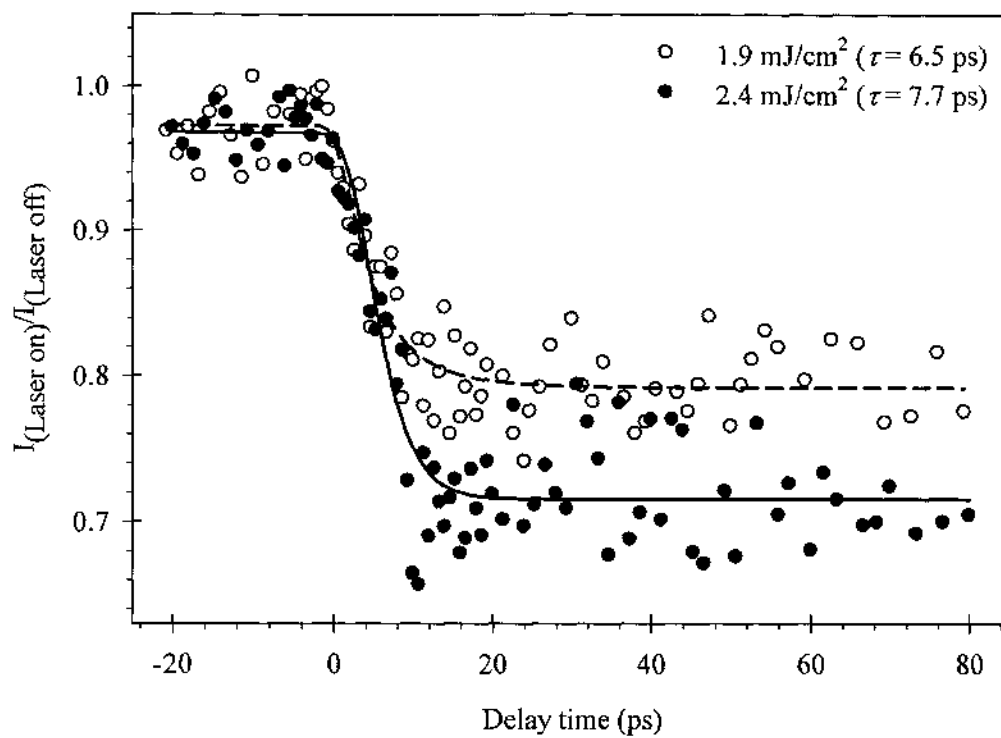


Fig. 7.5. Time dependent normalized intensity of Bragg peak (110) of photoexcited Bi nanoclusters by laser fluence of 1.9 mJ/cm^2 and 2.4 mJ/cm^2 .

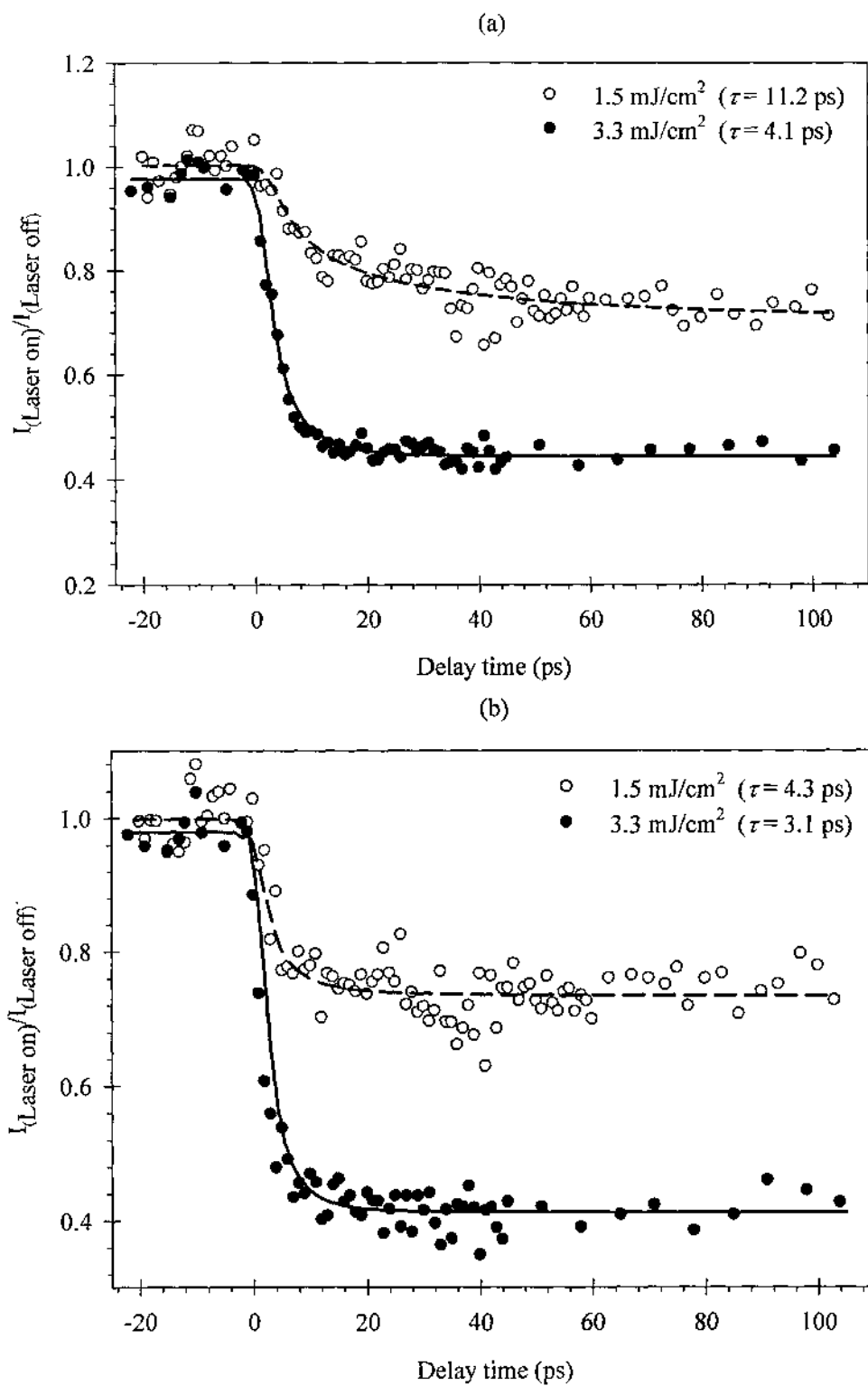


Fig. 7.6. Time evolution of Bragg peak intensity for (a) (012) planes, (b) (110) planes at two different fluences.

Another set of data was collected from Bi nanoclusters and shown in Fig. 7.7 - 10. These includes the relative change in Bragg peak position, $\Delta d/d$, normalized change in FWHM with delay time. It is worth to mention that, although the change in $\Delta d/d$ for Bi nanoclusters is clear and detectable, I didn't detect any change in $\Delta d/d$ for Bi islands, which need an extensive study and better understanding of the impact of Bi island shape and size on the different excitation and relaxation processes induced by ultrashort laser pulses.

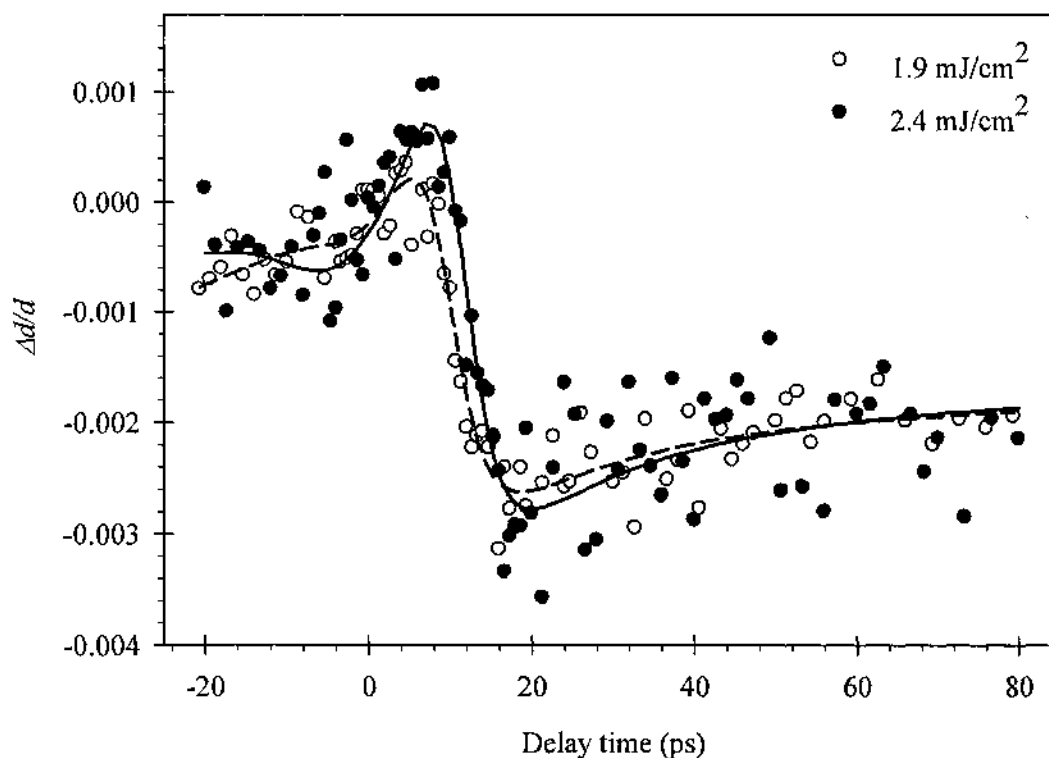


Fig. 7.7. Relative change in Bragg peak position ($\Delta d/d$) as a function of delay time for Bragg peak (012) of photoexcited Bi nanoclusters by laser fluence of 1.9 mJ/cm² and 2.4 mJ/cm².

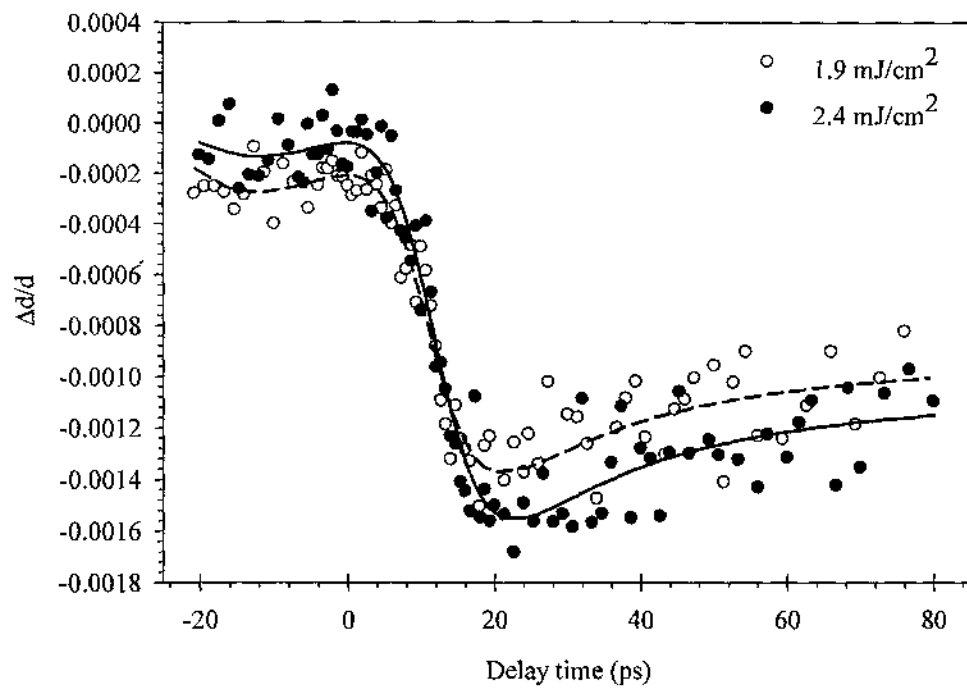


Fig. 7.8. Relative change in Bragg peak position ($\Delta d/d$) as a function of delay time for Bragg peak (110) of photoexcited Bi nanoclusters by laser fluence of 1.9 mJ/cm^2 and 2.4 mJ/cm^2 .

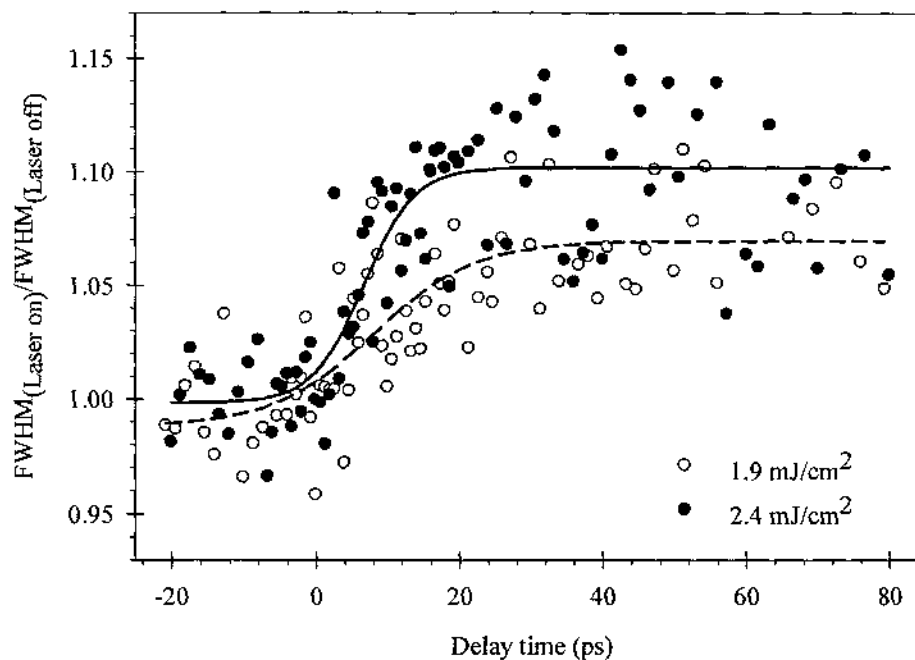


Fig. 7.9. Relative change in Bragg peak FWHM as a function of delay time of photoexcited Bi nanoclusters by laser fluence of 1.9 mJ/cm^2 and 2.4 mJ/cm^2 for (012) Bragg peak.

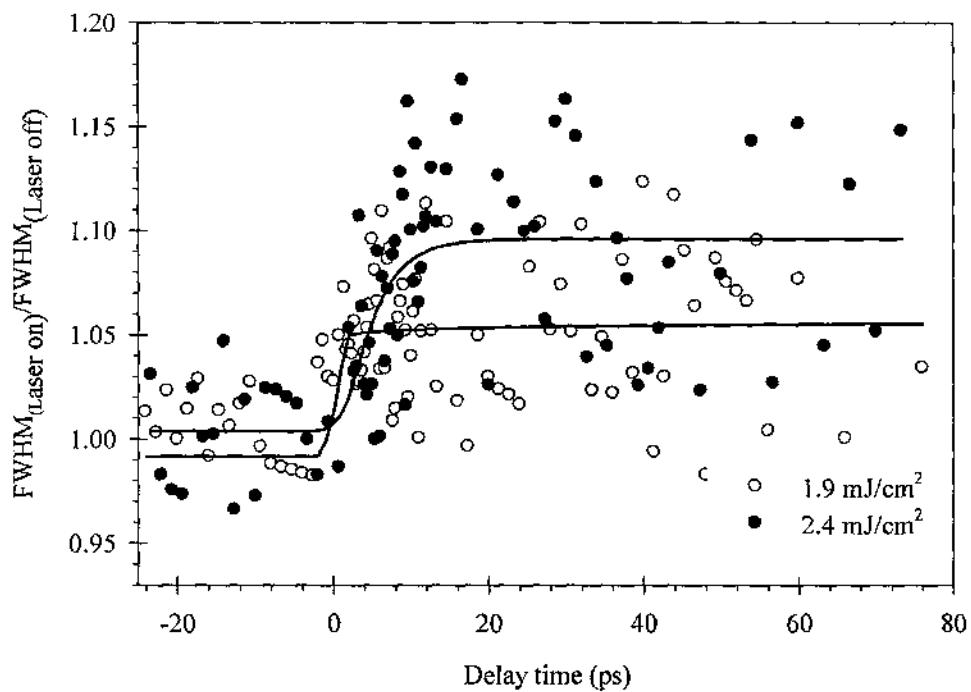


Fig. 7.10. Percentage change in Bragg peak FWHM as a function of delay time of photoexcited Bi islands by laser fluence of 1.9 mJ/cm^2 and 2.4 mJ/cm^2 for (012) Bragg peak.

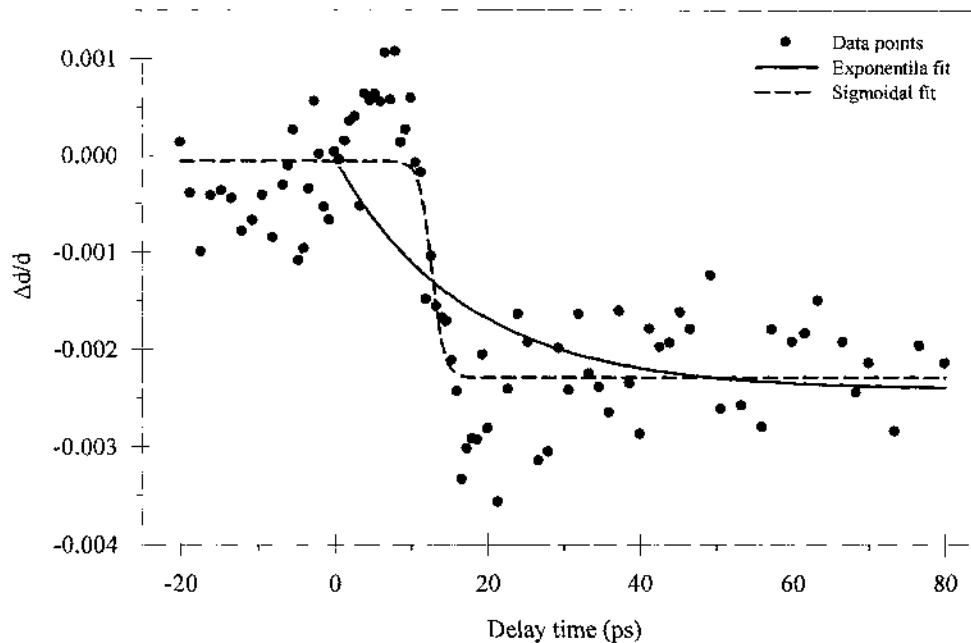


Fig. 7.11. Sample graph that shows the poor fitting of the exponential and Sigmoidal functions which therefore cannot be used to calculate the lattice thermalization time. A proper model is needed to fit properly such behavior.

7.4. Discussion

The semimetallic nature of bulk Bi arises from the 38 meV overlap between the L-point conduction and T-point valence band [6]. This semimetallic behavior of bulk Bi makes it a poor thermoelectric material due to the substantial bipolar contribution from both electrons and holes to the overall Seebeck coefficient which reduces the electronic thermal conductivity [7]. Seebeck effect refers to a phenomenon in which an electric current will flow when two dissimilar metals are connected in series and held at different temperatures, and vice versa.

However, the contribution to the Seebeck coefficient from the holes can be diminished by increasing the band gap between the conduction and valence bands. The band gap can be altered or completely removed, by reducing the size of the bulk material to the nanoscale. Bi nanowires and thin films can shift the conduction and valence band

edges away from each other and forcing semimetal-semiconductor (SM-SC) transition. A previous study [9] predicted a SM-SC transition at 77 K in 49 nm thick Bi wires grown along <012> and at room temperature for 16 nm thick wires. Additionally, the reduced dimensionality creates energy sub-bands with separation “ Δ' ” that’s inversely proportional to the square of the cluster diameter “ D^2 ” and electronic effective mass “ m^* ” according to; [7]

$$\Delta' = \frac{\pi^2 \times \hbar^2}{m^* \times D^2} \quad 7.2$$

where \hbar is Planck’s constant divided by (2π) .

Therefore the electron effective mass as well as the cluster size has direct impact on the conduction-valence band separation. As the cluster size goes beyond a critical value, a gap is formed between the conduction and the valence bands, and the overlap no longer exists, forcing the SM-SC transition, Fig.7.12.

The data reported here can give a qualitative picture of the SM-SC transition, or at least a modification in the electronic band structure as a result of reducing the dimensions, in Bi nanoclusters with the help of THEED setup due to its sensitivity to monitor different excitation and thermalization processes induced by femtosecond laser pulses. Femtosecond photoexcitation was explained in terms of the two temperature model (TTM) [10,11]. In the TTM, the laser induced heating in opaque materials is a two step process, *first* the electron gas, due to its low heat capacity compared to that of the lattice, absorbs the incident photon energy over a sub picoseconds time frame.

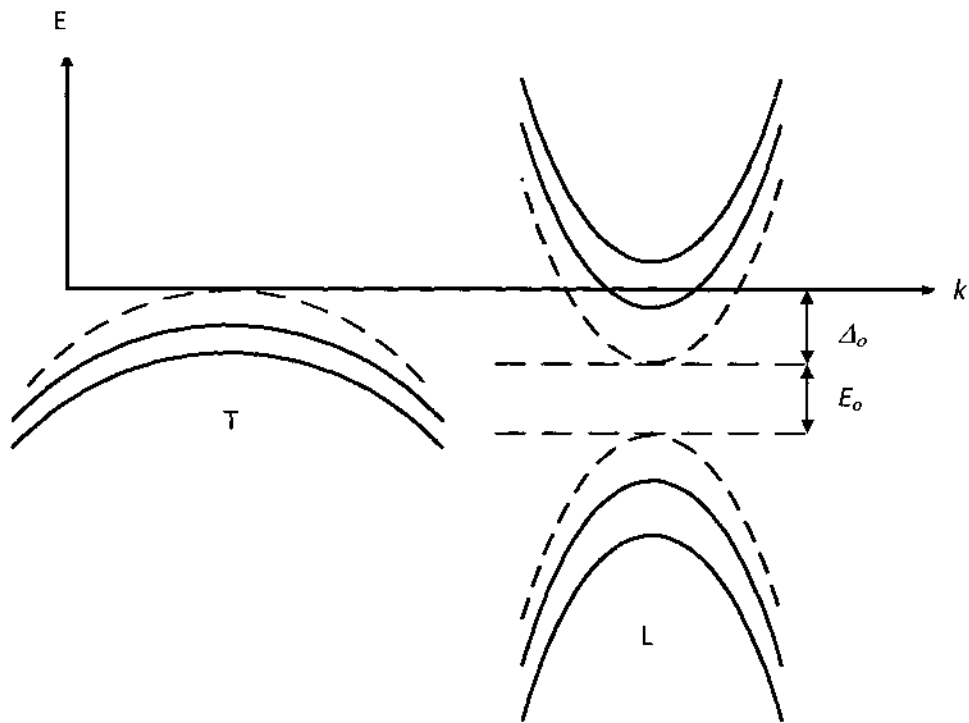


Fig. 7.12. Schematic diagram showing the electronic band structure of bulk Bi (dashed lines) compared to that of the nanowires/nanoclusters (solid lines). Reproduced from Ref. [9]. Δ_0 is the conduction-valence band overlap.

During this process, the electron temperature can shoot up to few hundreds-thousands of degrees while the lattice is still undisturbed. This process is followed by a process through which the electron gas re-establishes its Fermi-Dirac distribution in sub to few picoseconds (electron thermalization time). *Second*, electron-phonon collision is another process that takes the lattice out of its equilibrium followed by equilibration of the whole system over a few picoseconds that can be modeled by Bose distribution.

In SCs, as mentioned in detail in chapter 4, many processes are considered and contribute to charge carrier removal and consequently its density reduction. These processes are, but are not limited to, electron-hole recombination and/or diffusion into

deeper region in the sample and leaving the area of excitation. The diffusion is eliminated in our study since we are dealing with nanoclusters.

Electron - hole recombination may be radiative or non radiative in nature. In radiative processes, opposite to excitation, a photon is emitted which carries the excess carrier energy. In non radiative recombination processes which include Auger recombination, an electron recombines with a hole, and the excess energy will be carried out by another electron and excited to a higher energy level.

Thermal and structural effects come into the picture when the charge carrier and the lattice are in thermal equilibrium and the final lattice temperature is determined by the initial energy deposited by the ultrashort laser pulses into the sample. Melting or vaporization can occur if the lattice temperature exceeds the lattice melting or boiling temperature, respectively. In some cases, the material preserved its solid integrity at temperatures above its melting point, and in this case the lattice is said to be superheated. Auger heating is another significant mechanism that can increase the carrier relaxation time and consequently slows down the dynamics of carrier relaxation [12].

In the well known Auger process, the total energy of the electron-hole pair does not change, while in Auger heating, it does change. This process is not significant in bulk SC [13,14], while in SC nanoclusters it is very efficient due to quantum size effects on the electronic band structure. Therefore, according to the previous discussion we can conclude that, THEED setup can detect the anisotropic nature of the electronic properties of different planes in Bi nanoclusters. Some surfaces in Bi, (110), have metallic nature due to the bond nature along (110). While other surfaces, (012), shows the formation of

subbands upon cluster size reduction which will in turn lead to the increased lattice thermalization time.

7.5. Conclusions

The data presented here shows an observable increase in lattice thermalization time of S2 compared to that of S1. This can be attributed to the modification of the electronic band structure of the lattice as a result of SM-SC transition in S2 as a result of modification in the cluster size and shape during femtosecond laser annealing while raising the temperature of the as-deposited sample to about 470 K.

Additionally, we notice that, in general, the thermalization time of the surfaces oriented along $\langle 012 \rangle$ is higher than that of those oriented along $\langle 110 \rangle$ which reflects the anisotropic nature of the electronic band structure of Bi nanoclusters. Also, the Auger heating mechanism should be considered as an important factor that increases the relaxation time (50 ps in 2nm CdSe nanowire [15]).

The lattice thermalization time of the lattice could not be extracted from the time-resolved study of the lattice strain or FWHM of the Bragg peaks because the data did not fit properly to an exponential function similar to that used for the normalized intensity data and due to lack of the software used to provide a proper functions for fitting these data.

7.6. References of Chapter 7

- [1] R. E. Peierls, "More surprises in theoretical physics," Princeton University Press, 24-26 (1991).
- [2] S. Agergaard, Ch. Søndergaard, H. Li, M. B. Nielsen, S. V. Hoffmann, Z. Li and Ph. Hofmann, "The effect of reduced dimensionality on a semimetal: the electronic structure of the Bi(110) surface," *New Journal of Physics* 3, 15.1-15.10 (2001).
- [3] A. B. Shick, J. B. Ketterson, D. L. Novikov, A. J. Freeman "Electronic structure, phase stability, and semimetal-semiconductor transitions in Bi," *Phys. Rev. B* 60, 15484-15487 (1999).
- [4] F. Jona, "Low energy electron diffraction of surfaces of antimony and bismuth," *Surf. Sci.* 8, 57-67 (1967).
- [5] A. Esmail, M. Abdel-Fattah, and H. Elsayed-Ali, "Observation of lattice contraction with heating of bismuth nanoclusters near its melting point," (Accepted at *J. Appl. Phys.* (2011)
- [6] C. F. Gallo, b. B. S. Chandrasekhar, and P. H. Sutter, "Transport Properties of Bismuth Single Crystals," *J. App. Phys.* 34, 144-152 (1963).
- [7] S. B. Cronin, Yu-Ming Lin, O. Rabin, M. R. Black, G. Dresselhaus and M. S. Dresselhaus, "Thermoelectric transport properties of individual bismuth nanowires," in *Thermoelectric Materials 2001 - Research and Applications: MRS Symposium Proceedings*, edited by G. S. Nolas, D. C. Johnson, and D. G. Mandus, Materials Research Society Press, Boston, MA, December 2001.
- [8] H.J. Goldsmid, "Thermoelectric refrigeration," Plenum Press, New York, 1964.

- [9] M. R. Black, "The optical properties of bismuth nanowires," Ph.D. thesis, Department of Electrical Engineering and Computer Science - Massachusetts Institute of Technology, P. 39 (2003)
- [10] S. I. Anisimov, B. L. Kapeliovich, and T. L. Perelman, "Electron emission from metal surfaces exposed to ultrashort laser pulses," *Sov. Phys. JETP* 39, 375-378 (1974).
- [11] B. Rethfeld, A. Kaiser, M. Vicanek and G. Simon, "Ultrafast dynamics of nonequilibrium electrons in metals under femtosecond laser irradiation," *Phys. Rev.B*, 65, 214303 (1-11) (2002).
- [12] M. Achermann, A. P. Bartko, J. A. Hollingsworth AND V. I. Klimov, "The effect of Auger heating on intraband carrier relaxation in semiconductor quantum rods," *Nature Physics* 2, 557-561 (2006).
- [13] M. C. Downer and C. V. Shank, "Ultrafast heating of silicon on sapphire by femtosecond optical pulses," *Phys. Rev. Lett.* 56, 761-764 (1986).
- [14] P. Borri, S. Ceccherini, M. Gurioli, and F. Bogani, "Auger heating of carriers in GaAs/AlAs heterostructures," *Solid State Commun.* 103, 77-81(1997).
- [15] V. I. Klimov, A. A. Mikhailovsky, D. W. McBranch, C. A. Leatherdale, and M. G. Bawendi, "Quantization of multiparticle Auger rates in semiconductor quantum dots," *Science* 287, 1011-1013 (2000).
- [16] G. Sciaini, M. Harb, S. Kruglik, T Payer, C. Hebeisen, F. Heringdorf, M. Yamaguchi, M. Hoegen, R. Ernstorfer and R. J. Dwayne Miller, "Electronic acceleration of atomic motions and disordering in bismuth," *Nature* 458, 56-60 (2009).

CHAPTER 8

SUMMARY AND CONCLUSIONS

In summary, the framework of this thesis has two main tasks; the first is to build a high energy electron diffraction experiment that is capable of delivering highly energetic and very short electron pulses that will be used in the second task, which is studying in real time the excitation of Bi nanoclusters and Bi islands by ultrashort laser pulses using a pump probe technique. Another task was done during this thesis, which helped in giving more insight into the thermal melting of Bi nanoclusters using a conventional heating method.

The Bi sample was prepared by thermal evaporation in a vacuum at room temperature and transported in a vacuum system that is part of the pump-probe setup for further processing and analysis. We noticed with TEM images that the as-deposited sample is noncontinuous film, which suggests the island growth mechanism of Bi increases in size as the thickness increases. The Bi islands were obtained either by raising the temperature of the as-deposited film up to 525 ± 6 K or by exposing it to a femtosecond laser pulses of moderate energy density ($0.9 \text{ mJ/cm}^2 - 2.4 \text{ mJ/cm}^2$). The nanoclusters were obtained after exposing the as-deposited samples to a femtosecond laser pulses of energy density $0.9 \text{ mJ/cm}^2 - 2.4 \text{ mJ/cm}^2$, simultaneously while raising the temperature of the sample with a heating stage with a rate of $\sim 3 \text{ K.s}^{-1}$ up to $\sim 450 - 470$ K. This method produced Bi nanoclusters of average size $\sim 13 - 16$ nm. Exposing the sample to that range of fluence did not affect the crystal structure of the grown sample, but it enhanced the ring intensity of some peaks and dimmed the others, which was

explained previously in terms of the reorientation of the different planes within the grains of the grown sample.

The detected diffraction ring pattern is identified and we found that these rings are in very good agreement with the published ones and confirmed the hexagonal structure of the Bi film, nanoclusters, and islands.

We studied the Bi nanoclusters first by monitoring the ring pattern intensity, relative change in position and FWHM while raising its temperature from room temperature up to 525 K. We found the following reasonable conclusions;

- The onset of the melting of the Bi nanoclusters was $T \sim 500 \pm 6$ K, as measured by the reduction of the nanocluster size through the formation of a liquid shell detected by the width of the diffraction rings.
- The melting temperature of Bi nanoclusters was measured to be $\sim 525 \pm 6$ K and less than that of the bulk ($T_B = 544$ K), as expected and reported in previous studies, where the melting temperature is inversely proportional to the average cluster diameter. This was attributed to the reduced dimensionality of the Bi nanoclusters and its increase in surface to volume ratio, which increases the stress and speeds up the melting process.
- The Debye temperature of the annealed nanoclusters was found to be 53 ± 6 K along the (012) direction and 86 ± 9 K along (110) direction. At $T = 464 \pm 6$ K, the diffraction intensity started to deviate from Debye-Waller behavior due to increased lattice anharmonicity.
- The thermal expansion coefficient of the Bi (012) and (110) planes is positive up to $\sim 499 \pm 11$. However, the expansion coefficient of the Bi (012) planes showed

a transition from a positive to a negative value that occurs over the temperature range $T_c \sim 499 \pm 11$ to 511 ± 8 K. For the Bi (110) planes, the thermal expansion coefficient is positive up to their melting point, which is 525 ± 6 K. This behavior can be explained in terms of vibrational (phonon excitation) and/or non-vibrational (lattice potential deformation) effects on the lattice near melting [1].

- The study of the FWHM of the diffraction rings as a function of temperature confirmed the formation of a liquid shell of Bi at the onset of solid-liquid transformation. This shell includes Bi atoms in the liquid phase, detached atoms with high vibrational amplitude and vacancies.

The time-resolved ultrafast electron diffraction experiment was performed on Bi nanoclusters and islands to study in real time the structure dynamics of photoexcited Bi with femtosecond laser pulses. The structural dynamics evolution as a function of time is obtained by following the diffraction ring intensity drop, position and FWHM of two different set of planes, namely (012) and (110).

The first allowed us to monitor the structure change in a direction with Miller index $l \neq 0$ while the latter has orientation with $l = 0$, i.e., with (012) orientation, we can monitor the lattice response due to the excitation of optical phonon A_{1g} effects on the lattice potential, while for (110) we could not detect these effects [2]. Since the system resolution is not high enough to monitor the oscillation period or amplitude of A_{1g} mode but we can detect the consequences of its relaxation on the lattice potential through the measurements of the three parameters mentioned earlier.

The time-dependent intensity change of the ring pattern can be interpreted in terms of the increased lattice disorder due to ultrashort laser pulses (Debye-Waller effect) and can be used to estimate the temporal evolution of the lattice temperature.

In general, the fitting applied to the intensity-time curve showed that the relaxation time of the lattice in $\langle 012 \rangle$ direction is different from that along $\langle 110 \rangle$ direction. This is attributed to the anisotropy in the electronic band structure of Bi, and the splitting of the energy bands along $\langle 012 \rangle$ direction [3]. Additionally, lattice thermalization time of Bi nanoclusters is higher than that for Bi islands. This was explained in terms of a possible semimetal - semiconductor phase transition as a result of the reduced dimensionality of the Bi nanoclusters compared to that of Bi islands. The surface tension (pressure) of the surface atoms can displace one of the atoms along the body diagonal which in turn modify the band structure of the lattice and enhances the transition of Bi to a semiconducting material with indirect band gap.

The relaxation time represents the time needed for the lattice to become in equilibrium and follow Bose-Einstein distribution and generally used to give some information and interpret the thermalization processes that may include but not limited to Auger recombination (non-radiative), radiative recombination and surface and defect recombination. The temporal evolution of Bragg peak position showed that the behavior of the lattice along $\langle 012 \rangle$ direction is different (contraction) from that along $\langle 110 \rangle$ direction (expansion) over the first 6 ps of lattice excitation. We attributed this to the lattice potential disturbance as a result of the excitation of the A_{1g} phonons which are symmetric and of displacive nature.

The thermal effects of photoexcited Bi nanoclusters was also detected in the FWHM of the Bragg peaks with time as an increase in FWHM at $t > 0$ ps. This is due to the formation of thin liquid layer, which grows in thickness with time (lattice temperature increase). Change in the lattice strain and excitation of longitudinal acoustic phonons may also contribute to the increase in the FWHM of the ring pattern [4].

Finally, the lattice temperature evolution following the femtosecond laser excitation was calculated from the time evolution of the Bragg peak intensity and with the help of the Debye-Waller equation. We were able to measure a change in lattice temperature, 154 ± 9 K above room temperature, which corresponds to a final lattice temperature $T = 454$ K. This temperature is less than the melting temperature of Bi nanoclusters measured from static heating measurements, $T_{m(\text{nanoclusters})} = 525$ K. This is attributed to the low Debye temperature that was calculated in Ch.5.

Therefore, we have succeeded in building a time resolved high energy electron diffraction system capable of studying lattice structural evolution of photoexcited Bi nanoclusters with resolution that is better than 3 ps.

The system resolution can be improved by introducing the following modifications:

- 1- Moving the electron gun closer to the sample $\sim 1''$ to reduce the space charge effects which have a direct impact on the electron pulse broadening which in turn will improve the system resolution.
- 2- Placing the electromagnet inside the vacuum chamber in the space between the sample and the electron gun.
- 3- Additionally, a detailed study on the possible superheating of Bi nanoclusters is needed.

- 4- A detailed study of time evolution of Bi islands strain ($\Delta d/d$) is needed.
- 5- Effect of thermal history as well as the effect of annealing method, static versus laser, on the sample physical properties is also required.
- 6- A theoretical model is required to describe the time-resolved strain behavior of the nanoclusters and islands, from which the thermalization time can be extracted.

8.1. References of Chapter 8

- [1] G. Barrera, J. Bruno, T. Barron, and N. L. Allan, "Negative thermal expansion," *J. Phys.: Cond. Matter.* 17, R217-R252 (2005).
- [2] D. M. Fritz, D. A. Reis, B. Adams, R. A. Akre, J. Arthur, C. Blome, P. H. Bucksbaum, A. L. Cavalieri, S. Engemann, S. Fahy, R. W. Falcone, P. H. Fuoss, K. J. Gaffney, M. J. George, J. Hajdu, M. P. Hertlein, P. B. Hillyard, M. Horn-von Hoegen, M. Kammler, J. Kaspar, R. Kienberger, P. Krejcik, S. H. Lee, A. M. Lindenberg, B. McFarland, D. Meyer, T. Montagne, É D. Murray, A. J. Nelson, M. Nicoul, R. Pahl, J. Rudati, H. Schlarb, D. P. Siddons, K. Sokolowski-Tinten, Th Tschentscher, D. von der Linde, and J. B. Hastings,, "Ultrafast bond softening in bismuth: Mapping a solid's interatomic potential with X-rays," *Science* 315, 633-636 (2007).
- [3] T. K. Cheng, "The excitation and dynamics of coherent lattice vibrations in semimetals and narrow band-gap semiconductors," Ph.D. thesis, Dept of electrical engineering and computer science, Massachusetts Institute of Technology (1994).
- [4] A. Rouse, C. Rischel, and J. Gauthier, "Colloquium: Femtosecond X-ray crystallography," *Rev. Mod. Phys.* 73, 17-31 (2001).

APPENDIX A

CHARACTERIZATION OF THE ELECTRON PULSE

The photoelectrons (probe beam FWHM) which are generated from the PAEG play a crucial role in time-resolved high energy electron diffraction experiments, with which the resolution of the system is determined. There are many factors that affect the probe beam broadening and consequently the system resolution, these factors are;

1. Biasing potential (V_0), (electron energy), the higher the value of V_0 , the smaller the FWHM of the probe beam.
2. Acceleration region length (d), the distance between the cathode and the anode, again smaller d gives smaller FWHM of the probe beam.
3. Drift region, L , the distance from the anode to the samples, this distance is the main contribution to the pulse broadening and should be as small as possible.
4. Other factors that contribute to the pulse broadening are the initial energy spread of the photoelectrons and trajectory differences in the drift region.

Therefore, it is very important for us to estimate the resolution of our system based on our PAEG design. The PAEG schematic is shown in Fig. A.1 with the following operating conditions;

1. Acceleration potential = 35 kV, although the electron gun can operate at 45 kV, we decided to lower the operating voltage of the electron gun to reduce arcing and glow discharge.
2. $d \sim 3.5$ mm
3. $L = 20.3$ cm
4. Pinhole Dia. = 150 μm

5. Nickel mesh of 1000 mesh/in².

We have used Faraday cup and lock-in amplifier to measure the number of electrons/pulse that are falling on the sample and from which we were able to estimate the probe pulse FWHM at the sample.

Measurement 1

We set the UV intensity to certain value which give the same diffraction pattern of the same intensity to a previously captured images and measured an electron current, $I = 0.6 \pm 0.1$ pA. This value gives ~ 3750 electrons/pulse, we used this value and Fig. A.2 to estimate the broadening of the probe pulse which was estimated to be below 500 fs. This is because, Fig. A.2 accounts for only two values for $N = 1000$ and 5000 electrons/pulse and the number of electrons we got is 3750 electron/pulse. Therefore, we can assume that, the FWHM at that level of number of electrons is better than 500 fs in the drift region.

Measurement 2

The same procedures were repeated at higher UV intensity and this gave a current $I = 0.9 \pm 0.1$ pA and the estimated electrons/pulse were ~ 5600 . From Fig. D.2 this value gives ~ 500 fs FWHM for the probe pulse in the drift region.

Measurement 3

The highest UV intensity gave $I = 2.4 \pm 0.1$ pA, and 15000 electrons/pulse. We could not use Fig. A.2 to estimate the probe beam pulse width, instead we used Ref. [2]. We had to calculate the travel time in the drift region of the electrons by considering the previously mentioned parameters of the PAEG. $V_o = 35$ kV, will accelerate the electrons to 1.1×10^8 m/s.

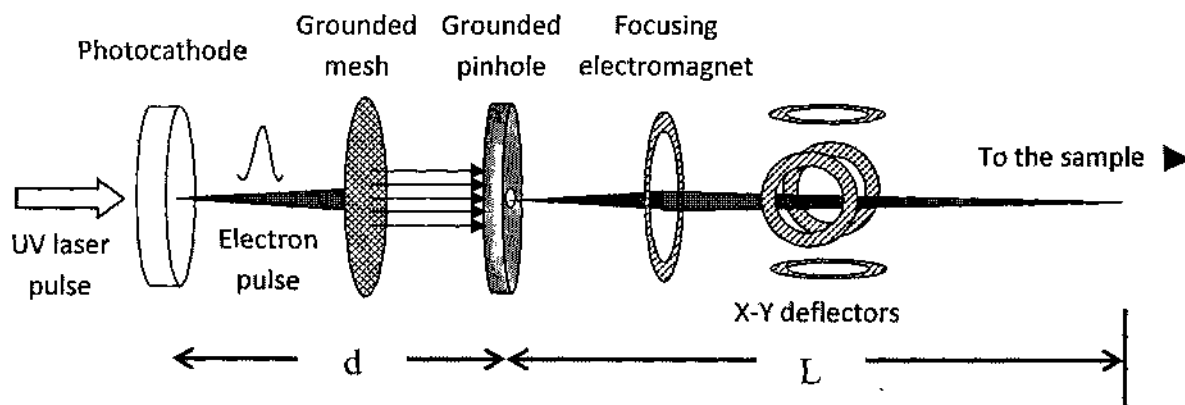


Fig. A.1. Schematic of the PAEG components.

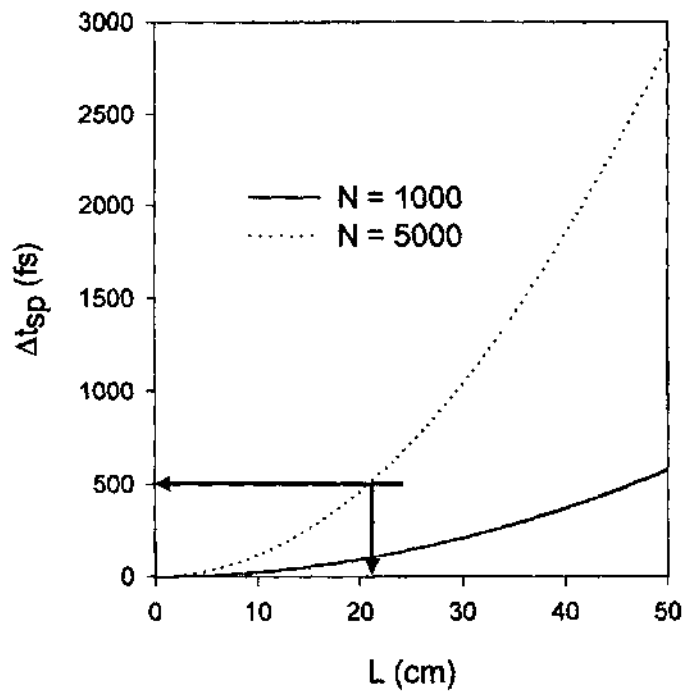


Fig. A.2. Effect of the drift region length on the electron pulse broadening for two cases in which number of electrons/pulse = 1000 electrons and 5000 electrons, reprinted from Ref. [1].

Since the drift region length = 0.2 m, therefore the total travel time for the electron in the drift region is $t = d/v = 0.2032/1.1 \times 10^8 = 1.8 \times 10^{-9}$ s = 1.8 ns, i.e., the electron needs 1.8 ns to travel from the anode to the sample. According to Fig. A.3, at 1.8 ns, the FWHM of the probe pulse is ~ 1 ps for Gaussian profile pulse and ~ 1.25 ps for flat head pulse at $N = 10,000$ e/pulse. Therefore, we expect our pulse at this UV level of intensity to be in the range of 1.5 ps since we are dealing with $N = 15,000$ e/pulse. Also, from Fig. A.3, for $N = 5,000$ e/pulse we have FWHM of 0.5 ps for Gaussian profile pulse and ~ 0.65 ps for flat head pulse which is consistent with our estimation in measurement 1 in accordance with Ref. [1].

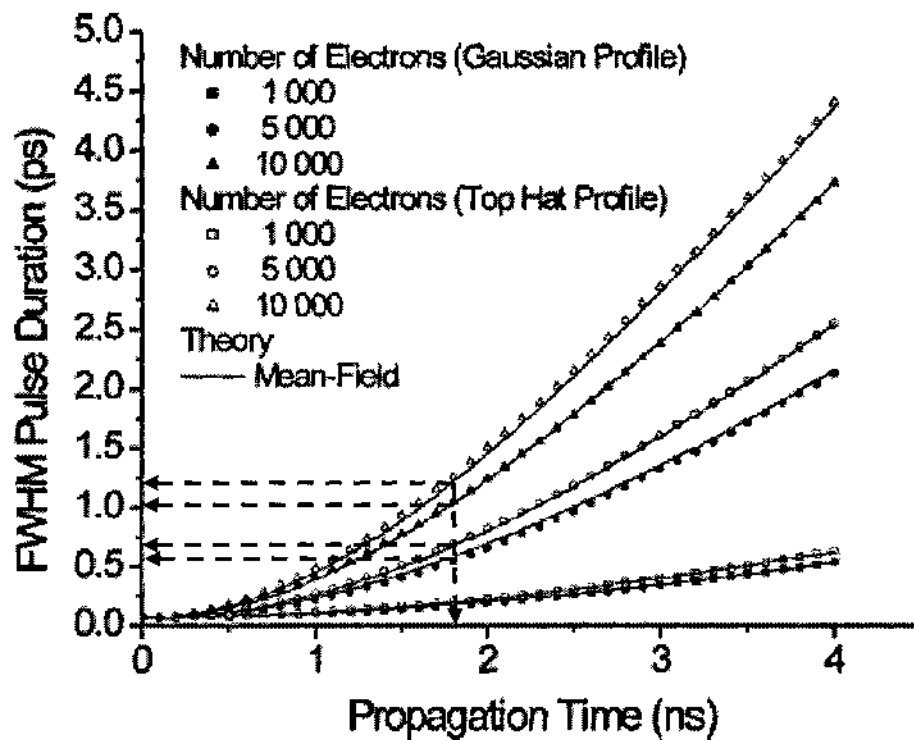


Fig. A.3. FWHM of the probe pulse vs propagation time in the drift region for Gaussian and “top hat” beams. Reprinted from Ref. [2].

References of Appendix A

1. Bao-Liang Qian and H. Elsayed-Ali, "Electron pulse broadening due to space charge effects in a photoelectron gun for electron diffraction and streak camera systems," *J. Appl. Phys.* 91, 462-468 (2002).
2. B. J. Siwick, J. R. Dwyer, R. E. Jordan, and R. J. D. Miller, "Ultrafast electron optics: Propagation dynamics of femtosecond electron packets," *J. Appl. Phys.* 92, 1643-1648 (2002).

APPENDIX B

EVAPORATOR AND PROCEDURES TO MAKE SAMPLES

B.1. System Components

The samples were prepared ex-situ in a six-way cross, eight-inch stainless steel chamber.

The chamber is equipped with the following,

- 1- Mechanical pump,
- 2- Turbo-molecular pump,
- 3- Crystal thickness monitor and controller,
- 4- Copper electrodes,
- 5- Tungsten filament and/or boats, and
- 6- Manual shutter

B.2. System Operation

- 1- Load the tungsten filament with Bi chunks and secure them with the copper electrodes inside the chamber.
- 2- Install the carbon-coated grids on the evaporation flange above the filament.
- 3- Secure the flange in place with a set of bolts and copper gasket and close the system and make sure that the valve is open.
- 4- Turn on the mechanical pump and after two minutes turn on the turbo pump.
- 5- Continuously check the pressure in the chamber by monitoring the reading of the Convector Gauge.
- 6- After two hours of operation, and if there is no leak in the system, the system is ready for evaporation.

- 7- Turn on the crystal thickness monitor controller and adjust the different sample parameters, such as sample density and the A-factor, these numbers are available in the operation manual of the crystal thickness controller.
- 8- Reset the controller.
- 9- Increase the current gradually and slowly through the filament and keep an eye on the controller monitor.
- 10- When the reading of the monitor starts to increase, stop increasing the current and wait till the required thickness is evaporated.
- 11- Turn off the current.
- 12- Wait about 15 minutes till the sample cools down.
- 13- Close the valve, turn off the turbo pump, and wait 5 minutes.
- 14- Open the vent valve of the turbo pump slowly.
- 15- When the turbo pump completely stops, turn off the mechanical pump.
- 16- Open the vacuum chamber by either opening the valve, or loosen the screws one after the other slowly.
- 17- Remove the samples and install them in the time-resolved system.

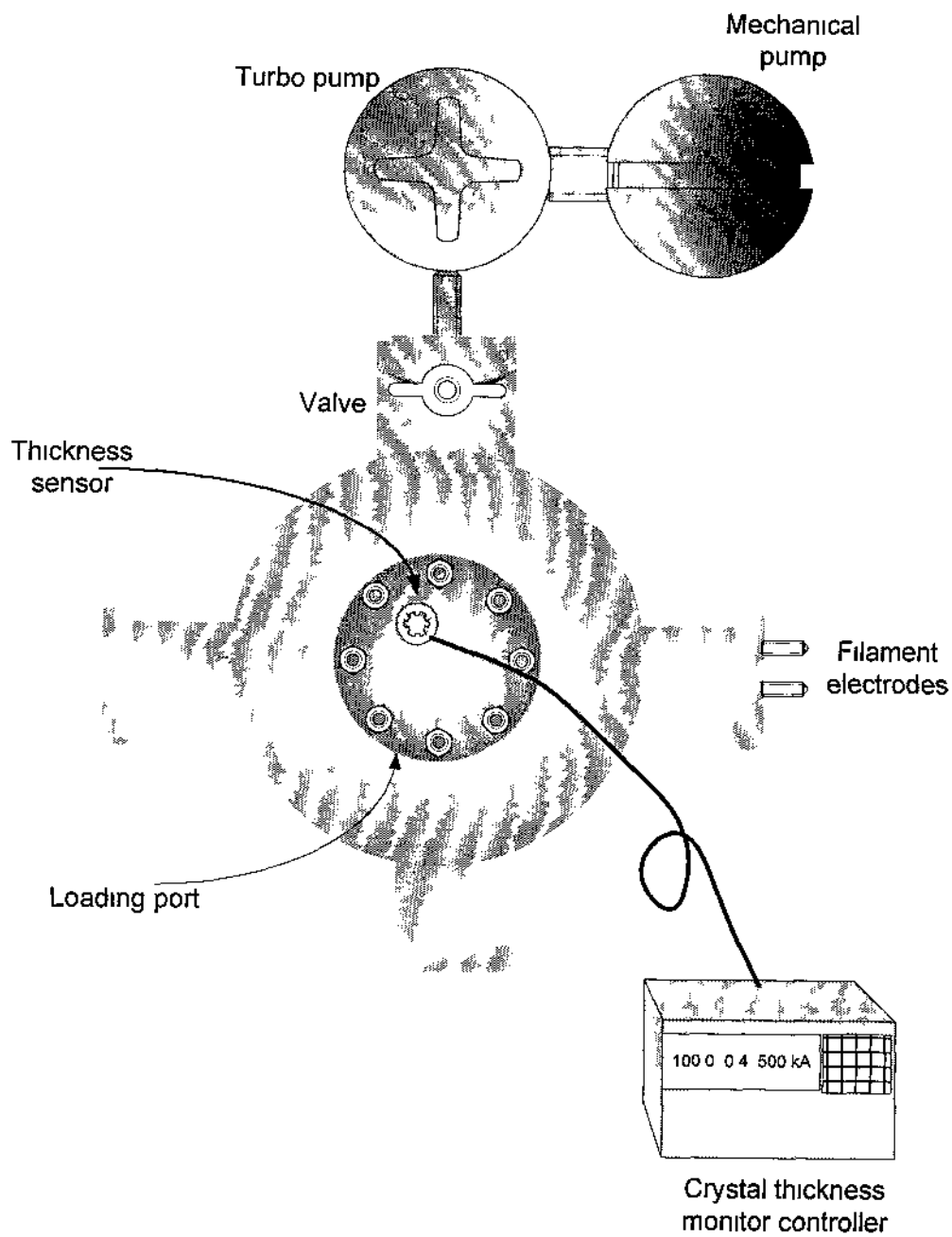


Fig. B.1. Evaporator system components.

APPENDIX C

VACUUM SYSTEM PUMP DOWN AND BRINGING BACK TO ATMOSPHERE PROCEDURE.

C. 1. System Components

The ultrahigh vacuum system (UHV) used to accomplish our goals consists of:

1. Custom made-multiport UHV chamber from Kurt J. Lesker company, Fig. C.1.
2. Lab-made high energy photoactivated electron gun capable of delivering electrons with energy 35-40 keV, Fig. 3.1(b).
3. Pumping station consisting of turbo molecular pump, 300 l/s, and mechanical pump, Fig. C.2.
4. Double microchannel plate detector (MCP) – phosphorous screen assembly. The MCP is a special plate manufactured with millions of micro channels which work independently as electron multipliers. A single electron at the input is accelerated by the applied potential (~ 1.5 kV) across the terminals of the MCP plates and multiplied as it passes through these channels to about 10^8 electrons at the output. These electrons are allowed to fall on the phosphorous screen, which is biased at ~ 4.1 kV, and generate photons with frequency in the visible range, usually green or blue depending on the type of screen coating.
5. XYZ sample holder and manipulator.
6. Custom-made heating stage.
7. High voltage feedthrough.
8. UHV valves and glass and quarts view ports.

C. 2. System Pump Down

1. After loading the samples into the system, open the valve.
2. Turn on the turbo-molecular pumping station; note that the mechanical pump starts first then few seconds later the turbo pump starts.
3. Within 3 minutes the turbo pump reaches its full speed of operation (56,000 rpm). If it did not reach that speed within that time frame, turn off the pumping station and check for leaks.
4. Keep the pumping station running for about two hours. During that time the pressure should be in the range of mid 10^{-7} Torr. If not, check for leaks.
5. Close the valve and turn on the ion pump.
6. If the ion pump did not start, turn it off and check for system leaks.
7. If everything goes right, the system should be ready within 24 hours to run the time-resolved experiment.

C. 3. Opening the System

1. Turn off the ion pump.
2. Wait 15 minutes and loosen one bolt slowly till the pressure starts to increase very slowly. Avoid gushing of air into the system rapidly as this may damage the delicate components in the vacuum system, the MCP and the electron gun.
3. Continue loosening the screws one after the other and leave the system to reach atmospheric pressure gradually.

Always remember that this system is very delicate, so try to be as gentle as possible whenever you pump it down or up.

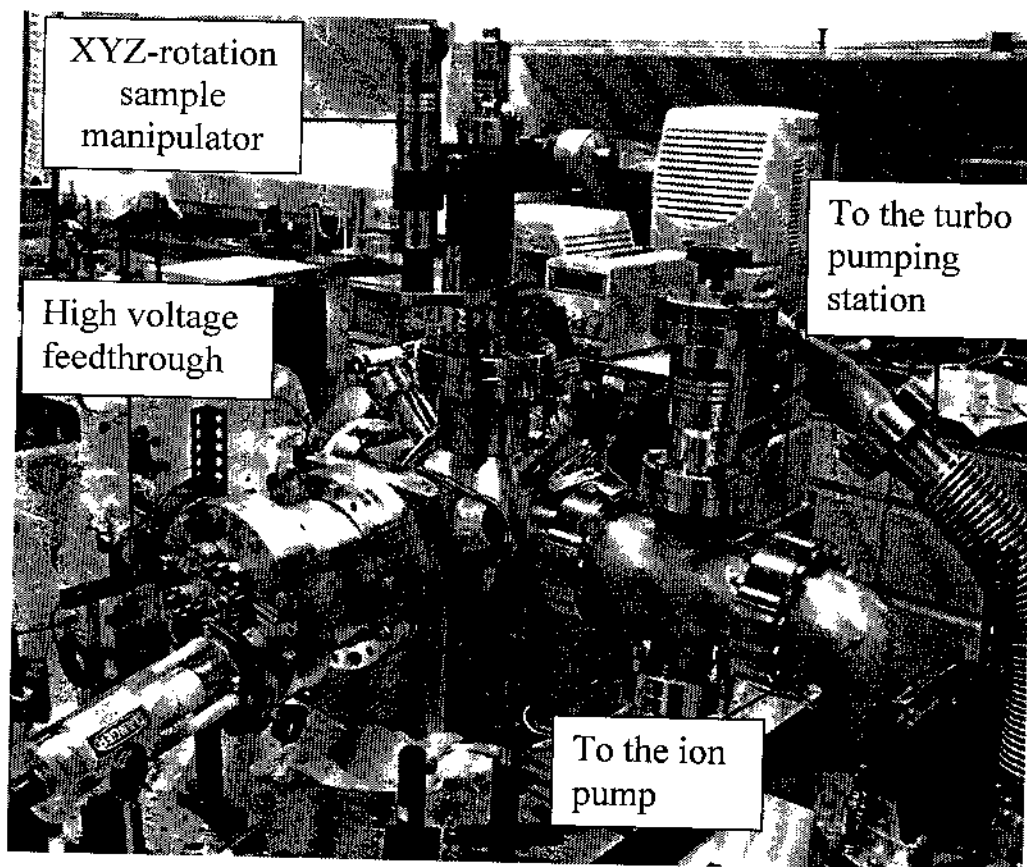


Fig. C.1. TR vacuum chamber

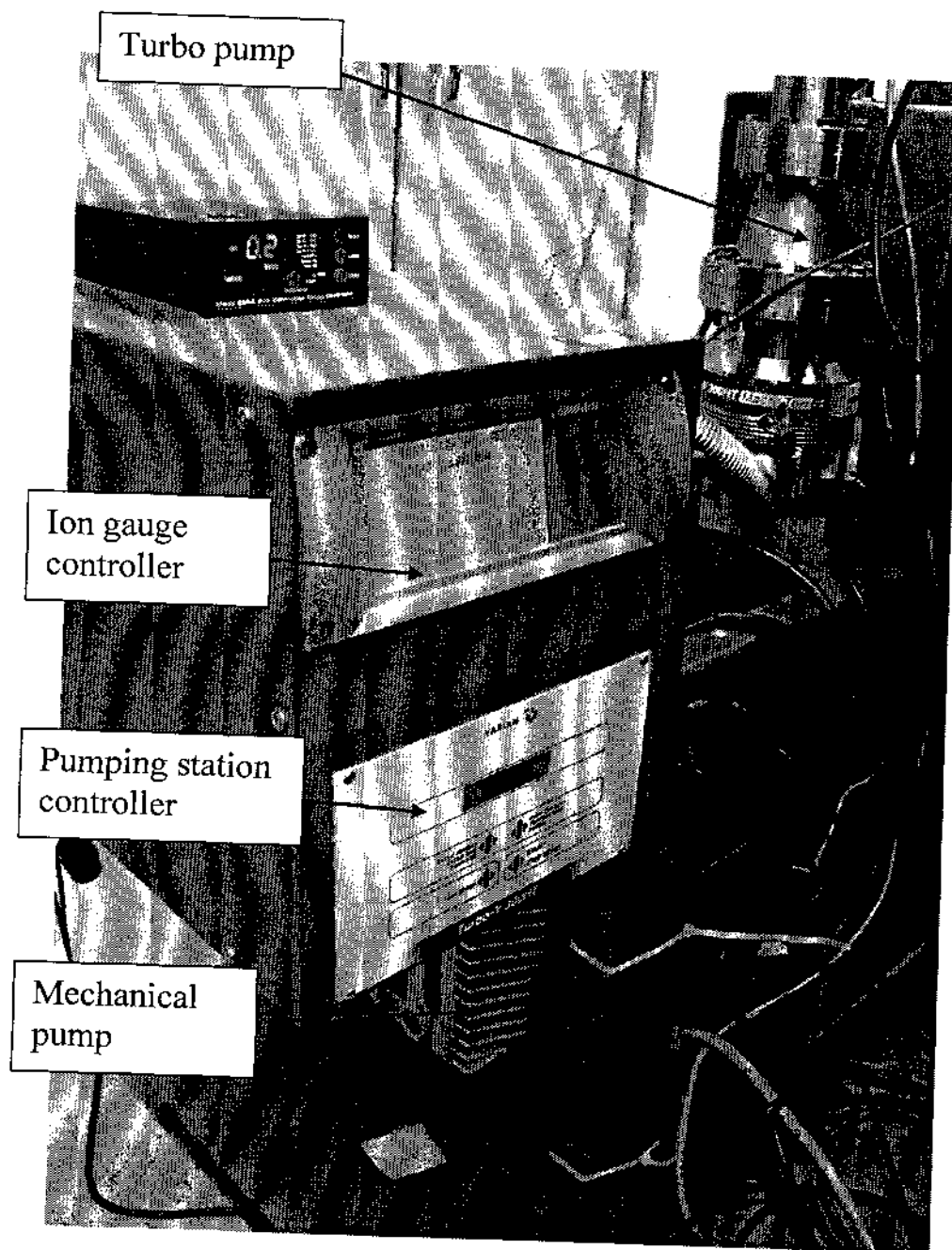


Fig. C.2. Pumping station consists of a turbo molecular pump and a mechanical pump.

APPENDIX D

FEMTOSECOND LASER SYSTEM OPERATION

D.1. General

- Before turning on the femtosecond laser system, Fig. D.1, make sure that the water level in the chillers is at an appropriate level.
- NEVER, NEVER and NEVER use regular water (city tap water).
- For the oscillator (TSUNAMI-SPCTRS PHYSICS), use distilled water, and for pumping laser (DARWIN-QUNATRONIX) use de-ionized water.

D.2. Turning on the Pumping Laser (DARWIN)

1. Turn the main key to the left, then press “SELECT” on the main panel, Fig. D.2.
2. Wait 3 minutes till the system is fully powered on.
3. Press “MENU” scroll down to “SETTINGS”
4. Press “TEMPERATURE” and adjust the temperature to 23.3 °C.
5. Press “SELECT” and scroll down to “MODE”
6. Select “PRF”, then “EXTERNAL”
7. Press “SELECT” and increase the current gradually to ~ 29 A.
8. Open the shutter.

D.3. Turning on the Oscillator (TSUNAMI)

1. Turn on the main power by pressing the white button, Fig. D.3.
2. Wait few minutes (~ 5 minutes) till the power is stabilized.
3. Hold the turn on button for few second till the power reading starts to increase.
4. When the power reading has reached its maximum value (~ 4.5 W), open the shutter.

5. Turn on the SDG (black switch at the back), and enable the laser output (front panel switch).
6. Leave the system running for at least 30 minutes to stabilize before running the time-resolved experiment.
7. Monitor the output power and make sure that the output power is constant over long periods of time.
8. When the system is running properly, the output power is ~ 1.4 mJ/pulse when running at 1 kHz.

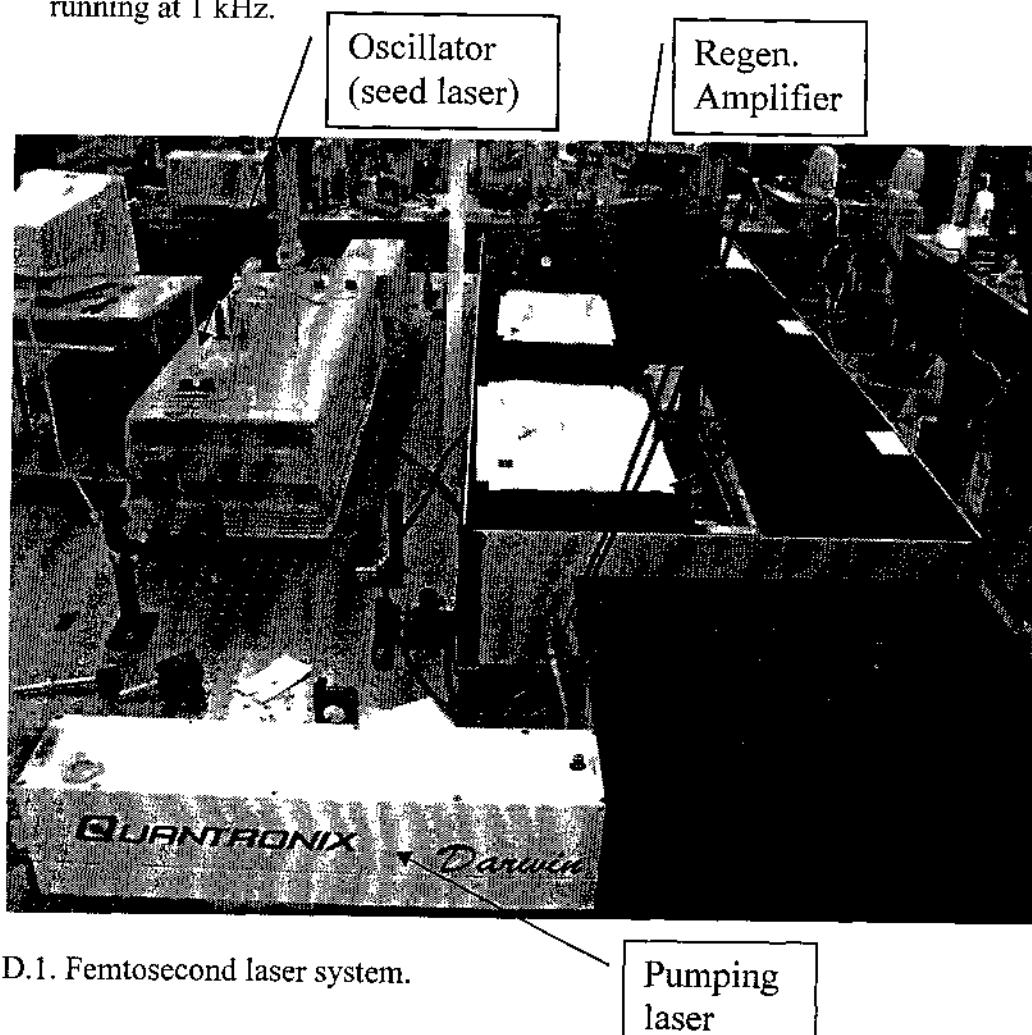


Fig. D.1. Femtosecond laser system.

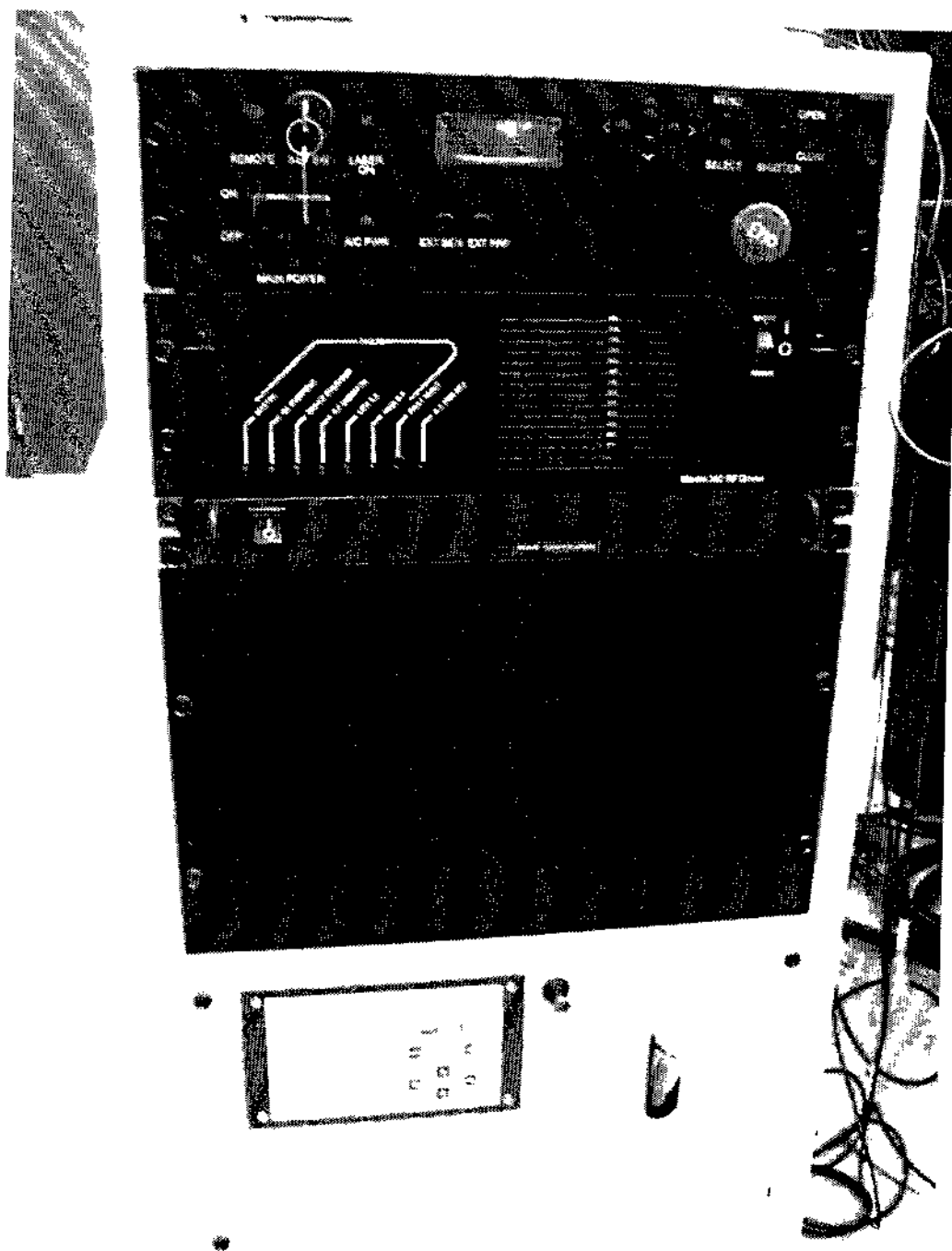


Fig. D.2. Main controller for the Darwin laser (pumping laser).

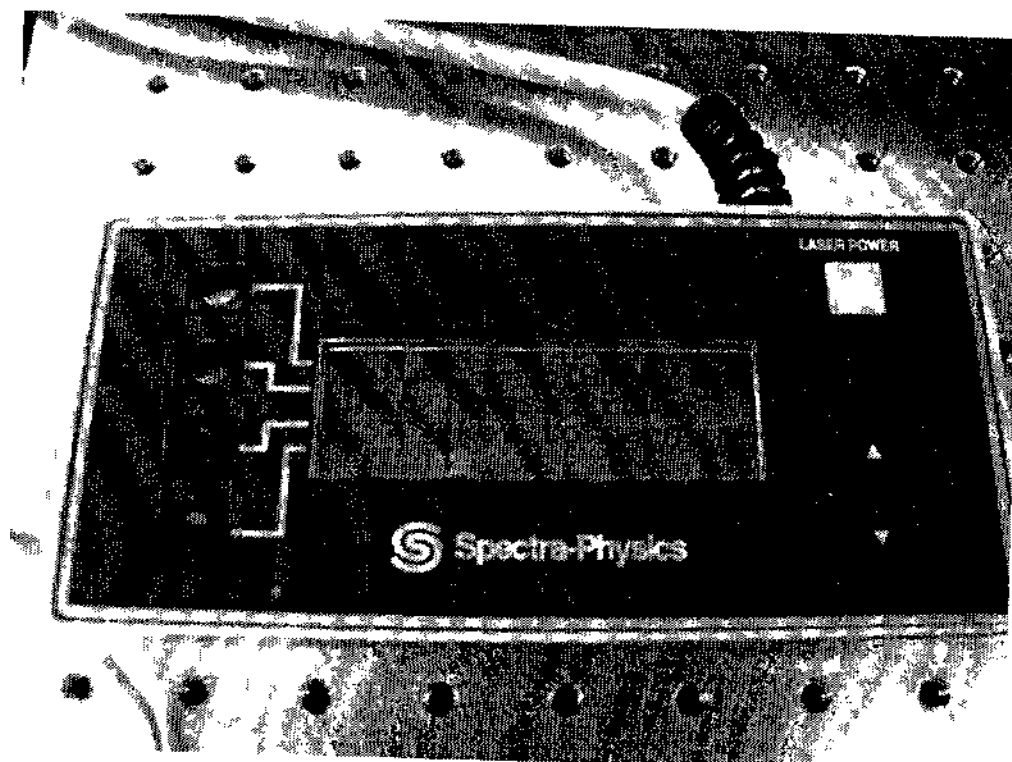


Fig. D.3. Control unit for the oscillator (seed laser)

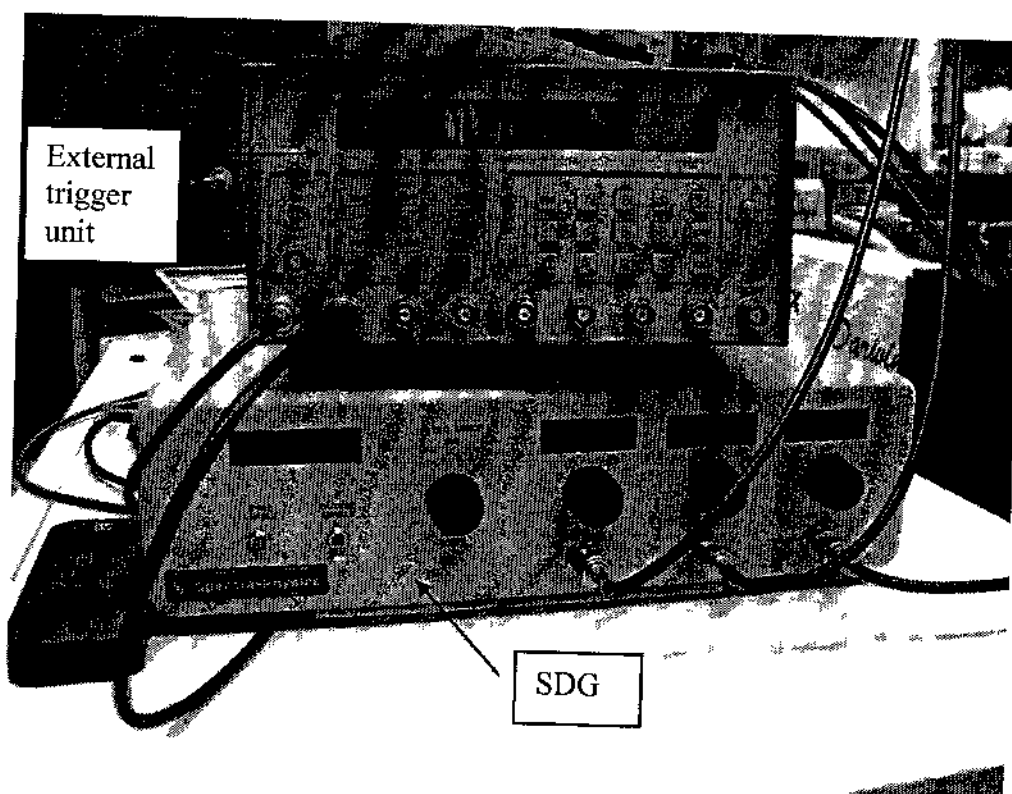


Fig. D.4. SDG for seed laser and external trigger unit of pumping laser.

APPENDIX E

PUMP-PROBE SETUP

Time-resolved electron diffraction setup is shown schematically in Fig. E.1 and the actual system picture is shown in Fig. E.2 with the pump and the probe beams paths.

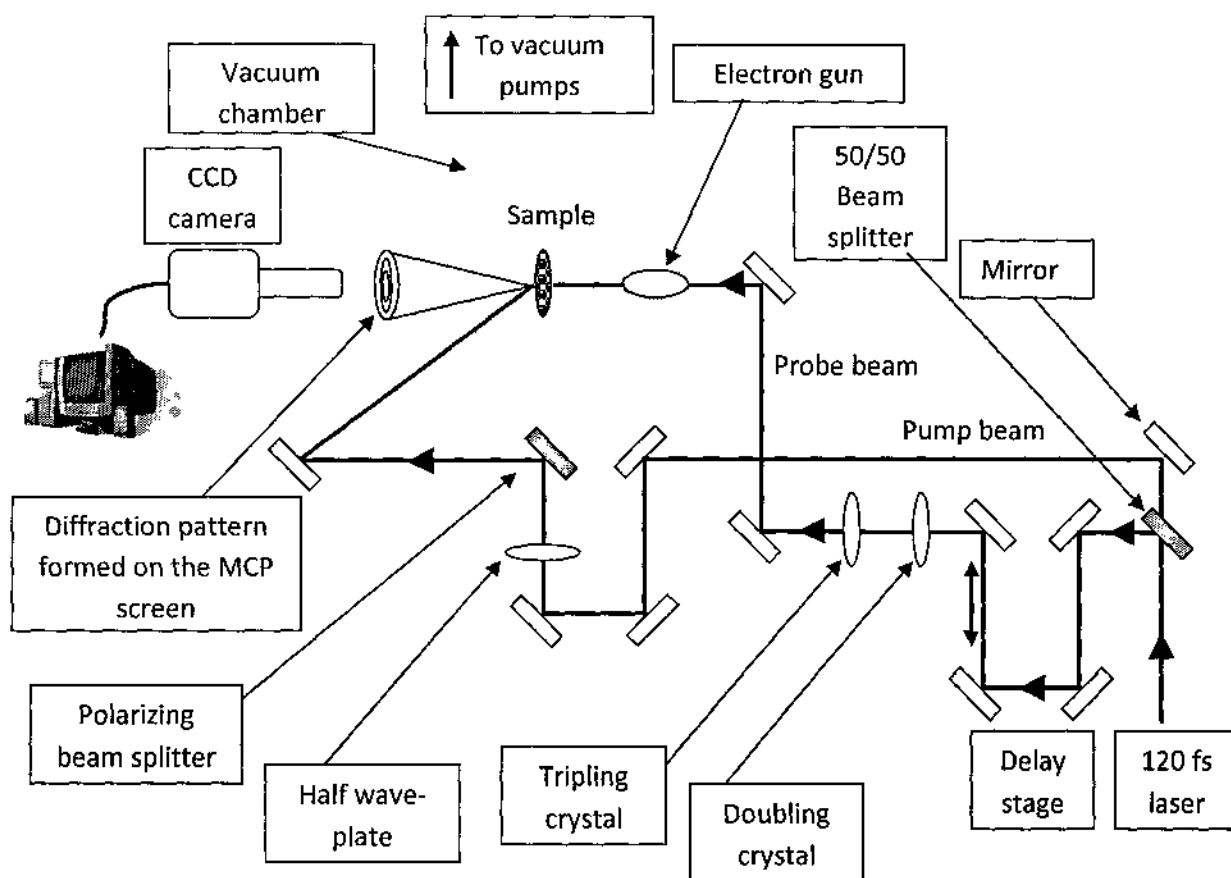


Fig. E.1. Layout of the time-resolved electron diffraction setup. A 120 fs pulse is generated from Ti:sapphire chirped pulse amplifier. The system is running at 1 kHz. In this setup, the laser pulse is divided into two parts; one is frequency tripled and used to generate photo-electron from photo-activated electron gun (probe beam), and the other part is used to excite the sample (pump beam). The synchronization between the two beams is granted since they are generated from a single beam.

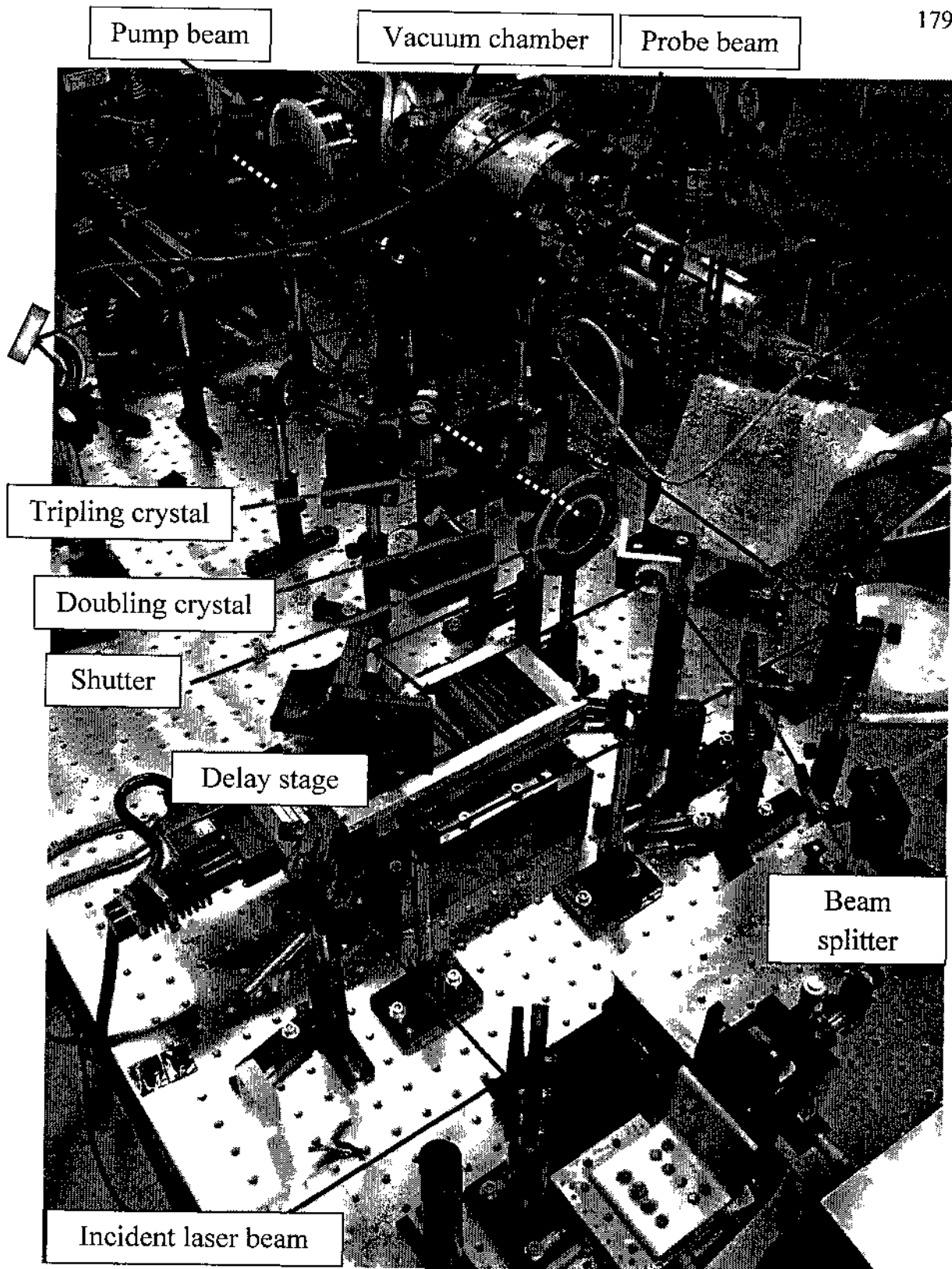


Fig. E.2. Actual pump-probe setup with pump and probe beam paths.

APPENDIX F

PROCEDURES USED TO ACQUIRE DATA (ELECTRON BEAM ALIGNMENT WITH LASER, LASER ALIGNMENT ON TARGET, AND CONDITION OF WORKING PHOTOCATHODE)

Prior to data acquisition, PAEG, MCP and phosphorous screen should be biased at the proper voltage as follows;

1. The electron gun operating voltage is -35 kV.
2. MCP biasing voltage is 1.4 – 1.6 kV.
3. Phosphorous screen biasing voltage is 4.1 kV – 4.4 kV.
4. A 60 V is used to get rid of the noise on the MCP.
5. Electromagnet focusing current is 4.9 A.
6. The current through the X-Y electromagnets (electron beam steering magnets) is adjusted such that the electron beam (probe) passes through the sample under study.
7. Steer the pump beam with the end mirror such that it passes through the sample. To do so, use the infrared viewer to see the transmitted beam from the exit window and white piece of paper. You should see an image of the TEM grid on that paper. The use of a power meter to measure the transmitted infrared is useless because the transmitted portion is too weak to be detected.
8. Compare the diffraction pattern when the pump beam is on to that when the pump beam is off; a reduction in the diffraction pattern intensity is observed if the delay stage is adjusted such that the probe beam is delayed with respect to the pump beam. Sometimes a detector was used to maximize IR transmission through the TEM grid.
9. Keep moving the delay stage back and forth in steps of 1 ps, and collect diffraction images at each delay time.

10. Analyze the data according to appendix H.
11. A graph of $I(t)/I(t_0)$ similar to Fig. 6.4.(a) should be obtained.
12. From that figure, the point where $I(t)/I(t_0)$ starts to drop below 1 is the $t = 0$ point.
13. A proper fitting to the data will help in determining that point.

APPENDIX G

OPERATION OF THE CAMERA, IMAGE ACQUISITION AND DELAY STAGE SOFTWARE

Computer controlled charge coupled detector (CCD) camera is used to capture the diffraction pattern of the Bi nanoclusters at different temperatures and at different delay times.

The operation of the camera is as follows,

1. Turn on the camera.
2. Run “WINVIEW” software for image acquisition.
3. If you want to focus the diffraction pattern, click on “ Δt ” icon and make the focus time 1 second, Fig. G.1.
4. Take a few more images with different acquisition times to check the best time for data acquisition that gives no saturated rings.
5. The exposure time in the previous step varies from sample to sample, UV alignment and intensity.
6. The operator should minimize the UV intensity to reduce the electron pulse broadening and may increase the exposure to compensate for the reduced UV intensity.
7. Turn on the delay stage controller,
8. Run the delay stage software “ESP TUNING” and press “ENTER”, Fig. G.2.
9. Enter the parameters shown in Fig. G.3

10. Vary the delay stage location in a proper steps and at each step capture the diffraction pattern with pump laser on and with pump laser off.
11. Repeat step 10 till you finish acquiring the diffraction pattern over a distance equivalent to at least 100 ps (80 above t_0 and 20 ps below t_0).
12. When done, close the CCD camera software and turn off the camera.
13. Send the delay stage to its initial location (0 cm on the stage).
14. Close the delay stage software and leave the controller power on.

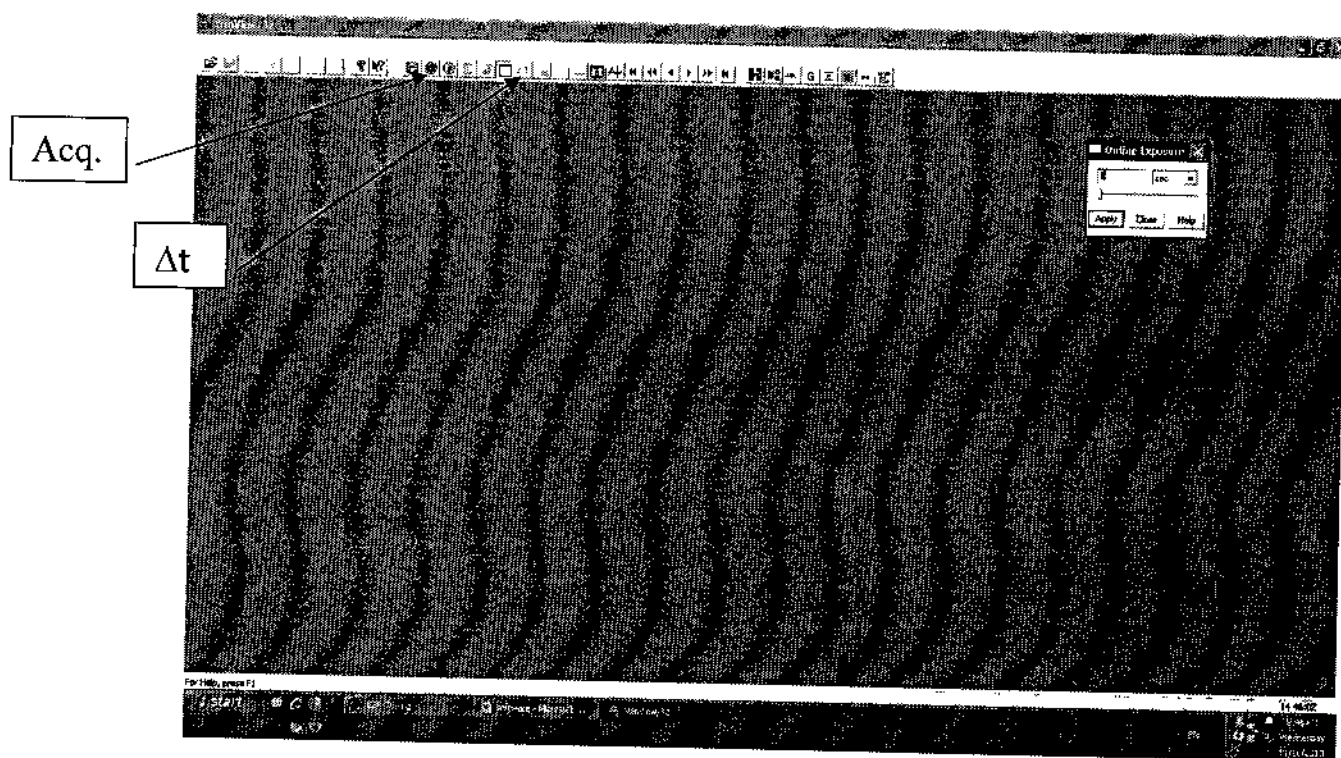


Fig. G.1. Winview software main panel for image acquisition.

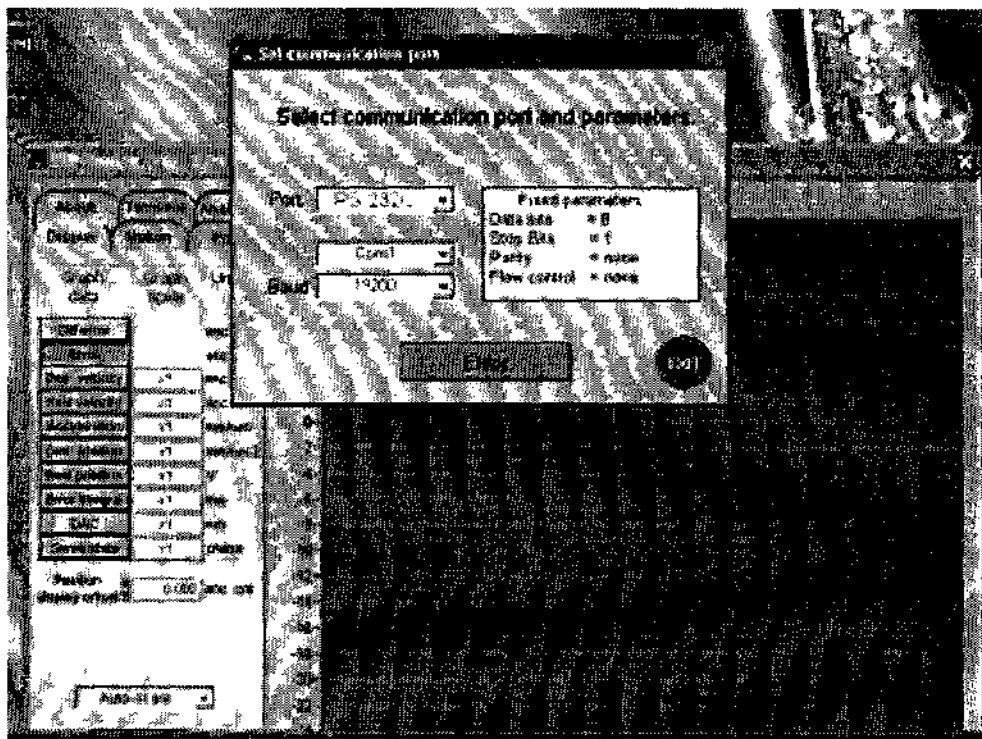


Fig. G.2. Delay stage software starting window.

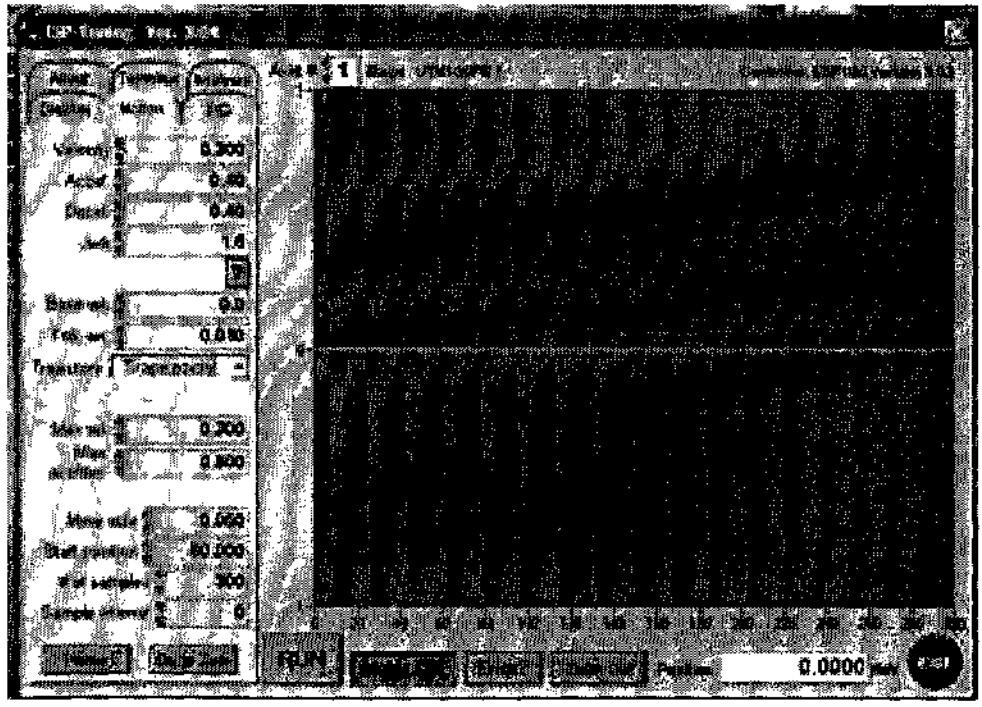


Fig. G.3. Delay stage software main control window.

APPENDIX H

HOW BRAGG PEAK INTENSITY, POSITION AND FWHM WERE MEASURED

In the following I am summarizing the steps that I have followed for data analysis and measuring the Bragg peak intensity, position and FWHM. The process of data analysis is very long, may take up to 7 days, and is tedious, just to analyze one run, which normally has 200 to 400 (sometimes more) different diffraction pattern images.

First: I used IMAGEJ to radially average the diffraction pattern, and convert it to pixel vs. intensity graph as follows;

1. Open the diffraction pattern using IMAGEJ, and select the circle button and draw a circle (any size), Fig. H.1 and Fig. H.2.

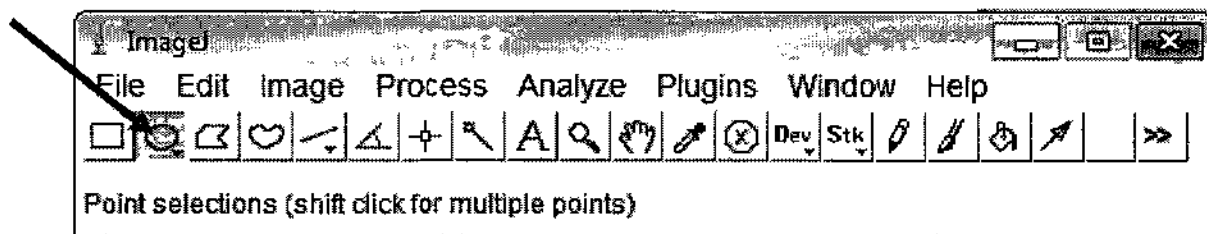


Fig.H.1. Main panel of ImageJ.

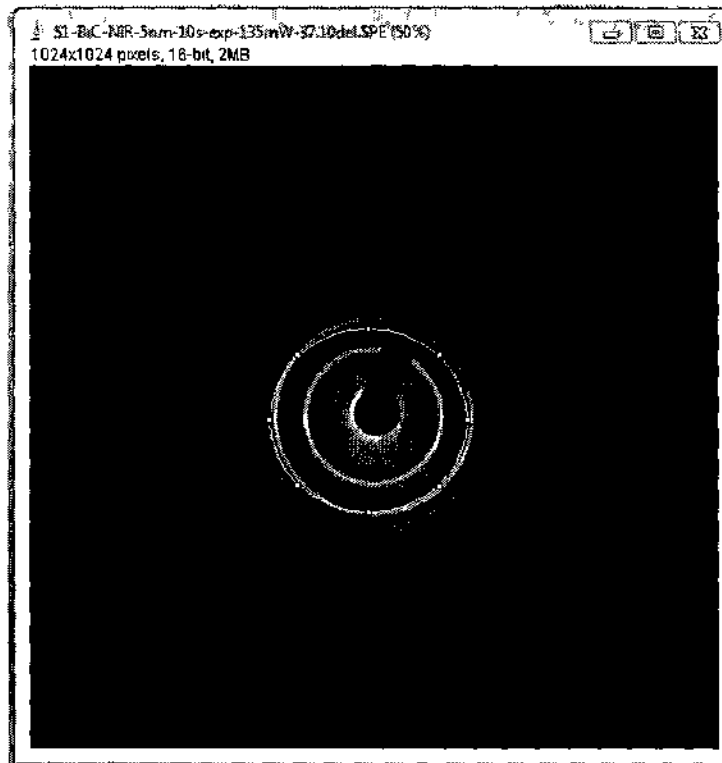


Fig.H.2.

2. Click PLUGINS, and select RADIAL PROFILE, Fig. H.3.

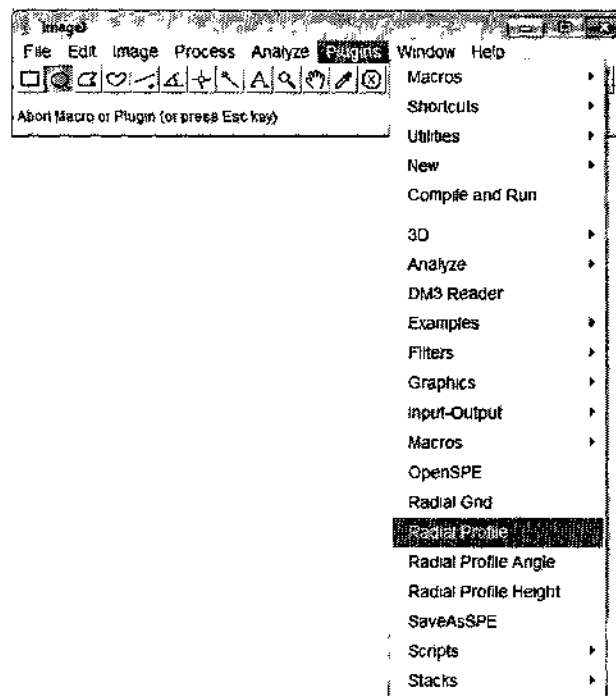


Fig.H.3.

3. A new window will pop up with X center, Y center and radius in pixels; change these numbers till the yellow circle matches EXACTLY one of the diffraction rings in the pattern. Usually we choose the most intense one (you may zoom in to get better matching results), Fig. H.4.

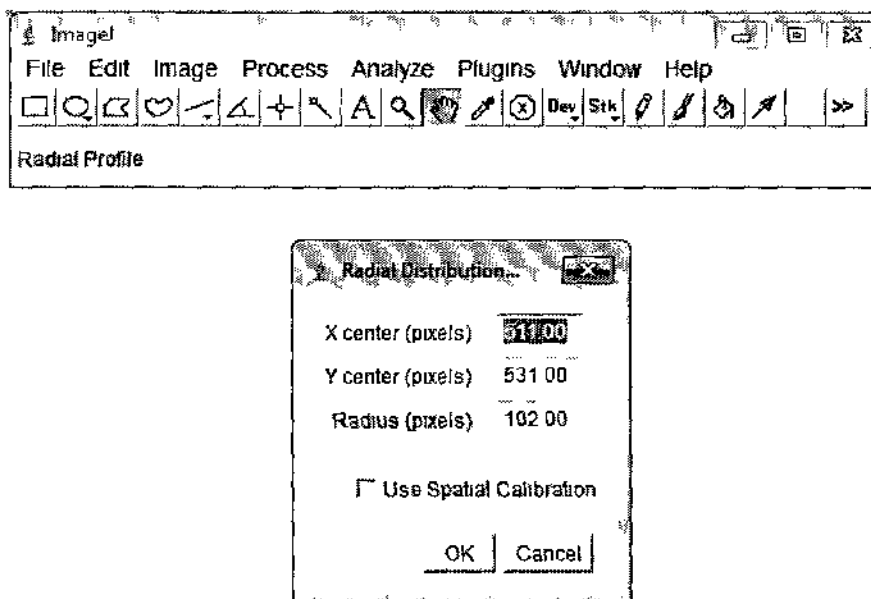


Fig.H.4.

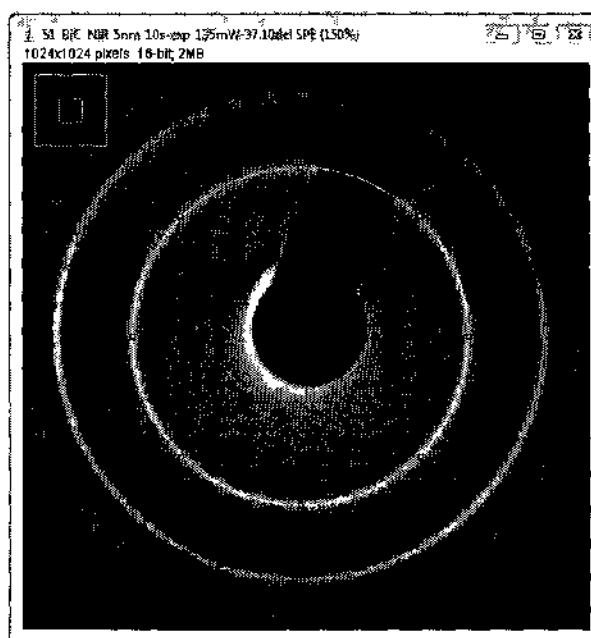


Fig.H.5.

4. After careful adjustment and matching, open PLUGINS again, and change ONLY the circle radius to a value that includes all the diffraction rings; in my case the circle radius is 350 pixels, which is big enough to include all the diffraction rings and click ok, Fig. H.6 and Fig. H.7.
5. Then click COPY.

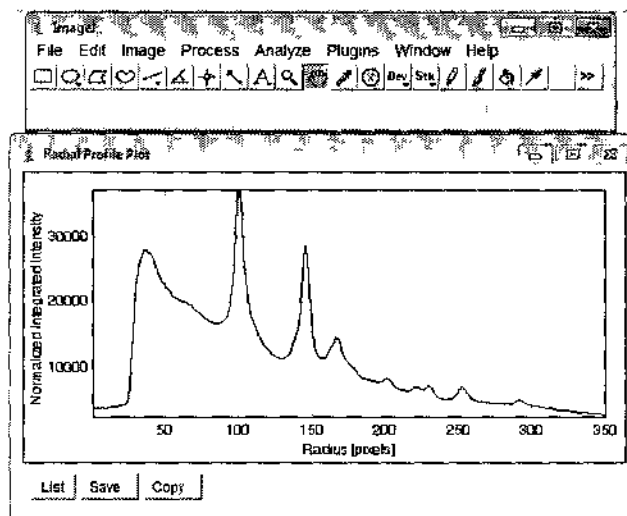


Fig.H.6.

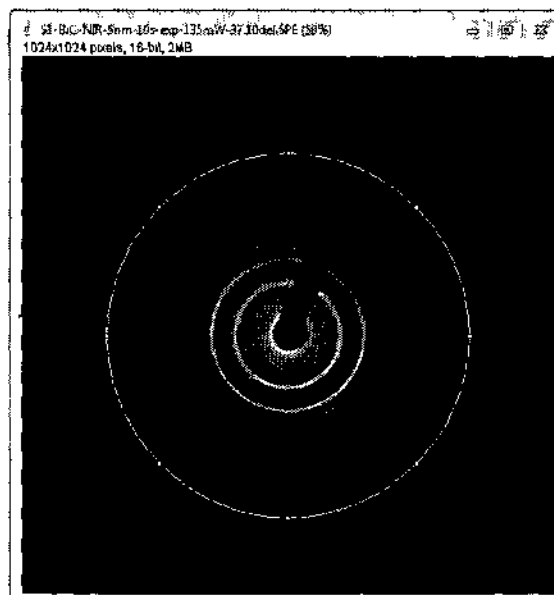


Fig. H.7

Second

6. Copy the data into EXCEL sheet; you may need to redraw the data to make sure you have copied the correct data.
7. Select part of the data that includes only the diffraction peaks and copy it to PEAKFIT software, Fig. H.8.

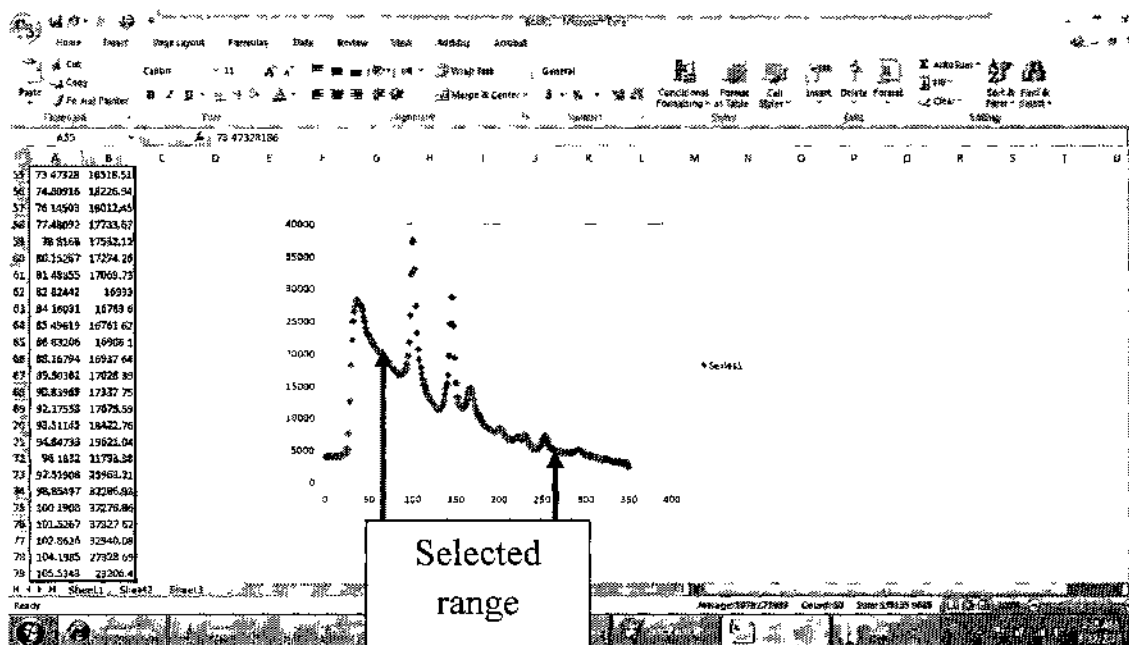


Fig.H.8.

Third

8. Paste the selected data from EXCEL sheet into PEAKFIT software, Fig. H.9.

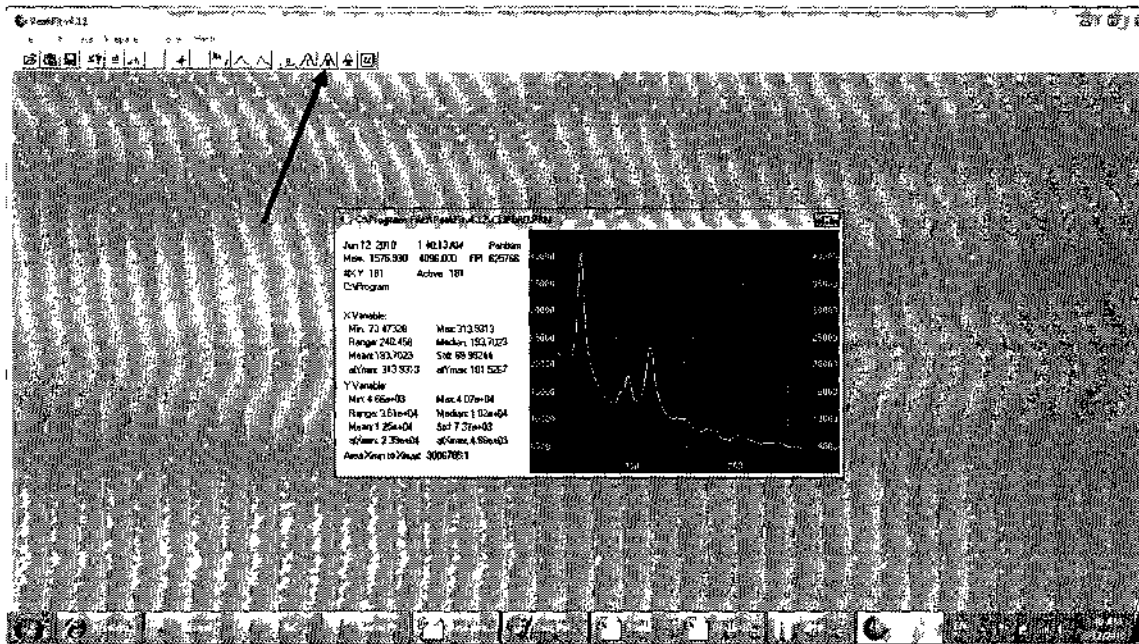


Fig.H.9. Main panel of PeakFit software V.4.2.

9. Remove the background from the data by clicking the curve that has letter B inside. There are set of prebuilt functions used for background removal. These functions are listed on the left side of the figure. Choose the one that gives best background removal, Fig. H.10.
10. Click the check mark.

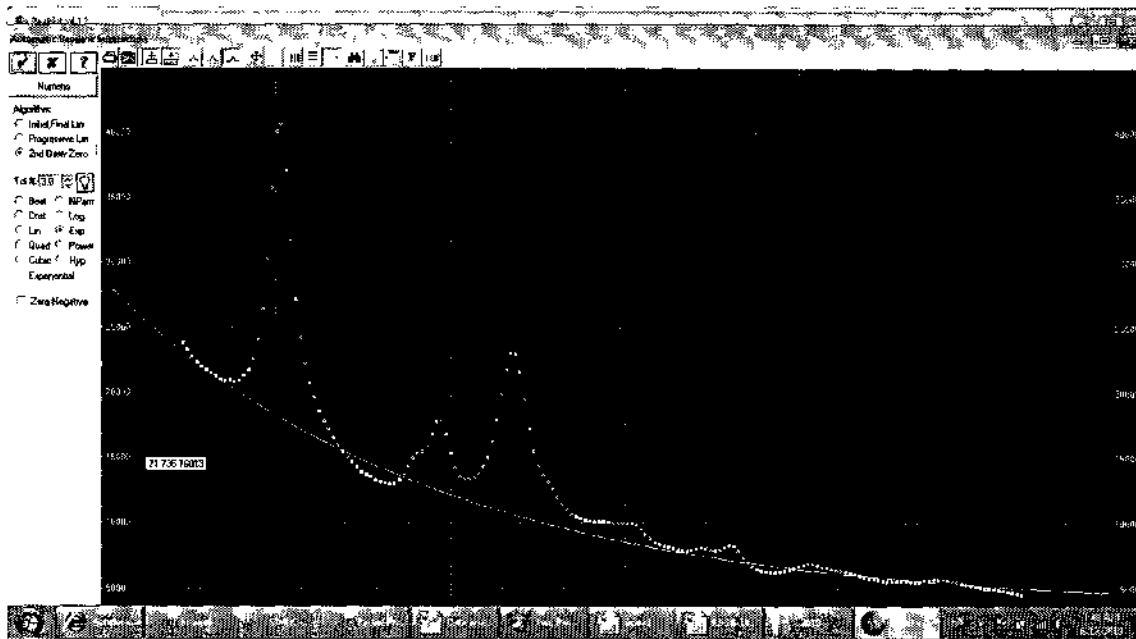


Fig. H.10

11. Now you have the diffraction pattern drawn as pixel Vs intensity without background, Fig. H.11.

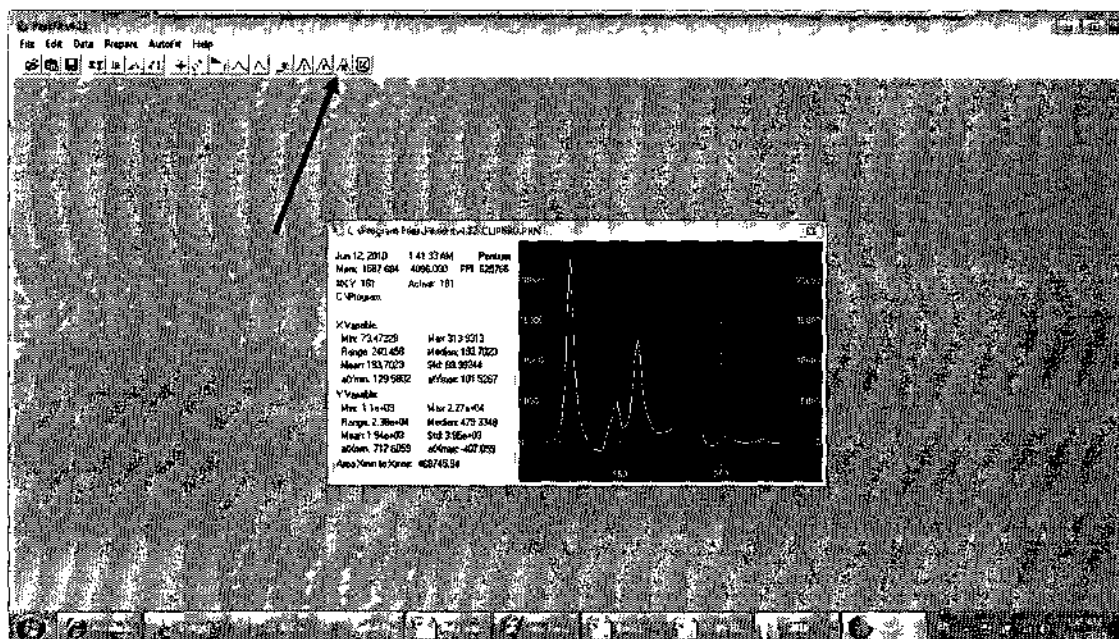


Fig. H.11

12. For fitting, click the icon on the top that has letter "I."

13. Click on the icon to the left bottom side of the graph that has small white page with lines, Fig. H12.

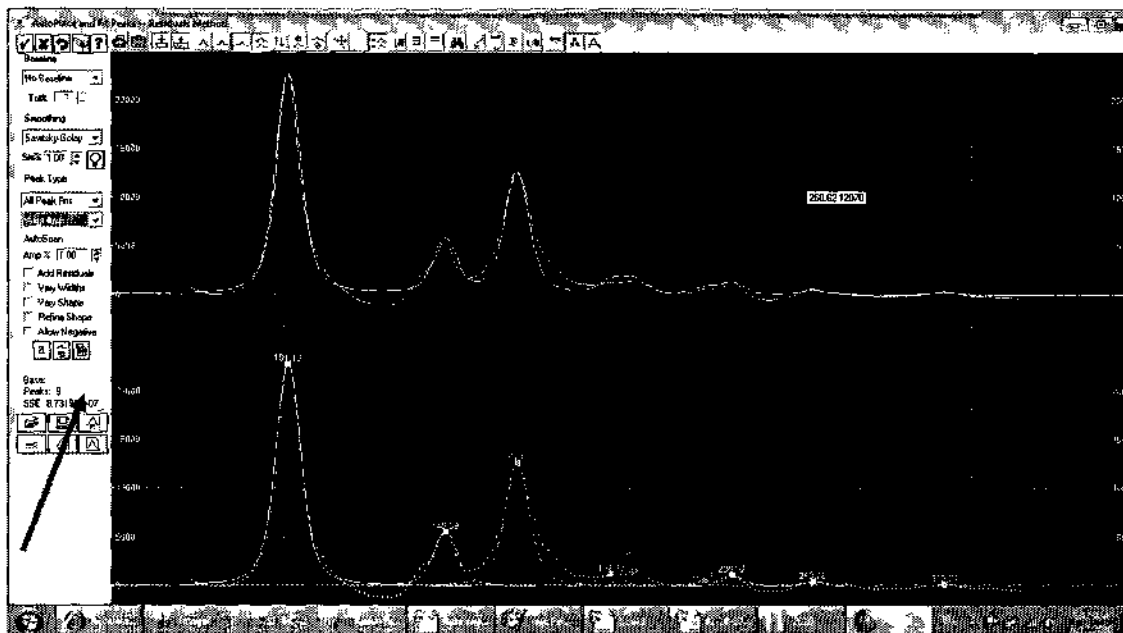


Fig.H.12.

14. A new window will pop up with all the information you need from the diffraction pattern (peak intensity, peak position, peak FWHM), Fig. H.13.

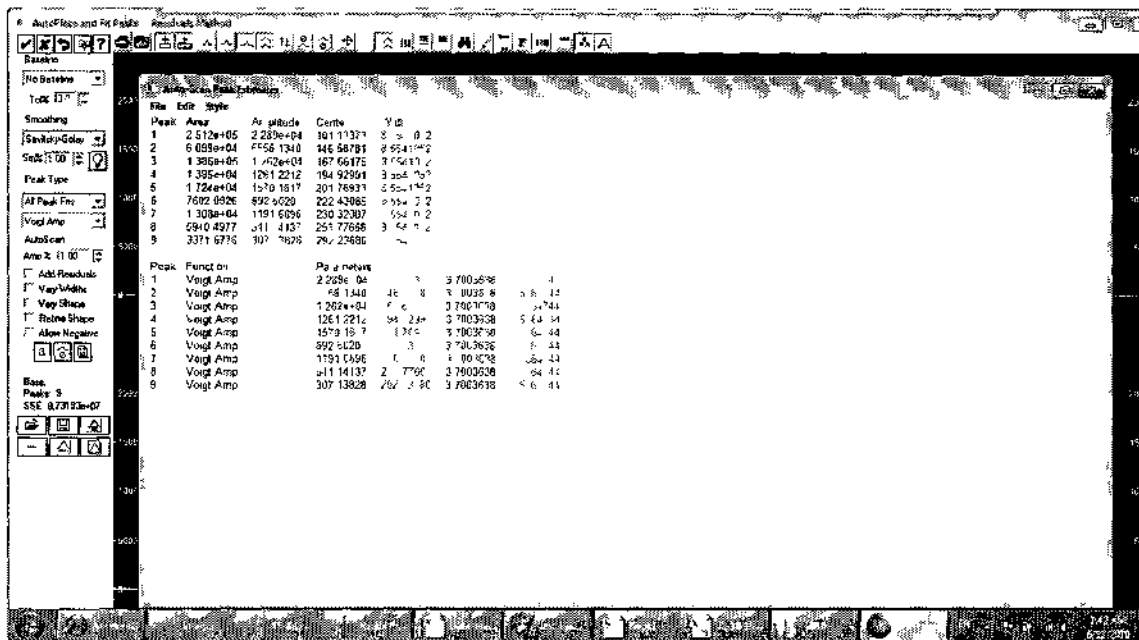


Fig. H.13

We need to copy these data into a new EXCEL sheet or any other software to draw these data vs. any parameter we have changed to obtain that diffraction pattern, for example, delay time, temperature, or laser power.

To do so;

15. Click "EDIT" then "ASCII editor"

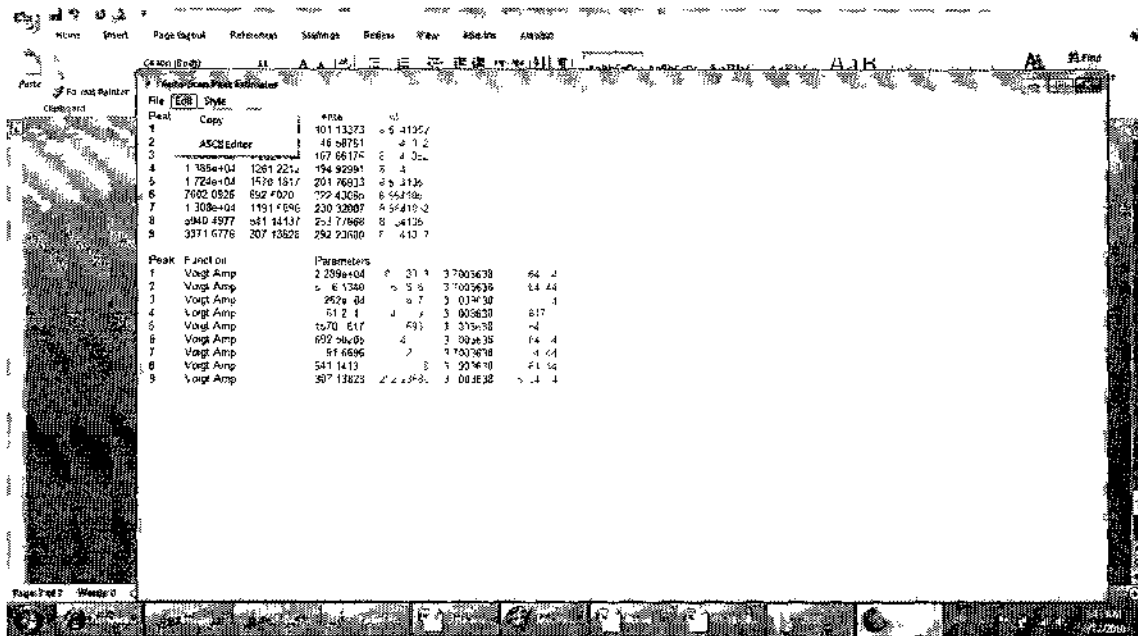


Fig. H.14

16. Select the data, copy and paste it to the pre-prepared EXCEL sheet that has the physical parameter you have changed to get the diffraction pattern.

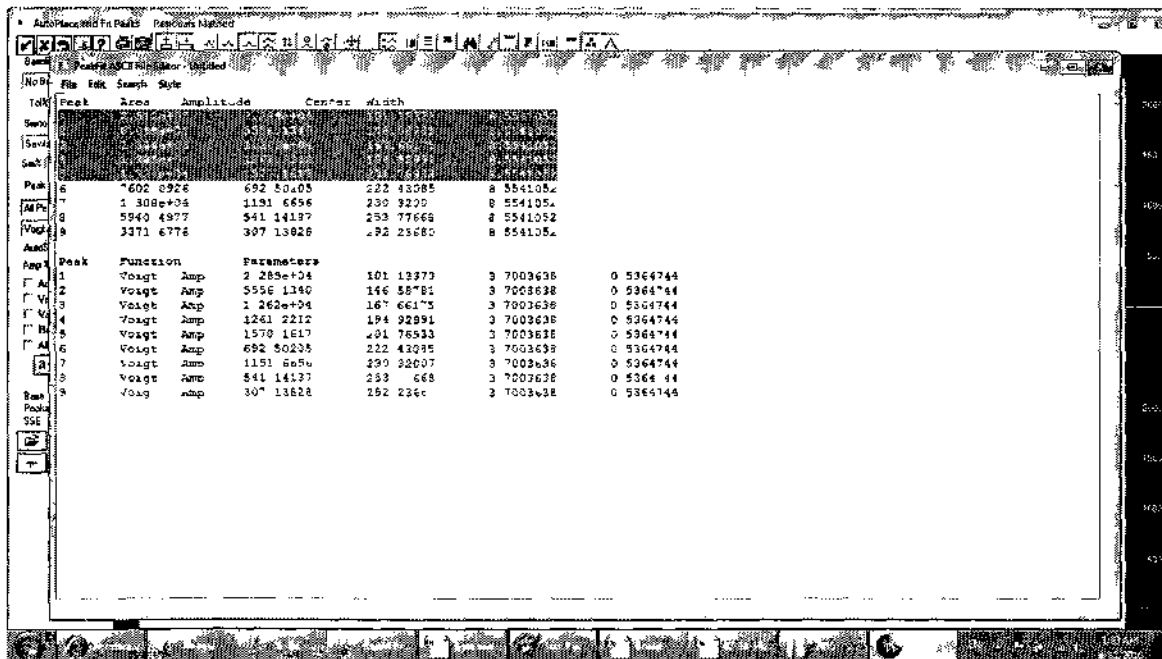


Fig.H.15.

17. Repeat those steps for the 200 images (or more).

18. Therefore, from a single run you should get for a single diffraction ring, intensity vs. delay time, peak position vs. delay time and FWHM versus delay time.

Example:

In this example, we can see clearly how the radial averaging parameters affects the calculated physical parameters, but do not affect the behavior of the lattice. The radial average parameters used to extract the data presented in Fig. H.16 and 17 are summarized in the following table.

	X-position	Y-position	Ring diameter
Fig. H.16	509	499	300
Fig. H.17	510	498	300

The data presented in Fig. H.16 and 17 are redrawn in Fig. H.18-19, respectively, up to 2.1 mJ/cm². From Fig. H.18, it is clear that the slopes of data in both directions (012) and (110) are almost the same, $-11 \times 10^{-4} \text{ (mJ/cm}^2\text{)}^{-1}$ and $-10 \times 10^{-4} \text{ (mJ/cm}^2\text{)}^{-1}$ respectively which means that the lattice before the inflection point expands with almost the same rate which is the same results presented in Ch. V. In Fig. H.19 the slope of the data along (012) direction, $-19 \times 10^{-4} \text{ (mJ/cm}^2\text{)}^{-1}$, is higher than that along (110) direction, $-6 \times 10^{-4} \text{ (mJ/cm}^2\text{)}^{-1}$. We conclude from the previous discussion that, although the data presented in Fig. H.16-17 gave the same behavior but it is critical to choose the proper radial average parameters in IMAGEJ software since a wrong parameters will over estimate the measured physical parameters. Therefore, I suggest the parameters used to produce Fig. H.16 to be the proper parameters in reproducing the data.

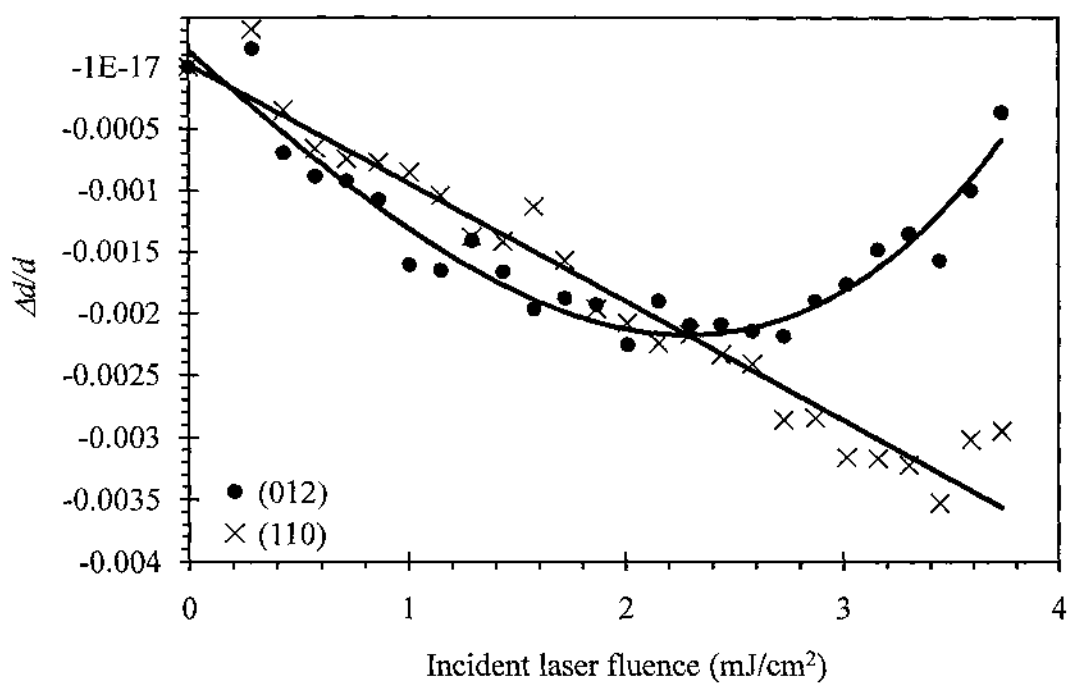


Fig. H.16

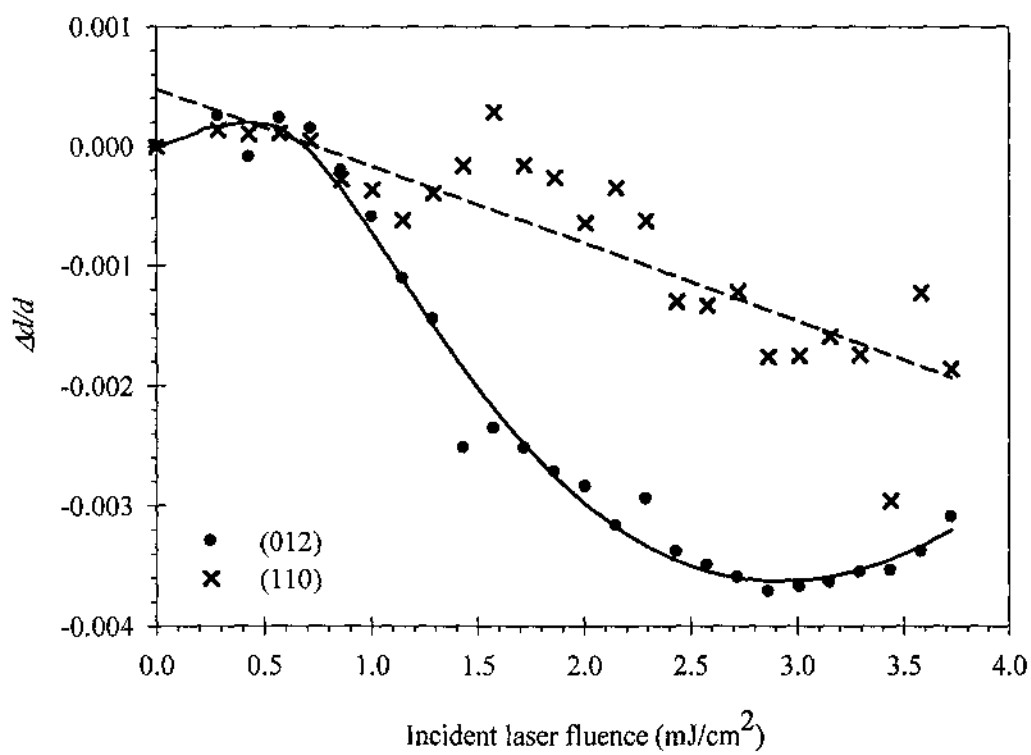


Fig. H. 17

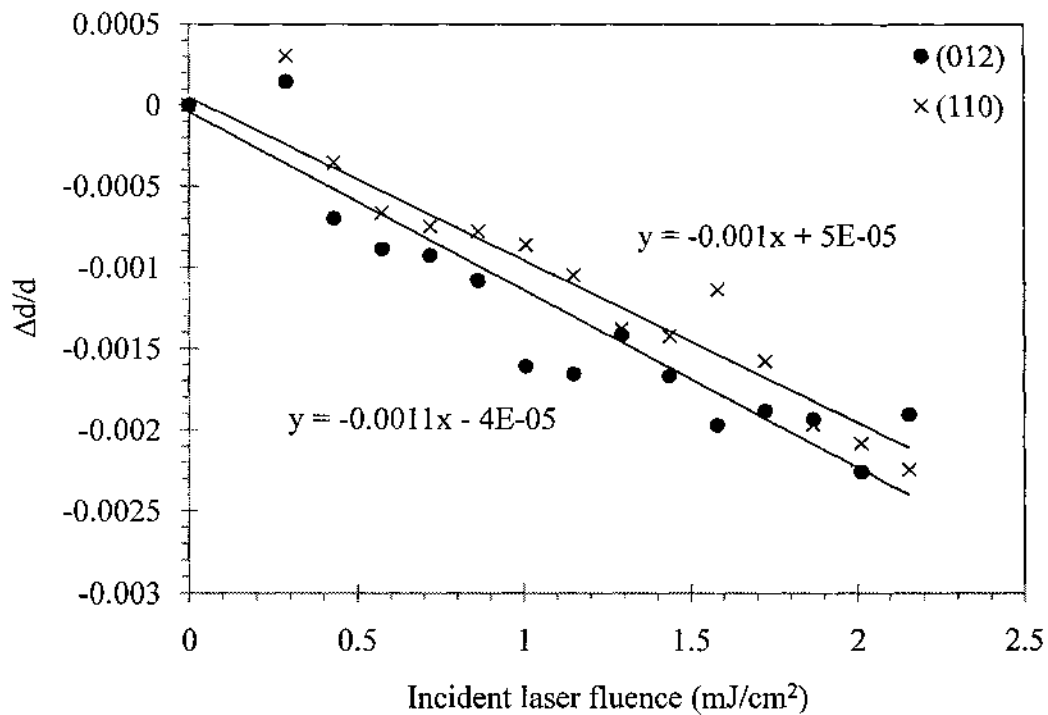


Fig. H.18

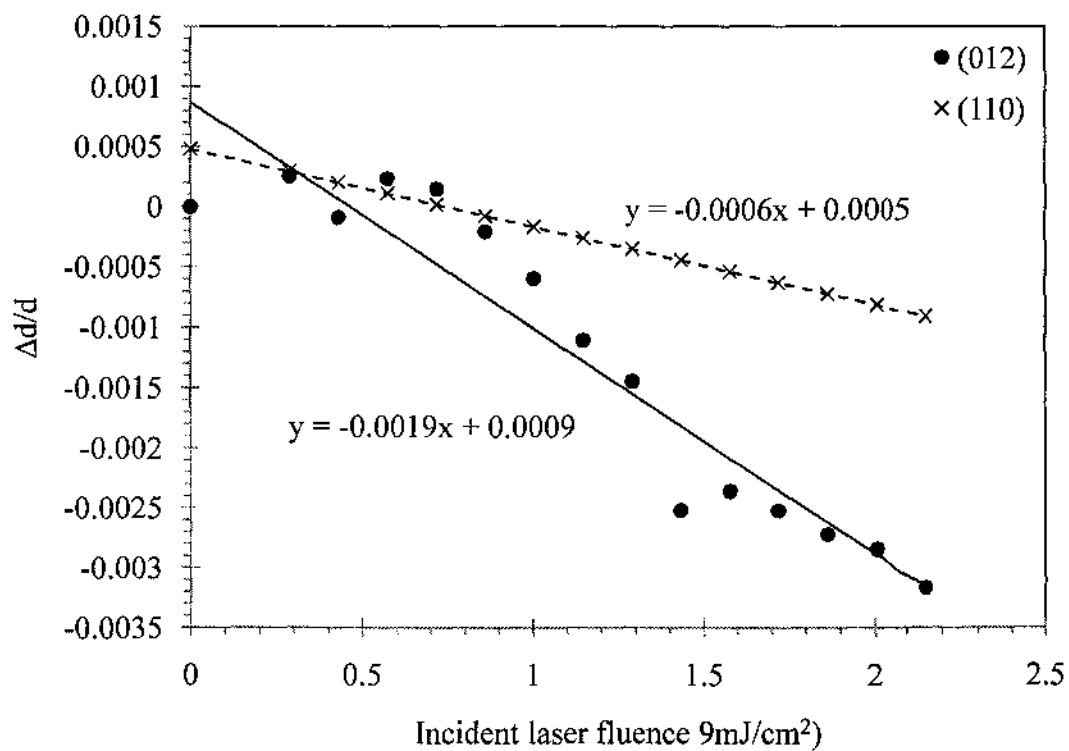
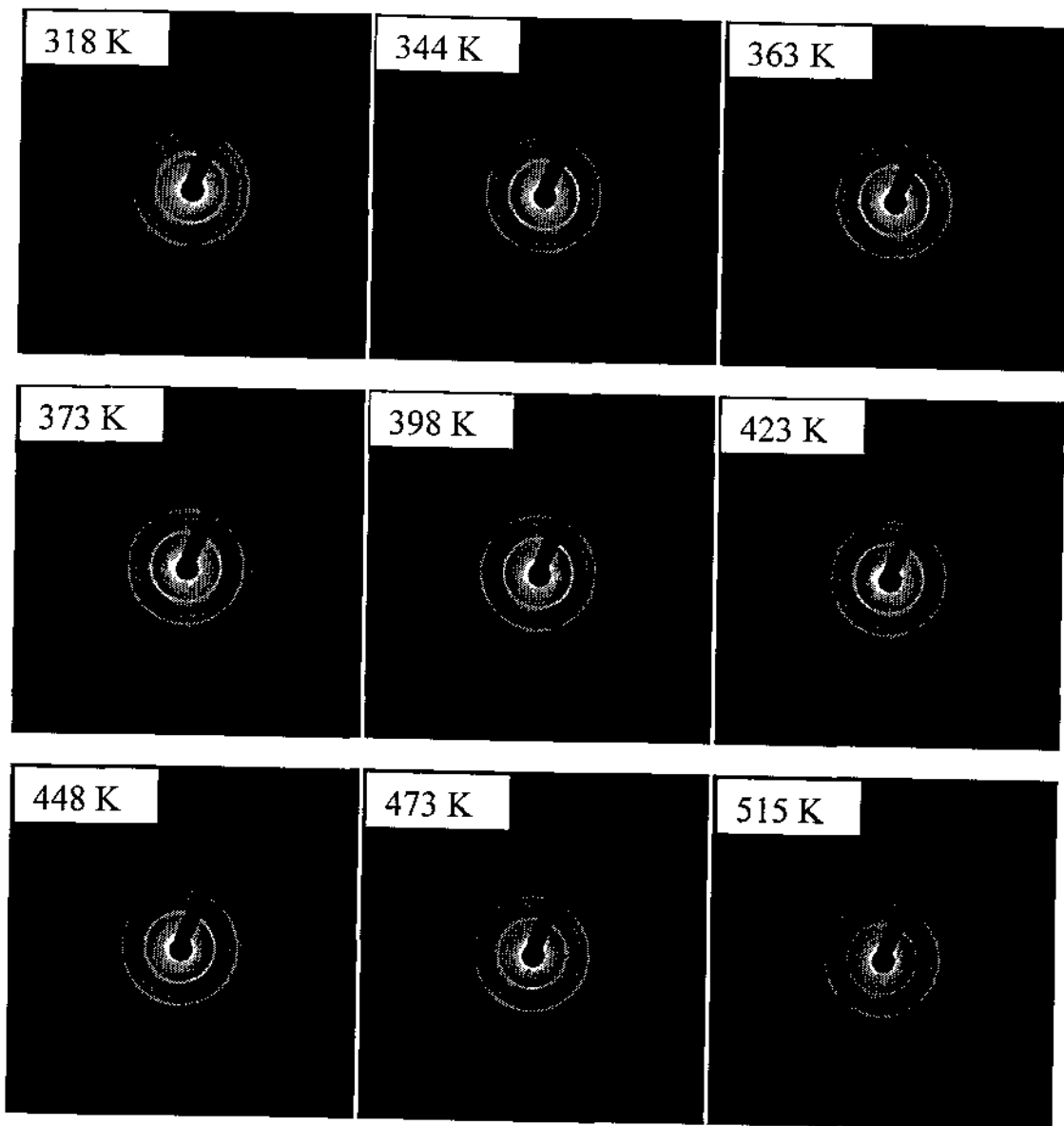


Fig. H.19

APPENDIX I

DATA SUMMARY ON CONTINUOUS HEATING

(a)



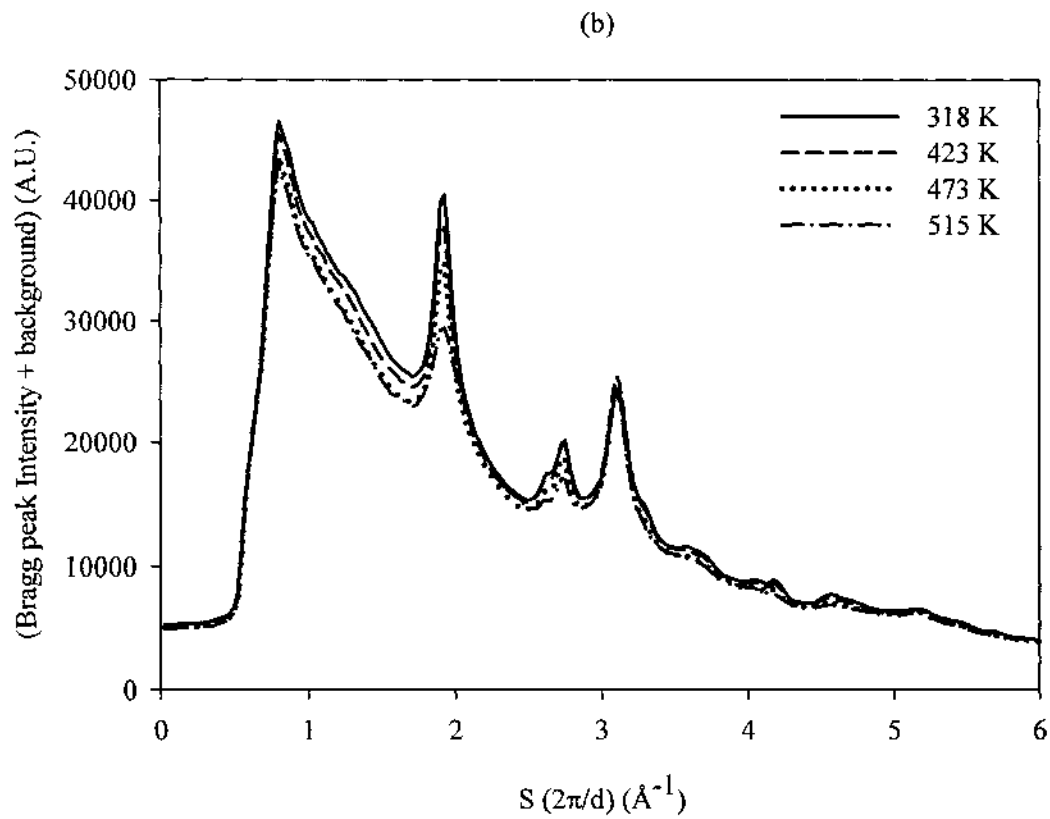
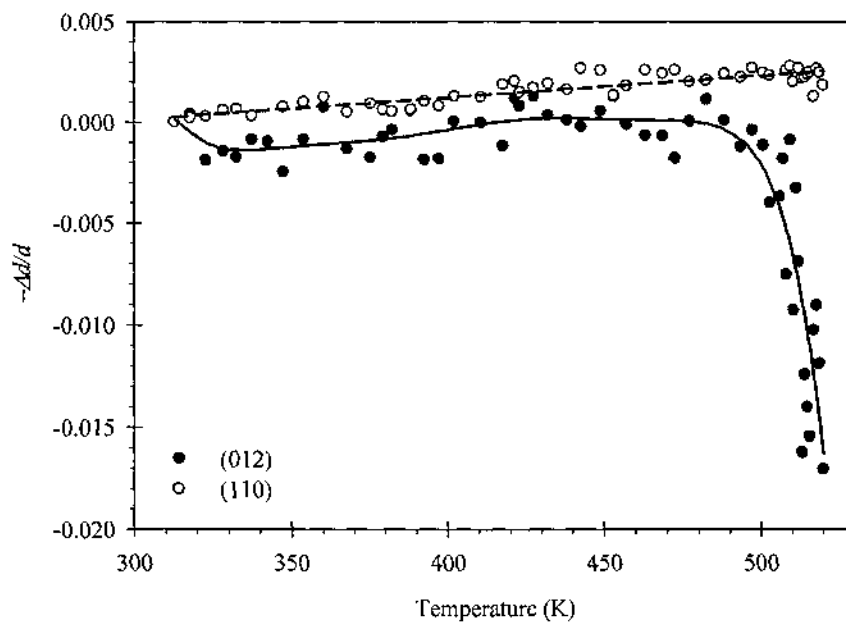
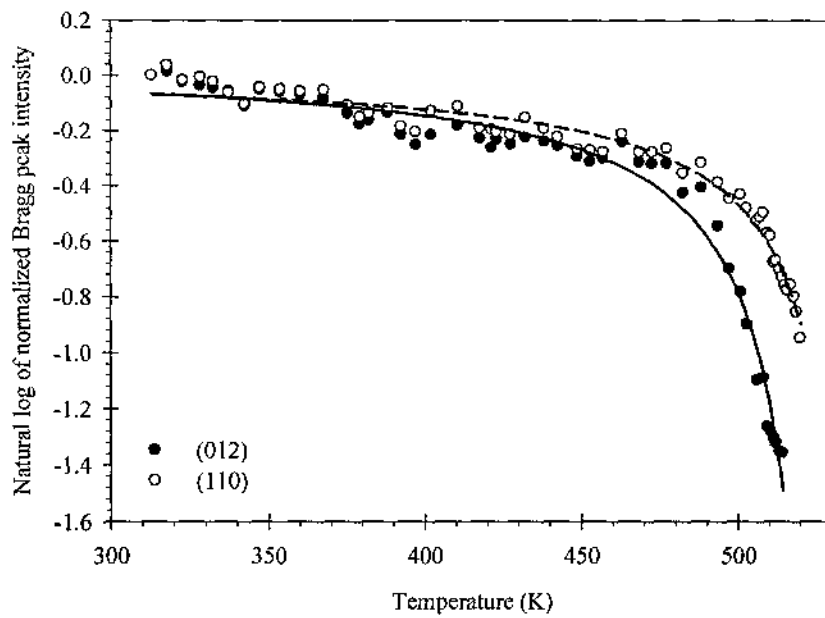
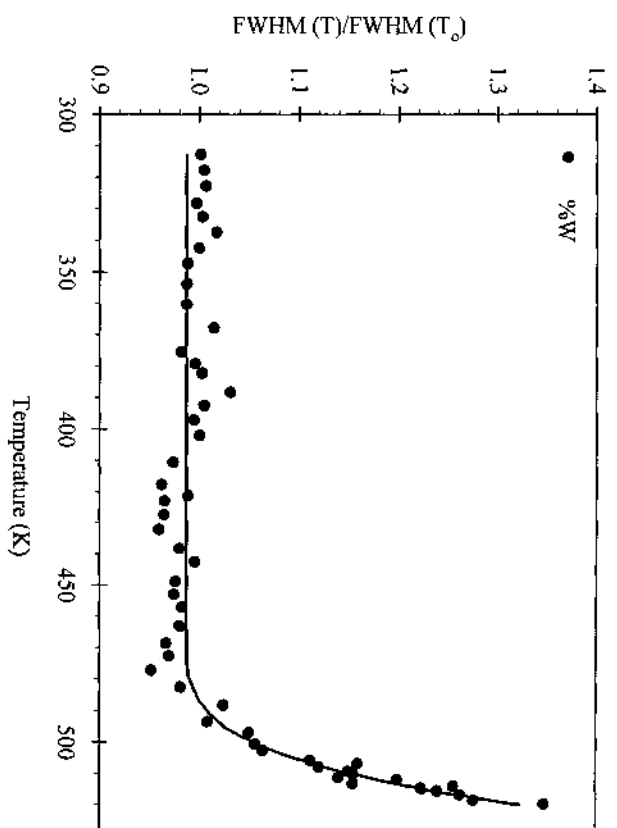


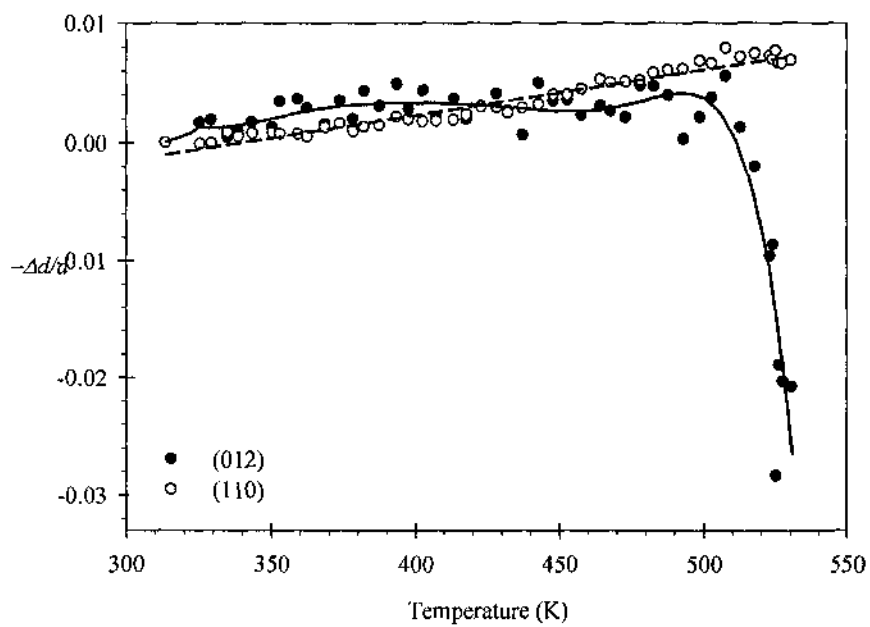
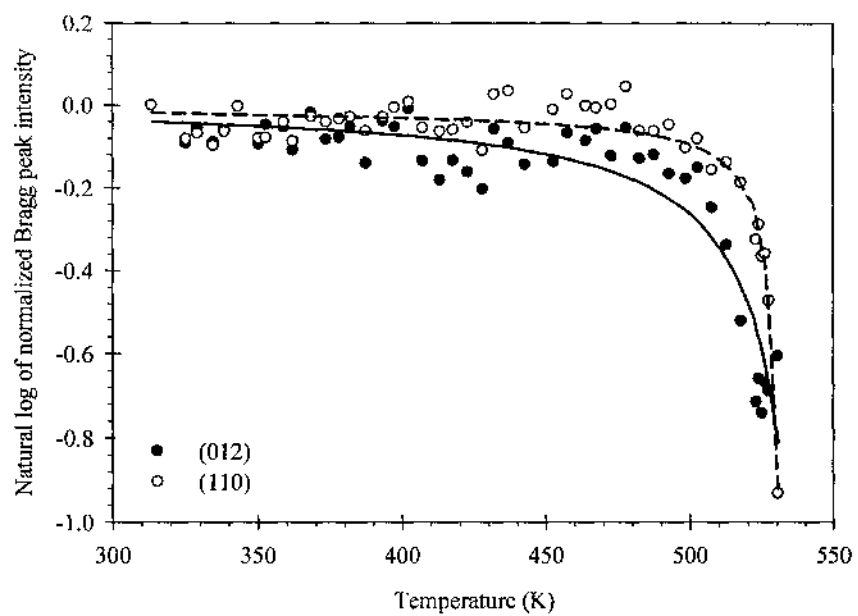
Fig. I.1. (a) Diffraction pattern of Bi nanoclusters at different temperatures and (b) the corresponding radial profile.

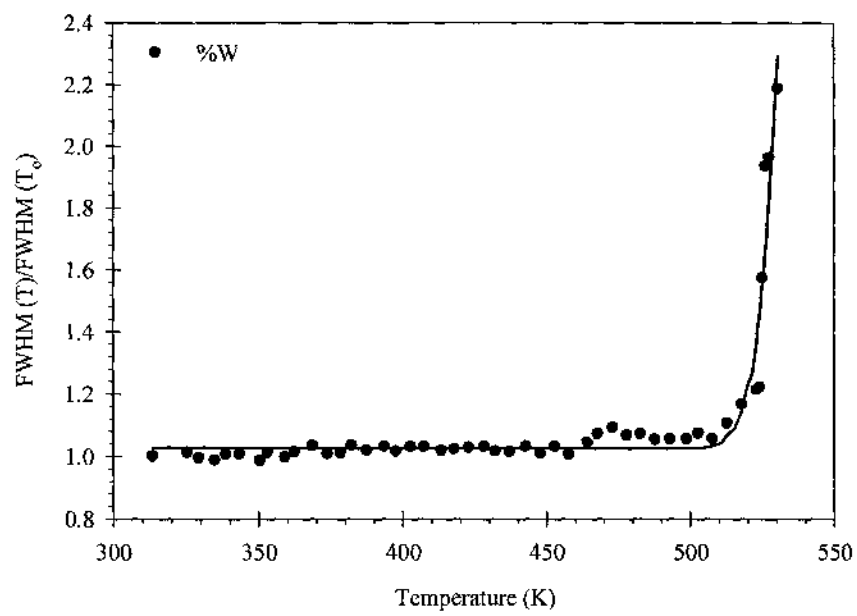
I.2. 10/29/08 - Bi Islands



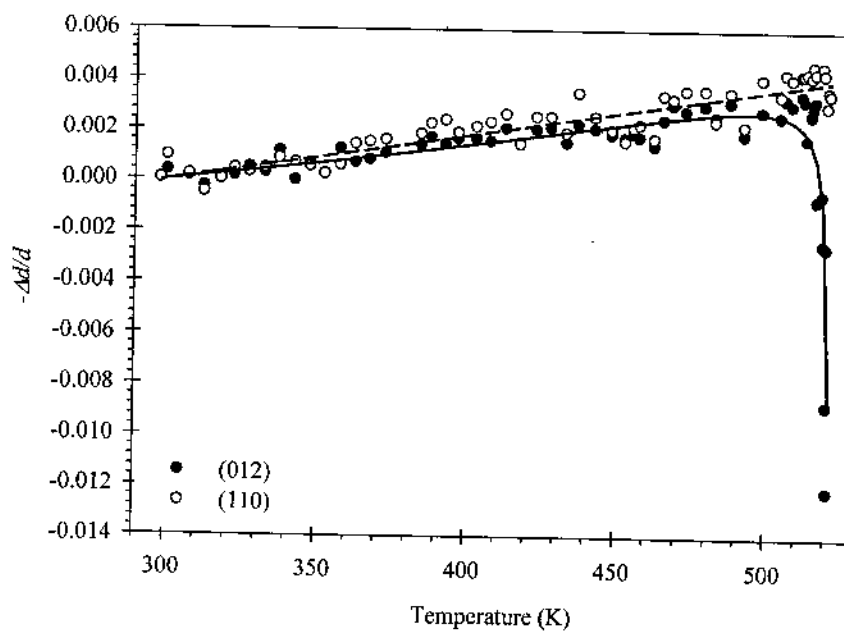
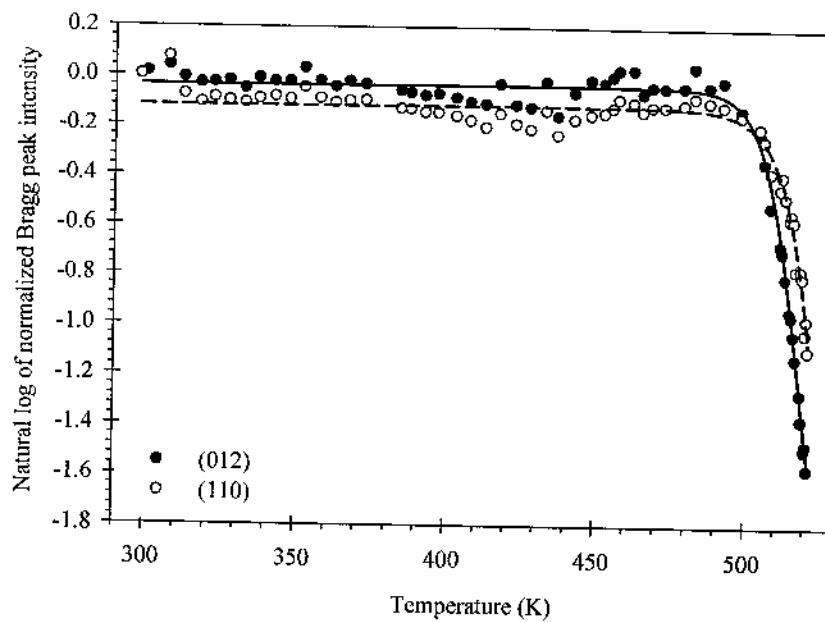


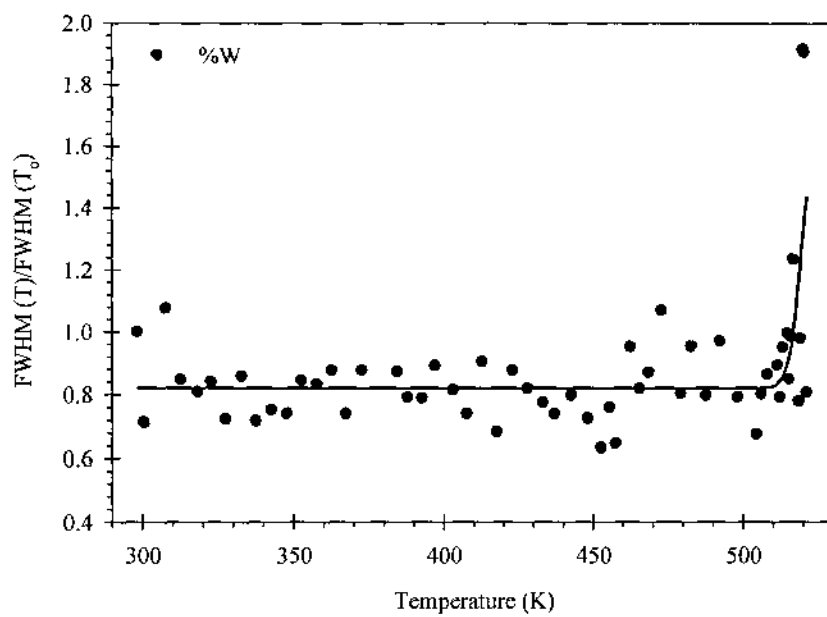
I.3. 5/21/09 - Bi Islands



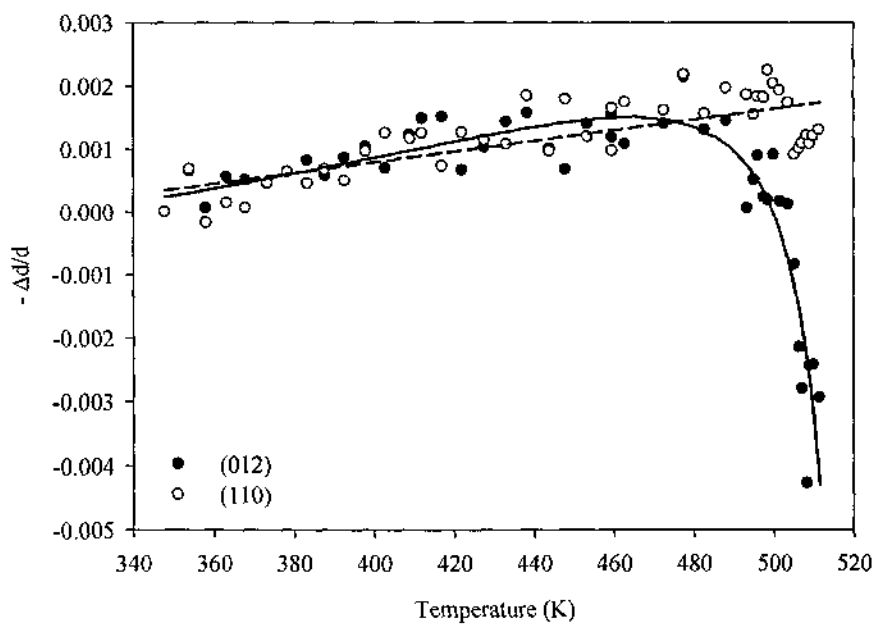
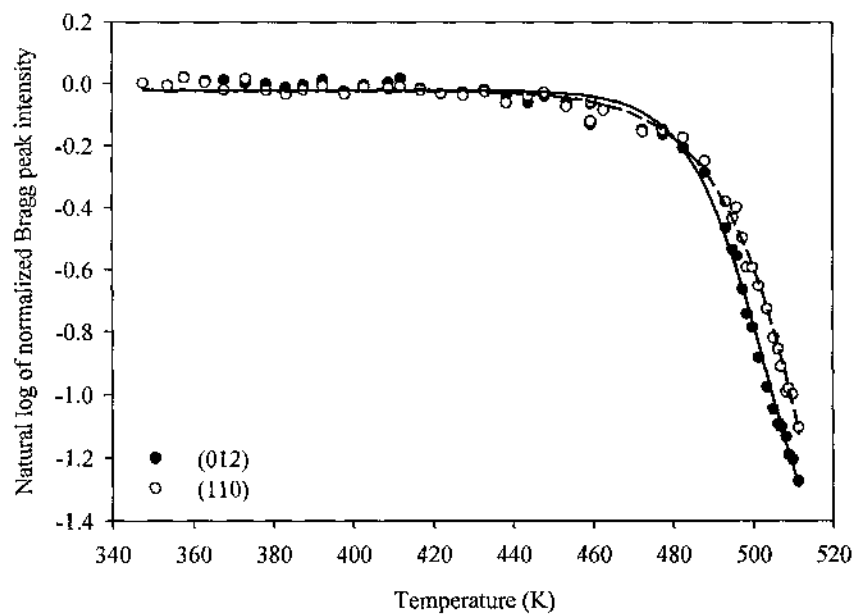


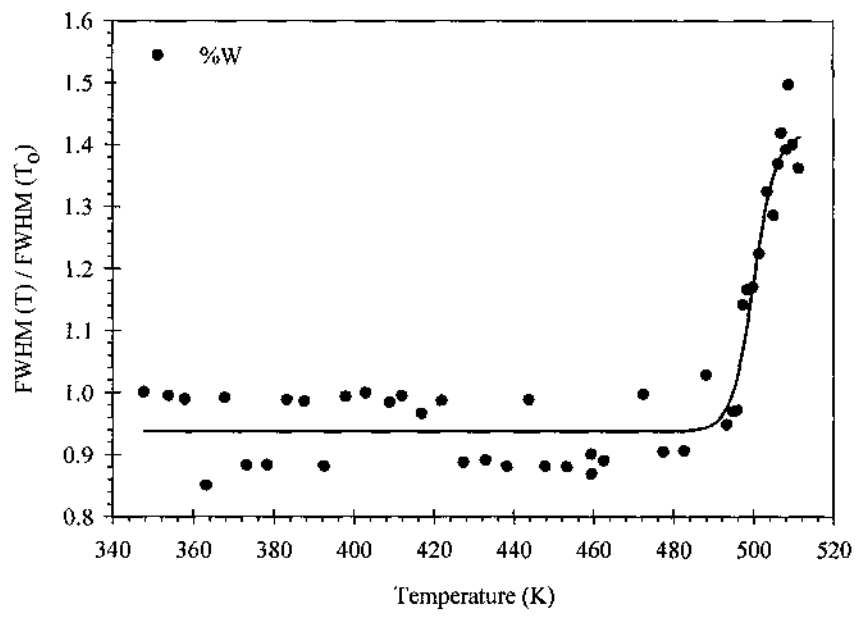
I.4. 11/26/2009 - Bi Islands



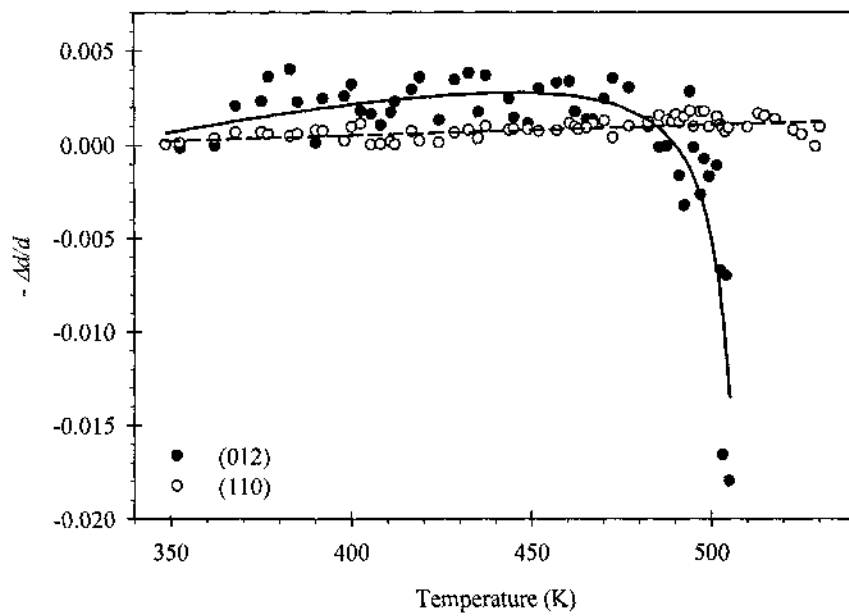
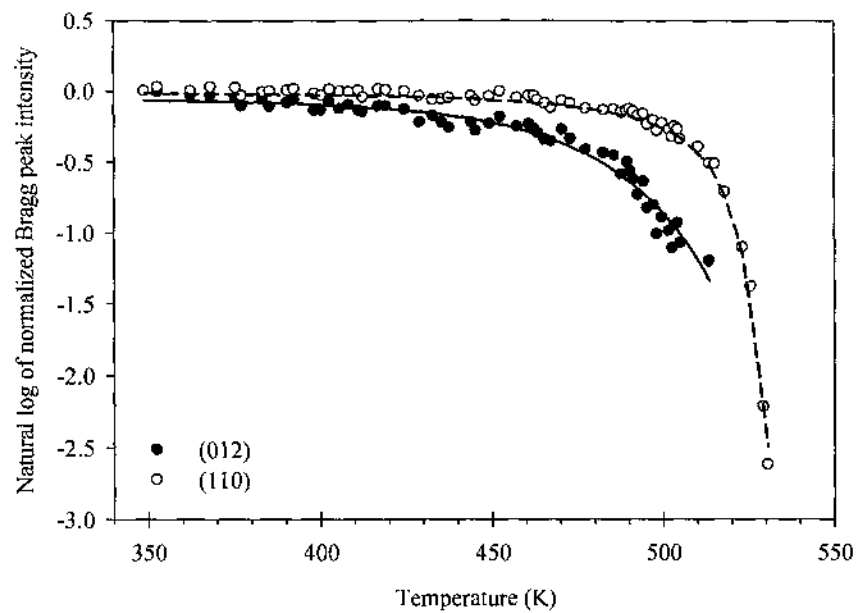


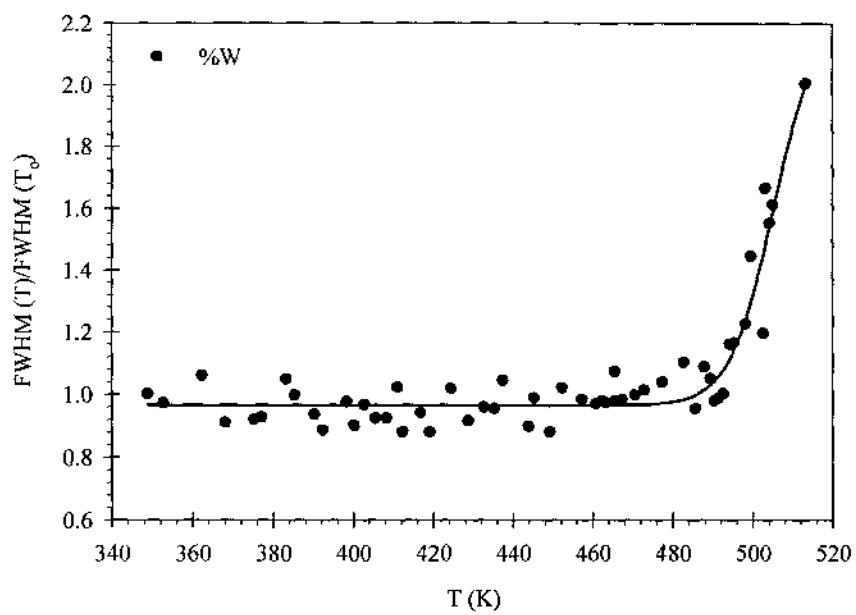
I.5. 12/2/2009 - Bi Islands



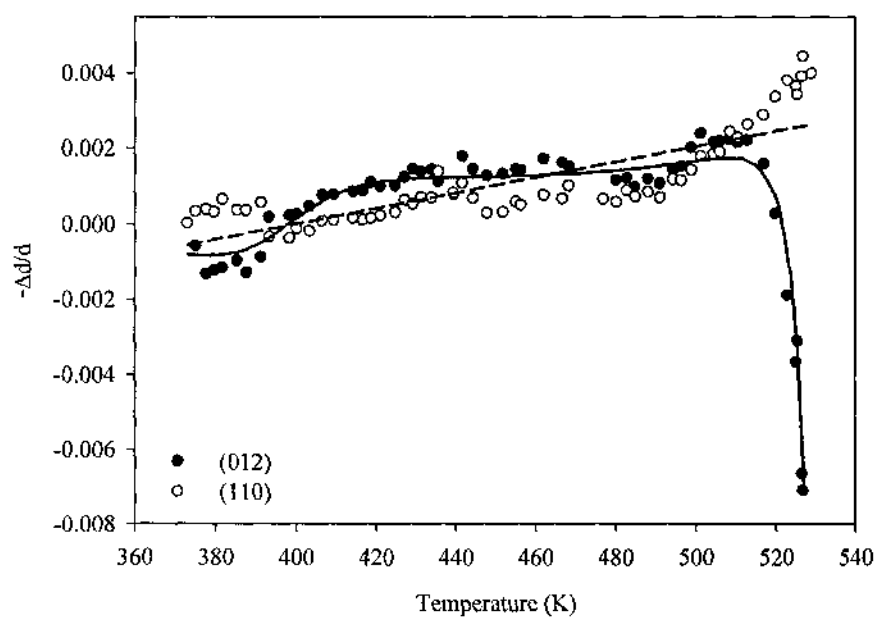
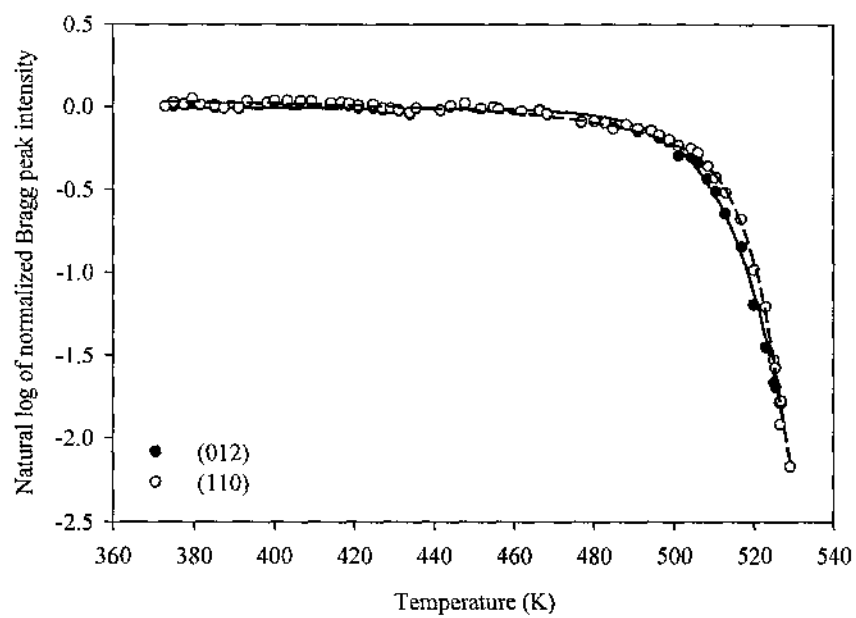


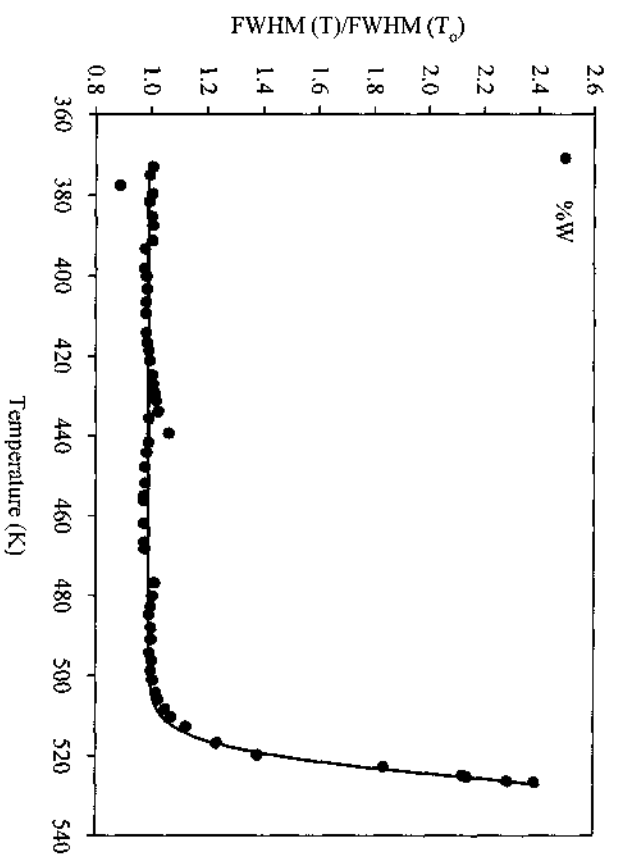
I.6. 12/3/2009 – Bi Islands



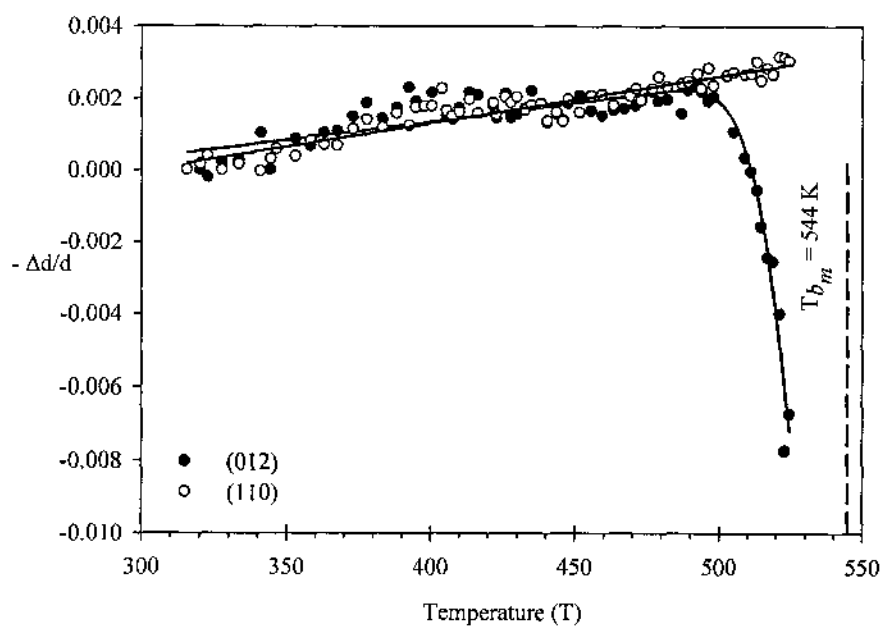
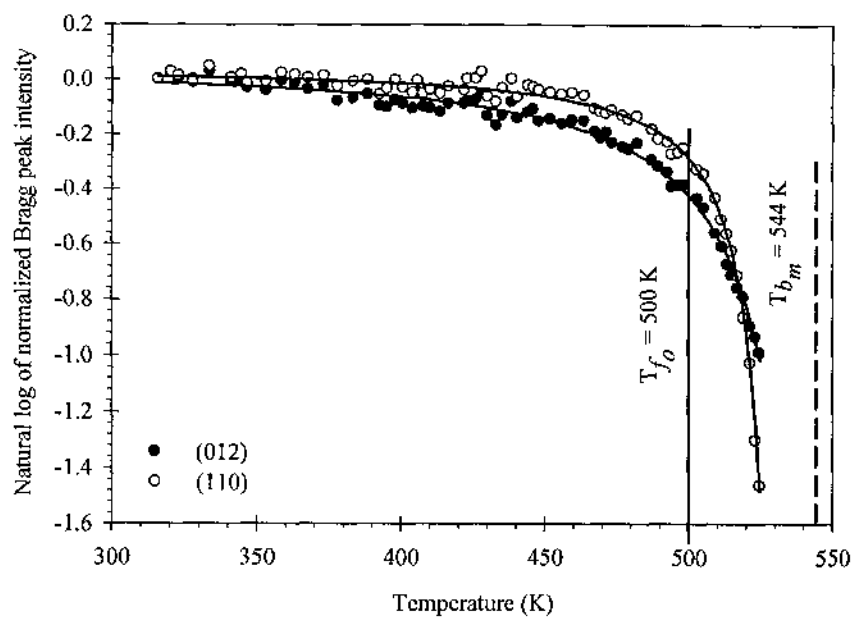


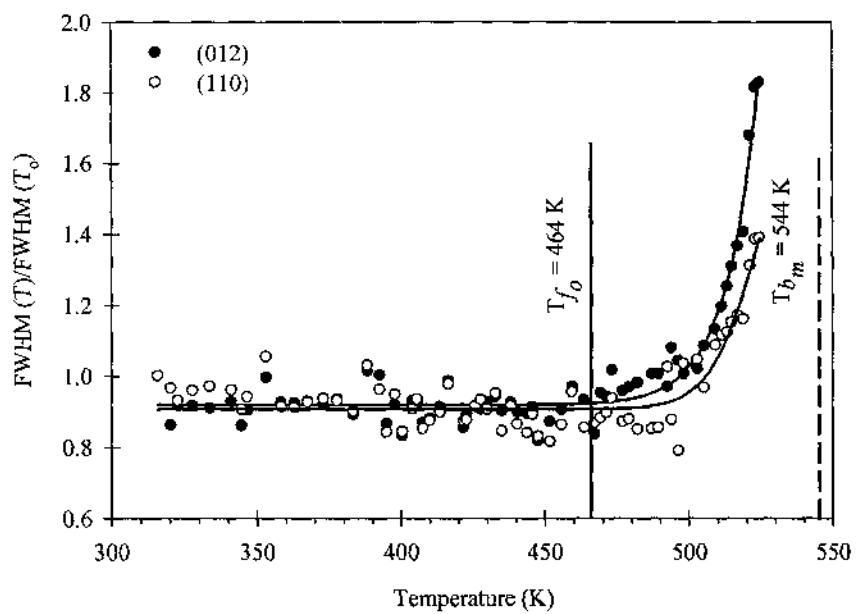
I.7. 1/28/2010 - Bi Islands





1.8. 3/16/2010 - Bi Nanoclusters



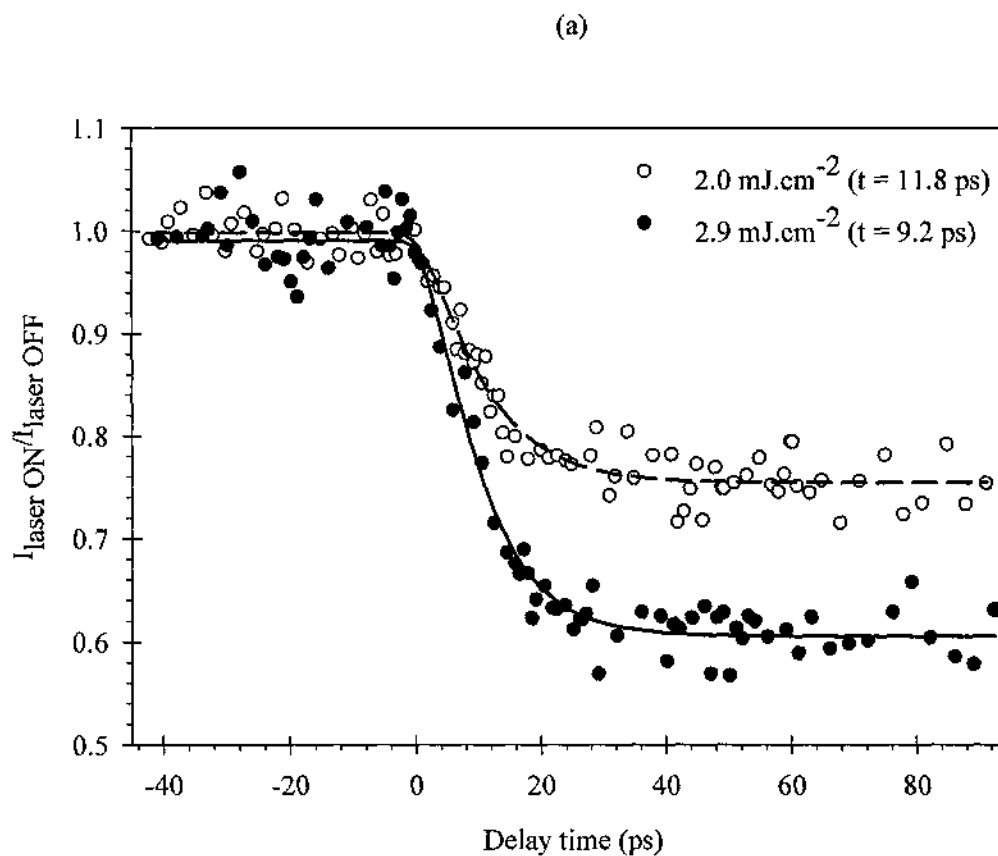


APPENDIX J
TIME-RESOLVED DATA SUMMARY COLLECTED FROM
BISMUTH NANOCCLUSERS

Note: For all runs, the UV level was as minimum as possible since we don't have means of measuring the UV power at the time of collecting the data.

J.1. Data Collected on 11/17/09,

Fig. J.1.1 Time evolution of Bragg peak intensity for (a) (012) planes, (b) (110) planes at different fluences.



(b)

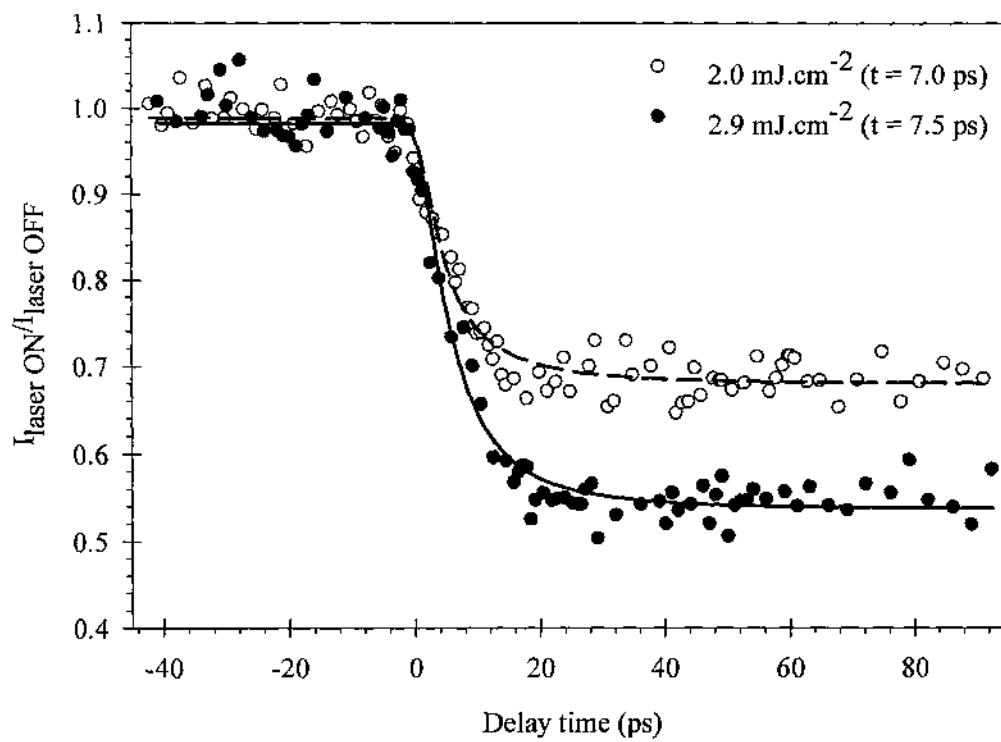
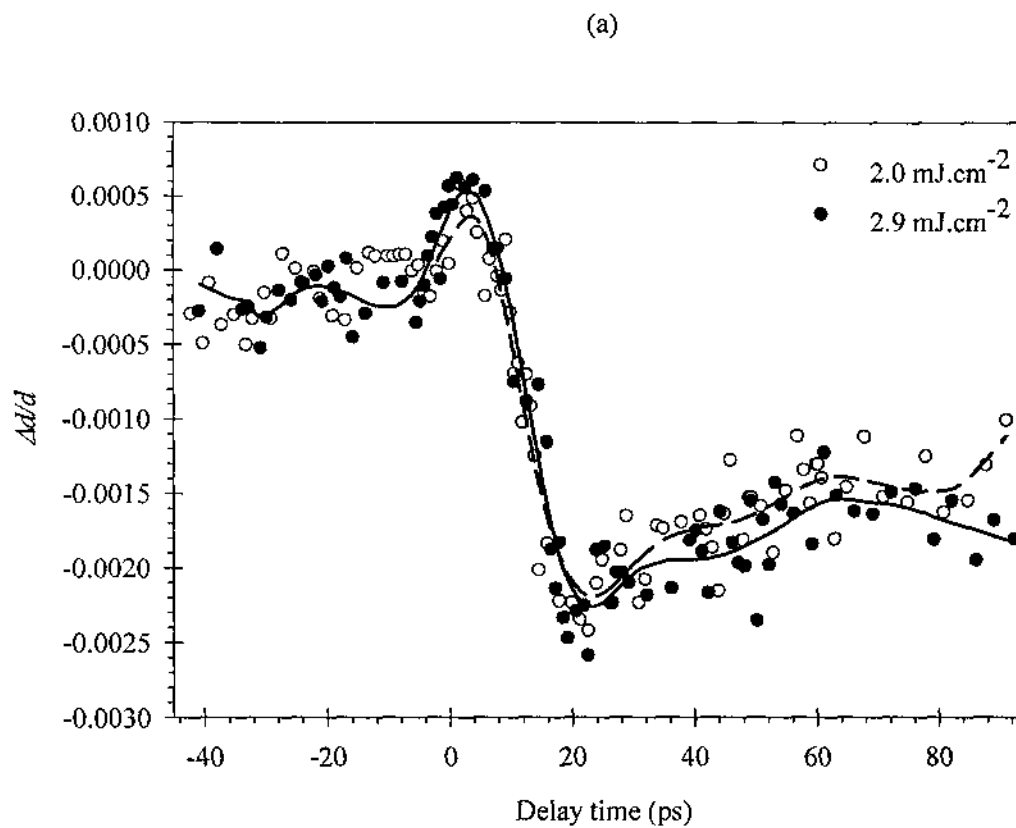


Fig. J.1.2. Time evolution of relative change in Bragg peak ring size at different fluences for (a) (012) planes and (b) (110) planes.



(b)

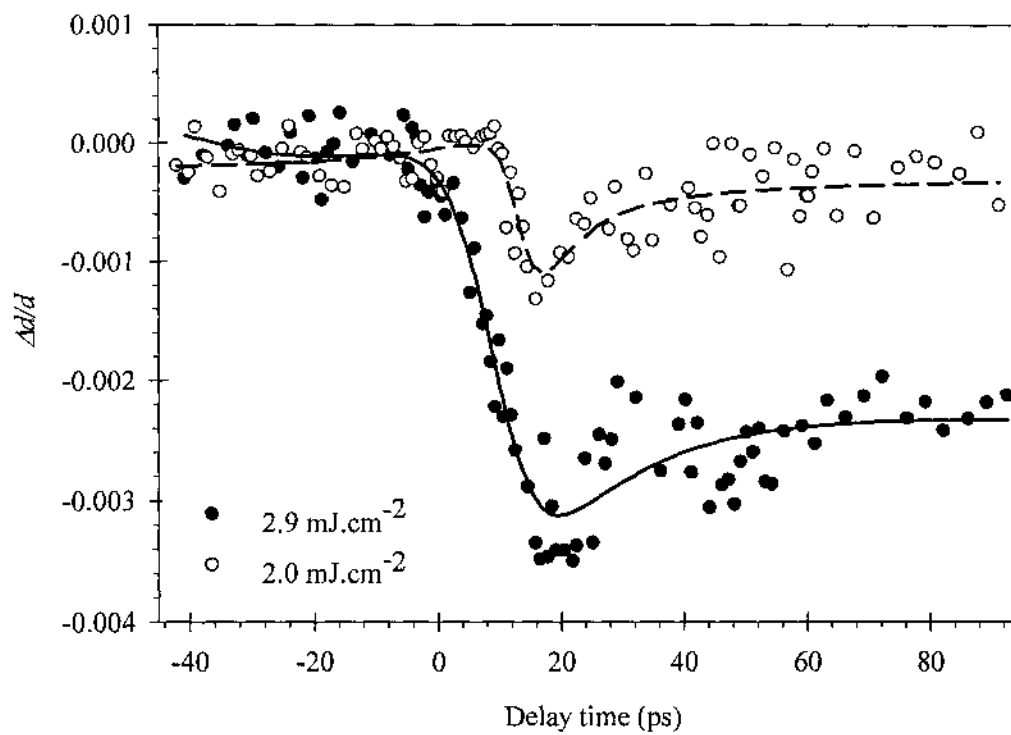
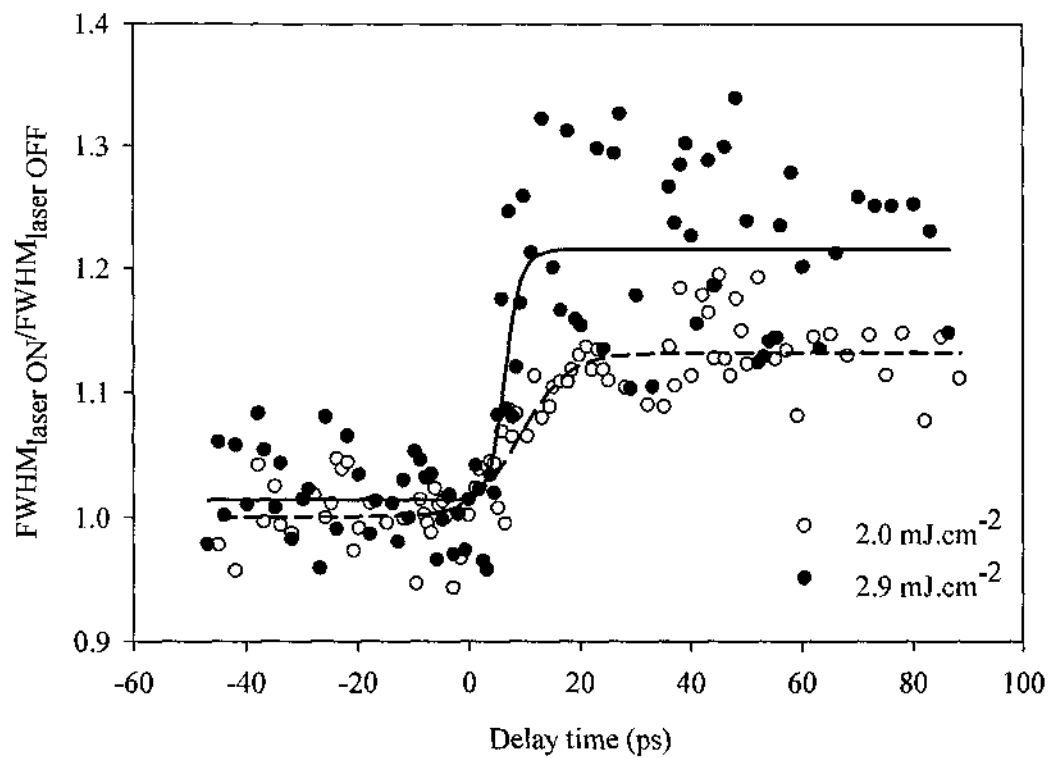
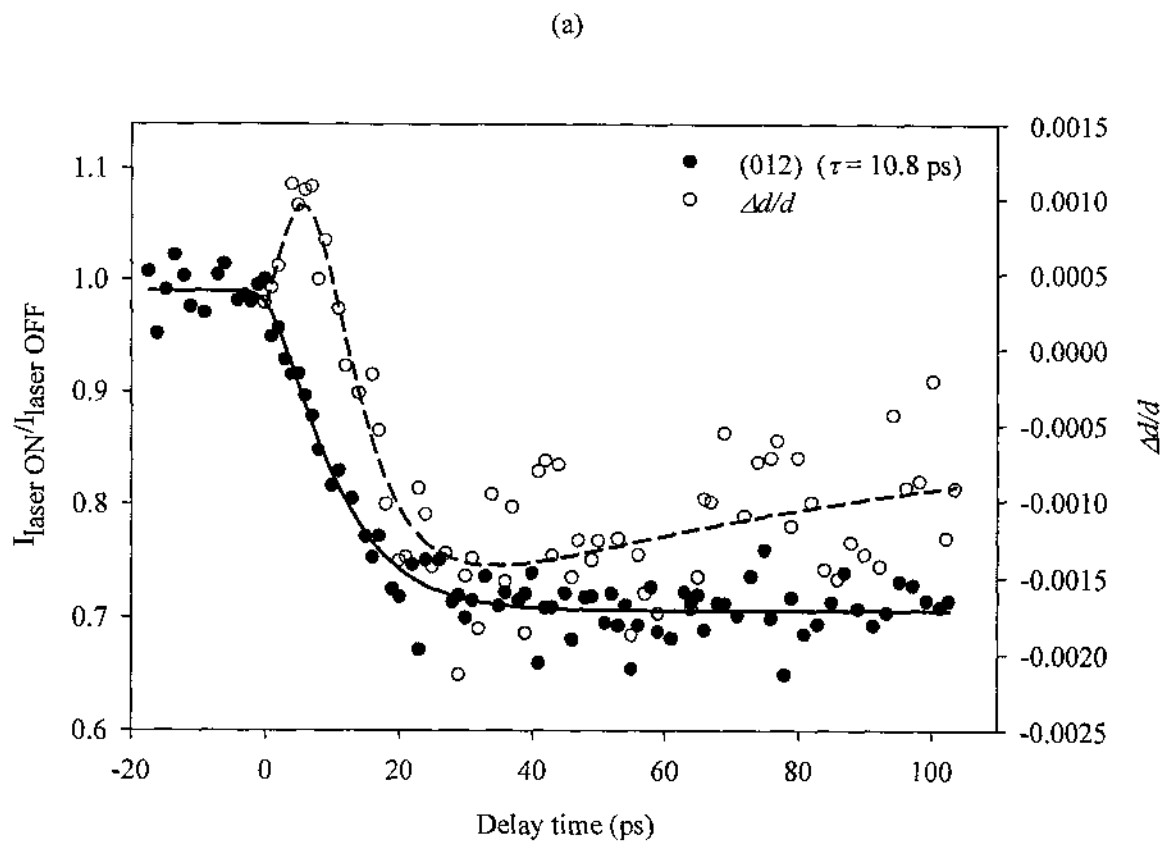


Fig. J.1.3. Time evolution of Bragg peak average FWHM at different fluences.



J.2. Data Collected on 02/11/10

Fig. J.2.1. Time evolution of Bragg peak intensity and relative change in ring radius ($\Delta d/d$) for (a) (012) planes, (b) (110) planes at 2.4 mJ.cm^{-2} laser fluence.



(b)

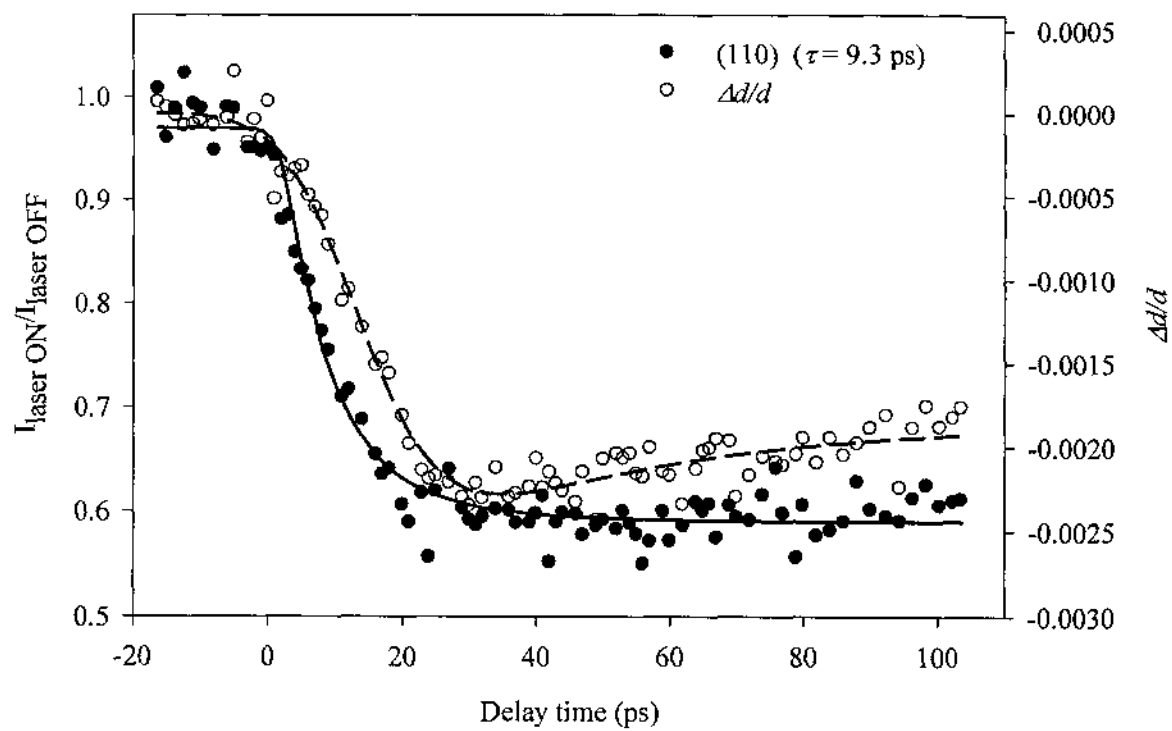
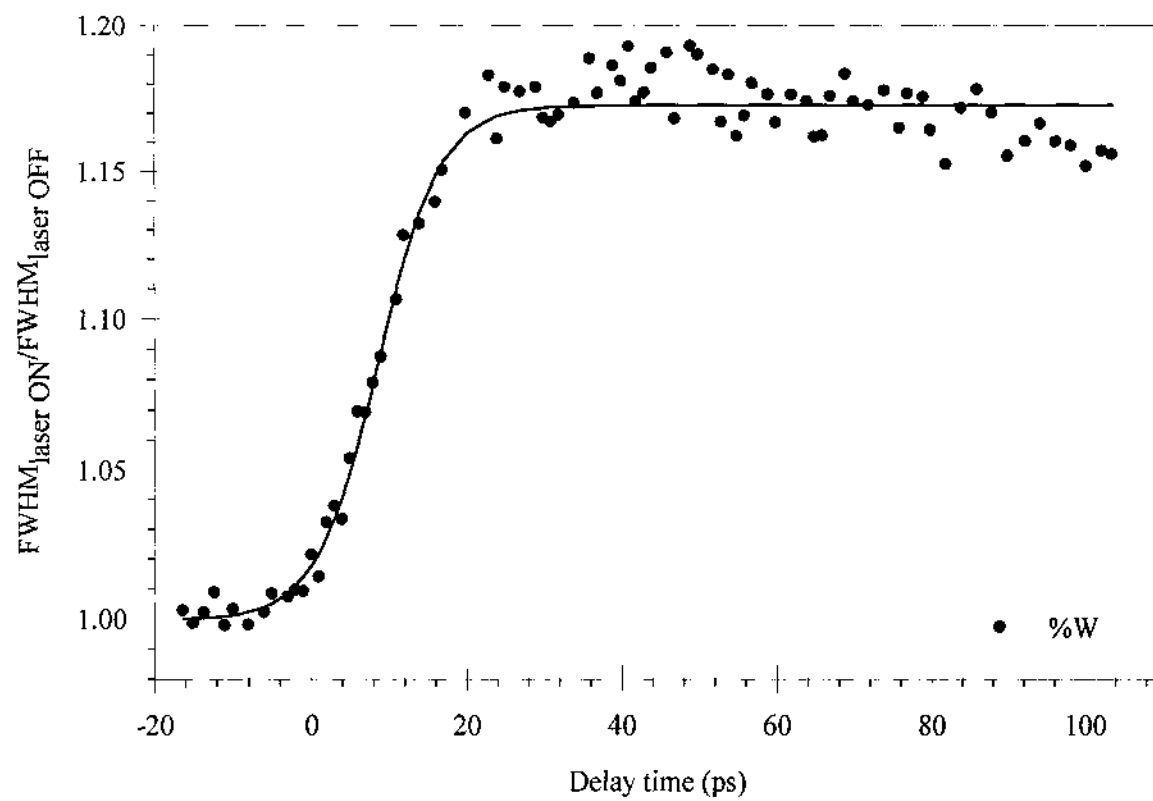
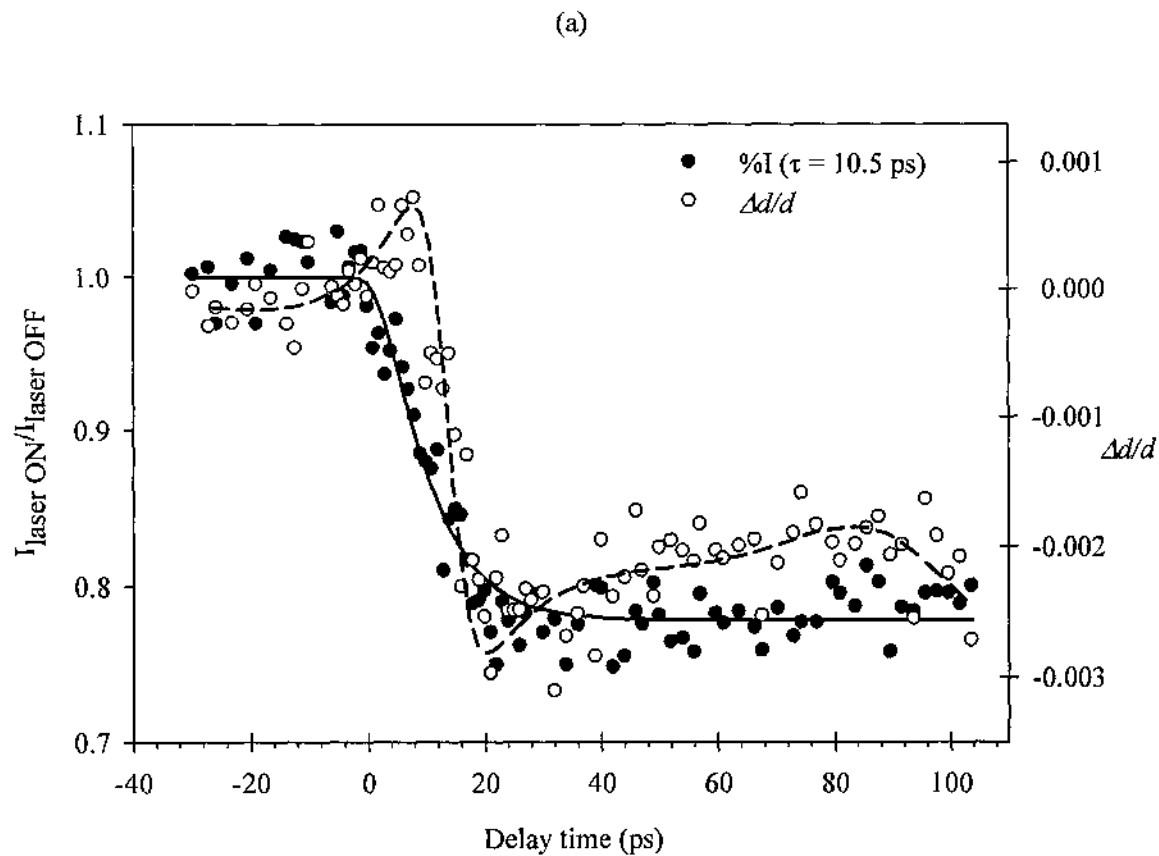


Fig. J.2.1 (c) Time evolution of Bragg peak FWHM at 2.4 mJ.cm^{-2} laser fluence.

J.3. Data Collected on 02/12/10

Fig. J.3.1. Time evolution of Bragg peak intensity (black) and relative change in ring radius ($\Delta d/d$) for (a) (012) planes, (b) (110) planes at $2.1 \text{ mJ}\cdot\text{cm}^{-2}$ laser fluence.



(b)

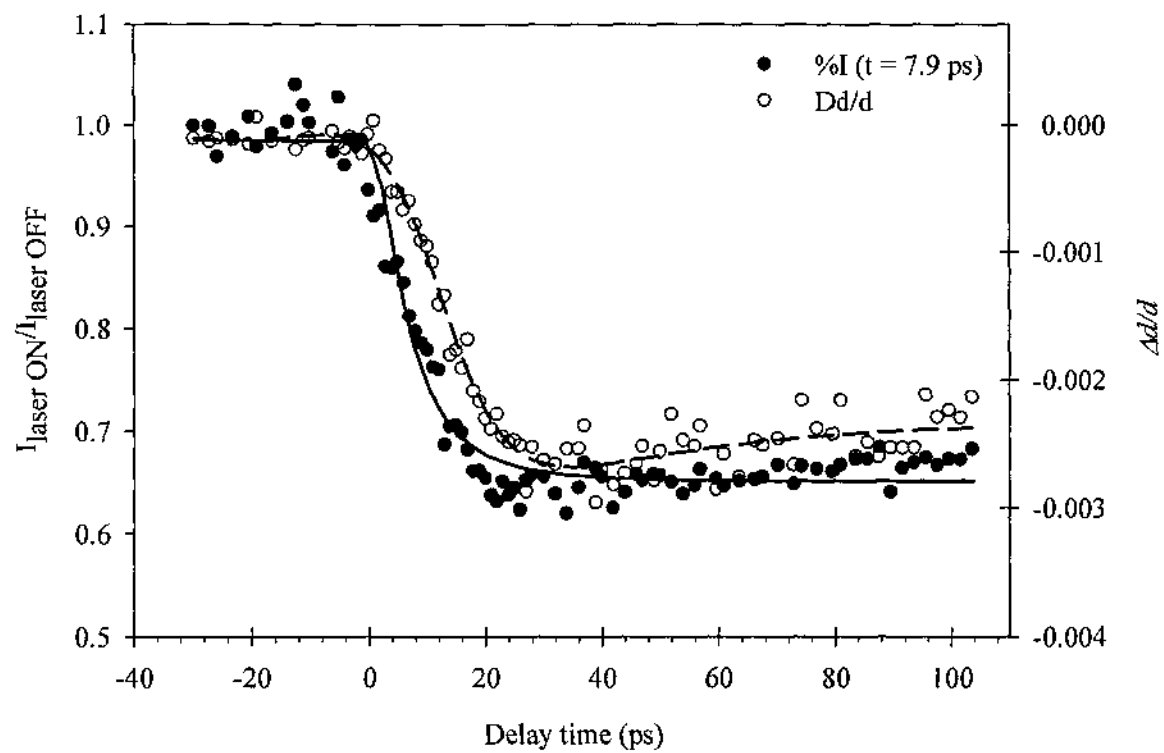
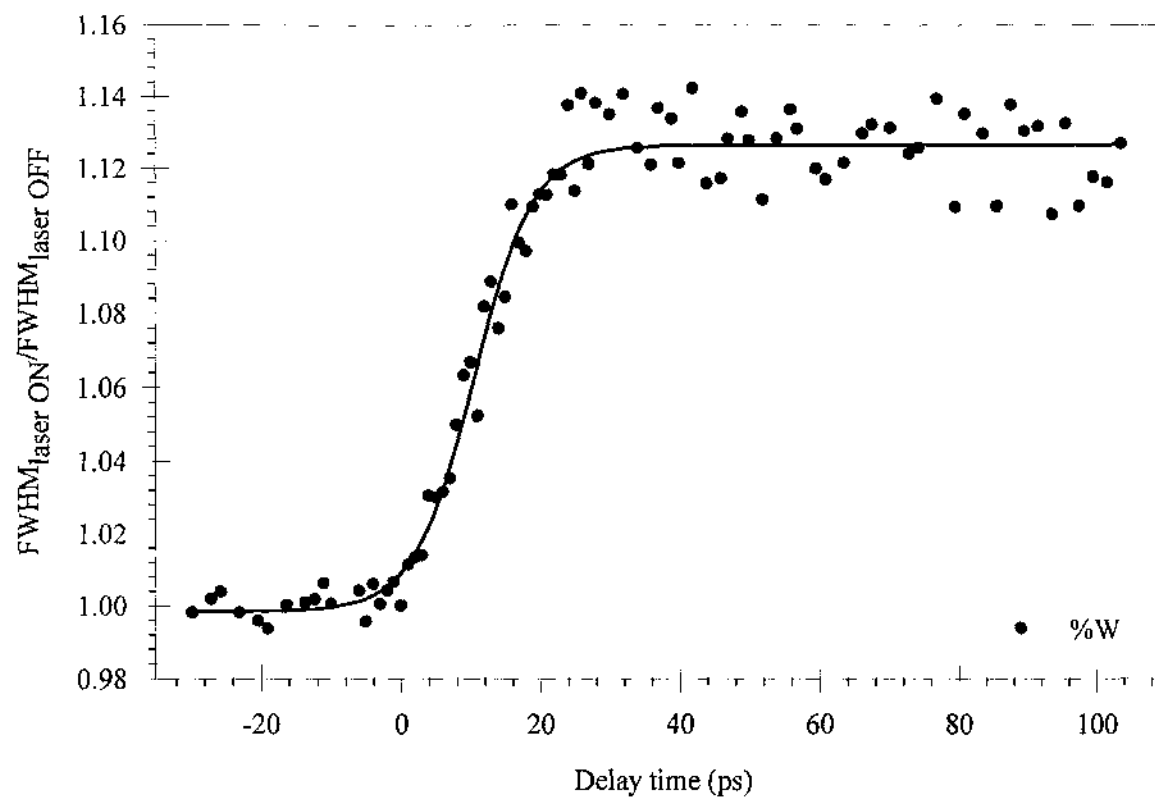
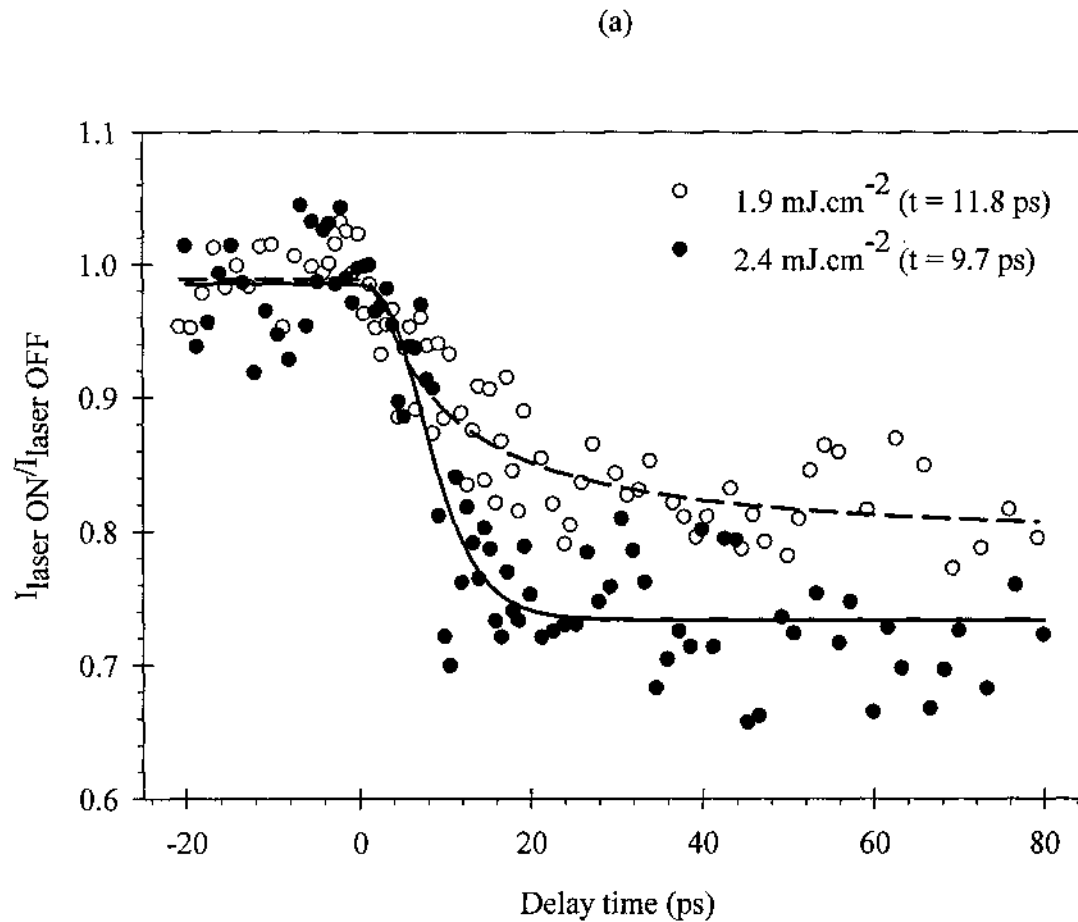


Fig. J.3.2. Time evolution of Bragg peak FWHM at 2.1 mJ.cm^{-2} laser fluence.

J.4. Data Collected on 08/19/2010

Fig. J.4.1. Time evolution of relative change in Bragg peak intensity at different fluences for (a) (012) planes and (b) (110) planes.



(b)

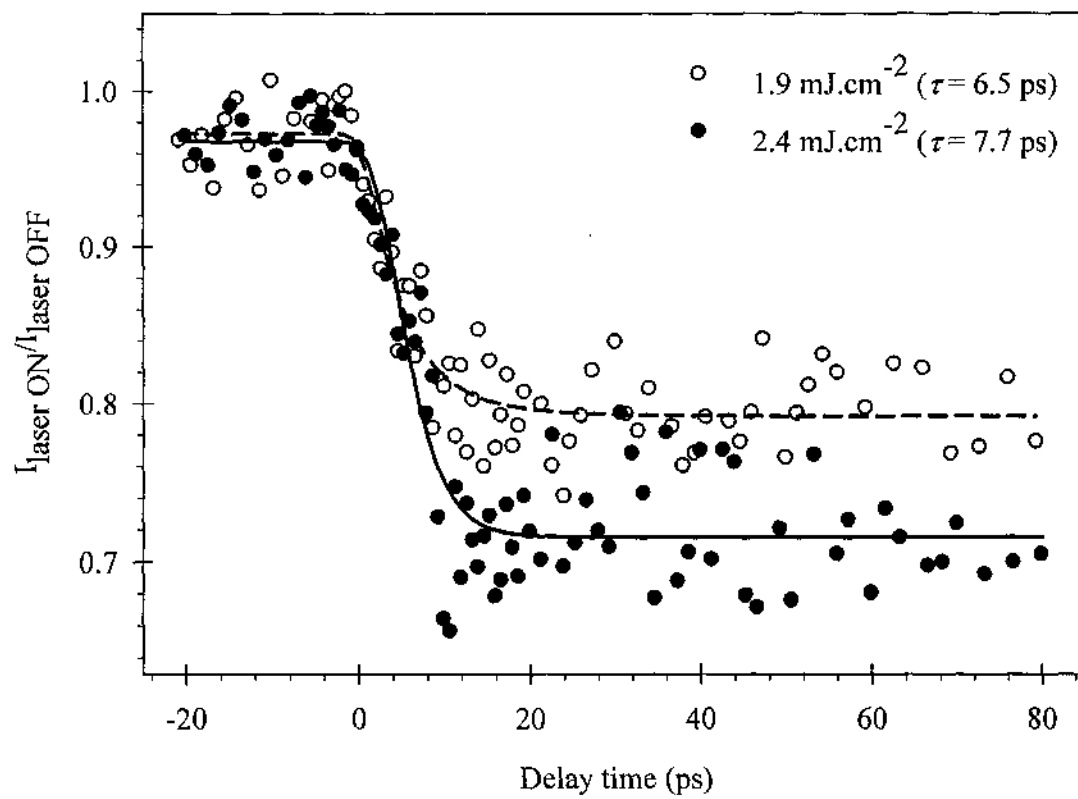
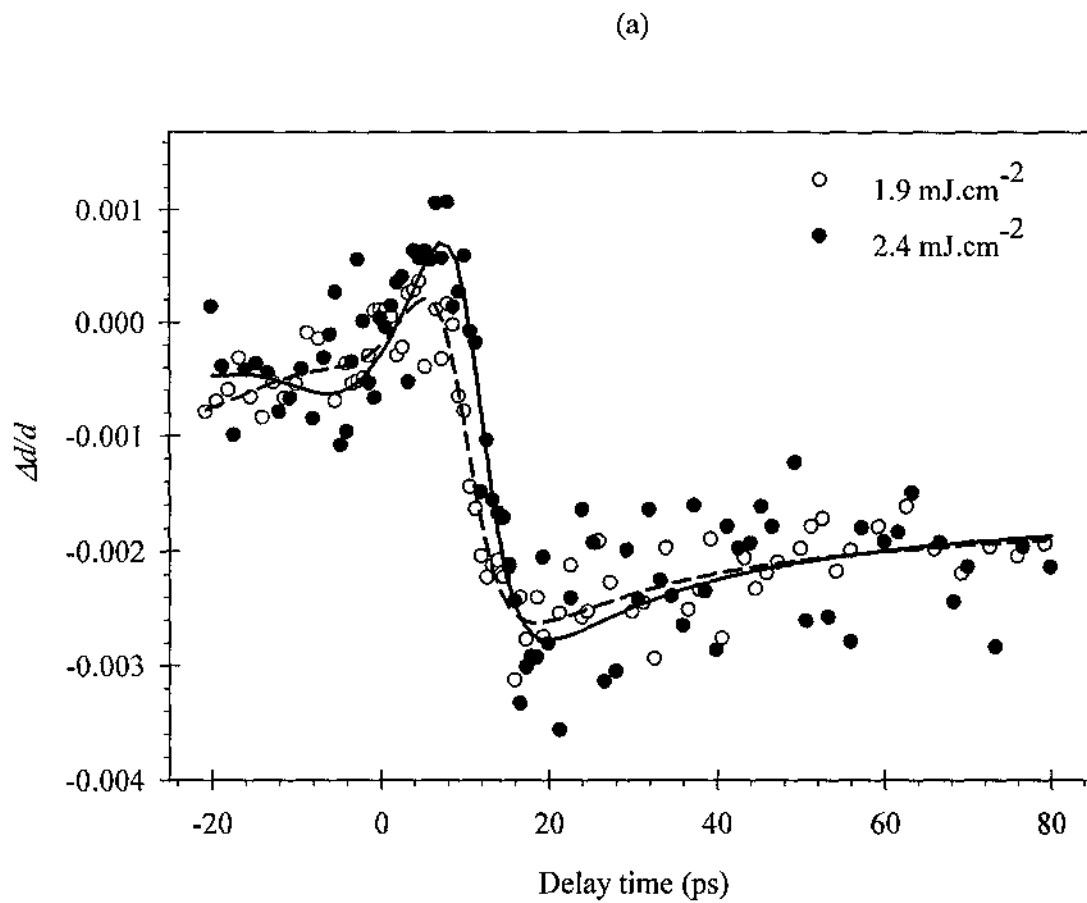


Fig. J.4.2. Time evolution of relative change in Bragg peak ring radius at different fluences for (a) (012) planes and (b) (110) planes.



(b)

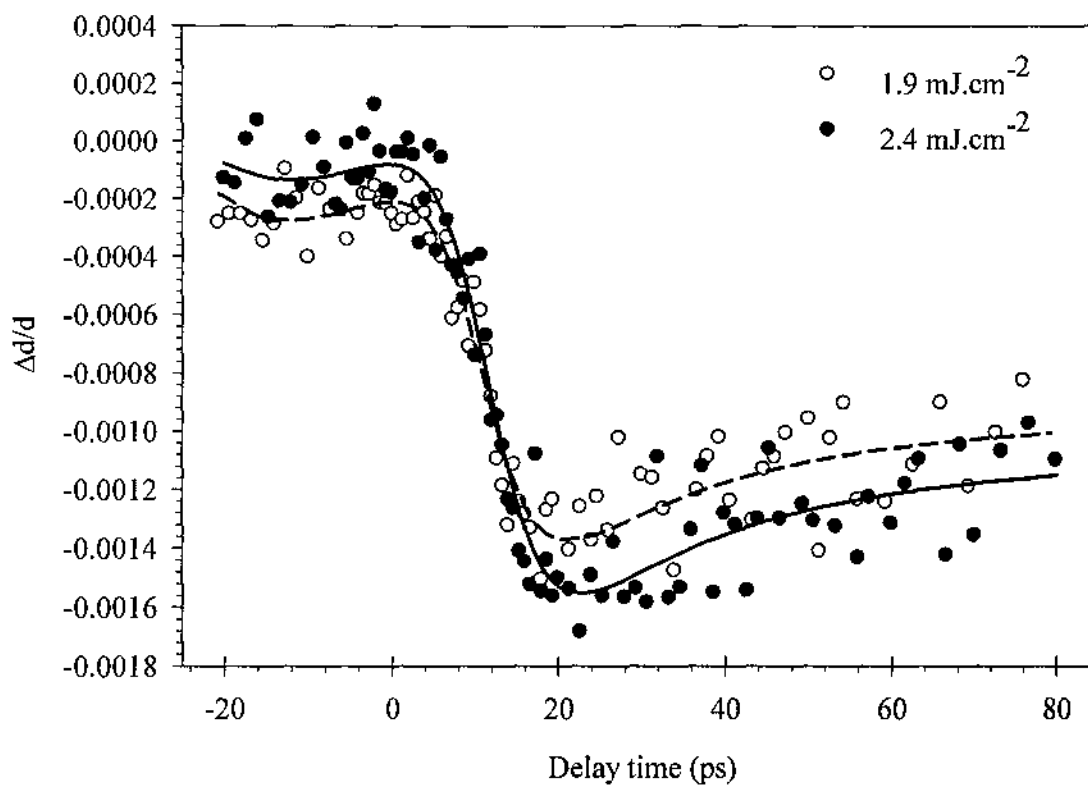


Fig. J.4.3. Time evolution of relative change in Bragg peak FWHM at different fluences.

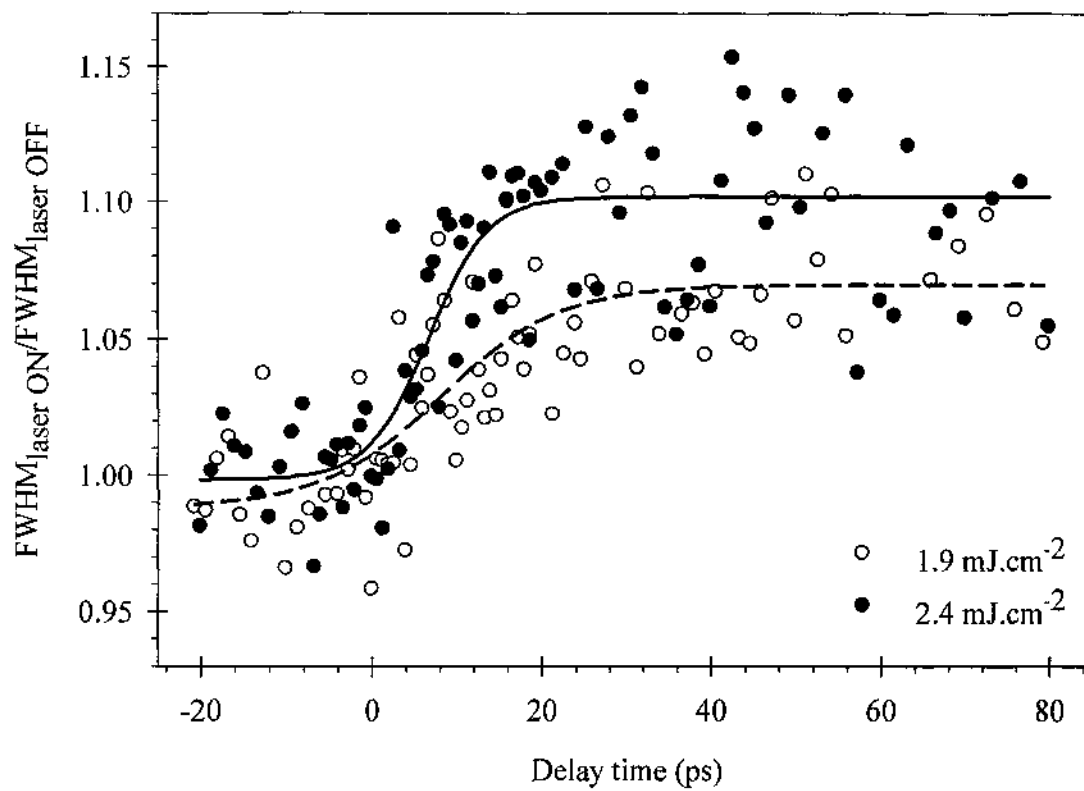
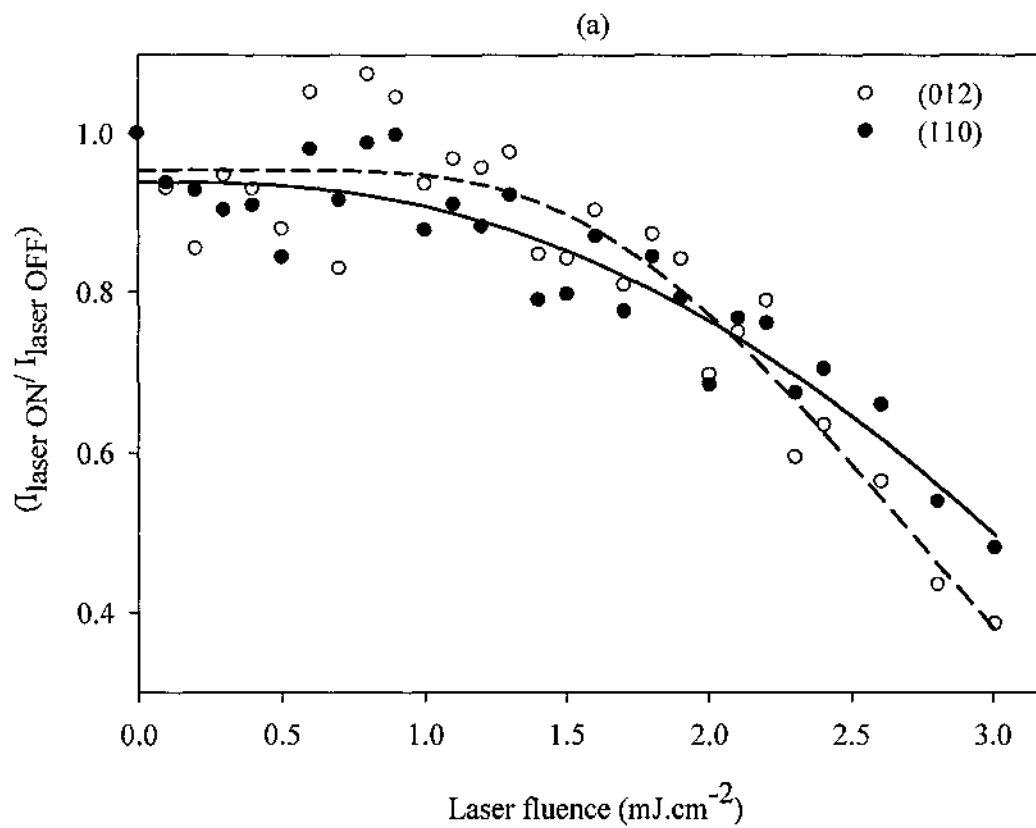
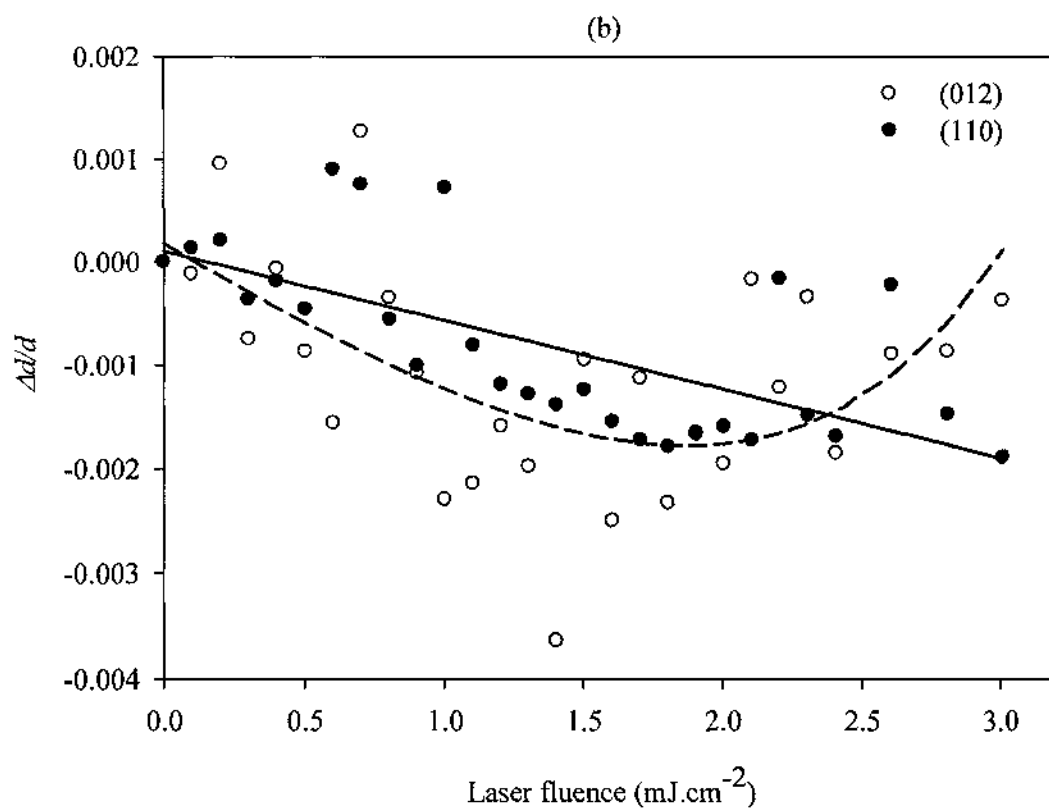
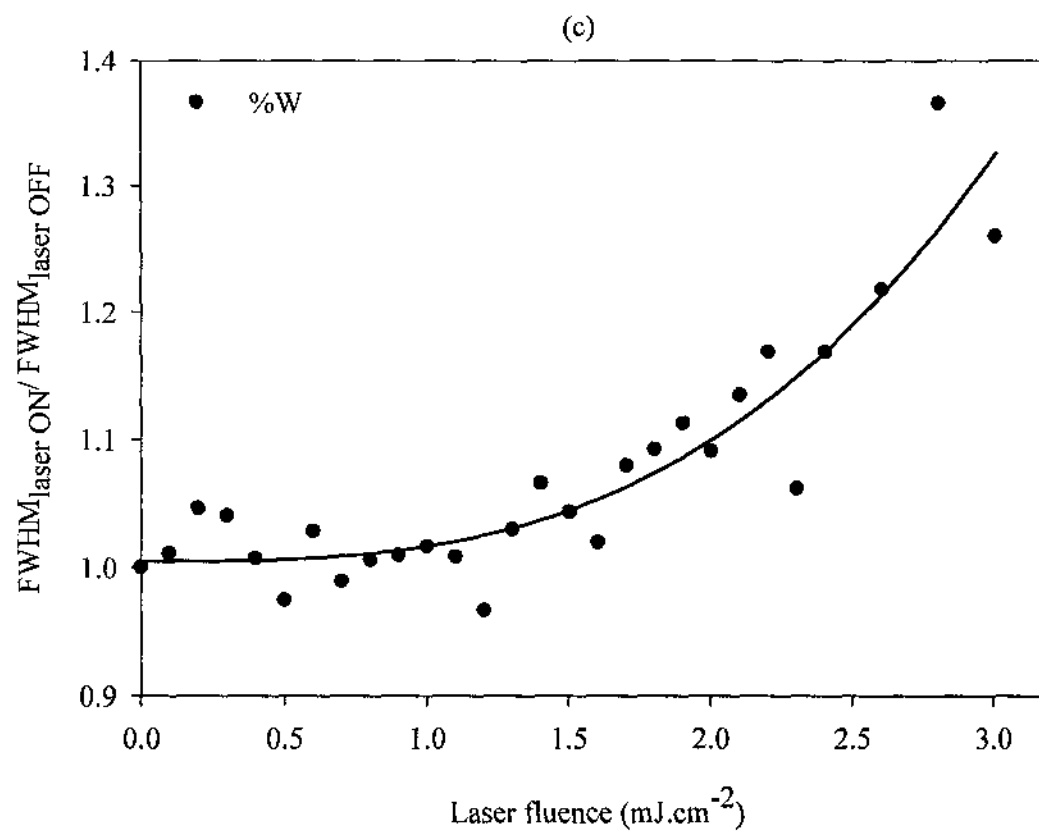


Fig. J.5. Fluence dependence of the Bragg (a) peak intensity, (b) $\Delta d/d$, and (c) normalized FWHM.

08/19/10







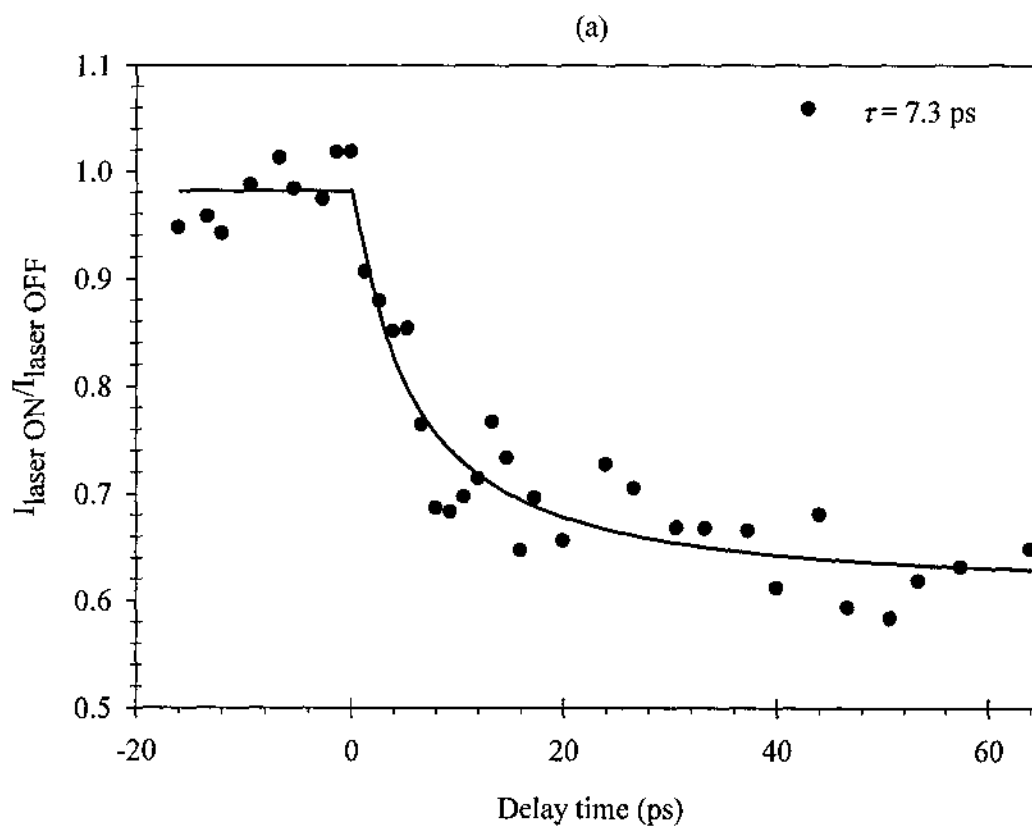
APPENDIX K

TIME-RESOLVED DATA SUMMARY COLLECTED FROM BI ISLANDS

I noticed that the Bragg peak ring size ($\Delta d/d$), for Bi islands did not give any useful information, just data points scattered everywhere.

K.1. Data Collected on 09/03/09

Fig. K.1.1 Time evolution of Bragg peak intensity for (a) (012) planes, (b) (110) planes at laser fluence = 2.4 mJ.cm^{-2} .



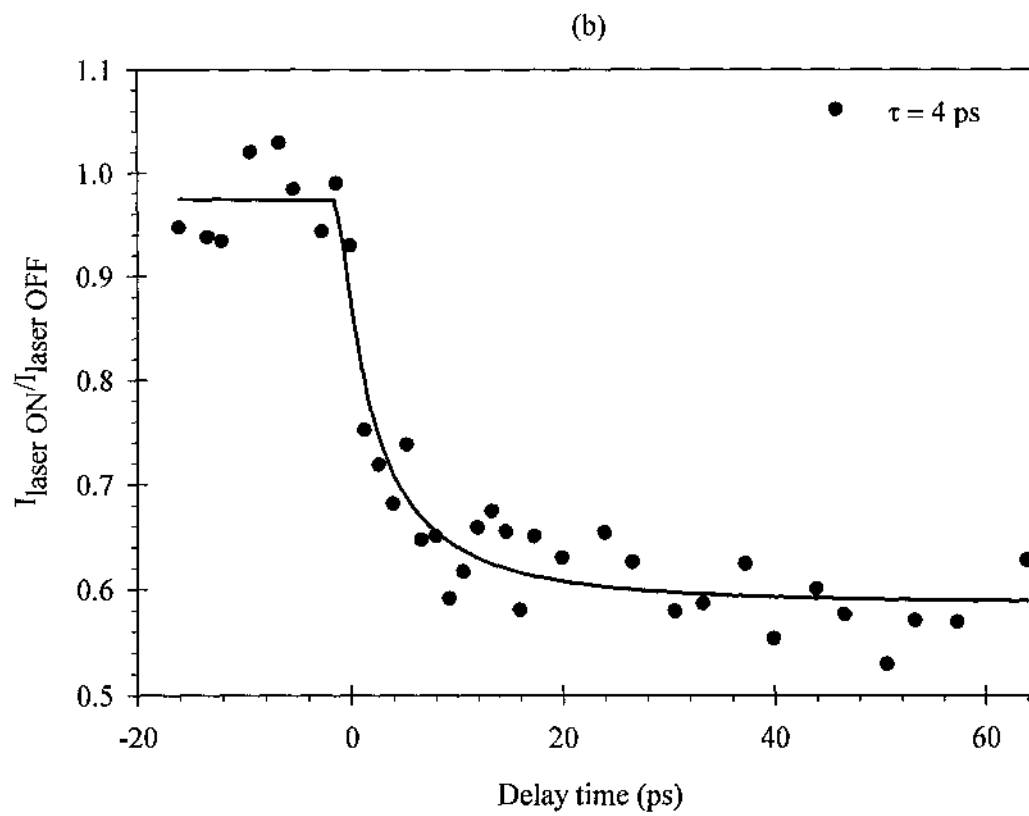
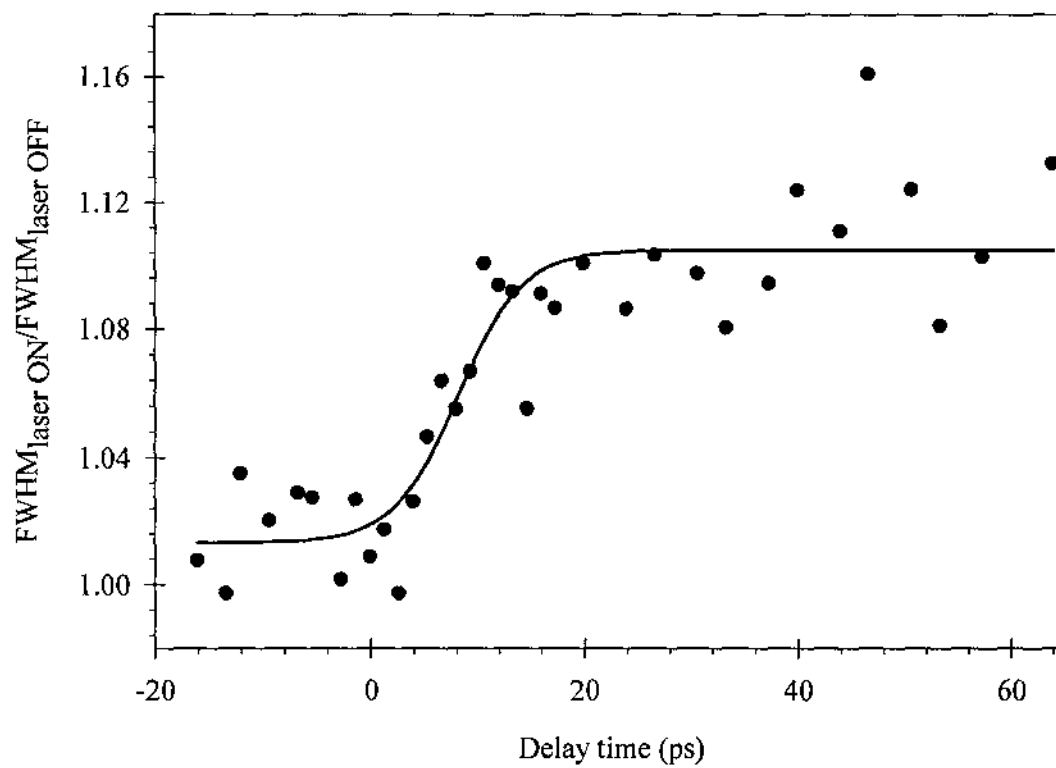
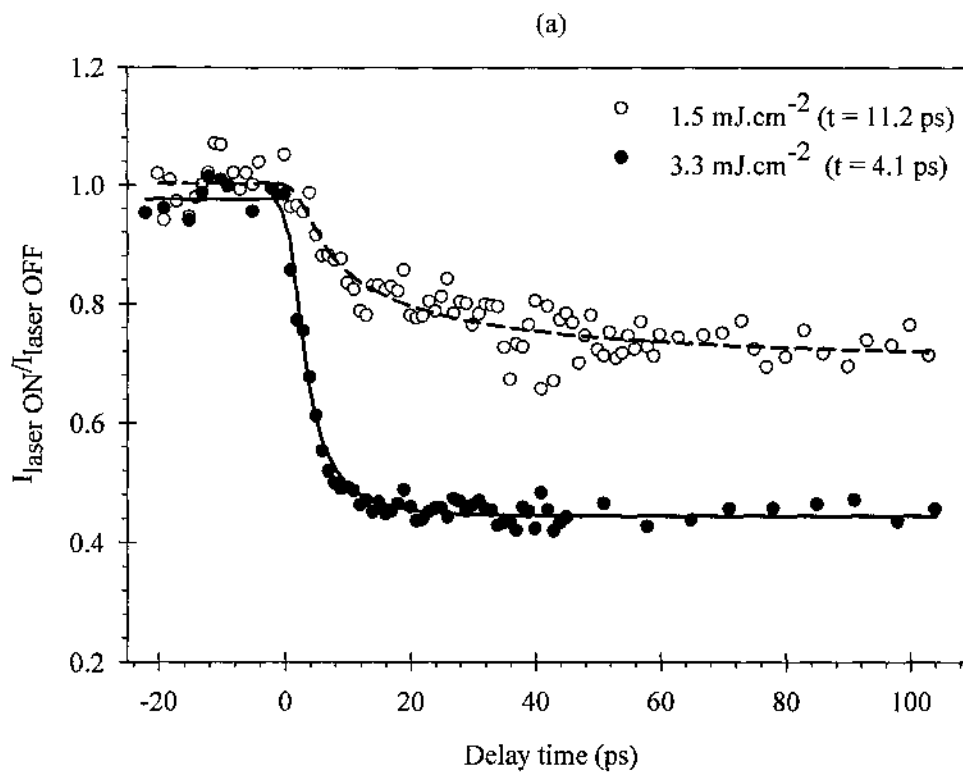


Fig. K.1.2. Time evolution of Bragg peak FWHM at laser fluence = 2.4 mJ.cm^{-2} .

K.2. Data Collected on 06/11/2009

Fig. K.2.1. Time evolution of Bragg peak intensity for (a) (012) planes, (b) (110) planes at two different fluences.



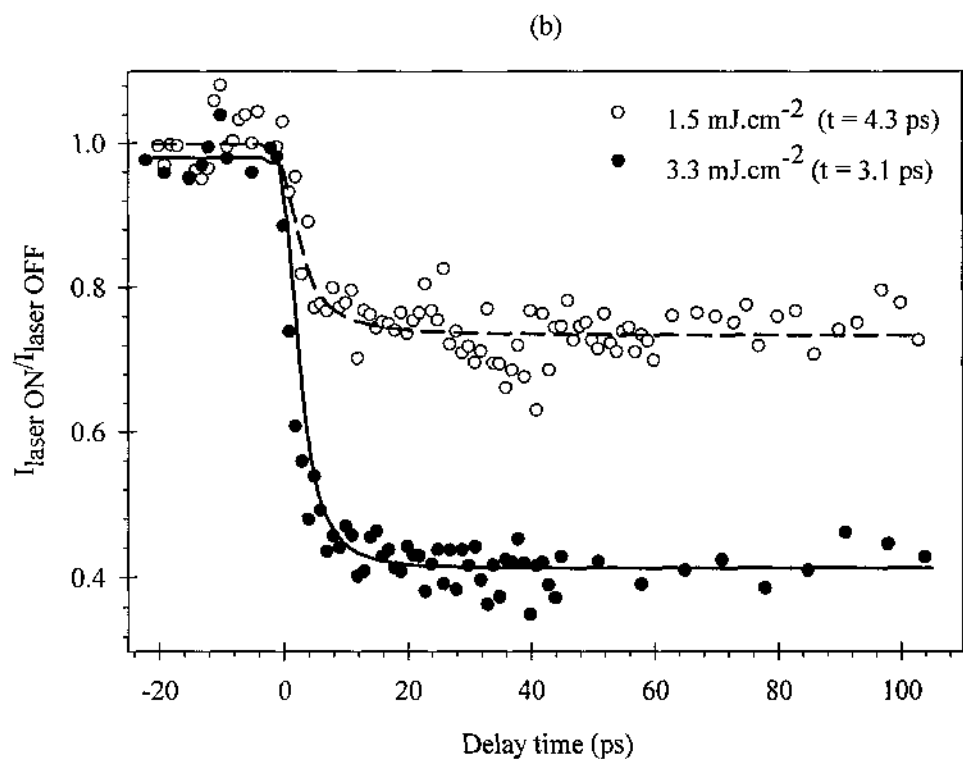
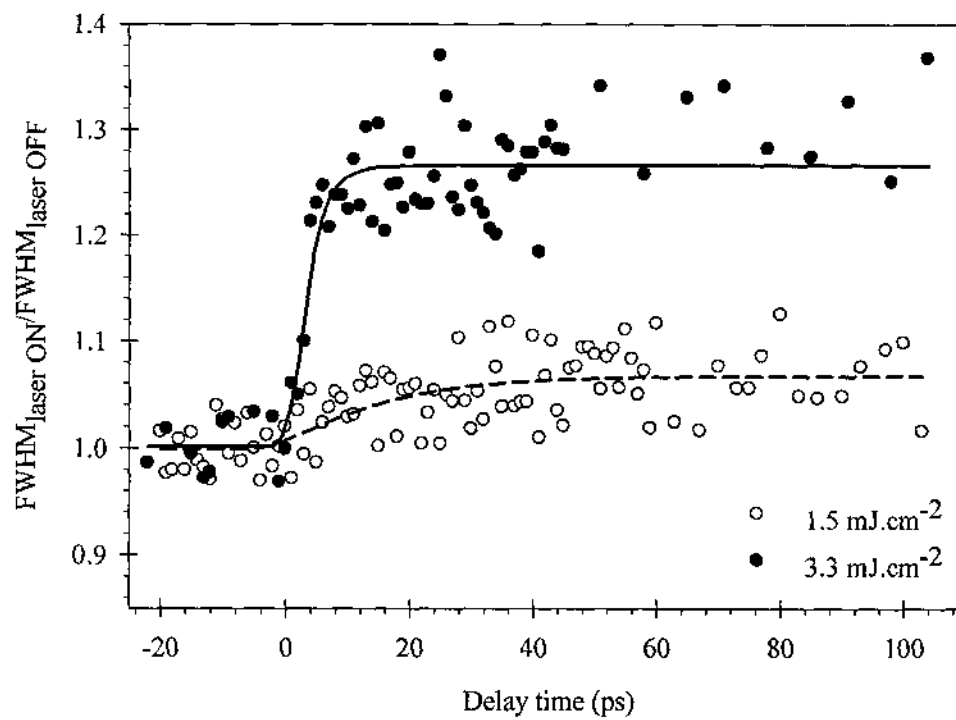
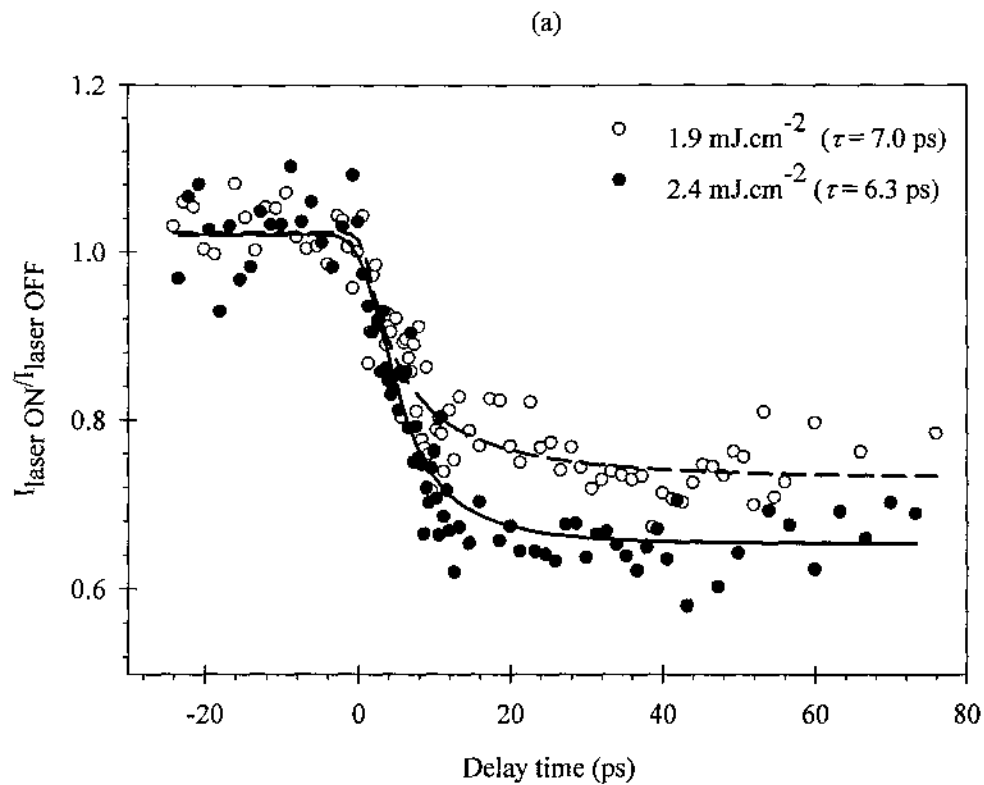


Fig. K.2.2. Time evolution of relative change in Bragg peak FWHM at different fluences.



K.3. Data Collected on 08/14/2010

Fig. K.3.1. Time evolution of Bragg peak intensity for (a) (012) planes and (b) (110) planes at two different fluences.



(b)

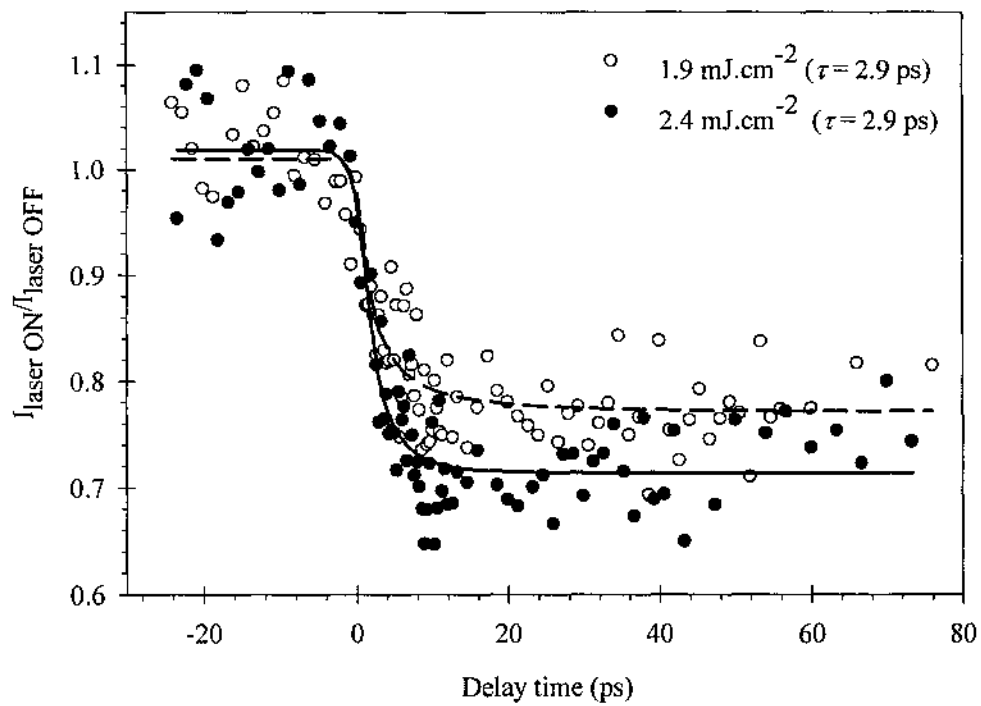


Fig. K.3.2. Time evolution of Bragg peak FWHM at different fluences.

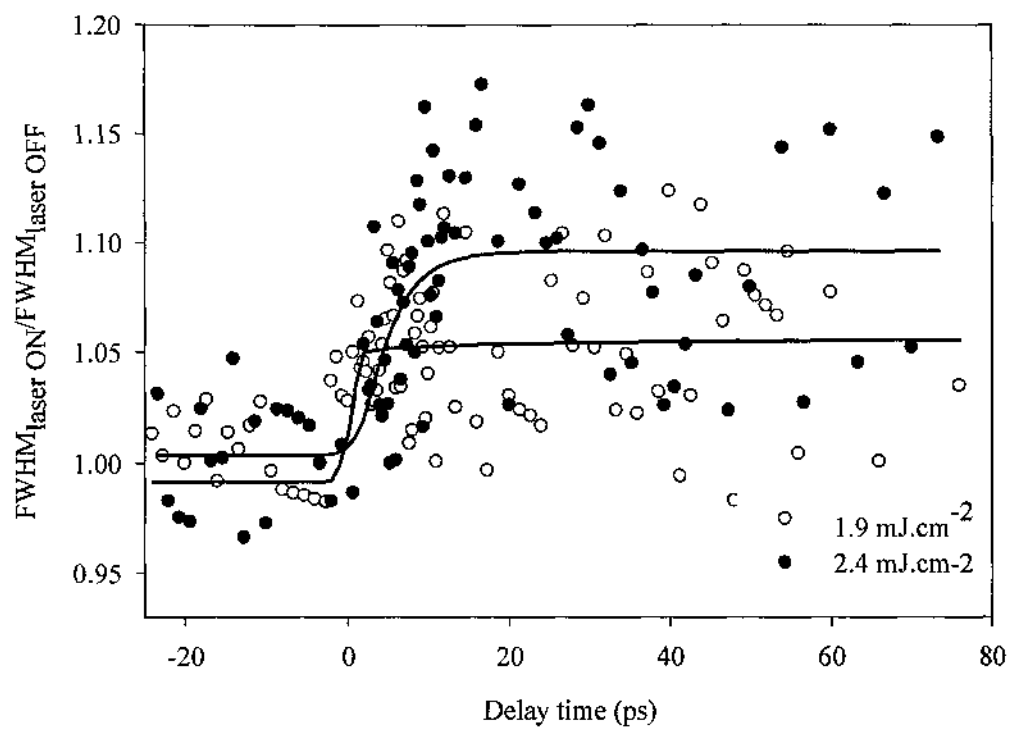
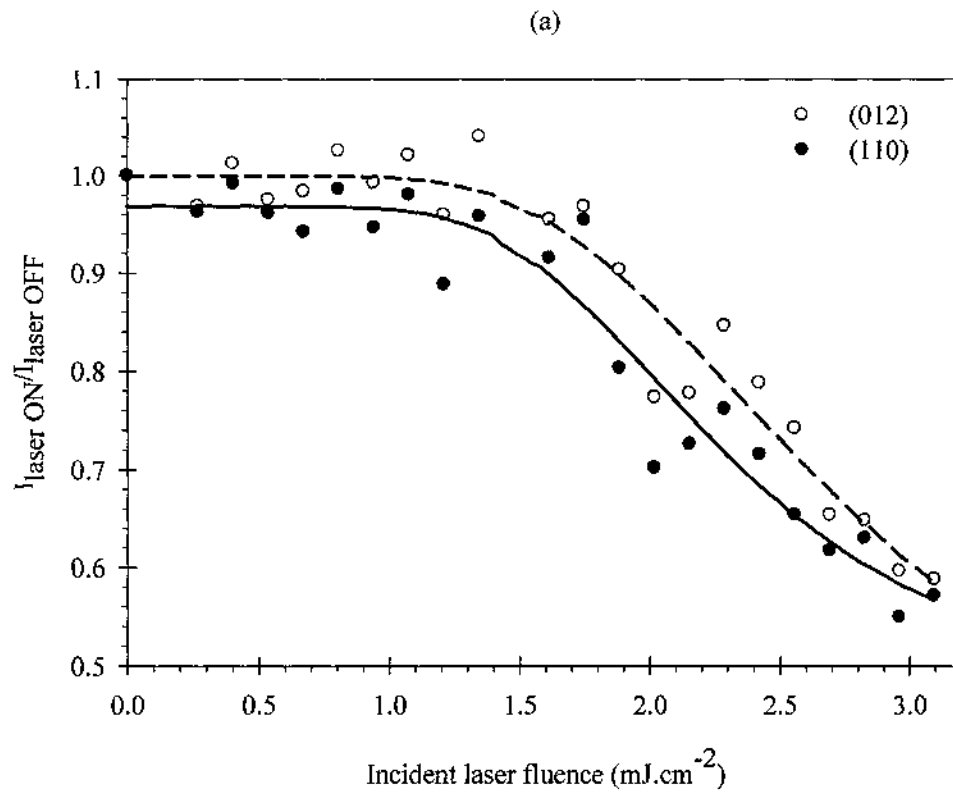
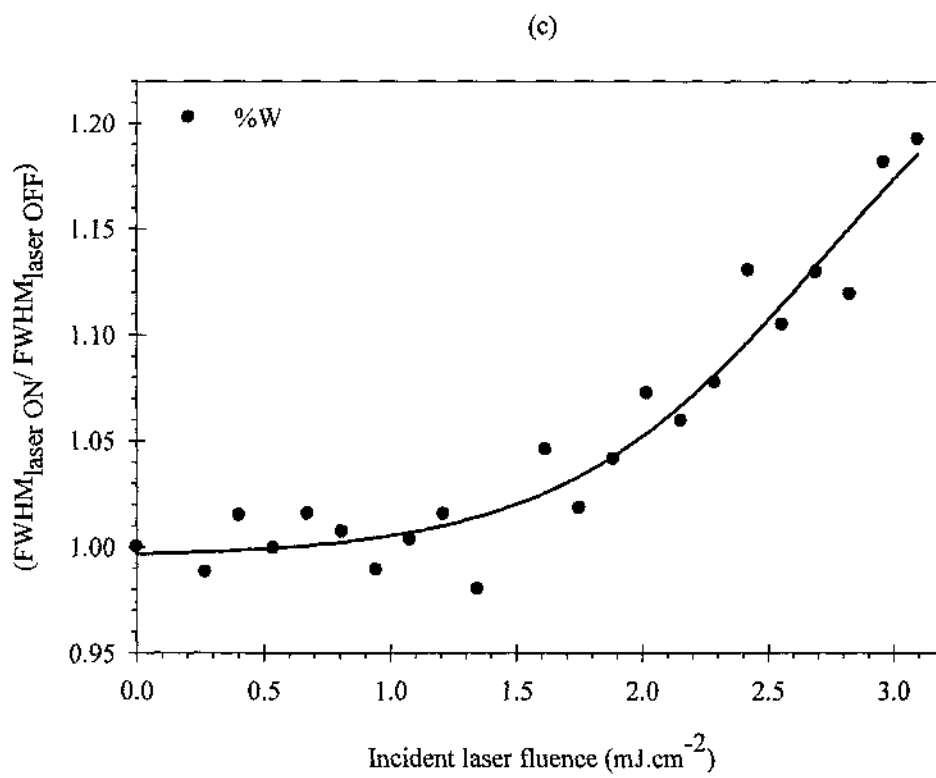
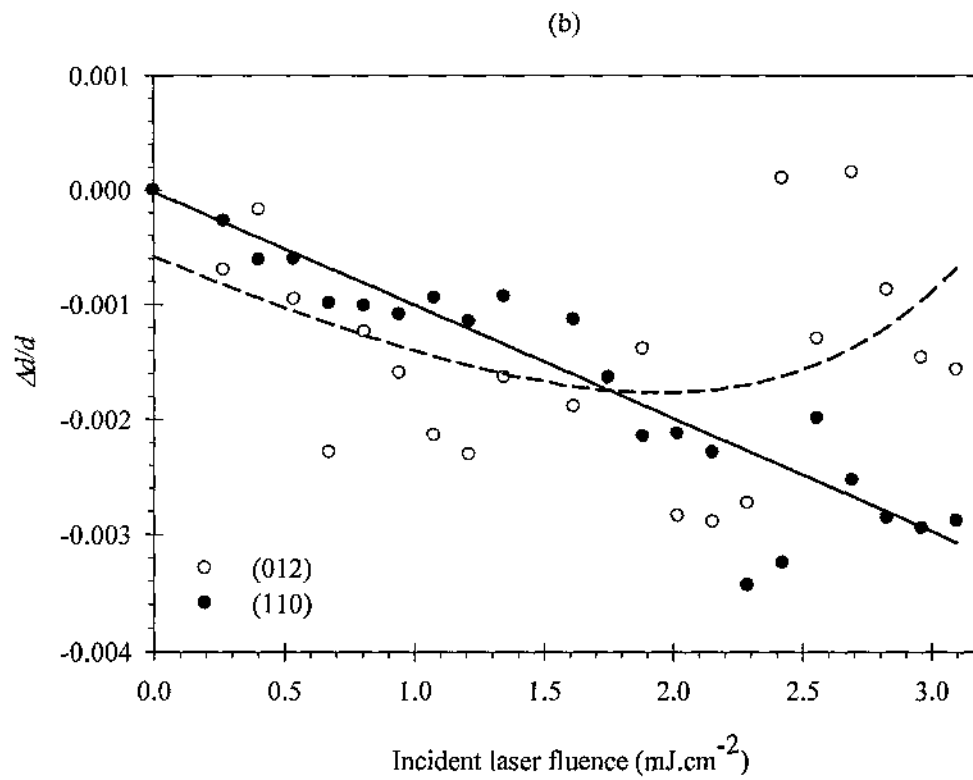


Fig. K.4. Fluence dependence of the Bragg (a) peak intensity, (b) $\Delta d/d$, and (c) normalized FWHM.

08/11/10



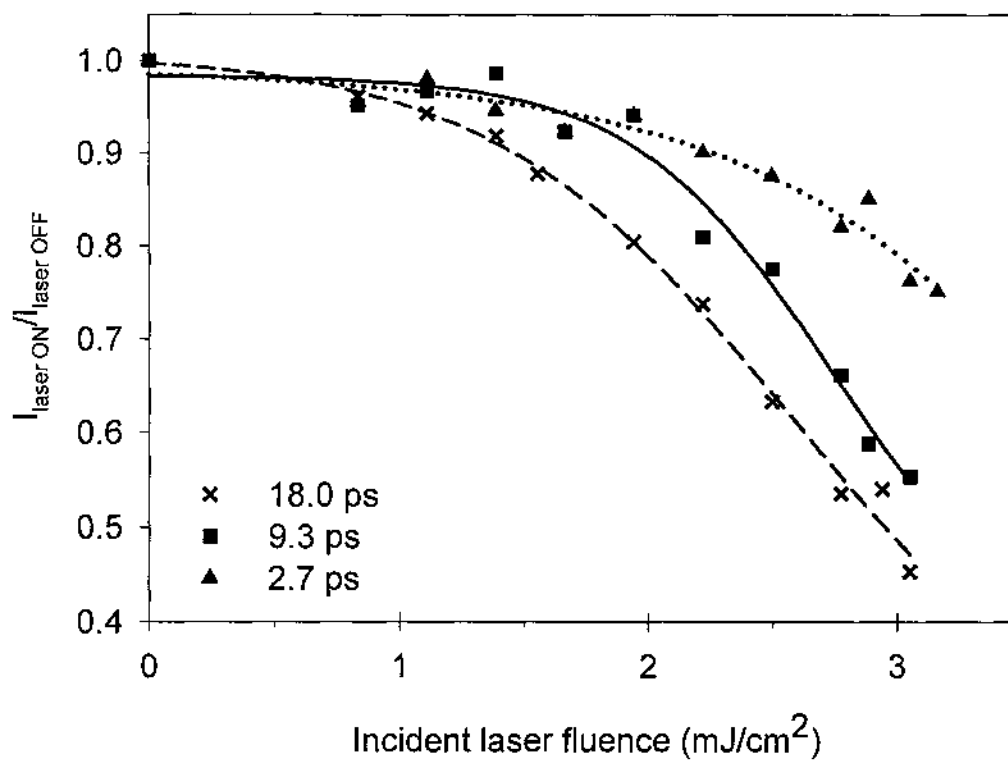


APPENDIX L

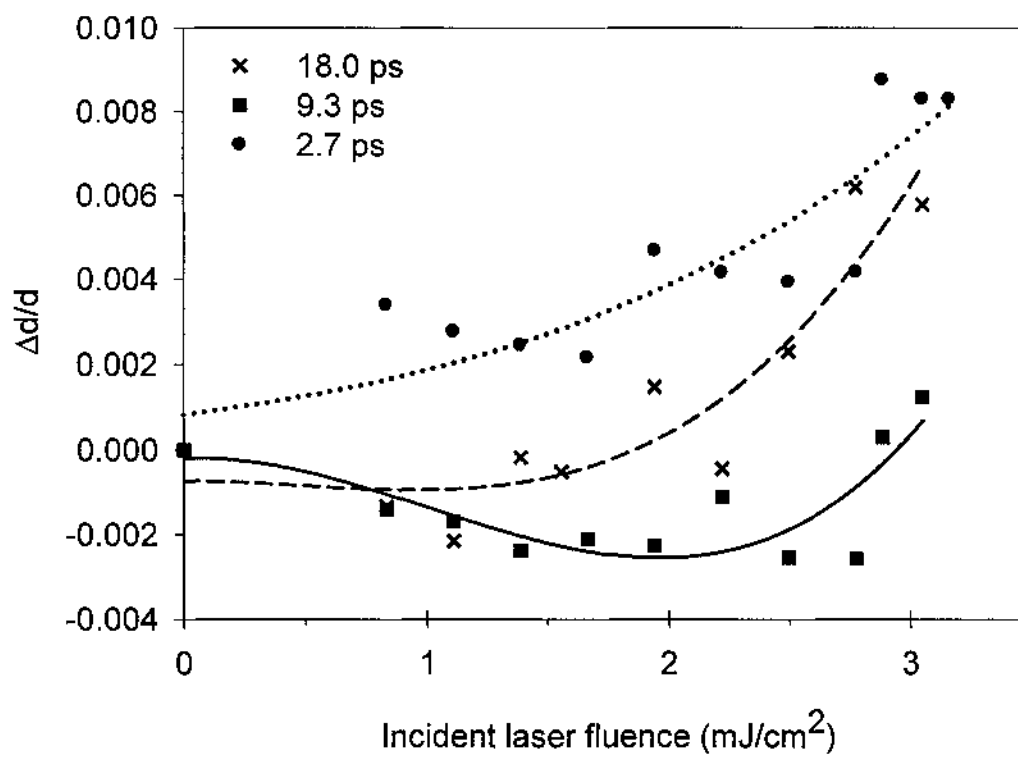
DATA COLLECTED TO STUDY SUPERHEATING OF BISMUTH ISLANDS

- The following power scans are made while the base temperature of the sample is at 373 K.
- The error in calculating the fluence is high, because it was discovered that the pump beam size is changing whenever an alignment is made to the regenerative amplifier, which is a factor that is not taken into account here when the laser fluence is calculated.
- The data were not repeated.
- Based on the previous comments, I can not make any conclusive remarks about them, but from these data, I expect a superheating in the Bi samples which needs further and detailed study.
- From the time resolved data, it is also showing the transient time dependence on the laser fluence.
- For these kinds of samples (Bi islands), the data for the strain ($\Delta d/d$) is just a set of scattered points.

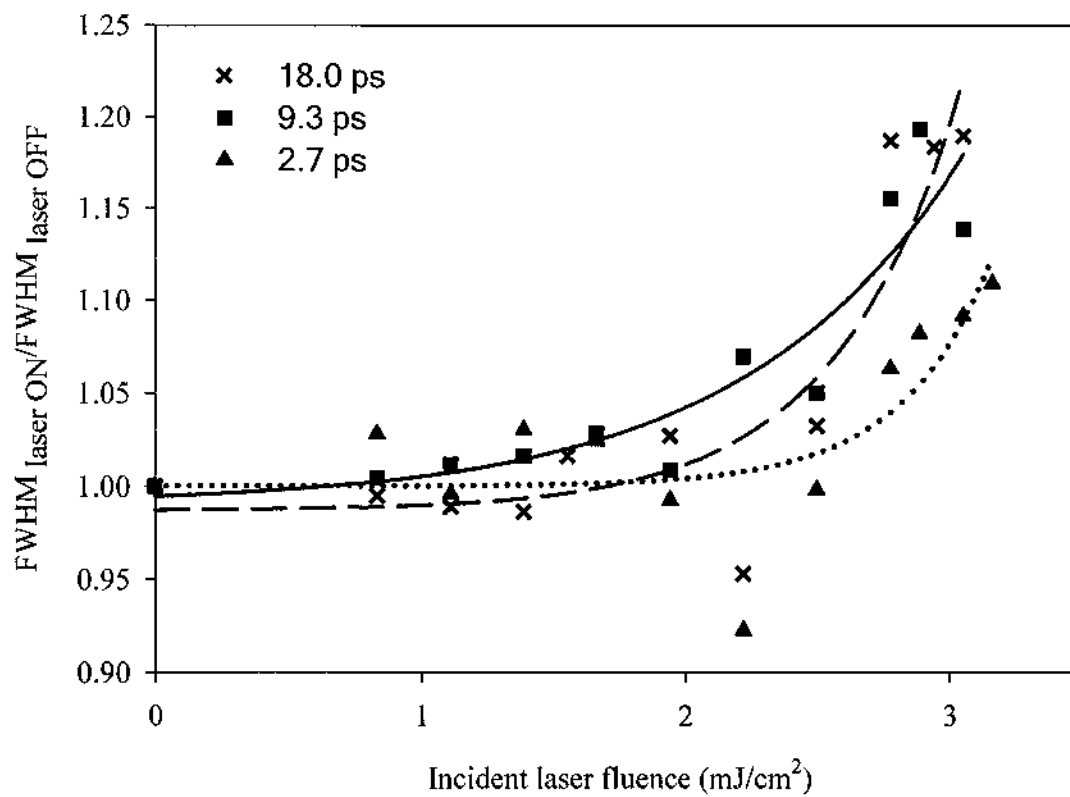
(012)



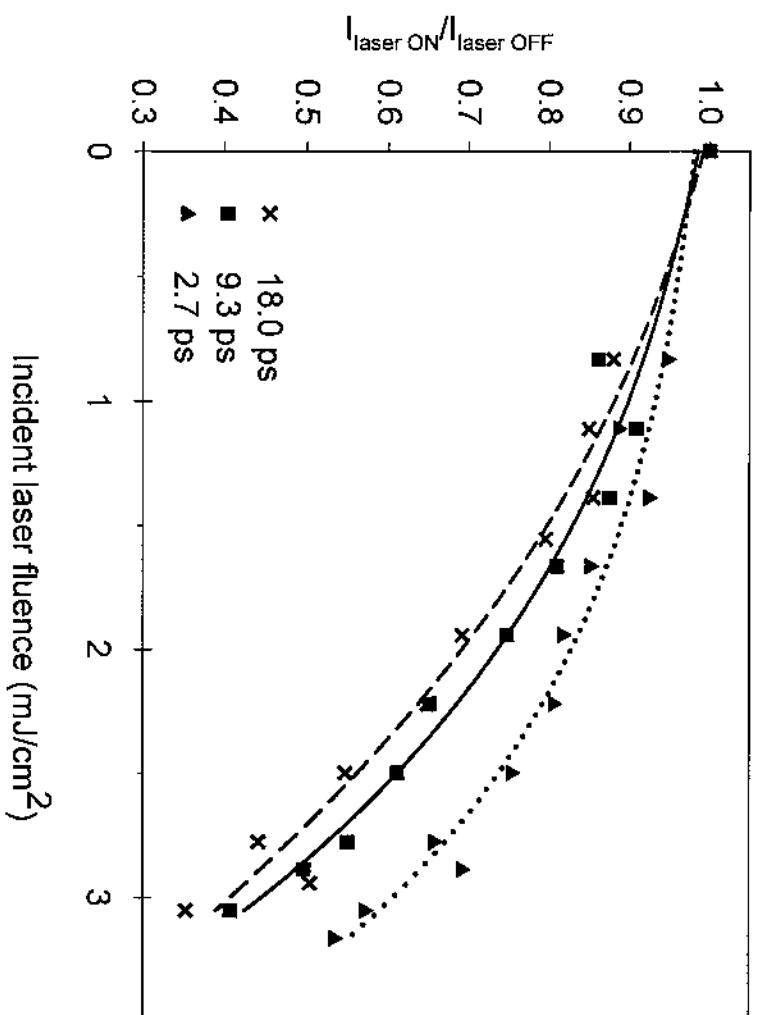
(012)



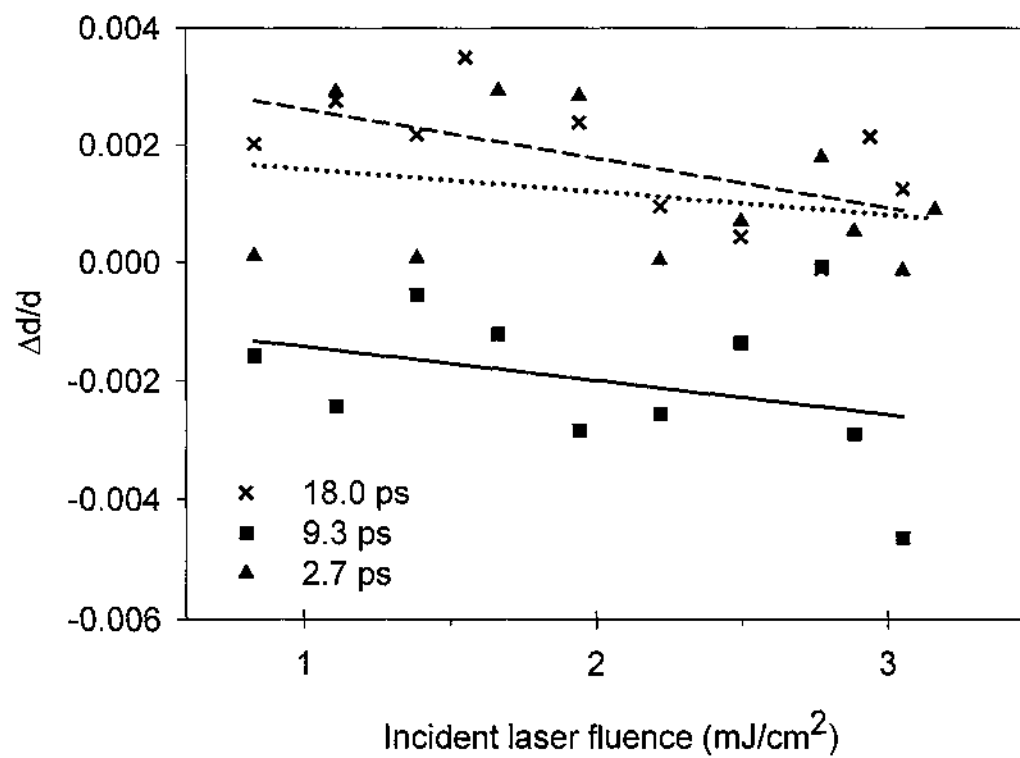
Normalized FWHM calculated from (012) Bragg peak as a function of the incident laser fluence at different delay times.



(110)

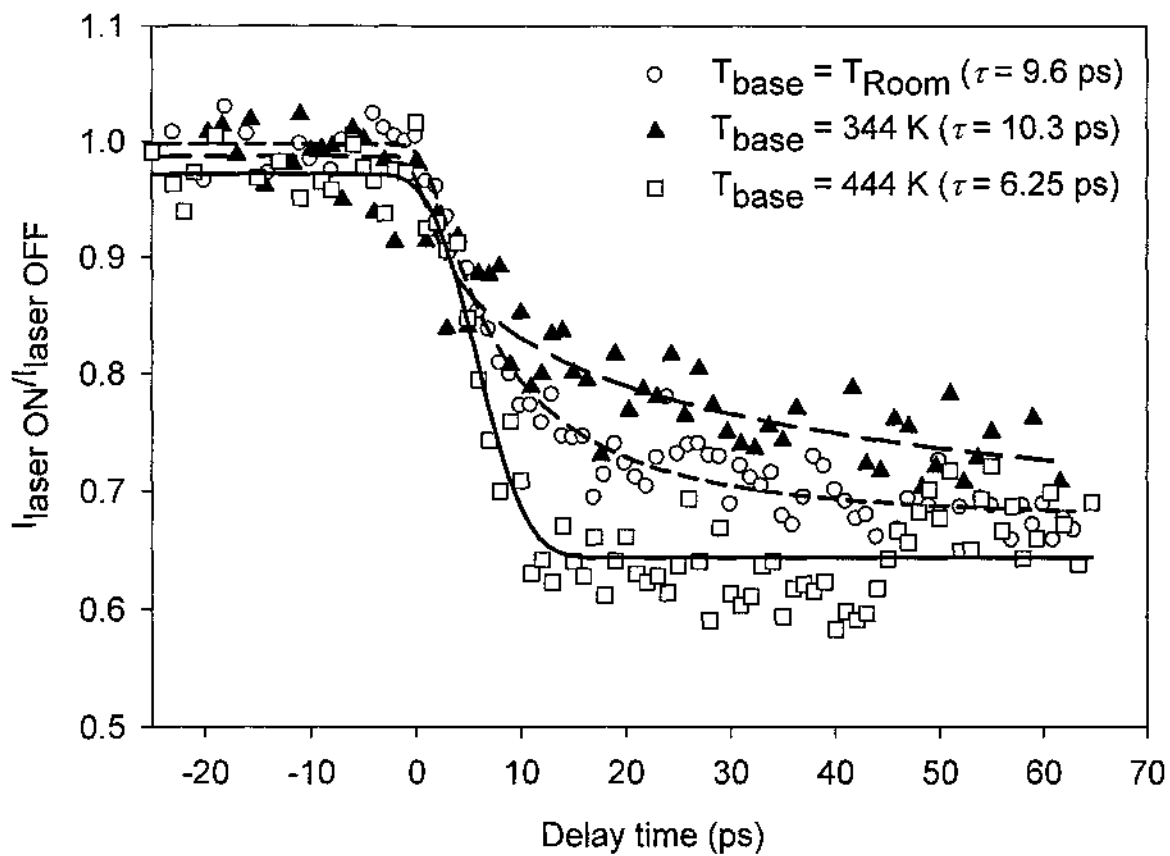


(110)

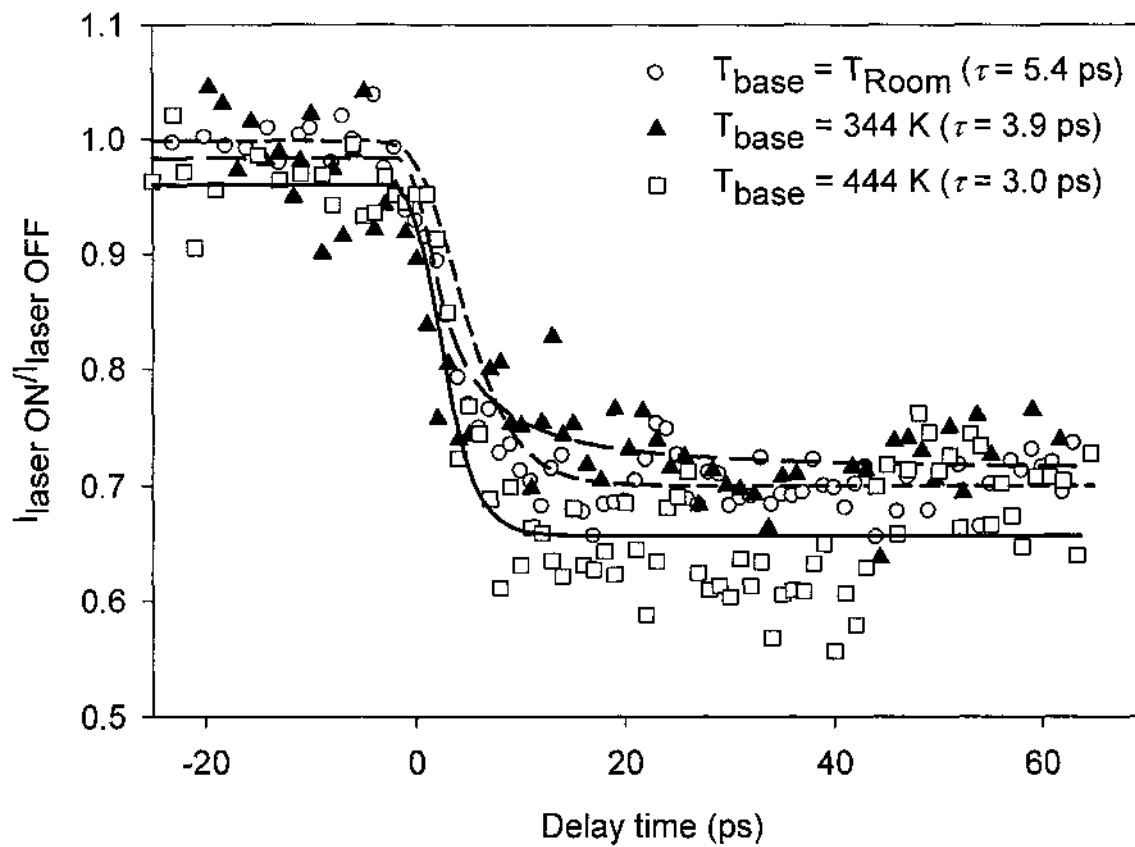


Time-resolved data

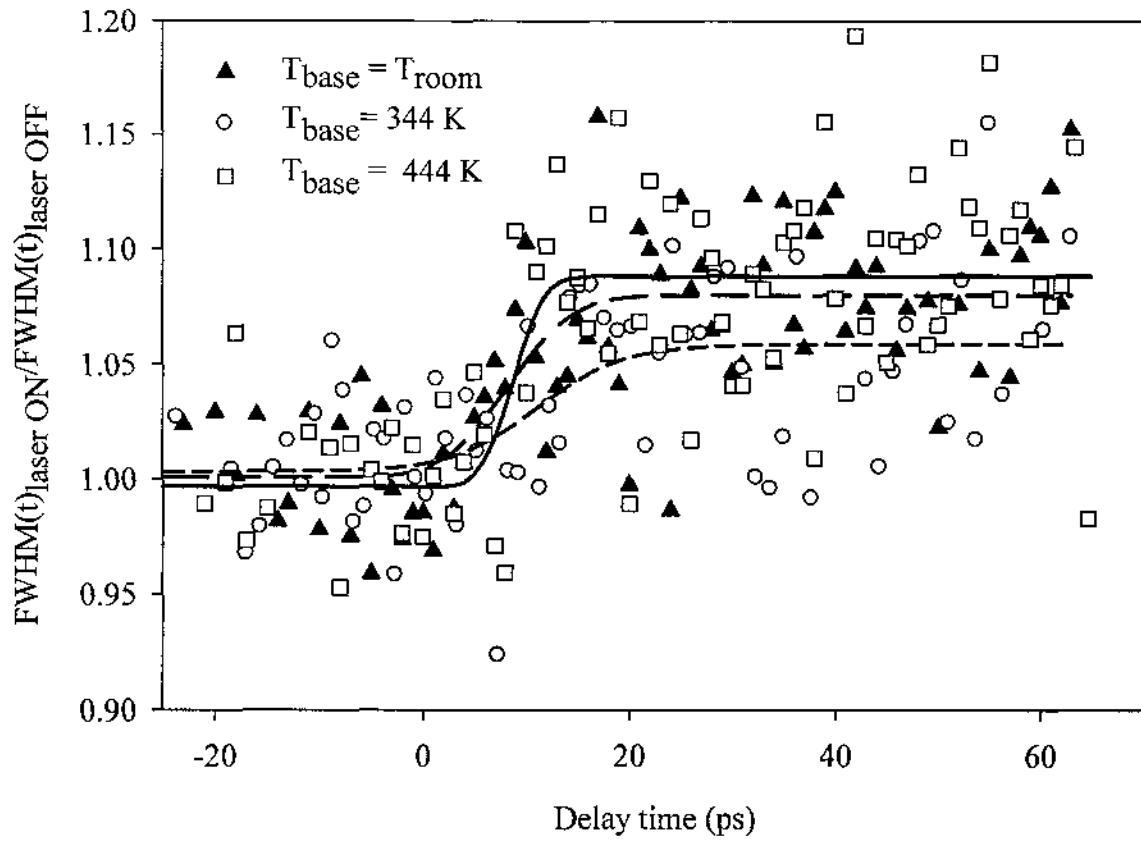
Time-dependent normalized Bragg peak intensity of Bi(012) planes at pump laser fluence = 2.5 mJ/cm^2



Time-dependent normalized Bragg peak intensity of Bi(110) planes at pump laser fluence = 2.5 mJ/cm²



Time-dependent normalized Bragg peak FWHM of Bi(012) planes at pump laser fluence = 2.5 mJ/cm²



APPENDIX M

LIST OF VENDORS AND DIFFERENT COMPONENTS USED IN FILM PREPARATION AND TIME-RESOLVED ELECTRON DIFFRACTION SETUP

L.1 Thermal Evaporation System

Unit description	Part number	Vendor
6 way high grade stainless steel vacuum chamber.	407008	http://www.mdcvacuum.com
UHV valve	313037	
70 l/s Turbo molecular pump	TG70FCND	http://www.osakavacuum.co.jp/en/
Mechanical pump	RV3	http://www.edwardsvacuum.com/
Evaporation filaments	-B5-0.04W -F12-3X0.030W	http://www.rdmathis.com/
TEM grids	Cu-400CN	http://www.grid-tech.com/
Inficon deposition monitor	XTM/2	http://www.inficonthinfilmdesposition.com/en/index.html

L.2 Time-Resolved Electron Diffraction System

Unit description	Part number (if applicable)	Vendor
Darwin 30 W pump laser	DARWIN-527-30-M	http://www.quantronixlasers.com/
Tsunami Ultrafast Ti:Sapphire Laser	3941-MIS USP	http://www.newport.com/
Regenerative Amplifier	SPITFIRE	
Ultrafast laser mirrors	TLM1-800-45P-1025	http://cvimellesgriot.com/Products/Products.aspx
Ultrafast beam splitter	BS1-800-30-1012-45UNP	
Delay stage	UTM100-PE.1	http://www.newport.com/Optical-Delay-Line-Kit/396220/1033/catalog.aspx
CCD camera, Pixis1024	7520-0001	http://www.princetoninstruments.com/?gclid=CMmA2v7gqKUCFeYD5QoqxYV7A
Custom made high grade stainless steel vacuum chamber	---	http://www.lesker.com
Rotational manipulator	HTBRM-275-12	www.mdcvacuum.com
XYZ manipulator	PSM-1502	
Perkin-Elmer ion pump, 220 l/s	---	http://www.duniway.com/html/cs-ip-section.htm
Turbo-Molecular pump, 300 l/s	V300-HT	http://www.varianinc.com
Mechanical pump	949-9315	
MCP/phosphorous screen assembly	---	http://www.burle.com/mcp_pmts.htm
High voltage power supply (screen)	PS350/5000V-25W	http://www.thinksrs.com/
High voltage power supply (MCP)	05R	
E-gun high voltage power supply	FC50N2.4	http://www.glassmanhv.com/glassman_tech.shtml

CURRICULUM VITAE FOR AHMED ESMAIL

EDUCATION

Master of Science (Physics), Cairo University, Egypt, 1997
Bachelor of Science (Physics), Cairo University, Egypt, 1990

TEACHING EXPERIENCE

Division of Languages, Mathematics, And Sciences, Tidewater
Community College, Chesapeake, VA
Assistant Professor (Adjunct), January 2010 – present

Department of Electrical and Computer Engineering, Old Dominion
University, Norfolk, VA
Research Assistant, November 2001 – December 2010
Teaching assistant, August 2001 – December 2010

Department of Physics, United Arab Emirates, Al-Ain, Abu-Dhabi
Physics Instructor, August 1998 – November 2001

Department of Physics, American University in Cairo, Cairo
Physics Instructor, August 1995 – August 1998

Department of Physics, Cairo University, Cairo
Teaching Assistant, December 1991 – August 1998

COURSES TAUGHT

Mechanics, Electricity and Magnetism, Electric Circuit, digital Electronics,
Modern Physics, Nuclear Physics, Solid State Physics, and designed and
maintained the website of ECE495/486 website

RESEARCH EXPERIENCE

Operated and maintained different laser systems (Ti:Sapphire femtosecond
and Nd:YAG picosecond lasers)
Operated and maintained different vacuum systems (containing ion pumps
and turbo molecular pump stations)
Operated and maintained Atomic Force Microscopy (AFM)
Designed, assembled and maintained a high energy photoactivated electron
sources
Deposited and characterized metallic and non-metallic thin films and
nanostructures

HONORS AND AWARDS

First place winner, American Vacuum Society, Mid-Atlantic Chapter Poster
Competition, April 2010
Second place winner, American Vacuum Society, Mid-Atlantic Chapter
Poster Competition, April 2009

Old Dominion University Scholarship, 2001-1010

Dr. M. Mokhtar Excellence Award (awarded to Physics graduates with Excellence), summer 1990

LIST OF PUBLICATIONS AND NATIONAL MEETING POSTERS

1. **A. Esmail**, H. Elsayed-Ali, "Quantum size effects in bismuth nanoclusters," AVS Mid-Atlantic Chapter, Science and Technology of Materials, Interfaces, and Processing - Jefferson lab., Newport News, VA., April 2011.
2. **A. Esmail**, M. Abdel-Fattah, H. Elsayed-Ali, "Nonuniformity in lattice contraction of bismuth nanoclusters," J. Appl. Phys., 109, 084317 (2011).
3. A. Bugayev, **A. Esmail**, M. Abdel-Fattah, and H. Elsayed-Ali, "Coherent phonons in bismuth film observed by ultrafast electron diffraction," AIP Advances 1, 012117(1-5) (2011).
4. A. Bugayev, M. Abdel-Fattah, **A. Esmail**, and H. Elsayed-ali, "Coherent phonons in polycrystalline bismuth film monitored by ultrafast electron diffraction," CLEO: Laser science to photonic applications, March 2011.
5. **A. Esmail**, H. Elsayed-Ali, "Time-resolved high energy electron diffraction study of semimetal-semiconductor phase transition in bismuth nanoclusters," (To be published, 2011).
6. **A. Esmail**, H. Elsayed-Ali, "Ultrafast electron diffraction study of photoexcited bismuth nanoclusters," AVS Mid-Atlantic Chapter, Science and Technology of Materials, Interfaces, and Processing - Jefferson lab. Newport News, VA., April 2010.
7. **A. Esmail**, H. Elsayed-Ali, "Study of solid-liquid phase transition in bismuth nanocrystals," AVS Mid-Atlantic Chapter, Science and Technology of Materials, Interfaces, and Processing - Jefferson lab. Newport News, VA., April 2009.
8. **A. Esmail**, H. Talaat, Y. A. Badr., "Raman study of phase transition in Lithium Ammonium Sulphate (LAS) single crystal," International conference in Laser spectroscopy and its applications, Cairo University, Fall 1996.
9. **A. Esmail**, H. Talaat, Y. A. Badr., "Order - Disorder phase transition in LAS single crystal," International conference in Laser spectroscopy and its applications, Cairo University, Fall1996.

ATTENDED SEMINARS, SUMMER SCHOOLS, AND CONFERENCES

1. American Vacuum Society, AVS Mid-Atlantic Chapter, Science and Technology of Materials, Interfaces, and Processing - Jefferson lab. Newport News, VA., April 2011
2. American Vacuum Society, AVS Mid-Atlantic Chapter, Science and Technology of Materials, Interfaces, and Processing - Jefferson lab. Newport News, VA., April 2010.
3. American Vacuum Society, AVS Mid-Atlantic Chapter, Science and Technology of Materials, Interfaces, and Processing - Jefferson lab. Newport News, VA., April 2009.
4. Atomic force microscopy training course, Applied Research Center, Newport News, 2008.

5. Introductory Course in programming with Visual Basic, United Arab Emirates University, 2000.
6. Electron microscopy course, Cairo University, 1996.
7. International Conference in Laser and its application, National Institute for Laser Enhanced Sciences, Cairo University, 1996.
8. FT- IR and FT- Raman spectroscopy course, Cairo University, 1996.
9. International course in symmetry and optical properties of solids, American University in Cairo, 1995.

COMPUTER SKILLS

1. Operating systems (Windows platforms).
2. Application software, MS Office, VISIO.
3. SigmaPlot and Origin (graphing, data fitting and analysis).
4. ImageJ (image processing and analysis).
5. Video editing.
6. Website design (Dream-Weaver and MS FrontPage)
7. Computer hardware and software, building and maintaining computer hardware

MEMBERSHIP

1. American Physical Society
2. American Chemical Society